Justus-Liebig-Universität Gießen

Fachbereich Medizin

Klinik für Diagnostische und Interventionelle Radiologie

„Entwicklung und Stellenwert der kardialen Magnetresonanztomografie“

Kumulative Habilitationsschrift

zur Erlangung der Lehrbefähigung für das Fach Radiologie im Fachbereich Medizin der Justus-Liebig-Universität Gießen

vorgelegt von

Dr. med. Fritz Christian Roller

Gießen 2021

Für Anna

und Fritz Hagen, Helene Sophia, Gergor Hubertus,

Bendix Laurenz und Grete Maria,

Fritz, Christiane † und Anneliese †

Inhaltsverzeichnis

Abkürzungen und Synonyme

CT	Computertomografie
ECV	extrazelluläres Verteilungsvolumen (engl. extracellular volume)
EGER	engl. early gadolinium enhancement ratio
ER	engl. edema ratio
FOV	Sichtfeld (engl. field of view)
FT	engl. feature tracking
LGE	engl. late gadolinium enhancement
LVEF	linksventrikuläre Ejektionsfraktion
LVH	linksventrikuläre Hypertrophie
MOLLI	modified look-locker inversion recovery (Sequenztyp)
mPAP	mittlerer pulmonalarterieller Druck (engl. mean pulmonary arterial pressure)
MRT	Magnetresonanztomografie
PVR	Pulmonaler Gefäßwiderstand (engl. pulmonary vascular resistance)
ROI	Regionen von Interesse (engl. regions of interest)
RVEF	rechtsventrikuläre Ejektionsfraktion
RVIP	rechtsventrikulärer Insertionspunkt
SSFP	steady-state free precession (Sequenztyp)
T1	Konstante der longitudinalen Relaxationszeit

1. Einleitung

1.1. Entwicklung und Stellenwert der kardialen Magnetresonanztomografie (MRT)

Die kardiovaskuläre Magnetresonanztomografie (MRT) hat sich über die beiden letzten Jahrzehnte in der klinischen Routine bei einer Vielzahl der kardialen Erkrankungen zu einer tragenden diagnostischen Säule entwickelt. Unter anderem stellt die kardiale MRT den Goldstandard in der Quantifizierung der links- und rechtsventrikulären Herzfunktion dar [1] und hat sowohl eine herausragende Rolle in der Ischämiediagnostik [2, 3] als auch für die Gewebecharakterisierung [4] erlangt.

Durch die relativ freie Wahl an anatomischen Schnittebenen können kardiale Anatomie, Herzfunktion, myokardiale Morphologie (mit und ohne den Einsatz von gadoliniumhaltigen Kontrastmitteln), Flussmessungen und angiografische Darstellungen bei hoher Reproduzierbarkeit der Ergebnisse in nur einer einzigen MRT-Untersuchung abgebildet werden. Insbesondere die Möglichkeit gleichzeitig Funktion und Morphologie beurteilen zu können, stellt ein absolutes Alleinstellungsmerkmal der kardialen MRT dar. Um die Jahrtausendwende war das Spektrum für kardiale MRT-Untersuchungen noch deutlich eingeschränkter und kardiale MRT-Untersuchungen wurden vorwiegend zur Charakterisierung von komplexen angeborenen Herzfehlern oder von Herztumoren angefertigt. Seitdem hat sich das Indikationsspektrum, auch durch den rasanten technischen Fortschritt und neue Entwicklungen sowie eine immer breitere Verfügbarkeit von modernen MRT-Geräten, deutlich ausgeweitet. Bei einer Vielzahl von unterschiedlichen kardiovaskulären Erkrankungen und Fragestellungen ist die kardiale MRT mittlerweile der Goldstandard bzw. die Bildgebungsmethode der ersten Wahl. Einen sehr guten, evidenzbasierten Überblick der Indikationen für kardialen MRT-Untersuchungen liefern die bereits 2011 veröffentlichten Konsensusempfehlungen der

Deutschen Gesellschaft für Radiologie, der Deutschen Gesellschaft für Kardiologie und der Deutschen Gesellschaft für Kinderkardiologie [5]. Allerdings bedürfen die Konsensusempfehlungen mittlerweile dringend, auch aufgrund der sehr guten wissenschaftlichen Datenlage und der gewonnen neuen Erkenntnisse, einer Überarbeitung.

Es ist davon auszugehen, dass sich das Indikationsspektrum für kardiale MRT-Untersuchungen dann noch ausweiten wird und einige bereits bestehende Indikationen – evidenzbasiert – in ihrem Indikationslevel weiter aufgewertet werden könnten. Neben den technischen Entwicklungen und der breiten Verfügbarkeit an modernen MRT-Geräten hat auch der stetige und nachhaltige Therapiefortschritt bei unterschiedlichen kardiovaskulären Erkrankungen einen relevanten Anteil am großen Erfolg der nicht-invasiven kardialen MRT-Diagnostik. Die Verlängerung der Lebenserwartung bei Patienten mit angeborenen Herzfehlern, 90% der Patienten mit angeborenen Herzfehlern erreichen mittlerweile das Erwachsenenalter [6], und die deutlich gesunkene Mortalität der koronaren Herzerkrankung, seit den 50er Jahren hat die Mortalität um etwa 60% abgenommen [7], führen zu einer Vielzahl an Folgeuntersuchungen. Fortschritte und Erfolge in Therapie und Diagnostik beeinflussen sich gegenseitig.

In den letzten Jahren haben neue MRT-Techniken Einzug in die kardiale MRT-Diagnostik gefunden und ergänzen die bereits etablierten Methoden. Die parametrische Bildgebung (das sogenannte Mapping), die eine Bestimmung und Quantifizierung gewebespezifischer Zeitkonstanten auf Voxelbasis im Myokard erlaubt, hat aufgrund ihrer hohen und untersucherunabhängigen Reproduzierbarkeit große Vorteile bei der myokardialen Gewebecharakterisierung verglichen zu den traditionell angewendeten Techniken der Gewebecharakterisierung im MRT.

Auch und gerade deswegen hat das myokardiale Mapping bereits Einzug in klinisch etablierte Diagnosealgorithmen, wie die erneuerten „Lake-Louise-Kriterien“ für die Diagnostik der nicht-ischämischen myokardialen Inflammation, gefunden [8]. Vielmehr noch erweist sich Mapping nicht nur in der Primärdiagnostik [9-11], sondern auch im Follow-up [12] bzw. dem Therapiemonitoring [13, 14] und als „Prognostikator“ [15, 16] in einigen Studien bei unterschiedlichen kardiovaskulären Erkrankungen als äußerst vielversprechend.

Neben der parametrischen Bildgebung könnten in Zukunft auch regionale myokardiale Wandbewegungsanalysen (sogenannten Strainanalysen), die über eine rein deskriptive Analyse der Wandbewegung in „steady-state free precession“ (SSFP) CINE-Sequenzen hinausgehen, die kardiale MRT-Diagnostik weiter verbessern und aufwerten. In ersten Studien konnten auch für Strainanalysen schon gute Ergebnisse gezeigt werden [17-19]. Beide Techniken besitzen somit viel Potential den Triumphzug der ohnehin so erfolgreichen und robusten Methode weiter auszubauen.

1.2. Extrakardiale Nebenbefunde in der nicht invasiven-Bildgebung kardialen Bildgebung

Für einige radiologische Untersuchungen, wo neben dem Zielorgan oder der Zielregion weitere partiell oder vollständig erfasste Organsystemen mitabgebildet werden, sog. Querschnittsuntersuchungen, wurden die Inzidenzen für zufällige Nebenbefunde bereits ausgiebig untersucht. So z.B. auch für die kardiale Computertomografie (CT) [20-25].

Die deutlich zunehmende Anzahl der kardialen MRT-Untersuchungen führt durch ein das Herz teils deutlich übersteigendes „field-of-view“ (FOV, Sichtfeld) und durch die Durchführung von Planungssequenzen zu einer partiellen oder vollständigen Abbildung

von thorakalen und abdominellen Organen und einer damit einhergehenden zufälligen Detektion von Nebenbefunden.

Grundsätzlich kann man signifikante und nicht-signifikante, zufällig detektierte extrakardiale Nebenbefunde unterscheiden. Nicht-signifikante extrakardiale Nebenbefunde, sind Befunde, die keiner weiteren Abklärung bedürfen bzw. keinen Einfluss auf den weiteren diagnostischen und therapeutischen Patientenpfad haben (z.B. blande Nieren- oder Leberzysten). Hingegen sind signifikante extrakardiale Nebenbefunde, Befunde, die eine weitere radiologische oder klinische Abklärung, weitere Laboruntersuchungen oder gar weitere therapeutische Interventionen erforderlich machen [26]. Es kann sich bei signifikanten extrakardialen Nebenbefunden auch um Befunde handeln, die für Beschwerden des Patienten verantwortlich sein könnten (z.B. eine klinisch nicht detektierte Rippenfraktur oder eine segmentale Lungenembolie, die eine kardiale Genese der Beschwerden vortäuschen), Befunde, die mehr oder weniger dringend einer weiteren Abklärung oder Kontrolle bedürfen (z.B. pulmonale Herdbefunde in Abhängigkeit ihrer Größe und dem Patientenrisikoprofil - Kriterien der Fleischner Gesellschaft [27]; zystische Pankreasläsionen - Kriterien des American College of Radiology [28]). Ein Tumornachweis kann in Abhängigkeit der Tumorentität und des Tumorstadiums einen geplanten transkutanen Aortenklappenersatz oder andere Kardiointerventionen verzögern oder gar verhindern.

Bei der Diagnostik und der Charakterisierung solcher Nebenbefunde kommt erschwerend hinzu, dass kardiale MRT-Untersuchungen überhaupt nicht für die Primärdiagnostik anderer Organsysteme bzw. angeschnittener Körperregionen optimiert sind. Das heißt, dass für die weitere Analyse und eine abschließende Beurteilung der Nebenbefunde, zum Beispiel bei unklaren Leberläsionen, aufwändige Ultraschall-, Computertomografie (CT)- oder MRT-Untersuchungen notwendig werden können. Diese

Untersuchungen sind dann mit Zeitaufwand und Folgekosten verbunden. Auch für die kardiale MRT gibt es bereits Studien, die die Relevanz von zufällig detektieren Nebenbefunden untersucht haben [29-31]. In einer Metaanalyse mit insgesamt 12 Studien und 7062 Patienten, konnten für 12% der Patienten signifikante, zufällig detektierte, extrakardiale Nebenbefunde gezeigt werden, die bei 1% der Patienten sogar einen Wechsel des Patientenmanagements zur Folge hatten [32].

2. Technische Grundlagen der kardialen MRT

2.1. Traditionelle MRT-Methoden zur Gewebedifferenzierung

Die kardiale MRT greift bei der myokardialen Gewebecharakterisierung traditionell auf drei Konzepte zurück, die vereint in den Lake-Louise-Kriterien den sogenannten und bisher anerkannten Goldstandard in der Diagnostik der nicht-ischämischen myokardialen Inflammation darstellen [33]. Bei den drei Konzepten handelt es sich um:

1. Nachweis eines myokardialen Ödems,
2. Nachweis einer myokardialen Hyperämie und
3. Nachweis von Narbengewebe.

Der Nachweis einer akuten Schädigung des Myokards wird mittels T2-gewichteter Techniken über eine Visualisierung myokardialer Ödeme ermöglicht. Dabei kann das myokardiale Ödem sowohl Ausdruck einer akuten Ischämie des Herzmuskels als auch Ausdruck einer akuten Inflammation sein.

In der Bildgebung der myokardialen Inflammation kommen für den Nachweis einer myokardialen Hyperämie zudem T1-gewichtete Techniken (Bildakquisition vor und nach Applikation von gadoliniumhaltigen Kontrastmitteln) zur Anwendung. Die Entzündungsreaktion des Myokards wird von einer durch Vasodilatation hervorgerufenen Mehrdurchblutung/Hyperämie begleitet. Durch die vermehrte

Perfusion und das erhöhte Blutvolumen zeigt sich eine vermehrte Anflutung von Kontrastmittel nach Bolusinjektion.

Sowohl die Ödembildgebung als auch die Hyperämiebildgebung sind bei der Beurteilung diffuser myokardialer Krankheitsprozesse allerdings limitiert. Deswegen wird versucht, myokardiale Ödeme und myokardiale Hyperämie semiquantitativ im Vergleich zur Skelettmuskulatur als „edema ratio (ER)“ und „early gadolinium enhancement ratio (EGER)“, zu analysieren. Dabei zeigt sich für die ER allerdings eine deutlich bessere Detektionsrate bei akuten Myokarditiden [34] gegenüber chronischen Krankheitsverläufen [35]. Zudem wird bei Patienten, die gleichzeitig an einer entzündlichen Skeletterkrankung leiden, durch Wassereinlagerungen im Gewebe unter Umständen ein falsch-negativer Befund erhoben. Neben solchen diagnostischen Ungenauigkeiten und Einschränkungen leiden beide Techniken auch an ihrer großen Artefaktanfälligkeit. Bewegung, Atmung und Arrhythmie verhindern die Detektion kleiner fokaler myokardialer Veränderungen [36].

Der Goldstandard für die Bildgebung von myokardialen Narben oder Fibrose, und der letzte Bestandteil des dreistufigen Konzepts der Gewebecharakterisierung, ist die Kontrastmittelspätanreicherung (das sogenannte „late gadolinium enhancement“). In der Kontrastmittelspätanreicherung wird das Myokard verzögert, das heißt mehr als 10 Minuten nach Kontrastmittelgabe, untersucht. Zu diesem Zeitpunkt zeigen sich vitale Myokardanteile schwarz und avitale Myokardanteile hell (getreu dem Motto „bright is dead“). Der Schwarz-Weiß-Kontrast dieser Technik beruht auf dem Auswasch-Verhalten des extrazellulären Kontrastmittels. Irreversibel geschädigte Myokardareale, z.B. im Rahmen eines Infarktes bei Zellnekrosen, erlauben einen Übertritt von Kontrastmittel in das interzelluläre Kompartiment bzw. ermöglicht die Erweiterung des interstitiellen

Raumes bei myokardialer Fibrose ebenfalls einen Übertritt des sonst extrazellulären Kontrastmittels.

Ursprünglich war das „late gadolinium enhacement“ (LGE) für die Infarktdiagnostik und die Visualisierung fokaler Zellnekrosen entwickelt worden, hat sich aber schon sehr schnell in der Bildgebung der Kardiomyopathien als wichtiger „Prognostikator“ herausgestellt. Das Vorhandensein von LGE ist bei Kardiomyopathien mit einem deutlich schlechteren Gesamtüberleben assoziiert, wie in Studien bei unterschiedlichen Kardiomyopathien schon gezeigt werden konnte [37-40]. Allerdings unterliegt auch das LGE Limitationen, denn zur Visualisierung von geschädigtem Myokard ist ein myokardialer Matrixumbau von mindestens etwa 15% erforderlich [41]. Potentiell relevante Myokardschädigungen unterhalb dieser Nachweisgrenze werden visuell gar nicht erfasst und zugrundeliegende Krankheitsprozesse können nicht erkannt werden. Da das Myokard zudem homogen schwarz oder weiß erscheint, werden neben fokalen Myokardschäden, die sich dem Nachweis entziehen insbesondere auch diffuse myokardiale Veränderungen erst gar nicht erfasst.

Bei allen drei Techniken der Gewebecharakterisierung handelt es sich somit um Techniken, die dafür optimiert sind, den Kontrast zwischen normalem/gesundem Gewebe und pathologischem/krankem Gewebe bezogen auf eine einzige Eigenschaft, Wassergehalt oder frühe bzw. späte Kontrastmittelaufnahme, zu maximieren. Hierdurch wird zwar eine visuelle und qualitative Beurteilung ermöglicht, Feinabstufungen oder gar Quantifizierungen sind, wie beschrieben, allerdings schlicht unmöglich.

2.2. Parametrische MRT-Methoden zur Gewebedifferenzierung

2.2.1. Technik T1-Mapping

Wie bereits angesprochen, lassen sich mittels LGE nur Myokardareale darstellen, die stark von einer Fibrosierung betroffen sind und sich eindeutig demarkieren. Über den Grad der Fibrose des restlichen Myokards [42], die Struktur des nicht LGE-positiven Myokards und über diffuse myokardiale Veränderungen lassen sich jedoch leider keine Aussagen treffen. Das bedeutet, dass LGE in der Diagnostik von Erkrankungen mit regional begrenzten Myokardschädigungen (akute oder chronische Infarkte) zwar ausreichend erscheint, aber bei kardialen Erkrankungen, wie zum Beispiel einer viral bedingten Myokarditis, die mit diffusen myokardialen Veränderungen einhergehen kann [43], nicht ausreichend ist.

Die parametrische Bildgebung stellt eine sehr gute Möglichkeit dar, die oben erörterten Schwächen der konventionellen MRT-Techniken bei der Gewebecharakterisierung zu überkommen und erlaubt eine quantitative Gewebebeurteilung anhand von absoluten Signalintensitäten zwischen unterschiedlichen MRT-Untersuchungen.

Beim Mapping wird eine prädefinierte Anzahl an Rohbildern, die zu unterschiedlichen Aufnahmezeitpunkten bei unterschiedlichen Inversionszeiten angefertigt werden, aufgenommen. Um eine Bildakquisition zum selben Zeitpunkt im Herzzyklus zu erreichen, erfolgt die Bildakquisition EKG-getriggert in der Regel in der Enddiastole. Nach einer softwaregestützten und automatischen Bewegungskorrektur werden für jeden Voxel Signalintensitätskurven ermittelt und für jede Voxel-Position die zugrundeliegende Gewebeeigenschaft quantifiziert. Die resultierenden Grauwerte des Voxels werden an der korrespondierenden Stelle in eine parametrische Karte (Map) eingetragen. Eine Kartenerstellung, auch als farbkodierte Karte, und Quantifizierung, kann je nach Wichtung sowohl für T1-Werte als auch für T2-Werte erfolgen. Die Werte werden in

Millisekunden (ms) angegeben. Es wurde bereits gezeigt, dass die T1-Zeiten durch Veränderungen in der Zusammensetzung des Interstitiums beziehungsweise des extrazellulären Volumens beeinflusst werden [44-46]. Erste Anhaltspunkte legen nahe, dass die T1-Zeiten mit einer myokardialen Fibrose korrelieren und deutlich veränderte Werte bei einer Reihe von kardialen Krankheitsprozessen aufweisen [47]. Unter anderem konnte schon gezeigt werden, dass die native T1-Zeit nicht nur bei Fibrose [48], sondern auch bei Ödem [49] und Amyloideinlagerung [50] erhöht ist und beim Morbus Fabry [51] und einer Eisenüberladung [52] reduziert ist.

Das T1-Mapping kann sowohl nativ als nach intravenöser Applikation von gadoliniumhaltigen Kontrastmitteln erfolgen. Allerdings ist eine alleinige Bestimmung der postkontrast T1-Zeiten in ihrer Aussage limitiert [53], denn im Gegensatz zum nativen T1-Mapping unterliegt das postkontrast Mapping mehreren Einfluss- bzw. Störgrößen. Einflussgrößen sind unter anderem die Nierenfunktion bzw. die Ausscheidung des Kontrastmittels, der Zeitpunkt der Messung nach erfolgter Kontrastmittelapplikation sowie die absolute Kontrastmitteldosis, die körperliche Konstitution und der Hämatokritwert. Deswegen können die postkontrast T1-Zeiten sehr stark variieren was eine Unterscheidung von normalem und pathologisch verändertem Myokard über die postkontrast T1-Zeiten erschwert [54]. Im Gegensatz dazu unterliegt das native T1-Mapping diesen Einflüssen nicht. Das native T1-Mapping kann sogar bei Patienten mit eingeschränkter Nierenfunktion äußerst vorteilhaft sein und das Risiko für eine Nephrogene systemische Fibrose (NSF) umgehen [55].

Beim nativen T1-Mapping kommen unterschiedliche Sequenzen zur Anwendung, die sich hinsichtlich Genauigkeit, Präzession und Reproduzierbarkeit unterscheiden [54]. Gerade „inversion recovery“ Sequenzen, wie die „modified look locker inversion recovery“ Sequenz (MOLLI), sind schon weitverbreitet und relativ ausgereift. Die MOLLI zeichnet

sich durch ein hohes Maß an Präzession und durch eine exzellente Reproduzierbarkeit aus, während die Genauigkeit eingeschränkt erscheint. Die gemessenen T1-Zeiten sind etwas unterschätzt, aber präzise und exzellent reproduzierbar [54].

2.2.2. Extrazelluläres Volumen - ECV

Wie schon beschrieben erschweren multiple Einflussfaktoren eine Unterscheidung von normalem und pathologisch verändertem Myokard anhand der postkontrast T1-Zeit [54]. Um solche Einflussfaktoren zumindest teilweise zu eliminieren, wurde das ECV eingeführt. Grundlage für die Berechnung des ECV bilden die vor und nach Kontrastmittelapplikation erstellten T1-Maps. Über den Partitionskoeffizient Lambda, Lambda ist definiert als die Differenz der T1-Zeiten im Myokard und im Blut vor und nach Kontrastmittelapplikation, und eine Hämatokritkorrektur lässt sich das ECV bestimmen. Die ECV-Bestimmung sollte in einem ausreichenden Equilibrium etwa 15 Minuten nach Kontrastmittelinjektion (Bolus) erfolgen [56, 57].

Die zugrundeliegende Formel für die Berechnung des ECV lautet:

ECV= (1 – Hämatokrit) * (1 / T1 Myokard postkontrast – 1 / T1 Myokard prekontrast) / (1 / T1 Blut postkontrast – 1 / T1 Blut prekontrast) [58]

Das ECV ist eine sensitive Methode bei der Beurteilung des Myokards, da das Verhältnis von zwei Kompartimenten, nämlich das Kompartiment der zellulären Bestandteile (vorwiegend Myozyten) und das Kompartiment der interstitiellen Bestandteile, berücksichtigt wird [47]. Das Verhältnis dieser beiden Kompartimente untereinander kann im Rahmen von myokardialen Krankheitsprozessen bzw. im Rahmen von physiologischen und pathophysiologischen Prozessen verändert sein [59]. Unter anderem konnte gezeigt werden, dass das postkontrast T1-Mapping für den nicht invasiven Nachweis einer myokardialen Fibrose geeignet ist [60]. Viel mehr noch konnten

schon Zusammenhänge zwischen einer ECV-Erhöhung und der Mortalität gezeigt werden [61]. Außer fibrotischen Veränderungen zeigen insbesondere Amyloideinlagerungen und das Myokardödem starke ECV-Erhöhungen [62].

3. Kardiale Wandbewegungsanalysen

3.1. Kardiale Funktionsbestimmung und Wandbewegungsanalyse

Die kardiale Funktionsanalyse erfolgt im MRT über die den linken Ventrikel komplett erfassenden Kurzachsenschnitte („steady state free precession"- SSFP CINE-Sequenzen), sogenannter Kurzachsenstapel, oder über einen transaxialen Stapel für die Funktionsanalyse des rechten Ventrikels. Ergänzend werden auch CINE Sequenzen im Zweikammerblick, Dreikammerblick und Vierkammerblick angefertigt, die zumindest visuelle Aussagen zu den Klappenfunktionen erlauben ohne allerdings Vitien näher quantifizieren zu können.

Über die CINE-Sequenzen wird neben der Analyse der absoluten und indizierten Ventrikelfunktion auch eine Analyse der regionären kardialen Wandbewegung ermöglicht. Dabei können globale und regionale Wandbewegungsstörungen zuverlässig beurteilt werden und dem etablierten 17-Segmentmodell der American Heart Association (AHA) zugeordnet werden [63]. Die regionalen oder globalen Wandbewegungsstörungen können dabei als Hypokinesie, Akinesie oder Dyskinesie beschrieben/klassifiziert werden. Einige Erkrankungen, wie z.B. die Tako-Tsubo-Kardiomyopathie mit ihrem „apical ballooning", einer apikalen und mittventrikulären Hypo-/Akinesie bei Persistenz der basalen Kontraktion, weisen sogar charakteristische Wandbewegungsmuster auf. Eine zuverlässige Quantifizierung der Wandbewegung wird über die CINE-Sequenzen allerdings nicht ermöglicht.

3.2. Regionale myokardiale Wandbewegungsanalyse - myokardialer Strain

Der myokardiale Strain gibt die relative Längenänderung (Verkürzung/Verlängerung) des Myokards während einer Herzkontraktion bezogen auf die Basislänge des Myokards in Ruhe an. Positive Werte entstehen bei Verlängerung und negative Werte bei Verkürzung des Myokards. Die Einheit ist dimensionslos und wird in Prozent angegeben [64]. Das ventrikuläre Myokard kann sich in unterschiedliche Richtungen verformen. Der globale longitudinale Strain (GL) beschreibt die Verformung des Myokards in Längsrichtung von der Basis zum Apex. Es resultiert folglich ein negativer prozentualer Wert des Strains, da eine Verkürzung in longitudinaler Richtung stattfindet. Der globale radiale Strain (GR) beschreibt die radiäre Verformung des Ventrikels von peripher nach zentral. Hier resultiert hingegen ein positiver prozentualer Wert, da die Myokarddicken während der Kontraktion zunehmen. Der globale zirkumferentielle Strain (GC) wiederum beschreibt die zirkuläre Verformung des Myokards und wird durch negative Werte repräsentiert [65].

Die Ursprünge der kardialen Wandbewegungsanalyse gehen schon auf die 1970er und 80er zurück. Neben einer chirurgischen Implantation von röntgendichten Markern (Fluoroskopie) wurden auch Ultraschallkristalle implantiert, um die Verformung des Myokards quantifizieren zu können [66-68]. Nachteile dieser Methoden waren der äußerst invasive Charakter, die limitierte Anzahl implantierbarer Materialien und die Beeinträchtigung der Myokardbewegung durch die Implantate selbst, was schließlich nach effektiveren und risikoärmeren Verfahren verlangte [69]. Die Echokardiografie rückte so zunehmend in den Mittelpunkt der Strainanalyse. So wurde auch das Feature Tracking (FT) ursprünglich für die Echokardiografie entwickelt. Es basiert auf einer Kombination aus Speckle-Tracking mit dem Tracking der Gewebe-Blut-Grenze während eines Herzzyklus, dem sogenannten Velocity-Vector-Imaging [70]. Durch den

Untersucher wird eine Grenze zwischen Endokard und Myokard manuell festgelegt und die Bewegung während des Herzzyklus automatisch von einer Analysesoftware anhand von Signalunterschieden (Gewebeunterschiede im Myokard, andere anatomische Gewebe; englisch „feature"/Eigenschaft des Gewebes) verfolgt (englisch „tracking").

Noch vor dem FT wurde für die Analyse der myokardialen Wandbewegung im MRT zunächst das sog. Tagging entwickelt. Die technischen Grundlagen des Taggings wurden bereits 1988 entwickelt und basieren auf einer nicht-invasiven, magnetischen Markierung des Myokards [69]. Im Tagging werden vor der Bildaufnahme Sättigungsebenen senkrecht zur Bildebene angelegt wodurch bei der anschließenden Aufnahme eine Signalreduktion des gesättigten Gewebes erreicht wird. Der Zeitpunkt der Aufnahme wird mithilfe eines Elektrokardiogramms (EKG) bestimmt. Das Resultat sind hypointense, netzartige Linien, die sich bei Kontraktion gemeinsam mit dem Myokard verformen und so eine Strainanalyse ermöglichen [71]. Ein großer Nachteil des Taggings ist allerdings, dass für eine spätere Analyse spezifische Protokolle und Sequenzen im MRT angefertigt werden müssen, was zu einer nicht unerheblichen Verlängerung der Untersuchungszeit führt.

Im Gegensatz dazu müssen beim FT keine extra Sequenzen akquiriert werden, denn die standardisiert akquirierten CINE-Sequenzen können für die weitere Analyse herangezogen werden [72]. Die Strain-Werte werden dann über die Grenzbewegung bzw. den Unterschied der Grenze zur definierten Ausgangsgrenze berechnet [73]. Mittlerweile sind schon Referenzwerte für unterschiedlichen Strainparameter auch unter Berücksichtigung geschlechtsspezifischer Unterschiede veröffentlicht [73-75]. In ersten Arbeiten konnte bei Patienten mit Myokarditiden [17-19], bei PH [76] oder auch bei Kardiomyopathien [77-80] vielversprechende Ergebnisse gezeigt werden.

4. Zielsetzung der vorliegenden Arbeit

Die Zielsetzung der vorliegenden, kumulativen Arbeit ist es neue MRT-Techniken und die Auswirkung der zunehmenden Anzahl kardialer MRT-Untersuchungen auf die Detektion von Nebenbefunden zu untersuchen.

Dabei soll der Stellenwert des nativen T1-Mappings in der Primärdiagnostik myokardialer Erkrankungen und bei der Quantifizierung morphologischer Veränderungen wie myokardialer Fibrose evaluiert werden. Zudem soll überprüft werden, ob das native T1-Mapping geeignet ist, Zusammenhänge mit kardialen und krankheitsspezifischen Biomarkern und zur kardiovaskulären Hämodynamik auch im Kontext eines Therapiemonitorings herzustellen.

Des Weiteren soll der Stellenwert von atrialen und ventrikulären myokardialen „feature tracking“ Strainanalysen und äquivalent deren Zusammenhänge zu krankheits-spezifischen Biomarkern und zur kardiovaskulären Hämodynamik untersucht werden.

5. Kumulative Habilitationsschrift – eingebrachte Manuskripte

5.1. **Roller F**, Fuest S, Meyer M, Harth S, Gündüz D, Bauer P, Schneider C, Rolfs A, Krombach G, Tanislav C. Assessment of cardiac involvement in Fabry Disease (FD) with native T1-mapping. Rofo 2019 Oct; 191(10): 932-939.

Gliederung 6.1.1.1.

5.2. **Roller FC**, Wiedenroth C, Breithecker A, Liebetrau C, Mayer E, Schneider C, Rolf A, Hamm C, Krombach GA. Native T1 mapping and extracellular volume fraction measurement for assessment of right ventricular insertion point and septal fibrosis in chronic thromboembolic pulmonary hypertension. Eur Radiol. 2017 May; 27(5): 1980-1991.

Gliederung 6.1.2.1.

5.3. **Roller FC**, Kriechbaum S, Breithecker A, Haas M, Liebetrau C, Schneider C, Rolf A, Guth S, Mayer E, Hamm C, Krombach GA, Wiedenroth CB Correlation of native T1 mapping with right ventricular function and pulmonary hemodynamics in patients with chronic thromboembolic pulmonary hypertension before and after balloon pulmonary angioplasty. Eur Radiol 2019 Mar; 29(3): 1565-1573.

Gliederung 6.1.3.1.

5.4. **Roller FC**, Brose A, Richter M, Schüssler A, Harth S, Tanislav C, Krombach GA. Value of Left Ventricular Feature Tracking Strain Analysis for Detection of Early Cardiac Involvement in Fabry Disease (FD). J Clin Med 2021 Aug; 10(16): 3734.

Gliederung 6.2.1.1.

5.5. Tello K, Dalmer A, Vanderpool R, Ghofrani HA, Naeije R, **Roller F**, Seeger W, Wilhelm J, Gall H, Richter MJ. Cardiac Magnetic Resonance Imaging-Based Right Ventricular Strain Analysis for Assessment of Coupling and Diastolic Function in

Pulmonary Hypertension. JACC Cardiovasc Imaging. 2019 Nov; 12(11 Pt 1): 2155-2164.

Gliederung 6.2.2.1.

5.6. Tello K, Dalmer A, Vanderpool R, Ghofrani HA, Naeije R, **Roller F**, Seeger W, Wiegand M, Gall H, Richter MJ. Right ventricular function correlates of right atrial strain in pulmonary hypertension: a combined cardiac magnetic resonance and conductance catheter study. Am J Physiol Heart Circ Physiol. 2020 Jan; 318(1): H156-H164.

Gliederung 6.2.3.1.

5.7. **Roller FC**, Schneider C, Schuhbäck A, Rolf A, Krombach GA. Cardiac MRI: diagnostic gain of an additional axial SSFP chest sequence for the detection of potentially significant extracardiac findings in the cardiac MRI examination setting. Rofo. 2014 Jan; 186(1): 42-6.

Gliederung 6.3.1.1.

Alle Manuskripte sind unter Gliederungspunkt **12.** in der in die kumulative Habilitationsschrift eingebrachten Reihenfolge angehängt.

6. Ergebnisse

6.1. Parametrische Bildgebung

6.1.1. Natives T1-Mapping in der Primärdiagnostik kardialer Erkrankungen

6.1.1.1. Assessment of cardiac involvement in Fabry Disease (FD) with native T1-mapping.

Um das Potential und die Eignung des nativen T1-Mappings in der Primärdiagnostik kardialer Erkrankungen abschätzen zu können, wurde eine Patientengruppe bzw. eine Erkrankung ausgesucht, bei der im konventionellen kardialen MRT in späteren Stadien krankheitstypische Veränderungen nachweisbar sein können, aber eine frühe oder diffuse kardiale Beteiligung durch die zuvor benannten und bekannten Limitationen der klassischen Methoden zur Gewebecharakterisierung im MRT stets verborgen bleiben. Zudem sollten möglichst kardiale und krankheitsspezifische Biomarkerveränderungen bei der Erkrankung vorliegen. Für das Anforderungsprofil erschien der Morbus Fabry als geeignete Erkrankung.

Beim Morbus Fabry handelt es sich um eine X-chromosomale Multiorganerkrankung des lysosomalen Metabolismus [81]. Aufgrund eines Mangels am Enzym alpha-Galactosidase können Glykosphingolipide nicht mehr abgebaut werden und akkumulieren in unterschiedlichen Organsystemen wie der Haut, den Nieren und dem Herzen. Homozygote Männer sind am stärksten von der Erkrankung betroffen. Die Betroffenen äußern unspezifische Beschwerden sowie Extremitätenschmerzen (Akroparesthesien) und entwickeln im Verlauf der Erkrankung ein zunehmendes Multiorganversagen [82]. Eine kardiale Beteiligung stellt die Haupttodesursache dar, denn durch die Einlagerung von Glykosphingolipiden in Myozyten, in Herzklappen und Endothel wird die Entwicklung einer linksventrikulären Hypertrophie (LVH) und einer kardialen Fibrose getriggert [83]. Die Fibrosierung wiederum triggert eine kardiale Dekompensation und ist bei Männern stärker ausgeprägt als bei Frauen [81, 84].

Für den Nachweis einer kardialen Morbus Fabry Manifestation hat sich die MRT in der Bildgebung bereits etabliert, denn neben einer LVH und einer linksventrikulären Funktionseinschränkung kann ein mittmyokardiales LGE der Inferolateralwand auftreten, was als charakteristisches Kennzeichen einer kardialen Beteiligung beschrieben wird [85].

Ähnlich wie bei anderen Kardiomyopathien ist der Nachweis von LGE von großer prognostischer Relevanz, denn Patienten mit LGE sprechen bedingt durch eine myokardiale Fibrose deutlich schlechter auf eine Enzymersatztherapie an [85]. Auf der anderen Seite profitieren besonders Patienten in frühen Krankheitsstadien, also ohne Nachweis von Fibrose bzw. LGE, am meisten von einer Enzymersatztherapie [86]. Für den Nachweis einer frühen kardialen Beteiligung ist das rein dichotome LGE aber limitiert, weswegen dringend neue Ansätze benötigt werden, die die frühe Detektion einer kardialen Beteiligung erlauben. Dabei bietet sich vor allem das native T1-Mapping an, da myokardiale Lipideinlagerungen die native T1-Zeit reduzieren [87].

Das Ziel der Studie war es deswegen die Wertigkeit des nativen T1-Mappings als krankheitsspezifisches Äquivalent einer kardialen Beteiligung bei Morbus Fabry zu untersuchen. Dafür wurden 16 Patienten mit einem genetisch gesicherten Morbus Fabry und 16 Kontrollpatienten an einem 1.5 Tesla MRT-System (Somatom Avanto, Siemens Healthineers, Forchheim, Deutschland) mit einem standardisierten MRT-Protokoll inklusive nativem T1-Mapping (optimierte MOLLI-Sequenz) untersucht.

Neben der linksventrikulären Funktion wurden die Wandbewegung, die LVH und die myokardiale Morphologie (via LGE und nativem T1-Mapping) untersucht. Die Messung der nativen T1-Zeit erfolgte in Regionen von Interesse (ROI) im interventrikulären Septum auf mittventrikulären Kurzachsenschnitten.

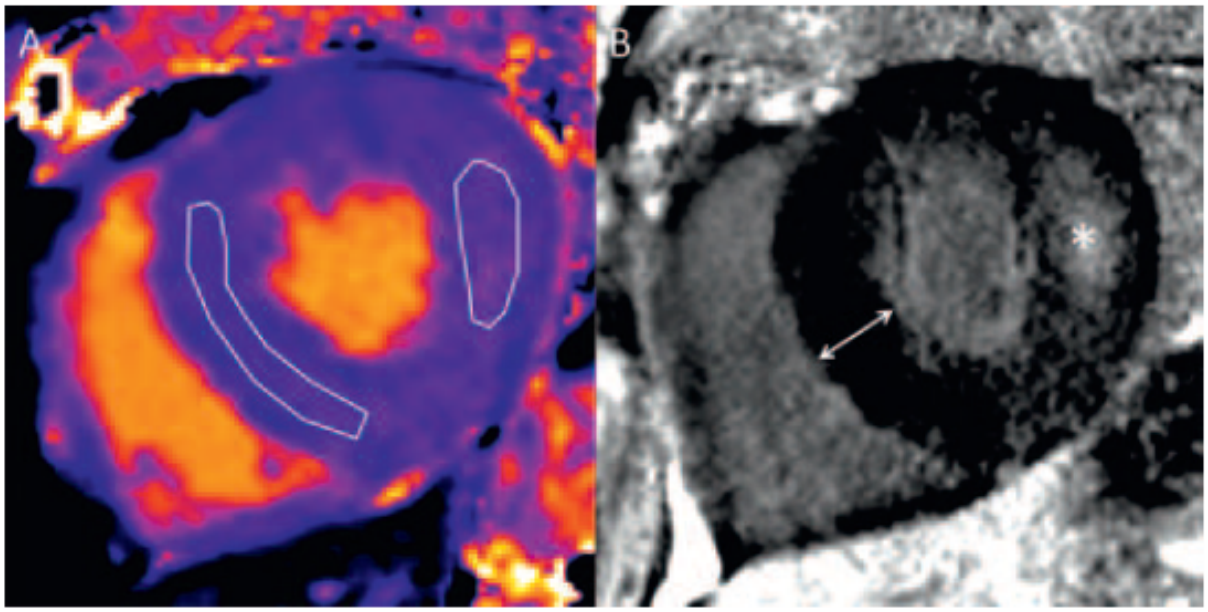

Abbildung 1: Zeigt eine mittventrikuläre native T1-Map (A) und das korrespondierende LGE-Bild (B) bei einem 52jährigem männlichen Morbus Fabry Patienten. In der nativen T1-Map wurden Messungen in ROI (Septum und Narbe/Lateralwand) vorgenommen. Die native T1-Zeit im Septum war auf 888ms reduziert und mit 954ms für die Lateralwand normal. Im LGE-Bild zeigt sich eine deutliche mittmyokardiale, fabrytypische Narbe der Lateralwand (weißer Stern). Die Myokarddicke septal (weißer zweigipfliger Pfeil) beträgt 20mm.

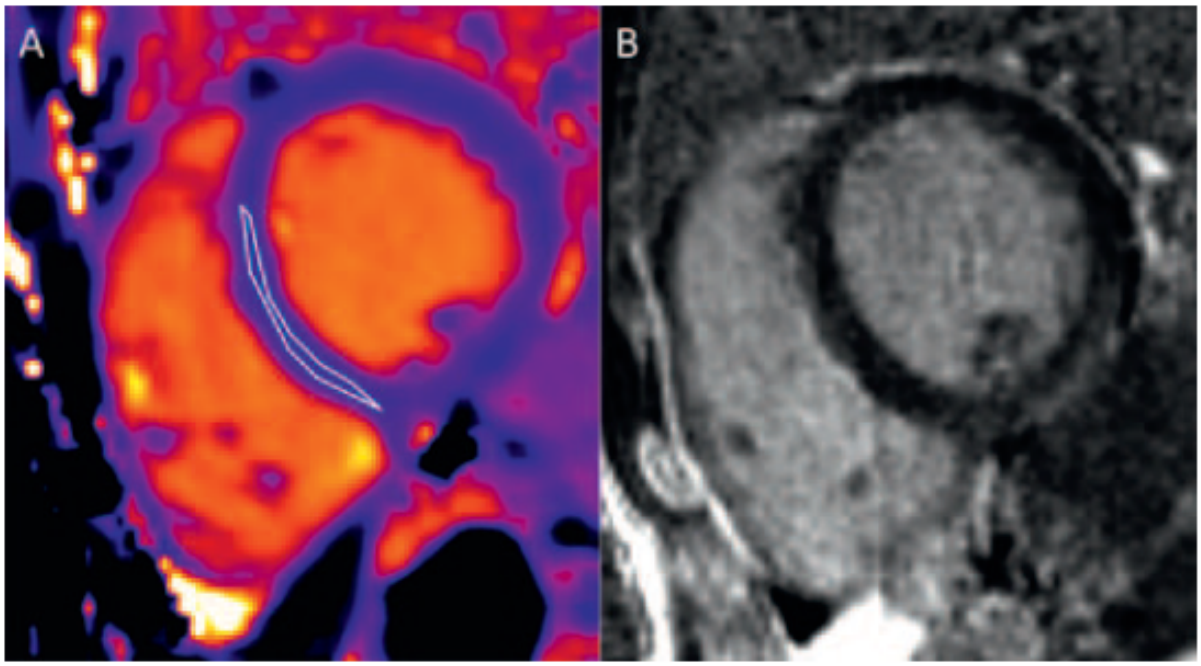

Abbildung 2: Zeigt eine mittventrikuläre native T1-Map (A) und das korrespondierende LGE-Bild (B) bei einem 27jährigem männlichen Morbus Fabry Patienten. In der nativen T1-Map wurde eine Messung in der ROI im Septum vorgenommen. Die native T1-Zeit war auf 872ms reduziert. Es zeigt sich weder LVH noch LGE.

Die nativen T1-Zeiten wurden zudem zu kardialen (cTnI) und krankheitsspezifischen (LysoGb3) Biomarkern korreliert. Bei den Patienten mit Morbus Fabry waren die medianen native T1-Zeiten verglichen zum Kontrollkollektiv signifikant reduziert (889.0 ms versus 950.6 ms; $p < 0.003$).

Verglichen zur LVH und dem LGE – nur 5 Morbus Fabry Patienten hatten ein fabrytypisches LGE der Inferolateralwand – zeigte vor allem die native T1-Zeit eine gute Diskriminierung von LysoGb3-positiven Patienten auch ohne den Nachweis morphologischer kardialer Veränderungen oder kardialer Biomarkererhöhungen (cTnI). Vielmehr noch zeigte die native T1-Zeit eine gute und signifikante negative Korrelation zur Lyso-Gb3 ($r = - 0.582$; $p = 0.018$).

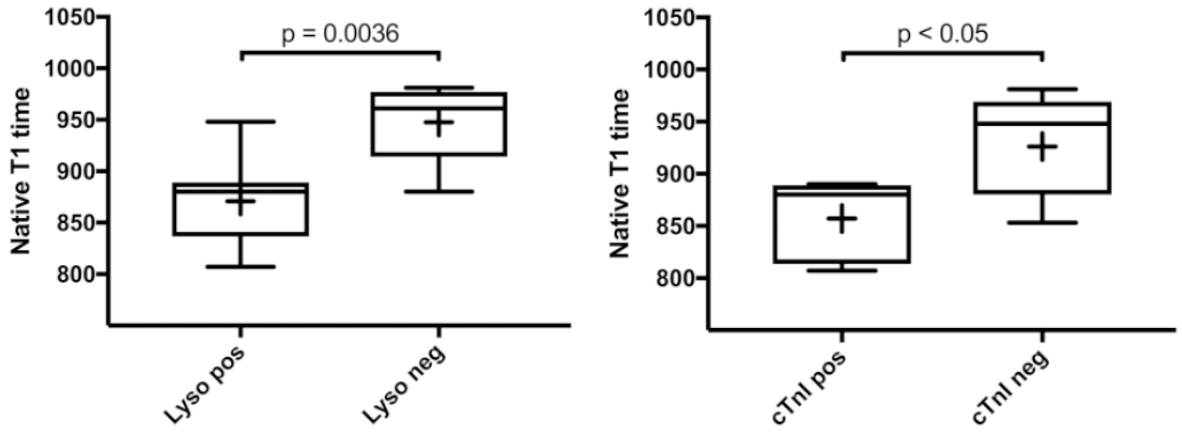

Abbildung 3: Die beiden Box-Plots veranschaulichen die bei LysoGb3 positiven und bei LysoGb3 negativen Morbus Fabry Patienten gemessenen nativen T1-Zeiten sowie die bei cTnI positiven und cTnI negativen Morbus Fabry Patienten gemessen nativen T1-Zeiten. Sowohl für Lyso-Gb3 positive als auch für cTnI positive Morbus Fabry Patienten waren die nativen T1-Zeiten signifikant reduziert.

Aus den Ergebnissen kann man schlussfolgern, dass eine pathologisch reduzierte myokardiale T1-Zeit eine kardiale Beteiligung bei Patienten mit Morbus Fabry anzeigt und eine frühzeitige Detektion ermöglicht, noch bevor andere bildgebende morphologische Kriterien, wie LVH und LGE, oder auch kardiale Biomarkererhöhungen

(cTnI) nachweisbar sind. Neben den reduzierten nativen T1-Zeiten können EKG- und Langzeit-EKG-Veränderungen [88] sowie kardiale Biomarker wie TnI [89] einen frühen kardialen Zellschaden anzeigen.

Unsere Ergebnisse sind von großer therapeutischer Relevanz und in Übereinstimmung mit den Ergebnissen anderer Arbeitsgruppen, die ebenfalls reduzierte myokardiale native T1-Zeiten bei Patienten mit Morbus Fabry zeigen konnten [51, 90]. Vielmehr noch konnte in einer weiteren Studie gezeigt werden, dass die native T1-Zeit gut geeignet ist zwischen einer kardialen Morbus Fabry Manifestation und anderen kardialen Erkrankungen mit LVH zu diskriminieren und dass die native T1-Zeit das wichtigste Diagnosekriterium unabhängig von Geschlecht, kardialer Morphologie oder Funktion ist, was auf eine kardiale Fabrymanifestation hindeutet [90]. Gegenüber den anderen Studien ist die von uns durchgeführte Analyse des Zusammenhangs zwischen der nativen T1-Zeit und dem Biomarker LysoGb3 als krankheitsspezifisches Äquivalent neu und vielversprechend.

6.1.2. Natives T1-Mapping und ECV zur Fibrosegradquantifizierung

6.1.2.1. Native T1 mapping and extracellular volume fraction measurement for assessment of right ventricular insertion point and septal fibrosis in chronic thromboembolic pulmonary hypertension.

Nachdem sich in unserer ersten Studie eine gute Eignung des nativen T1-Mappings in der Primärdiagnostik gezeigt hatte, sollte nun das Potential des nativen T1-Mappings und des ECV bei der Quantifizierung der myokardialen Fibrose untersucht werden. Hierfür eignet sich ein Patientenkollektiv bzw. eine Erkrankung, bei der eine hohe krankheitsspezifische LGE-Prävalenz in gut messbaren Myokardarealen vorliegt am besten. Bei Patienten mit PH zeigt sich sehr häufig ein krankheitsspezifische LGE in den rechtsventrikulären Insertionsregionen (RVIP), welches sich im Rahmen einer septomarginalen Trabekularisierung auch auf das Septum ausdehnen kann.

Die chronisch thrombembolisch pulmonalarterielle Hypertonie (CTEPH) – eine Ätiologie der pulmonalen Hypertonie (PH) – ist als PH mit persistierenden Perfusionsdefekten nach einmaliger oder mehrmaliger Embolie definiert [91]. Bei der CTEPH handelt es sich um eine seltene, eher unterdiagnostizierte Erkrankung mit einer geschätzten Inzidenz zwischen 0.5-3.8% nach einmaliger Embolie und etwa 10% nach mehrmaligen Embolien [92-95].

Bei der CTEPH finden Gefäßveränderungen auf dem Boden einer unvollständigen Thrombusauflösung, eines Thrombusumwandlungsprozesses („remodeling“) und einer Neoangiogenese statt [96]. In späteren Erkrankungsstadien dehnen sich die Gefäßumwandlungsprozesse dann von zentral auch auf primär durch die Thrombembolie nicht betroffene Gefäßanteile aus, wobei die Gefäßwandveränderungen in diesem Stadium denen der idiopathischen pulmonalen Hypertonie ähneln [97]. Die Veränderungen bedingen ein Ansteigen des mittleren pulmonalarteriellen Drucks (mPAP) und des mittleren pulmonalen Gefäßwiderstandes (PVR).

Bei allen Formen der PH führen der steigende pulmonalarterielle Druck und der zunehmende Gefäßwiderstand zu einer rechtsventrikulären Belastung und einem kardialen Umbauprozess mit Entwicklung einer rechtsventrikulären Hypertrophie. Wenn dieser adaptive entgegensteuernde Prozess nicht mehr aufrechterhalten werden kann, dilatiert der rechte Ventrikel und es entsteht eine rechtsventrikuläre Dysfunktion [98]. Die rechtsventrikuläre Funktion wird im Verlauf schlechter und der rechtsventrikuläre diastolische Druck nimmt weiter zu [99,100]. Aufgrund der Druckbelastung nimmt das Schlagvolumen des rechten Ventrikels ab und es entwickelt sich eine abnormalen Wandbewegung des interventrikulären Septums in der frühen Diastole, was im englischsprachigen Raum als „septal bounce“ bezeichnet wird [101]. Diese Vorgänge führen dann auch zu einer Einschränkung der linksventrikulären Füllung bzw. einer linksventrikulären diastolischen Dysfunktion. Das interventrikuläre Ventrikelseptum und insbesondere die rechtsventrikulären Insertionspunkte (RVIP) sind im Rahmen der kardialen Erkrankungskaskade der PH großen mechanischen Beanspruchungen durch Kompressions-, Zug- und Scherkräften ausgesetzt. In MRT-Studien konnte gezeigt werden, dass bei Patienten mit PH sehr häufig ein PH-typisches trianguläres LGE in den RVIP (bei 83.0% bis 91.3% der Fälle) vorkommt [98, 102-105], was die Annahme begleitender rechtsventrikulärer Umbauprozesse unterstützt. In einem Fallbericht bei einem Patienten mit CTEPH und typischem LGE in den RVIP konnte postmortem eine plexiformen Fibrose in den RVIP nachgewiesen werden [106], andererseits können in diesen Regionen auch Faserveränderungen und eine interstitielle Fibrose bei Gesunden nachgewiesen werden [107], was generell dafürsprechen könnte, dass diese Region dem größten mechanischen Stress ausgesetzt ist. Eine exakte Abklärung der histologischen Veränderungen ist jedoch sehr schwierig, da diese Regionen einer endomyokardialen Biopsie (EMB) nicht zugänglich sind [98].

Wie schon angesprochen ermöglicht das native T1-Mapping im Gegensatz zum LGE, dass aufgrund seiner Dichotomie zur Quantifizierung von Veränderungen ungeeignet ist, eine Quantifizierung von Veränderungen und somit eine Gewebscharakterisierung ohne Kontrastmittel. Zusätzlich ermöglicht eine Messung der T1-Zeit vor und nach Kontrastmittelapplikation mit Hämatokritkorrektur eine Quantifizierung des extrazellulären Volumenanteils (ECV) [62]. Für beide Techniken konnten in einigen Studien schon vielversprechende Ergebnisse bei der Quantifizierung von Fibrose gezeigt werden [108-110]. Die Ergebnisse einer tierexperimentellen Studie bei chronischer PH deuten darauf hin, dass mittels Mapping und ECV auch eine Quantifizierung der Fibrose in den Insertionsregionen möglich ist [111].

Das Ziel unserer Studie war es deswegen das Potential des nativen T1-Mapping und des ECV bei der Quantifizierung der septalen und RVIP Fibrose zu untersuchen. Hierfür wurden prospektiv 24 Patienten mit inoperabler CTEPH, die eine kardiale MRT-Untersuchung im Rahmen der präinterventionellen Routineuntersuchungen vor geplanter BPA erhielten und 24 Kontrollpatienten in die Studie eingeschlossen. Alle Patienten wurden an einem 1.5 Tesla MRT-System (Somatom Avanto, Siemens Healthineers, Forchheim, Deutschland) mit einem standardisierten MRT-Protokoll untersucht. Die Auswertung beinhaltete eine kardiale Funktionsanalyse, eine Auswertung der Kontrastmittelspätanreicherung (LGE) sowie die Auswertung des nativen T1-Mappings und des ECV. Als Kontrastmittel wurde Gadobenate dimeglumine (Gd-BOPTA; Multihance; BRACCO Imaging) in einer Dosierung von 0,15mmol pro Kilogramm Körpergewicht verwendet. Die Kontrastmittelspätanreicherung wurde 12 Minuten nach Kontrastmittelinjektion untersucht, das ECV bzw. das dafür notwendige postkontrast Mapping wurde 15 Minuten nach Kontrastmittelinjektion untersucht. Die nativen T1-Zeiten, die postkontrast T1-Zeiten sowie der Blutpool wurden in ROI auf basalen

Kurzachsenschnitten gemessen. Als ROI wurden das Septum, der oberen und untere RVIP sowie die Lateralwand als Referenz definiert. Um den Einfluss von Größenunterschieden bei den Messungen der ROI auszuschließen wurden zudem die ROI-Mittelwerte verglichen.

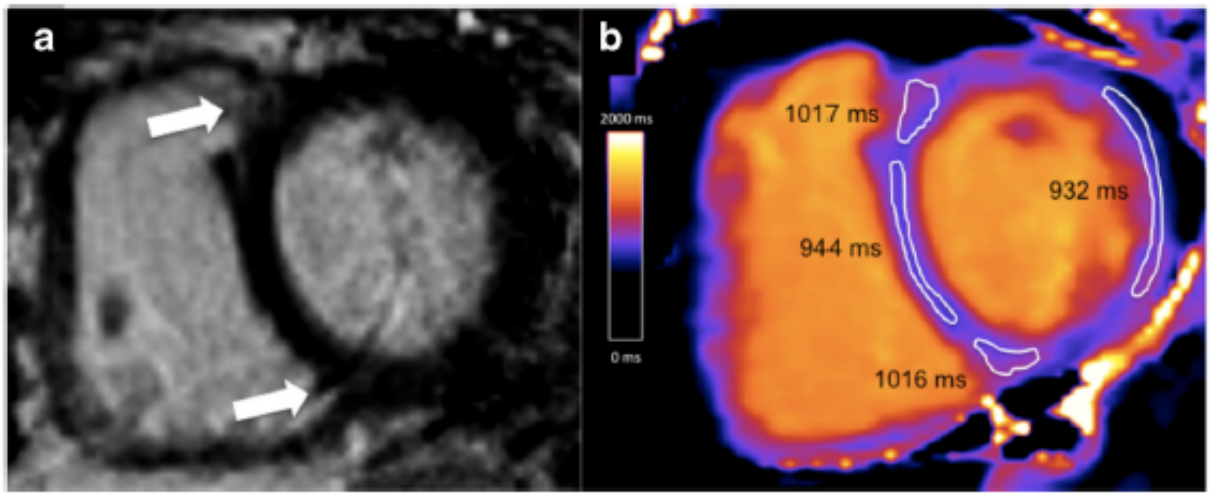

Abbildung 4: LGE-Bild (a) und korrespondierende native T1-Map (b) (basale Kurzachsenschnitte) bei einer 64jährigen Patientin mit CTEPH. Kein Nachweis eines LGE in den RVIP (weiße Pfeile). Es lassen sich allerdings gering erhöhte native T1-Zeiten in den ROI in den RVIP messen, während die nativen T1-Zeiten im Septum und in der Lateralwand normal sind.

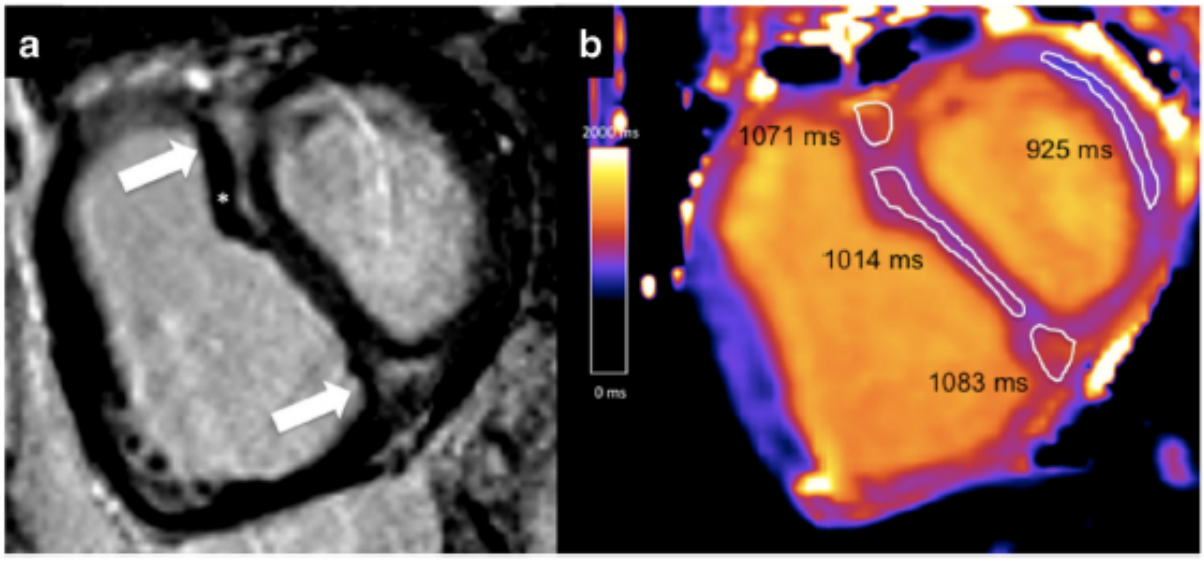

Abbildung 5: LGE-Bild (a) und korrespondierende native T1-Map (b) (basale Kurzachsenschnitte) bei einem 58jährigen Patienten mit CTEPH. Nachweis eines LGE in den RVIP mit Ausdehnung in das Septum (weißer Stern). Es lassen sich deutlich erhöhte native T1-Zeiten in den ROI in den RVIP und im Septum messen, während die native T1-Zeit der Lateralwand normal ist.

Die gemessenen nativen T1-Zeiten und die ECV-Werte wurden zur rechtsventrikulären Ejektionsfraktion und zum invasiv im Rechtsherzkatheter gemessenen mPAP und der PVR korreliert.

Bei deutlich erhöhtem mPAP und PVR zeigte sich verglichen zum Kontrollkollektiv eine signifikant reduzierte rechtsventrikuläre Funktion (RVEF) mit signifikant erhöhten enddiastolischen und endsystolischen Volumina des rechten Ventrikels (alle $p < 0.001$), während die Funktion des linken Ventrikels keine signifikanten Unterschiede zeigte. Insgesamt zeigte sich bei 15 CTEPH-Patienten (62.5%) ein LGE in den Insertionsregionen. Sowohl für die native T1-Zeit als auch für das ECV zeigten sich signifikant erhöhte Werte für das Septum sowie in den rechtsventrikulären Insertionsregionen verglichen zur Kontrollgruppe (alle $p < 0.001$) während für die Lateralwand keine Unterschiede bestanden. Innerhalb der CTEPH-Patienten zeigten sich zudem teilweise signifikant höhere native T1-Zeiten und ein signifikant höheres ECV bei den CTEPH-Patienten mit LGE verglichen zu den CTEPH-Patienten ohne LGE. Interessanterweise zeigten sich aber auch teilweise signifikant erhöhte native T1-Zeiten und ein signifikant erhöhtes ECV bei den CTEPH-Patienten ohne LGE verglichen zur Kontrollgruppe. Die Inter- und Intraobservervariabilitäten für das native T1-Mapping und das ECV in allen Regionen waren exzellent. Vielmehr noch zeigte sich eine sehr gute signifikante negative Korrelation der flächenadjustierten nativen T1-Zeit des Septums zur RVEF ($k = -0.92$; $p = 0.01$) sowie eine gute signifikante positive Korrelation zum mPAP ($k = 0.83$; $p = 0.04$).

Aus den Ergebnissen lässt sich schlussfolgern, dass die native T1-Zeit und das ECV eine Visualisierung, Charakterisierung und Quantifizierung von myokardialer Fibrose ermöglicht. Aufgrund der guten Korrelationen sowohl zur rechtsventrikulären Funktion als auch zur pulmonalen Hämodynamik hat das native T1-Mapping zudem

möglicherweise großes Potential bei der Beurteilung Krankheitsschwere, der Prognose und der Therapieüberwachung.

T1 Values	RV EF %	PA Pressure mmHg
>975 ms	35.6	40.1
>1000 ms	34.7	42.1
>1025 ms	33.2	43.9
>1050 ms	29.4	47.5
>1075 ms	31.5	46.6
>1100 ms	28.2	45.3
Correlation		
k Pearson	-0.92	0.83
p Value	0.01	0.04

Abbildung 6: Die Abbildung zeigt die Grenzwerte der flächenadjustierten nativen T1-Zeit und deren Korrelationen zur RVEF und zum mPAP.

6.1.3. Eignung des nativen T1-Mappings in der Verlaufs- und Therapiebeurteilung

6.1.3.1. Correlation of native T1 mapping with right ventricular function and pulmonary hemodynamics in patients with chronic thromboembolic pulmonary hypertension before and after balloon pulmonary angioplasty

Um Aussagen zu Gewebsveränderungen und myokardialen Umbauprozessen („remodeling“) unter einer laufenden Therapie oder nach Therapieabschluss treffen zu können, ist ein Patientenkollektiv bzw. eine Erkrankung, bei der einerseits die im Rahmen der Erkrankung entstehenden kardialen Veränderungen und Einschränkungen quantifizierbar sind und andererseits durch eine Therapie verbessert oder gar normalisiert werden können am besten geeignet. Wie die erste Studie zur CTEPH bereits zeigen konnte erlaubt das native T1-Mapping die Quantifizierung einer kardialen Fibrose. Aufgrund der unterschiedlichen und guten Therapiefähigkeit ist das Krankheitsbild auch hervorragend geeignet um Therapieeffekte auf rechtsventrikuläre Funktion, pulmonale Hämodynamik und rechtsventrikuläre Umbauprozesse („remodeling“) zu untersuchen. Im Gegensatz zu den anderen Ätiologien der PH nimmt die CTEPH, trotz der PH-einheitlichen kardialen Krankheitskaskade mit Rechtsherzbelastung und Umbauprozessen eine Sonderstellung ein, da sie die einzige PH-Ätiologie ist, die kurativ über eine pulmonale Endarterieektomie (PEA) behandelbar ist [112, 113]. Durch die PEA wird der pulmonalarterielle Druck und der Gefäßwiderstand bei sehr guten Langzeitüberlebensraten normalisiert [113, 114]. Allerdings ist etwa ein Drittel der Patienten mit CTEPH für eine PEA, aufgrund von peripheren Gefäßverschlüssen, die einer Operation nicht zugänglich sind, ungeeignet [91] – was dann auch als inoperable CTEPH bezeichnet wird. Neben einer empfohlenen medikamentösen Therapie mit Riociguat [115], einer Guanylatcyclase die sowohl die pulmonale Hämodynamik als auch die

physische Belastbarkeit der Patienten verbessert [116], hat sich bei Patienten mit einer inoperablen CTEPH die pulmonale Ballonangioplastie (BPA) als sehr gute und vielversprechende Therapieoption in den letzten Jahren etabliert [115, 117, 118]. Vereinzelt kommen gar kombinierte Therapieansätze aus PEA und BPA zur Anwendung [119].

Die kardiale MRT wiederum ist hervorragend geeignet kardiale Struktur, rechtsventrikulären Funktion und Morphologie nicht-invasiv zu beurteilen. In Studien wurden unter anderem bereits Effekte der PEA [120, 121] und der medikamentösen Therapie [122] auf biventrikuläre Herzfunktion und pulmonale Hämodynamik bei Patienten mit CTEPH untersucht. In aktuelleren Studien wurden nun auch Therapieeffekte der BPA bei Patienten mit inoperabler CTEPH im MRT untersucht. Dabei zeigten sich ebenfalls Verbesserungen der biventrikulären Funktion, des pulmonalen Flusses und der interventrikulären Dyssynchronie [123, 124].

Das Ziel unserer Folgestudie war es deswegen die vielversprechenden Ergebnisse des nativen T1-Mappings bei der Quantifizierung der septalen und RVIP Fibrose (5.1.2) aus der ersten Studie im Rahmen eines Therapiemonitorings zu untersuchen. Hierfür wurden 21 konsekutive Patienten mit inoperabler CTEPH, die vor und 6 Monate nach BPA einen RHK und eine standardisierte kardiale MRT-Untersuchung an einem 1.5 Tesla MRT-System (Somatom Avanto, Siemens Healthineers, Forchheim, Deutschland) inklusive nativem T1-Mapping erhielten, prospektiv in die Studie eingeschlossen. Die Studienaufbau sowie die invasiven und nicht-invasiven Messungen und Auswertungen entsprachen denen der ersten Studie. Die nativen T1-Zeiten wurden in den RVIP und im Septum gemessen, außerdem wurde wie schon in der ersten Studie die flächenadjustierte native T1-Zeit bestimmt und zur rechtsventrikulären Funktion und zur pulmonalen Hämodynamik korreliert (mPAP und PVR).

Die BPA führte bei den CTEPH-Patienten zu einer signifikanten Verbesserung der Rechtsherzfunktion und der pulmonalen Hämodynamik (je $p < 0.01$) bei nicht signifikant verbesserter Linksherzfunktion. Des Weiteren zeigte sich eine statistisch hoch signifikante Reduzierung der flächenadjustierten nativen T1-Zeit nach erfolgter BPA ($p = 0.0009$). Während sich vor BPA eine signifikante moderat negative Korrelation zur RVEF ($r = -0.61$; $p = 0.0036$) und signifikante moderat positive Korrelationen zum mPAP ($r = 0.59$; $p < 0.01$) und der PVR ($r = 0.53$; $p < 0.05$) zeigten, waren nach BPA noch Korrelationstrends nachweisbar waren ($r = -0.21$, $r = 0.30$ und $r = 0.35$).

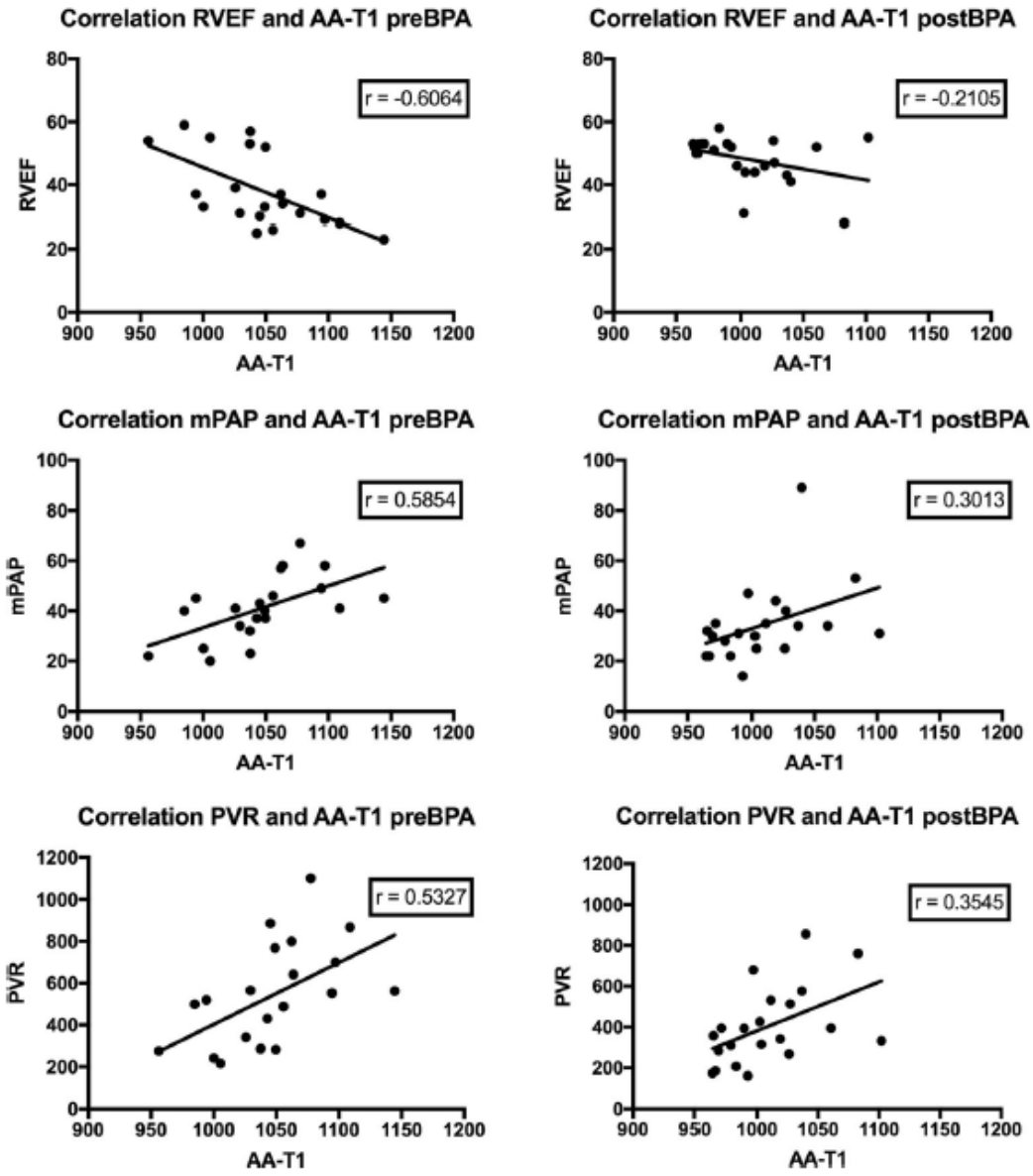

Abbildung 7: Die Abbildung zeigt die Korrelationen der flächenadjustierten nativen T1-Zeit zur RVEF, dem mPAP und der PVR vor und nach erfolgter BPA.

Aus diesen Ergebnissen lassen sich die folgenden Schlüsse ableiten: Die signifikante Verbesserung der nativen T1-Zeit im Septum bei gleichzeitiger Normalisierung von rechtsventrikulärer Funktion und pulmonaler Hämodynamik legt nahe, dass die im Septum gemessenen nativen T1-Zeiten Gewebsveränderungen im Rahmen der PH anzeigen. Zudem verbessert die BPA nicht nur die pulmonale Hämodynamik, sondern induziert auch einen Umbauprozess „reverse remodeling“ des rechtsventrikulären, septalen Myokards, was wiederum mit einer Verbesserung der rechtsventrikulären Funktion einhergeht. Möglicherweise eignet sich das native T1-Mapping deswegen zukünftig sogar bei der Präselektion und Identifikation von Patienten, die besonders gut von einer BPA-Therapie profitieren würden.

6.2. Regionale myokardiale Wandbewegungsanalyse – Myokardialer Strain

6.2.1. Linksventrikulärer myokardialer Strain in der Primärdiagnostik kardialer Erkrankungen

6.2.1.1. Value of left ventricular feature tracking strain analysis for detection of early cardiac involvement in Fabry Disease (FD)

Ähnlich wie in unserer Studie zur Überprüfung der Eignung des nativen T1-Mappings für die Primärdiagnostik, kann der Morbus Fabry auch sehr gut dazu herangezogen werden das Potential von FT-Strainanalysen zu überprüfen, da in konventionellen kardialen MRT-Untersuchungen – wie angesprochen – zumeist erst relativ spät krankheitstypische Veränderungen des Morbus Fabry nachweisbar sind.

Da in unterschiedlichen echokardiographischen Studien bereits Veränderungen des myokardialen Strains bei Patienten mit Morbus Fabry gezeigt werden konnten [125-128], war es das Ziel unserer Studie die Wertigkeit von FT-Strainanalysen zur Detektion einer frühen kardialen Beteiligung bei Morbus Fabry zu untersuchen.

Hierfür wurden insgesamt 28 Patienten mit einem genetisch gesicherten Morbus Fabry und 28 Kontrollpatienten an einem 1.5 Tesla MRT-System (Somatom Avanto, Siemens Healthineers, Forchheim, Deutschland) mit einem standardisierten MRT-Protokoll untersucht. Neben der linksventrikulären Funktion wurde die linksventrikuläre Wandbewegung mittels FT-Strainanalysen (globaler longitudinaler Strain (GL), globaler radiärer Strain (GR) und der globaler zirkumferentieller Strain (GC)) und die myokardiale Morphologie (via LGE und nativem T1-Mapping) analysiert. Die FT Strainanalysen und die Messung der nativen T1-Zeit erfolgte mittels kommerzieller Software (cvi^{42}, Circle Cardiovascular Imaging, Calgary, AB, Canada). Die nativen T1-Zeiten wurden in Regionen von Interesse (ROI) im interventrikulären Septum auf basalen Kurzachsenschnitten gemessen.

Die nativen T1-Zeiten und die gemessenen Strainwerte wurden untereinander und mit dem fabryspezifischen Biomarker LysoGb3 korreliert.

Außerdem wurde die Intra- und Interobserver-Variabilität für das native T1 Mapping und alle Strainwerte bestimmt. Abbildung 1 zeigt die Messung der septalen nativen T1-Zeit, ein LGE-Bild mit einer flauen Narbe/Kontrastmittelspätanreicherung der Inferolateralwand und Bilder einer Strainanalyse (GL und GC) mit Messung des GL Strains.

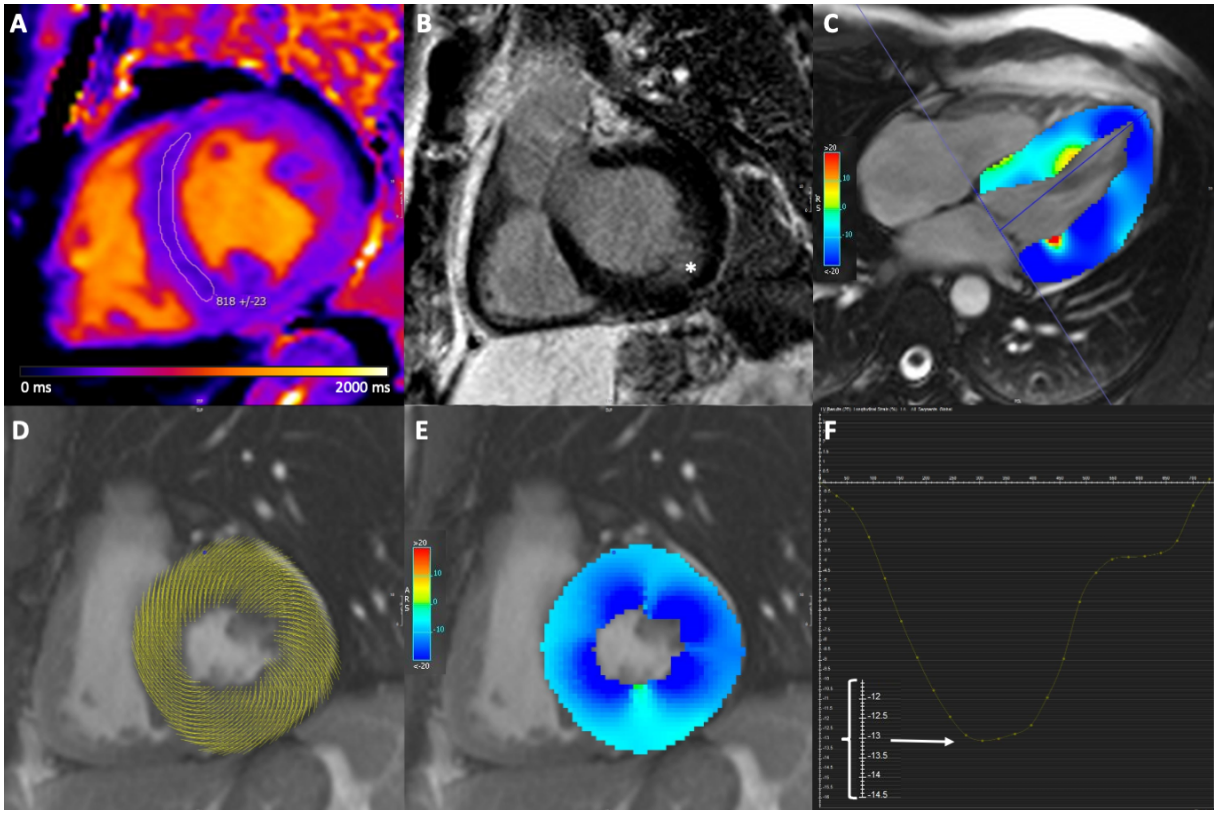

Abbildung 1: Native T1-Map (A) mit Messung der nativen T1-Zeit in einer septalen ROI und LGE-Bild mit inferolateraler Narbe (weißer Stern). CINE-SSFP-Sequenz mit farbkodierter Analyse des GL Strains (C). (F) zeigt einen reduzierten GLS mit 13.2%. (D) zeigt eine CINE-SSFP-Sequenz in der kurzen Achse mit Analyse des GC Strains mit myokardialen Punkten/Vektoren und als farbkodierte Analyse.

6 Morbus Fabry Patienten hatten eine LVH und 7 Patienten ein fabrytypisches LGE der Inferolateralwand. Zudem zeigte sich eine signifikante Reduzierung der septalen nativen T1-Zeit bei den Morbus Fabry Patienten mit 921.1 ms ± 49.4 SA verglichen zum

Kontrollkollektiv mit 951.0 ms ± 47.3 SA. Die mittlere LysoGb3-Konzentration der Morbus Fabry Patienten betrug 17.8 ng/ml ± 38.1 SA.

Die Linksherzfunktion (LVEF) war sowohl für die Morbus Fabry Patienten als auch im Kontrollkollektiv normal. Allerdings waren sowohl das enddiastolische Volumen als auch das Schlagvolumen signifikant höher im Kontrollkollektiv. Für den Strain ergaben sich signifikante Reduzierungen des GR Strains ($p = 0.018$) und des GL Strains ($p < 0.001$) bei den Morbus Fabry Patienten.

Table 3: Correlations of Strain values, LysoGb3, myocardial mass and native T1

	r	95% CI	p value
Septal native T1 to GRS	0.3272	-0.06385 to 0.6311	0.089
Septal native T1 to GCS	-0.4687	-0.7221 to -0.1044	0.012
Septal native T1 to GLS	-0.3251	-0.6297 to -0.06620	0.092
LysoGb3 to GRS	-0.288	-0.6028 to 0.1091	0.14
LysoGb3 to GCS	0.384	0.00114 to 0.6687	0.044
LysoGb3 to GLS	0.5498	0.2114 to 0.7706	0.002
Septal native T1 to LysoGb3	-0.6519	-0.8281 to -0.3584	< 0.001

GRS – global radial strain, GCS – global circumferential strain, GLS – global longitudinal strain, r – correlation coefficient, CI – confidence interval, p – significance value

Zudem konnten bei allen Morbus Fabry Patienten signifikante Korrelationen der septalen nativen T1-Zeit zum GC Strain und zur LysoGb3 sowie signifikante Korrelationen von GC Strain und GL Strin zur LysoGb3 gezeigt werden (Tabelle 3).

Table 4: Cardiac function and morphology: FD Lyso-Gb3+ versus Lyso-Gb3-

	LysoGb3+ **n = 18**	**LysoGb3-** **n = 10**	**p value**
LVEF (%)	65.9 ± 8.8	66.1 ± 6.9	0.98
EDV (ml)	111.5 ± 34.1	103.0 ± 30.0	0.86
ESV (ml)	38.4 ± 16.3	35.8 ± 9.1	0.98
SV (ml)	73.1 ± 22.5	70.3 ± 20.0	0.76
Septal diameter (mm)	10.7 ± 4.1	8.0 ± 1.3	0.059
Myocardial Mass (g)	135.4 ± 64.1	96.8 ± 25.5	0.10
Septal native T1 time (ms)	902.0 ± 49.4	955.5 ± 25.8	0.005
GRS (%)	32.2 ± 10.0	36.3 ± 5.1	0.41
GCS (%)	-19.6 ± 3.7	-20.5 ± 2.3	0.58
GLS (%)	-17.0 ± 3.7	-19.7 ± 1.4	0.03
LGE (n; %)	7 (70%)	0	

Values are mean ± SD, LVEF – left ventricular ejection fraction, EDV – enddiastolic volume, ESV – endsystolic volume, SV – stroke volume, GRS – global radial strain, GCS – global circumferential strain, GLS – global longitudinal strain, late gadolinium enhancement, p – significance value

In der Subgruppenanalyse zwischen Morbus Fabry Patienten mit erhöhter LysoGb3-Konzentration und normaler LysoGb3-Konzentration ergaben sich sowohl für den GL Strain als auch für die native T1-Zeit signifikante Unterschiede während alle anderen linksventrikulären Funktionsparameter, die myokardiale Masse und die Septumdicke nicht signifikant differierten (Tabelle 4).

Table 5: Correlations of Strain values, LysoGb3 and native T1 in LysoGb3+ patients

	r	95% CI	p value
Septal native T1 to GRS	0.4410	-0.04752 to 0.7593	0.067
Septal native T1 to GCS	-0.612	-0.8435 to -0.1889	0.007
Septal native T1 to GLS	-0.394	-0.7370 to 0.09780	0.101
LysoGb3 to GRS	-0.4708	-0.7747 to 0.009960	0.049
LysoGb3 to GCS	0.6522	0.2524 to 0.8617	0.034
LysoGb3 to GLS	0.4602	-0.02347 to 0.7693	0.043
Septal native T1 to LysoGb3	-0.6279	-0.8508 to -0.2136	0.005

GRS – global radial strain, GCS – global circumferential strain, GLS – global longitudinal strain, r – correlation coefficient, CI – confidence interval, p – significance value

Vielmehr noch konnten signifikante Korrelationen der septalen nativen T1-Zeit zum GL Strain und zum GC Strain sowie signifikante Korrelationen der LysoGb3 zu allen Strainparametern und eine signifikante Korrelation der septalen nativen T1-Zeit zur LysoGb3 bei LysoGb3 positiven Morbus Fabry Patienten gezeigt werden (Tabelle 5).

Des Weiteren konnte eine Subgruppenanalyse von LysoGb3 negativen Morbus Fabry Patienten, LysoGb3 positiven Morbus Fabry Patienten und LysoGb3 positiven Morbus Fabry Patienten mit LVH oder LGE einen kontinuierlichen signifikanten Anstieg der LysoGb3-Konzentration über die Subgruppen zeigen, der von zunehmenden teils signifikanten Reduzierungen der septalen nativen T1-Zeit und einer kontinuierlichen teils signifikanten Verschlechterung de GLS begleitet wird (Tabelle 6).

Table 6: LysoGb3, septal native T1 and GLS in FD subgroups

	LysoGb3-	**LysoGb3+**	**LysoGb3+**
		LVH and LGE-	**LVH or LGE+**
	n = 10	**n = 11**	**n = 7**
LysoGb3 (ng/ml)	0.64 ± 0.20	12.65 ± 27.77	50.40 ± 59.00
p		**< 0.001**	**< 0.001**
p		**0.008**	
Native T1 time (ms)	955.5 ± 25.8	913.7 ± 50.1	873.0 ± 38.4
p		**0.06**	0.22
p		**0.002**	
GLS (%)	19.7 ± 1.4	17.9 ± 3.2	15.7 ± 4.2
p		0.17	0.28
p		**0.01**	

GLS – global longitudinal strain, p – significance value

Die Ergebnisse lassen folgenden Schluss zu: Die kontinuierliche Verschlechterung des GL Strains und kontinuierliche zunehmende Reduzierung der septalen nativen T1-Zeit von LysoGb3 negativen Morbus Fabry Patienten über LysoGb3 positiven Morbus Fabry Patienten zu LysoGb3 positiven Morbus Fabry Patienten mit LGE oder LVH legt den Verdacht nahe, dass Wandbewegungsstörungen schon früh im Rahmen einer kardialen Beteiligung eines Morbus Fabry vorkommen.

6.2.2. Rechtsventrikulärer myokardialer Strain zur Beurteilung von RV-Funktion und pulmonaler Hämodynamik

6.2.2.1. Cardiac Magnetic Resonance Imaging-Based Right Ventricular Strain Analysis for Assessment of Coupling and Diastolic Function in Pulmonary Hypertension

Aufgrund der komplexen Pathophysiologie mit Druck- und Volumenbelastungen des rechten Ventrikels und des rechtsventrikulären Ausflusstraktes kann die PH auch sehr gut dafür herangezogen werden die Eignung und den Nutzen neuer, nicht invasiver Methoden, wie den von FT Strainanalyse, mit etablierten und aufwendigen invasiven Messungen der kardialen Funktion und pulmonalen Hämodynamik zu vergleichen und zu evaluieren. Die PH verursacht einen zunehmenden und Nachlast-getriggerten Umbauprozess des rechten Ventrikels, der mit einer zunehmenden Kontraktilität, die zur Aufrechterhaltung der rechtsventrikulären-pulmonalarteriellen Kopplung („Couplings“) dient, einer diastolischen Versteifung des Ventrikels und der möglichen Entwicklung einer rechtsventrikulären Dilatation mit Rechtsherzversagen einhergeht [129]. Hieraus wird deutlich, dass die Beurteilung der rechtsventrikulären Funktion eine wesentliche Rolle im Management von Patienten mit PH spielt. Für die Beurteilung der Rechtsherzfunktion wiederum stellt die kardiale MRT den Goldstandard bzw. die Bildgebungsmethode der ersten Wahl dar [130]. Es konnte bereits gezeigt werden, dass die RVEF und der Quotient aus Schlagvolumen und endsystolischem Volumen als Surrogate der rechtsventrikulären Kontraktilität den Beginn einer rechtsventrikulären Dilatation vorhersagen können und prognostische Relevanz haben [131-133]. Das FT wiederum, eine neuere Methode in der kardialen MRT zur Quantifizierung des myokardialen Strains, ist assoziiert mit der rechtsventrikulären Funktion bei pulmonaler Hypertonie und zeigt einen stärkeren Zusammenhang zur Mortalität als die LVEF bei der dilatativen Kardiomyopathie [78, 134]. Andererseits sind die genauen physiologischen

Korrelate des rechtsventrikulären Strains bei chronischer Überladung des rechten Ventrikels und dessen Beziehungen zu direkten Messungen wie rechtsventrikulärer diastolischer Steifheit (Eed), rechtsventrikulärer endsystolischer Elastizität (Ees), der pulmonalarteriellen Elastizität (Ea) sowie zur rechtsventrikulären-pulmonalarteriellen Kopplung (Ees/Ea) weiterhin unklar. Die exakte und direkte Messung dieser funktionellen Parameter erfordert eine Erstellung von Druck-Volumen-Kurven („pressure-volume loops"), die nur invasiv, technisch sehr aufwendig und kostenintensiv mittels geeigneter Katheter erfolgen kann [135]. Auch und gerade deswegen sind nicht invasiv und einfach messbare Surrogate dieser Parameter im kardialen MRT wünschenswert.

Das Ziel der Studie war es deswegen die Zusammenhänge der im MRT ermittelten rechtsventrikulären Strainwerte mit den invasiv gemessenen und aus Druck-Volumen-Kurven abgeleiteten Messungen der rechtsventrikulären Kontraktilität, Steifheit sowie zu weiteren Nachlastparametern zu untersuchen, um den pathophysiologischen und klinischen Wert der rechtsventrikulären Strainanalyse bei PH zu definieren. Hierfür wurden 38 Patienten mit PH, die innerhalb von 24 Stunden sowohl eine kardiale MRT an einem 1.5 Tesla MRT-System (Somatom Avanto, Siemens Healthineers, Forchheim, Deutschland) zur Bestimmung der globalen rechtsventrikulären Strainwerte (longitudinaler, radiärer und zirkumferentieller) und einen Rechtsherzkatheter/Conductance-Katheter zur Evaluierung der rechtsventrikulären und pulmonalen Hämodynamik mit Druck-Volumen-Kurven erhielten, in die Studie eingeschlossen. Die FT Strainanalyse erfolgte mittels kommerzieller Software (cvi^{42}, Circle Cardiovascular Imaging, Calgary, AB, Canada). Die Zusammenhänge wurden mittels Korrelationen, Regressionsanalyse und Receiver-Operating-Characteristic (ROC) untersucht. Dabei zeigten sich vielversprechende Korrelationen der rechtsventrikulären

Strainparameter zur rechtsventrikulären-pulmonalarteriellen Kopplung („Coupling“), der rechtsventrikulären Elastizität und Steifheit, der Nachlast sowie der rechtsventrikulären diastolischen Dysfunktion allerdings nicht zur Kontraktilität. In einer multivariaten Analyse konnte zudem gezeigt werden, dass der rechtsventrikuläre globale radiäre Strain (GR) mit einer rechtsventrikulären-pulmonalarteriellen Entkopplung einhergeht und der rechtsventrikuläre globale longitudinale (GL) Strain mit der rechtsventrikulären diastolischen Steifheit einhergeht. Vielmehr noch konnte mittels Ratio aus rechtsventrikulärem globalem longitudinalem (GL) Strain und dem indizierten (Körperoberfläche/“body surface area“) rechtsventrikulärem enddiastolischem Volumen (EDVi) die rechtsventrikuläre diastolische Steifheit mit einer „area under the curve“ (AUC) von 0.908 in der ROC-Analyse vorhergesagt werden.

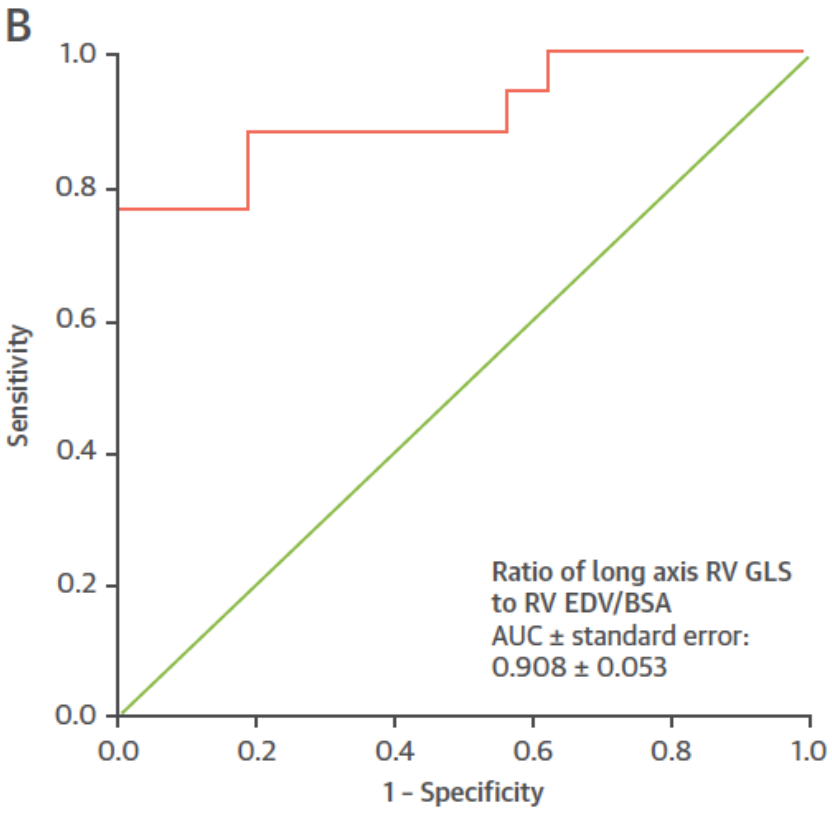

Abbildung 8: Die Abbildung zeigt die ROC-Kurve mit der AUC für das Verhältnis aus globalem longitudinalem rechtsventrikulärem Strain und rechtsventrikulärem indiziertem EDV.

Aus den Ergebnissen lässt sich somit schlussfolgern, dass die im MRT gemessenen Strainwerte bei chronischer rechtsventrikulärer Überladung aufgrund ihres Bezuges zur rechtsventrikulären-pulmonalarteriellen Entkopplung und zur rechtsventrikulären diastolischen Steifheit eine vielversprechende Alternative zu gegenwärtigen invasiven und aufwendigen kathetergestützten Messungen bei Patienten mit PH darstellen.

6.2.3. Rechtsatrialer Strain

6.2.3.1. Right ventricular function correlates of right atrial strain in pulmonary hypertension: a combined cardiac magnetic resonance and conductance catheter study

Das Rechtsherzversagen stellt die führende Todesursache bei Patienten mit PH dar [126]. Zudem haben die PH und das Rechtsherzversagen wiederum Einfluss auf die Größe, die Funktion und den Druck im rechten Vorhof, was mit einer schlechteren Prognose einhergeht [100, 136-138]. Eine aktuelle zweidimensionale, echokardiographische „speckle-tracking“ Studie suggeriert, dass die Reservoir-Funktion und passive Füllungsfunktion des rechten Vorhofes bei schwerer PH unabhängig von der Größe des rechten Vorhofes und des vorliegenden Druckes eingeschränkt sind und somit das Rechtsherzversagen und die Überladung reflektieren [137]. Dies legt nahe, dass der Einfluss des Rechtsherzversagens auf den rechten Vorhof einen integralen Bestandteil der Pathophysiologie der PH darstellt, und dass die Beurteilung der rechtsatrialen Funktion essentiell für ein besseres Verständnis der rechtsventrikulären Funktion bei PH ist. Auch deswegen wird der Interaktion der rechtsatrialen-rechtsventrikulären Achse und Kopplung im Rahmen der PH zunehmend Aufmerksamkeit geschenkt. Einigen echokardiographischen Studien haben bereits den Einfluss auf die rechtsatriale Deformierung und Funktion untersucht, wobei der rechtsatrialen Reservoir-Funktion eine Schlüsselrolle bei der PH-Progression nachgesagt wird [139-141]. Bisher ist die funktionelle Relevanz der rechtsatrialen Funktion bei PH allerdings unklar.

Deswegen war es das Ziel der Studie, nachdem sich die rechtsventrikuläre Strainparameter in unserer ersten Studie schon als eine vielversprechende Alternative zu invasiven Messungen der rechtsventrikulären und pulmonalen Hämodynamik bei PH Patienten erwiesen haben, die Zusammenhänge der im MRT ermittelten rechtsatrialen

Funktion und ihrer Korrelate mit den invasiven Messungen im Rechtsherzkatheter zu untersuchen.

Insgesamt wurden dafür 54 Patienten mit PH oder CTEPH prospektiv in die Studie eingeschlossen. Bei allen Patienten erfolgte einen Tag nach dem MRT an einem 1.5 Tesla MRT-System (Somatom Avanto, Siemens Healthineers, Forchheim, Deutschland) eine Rechtsherzkatheteruntersuchung mit einem Swan-Ganz-Katheter zur Ermittlung der Druck-Volumen-Kurven. Zudem wurden mit einem Immunoassay die „brain natriuretric peptides“ BNP-Werte ermittelt. Die Auswertung der Rechtsherzfunktion erfolgte mittels kommerzieller Software (cvi[42], Circle Cardiovascular Imaging, Calgary, AB, Canada), wobei die Auswertung des rechtsatrialen FT auf der SSFP CINE-Sequenz im 4-Kammerblick erfolgte. Für die Strainwerte wurden die Inter- und Intraobservervariabilitäten bestimmt. Neben der rechtsatrialen Reservoirfunktion wurden der aktive und der passive Strain bestimmt – die 3 physiologischen Phasen der atrialen Mechanik bzw. Phasenfunktionen des rechten Vorhofes. Die Reservoirfunktion repräsentiert die atriale Füllung in der ventrikulären Systole über den venösen Rückfluss, die Conduitfunktion bzw. der passive Strain repräsentiert die passive früh diastolische Blutpassage im Rahmen der ventrikulären Füllung und der aktive Strain die beschleunigte, aktive Füllung des rechten Ventrikels in der späten Diastole.

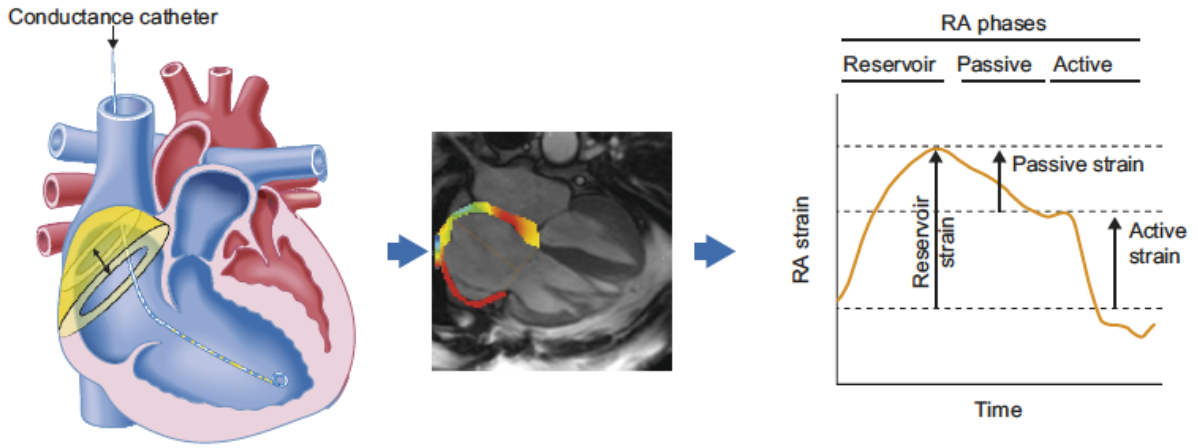

Abbildung 9: Die Abbildung zeigt die ROC-Kurve mit der AUC für das Verhältnis aus globalem longitudinalem rechtsventrikulärem Strain und rechtsventrikulärem indiziertem EDV.

Mittels Conductance-Katheter wurden der pulmonale vaskuläre Gefäßwiderstand (PVR), der mittlere pulmonalarterielle Druck (mPAP) und über die gemessenen Druck-Volumen-Kurven die pulmonalarterielle Elastizität (Ea), die endsystolische rechtsventrikuläre Elastizität (Ees), die rechtsventrikuläre diastolische Steifheit (Eed) und die rechtsventrikuläre-pulmonalarterielle Kopplung („Coupling“) ermittelt. Die Ergebnisse wurden mittels Korrelationen sowie uni- und multivariaten Regressionsanalysen analysiert. Dabei zeigte sich eine Korrelation der rechtsventrikulären diastolischen Steifheit (Eed) und des Durchmessers der Vena cava inferior zur Phasenfunktion des rechten Vorhofes. Demgegenüber zeigten die pulmonalarterielle Elastizität (Ea) und die endsystolische rechtsventrikuläre Elastizität (Ees) keine Korrelation zur Phasenfunktion des rechten Vorhofes.

Daraus lässt sich schlussfolgern, dass sich die Phasenfunktion des rechten Vorhofes in Relation zur eingeschränkten diastolischen Funktion des rechten chronisch überladenen Ventrikels verändert und zum venösen Rückwärtsfluss und der venösen Kongestion beiträgt. Auf der Basis dieser Ergebnisse sollte der rechtsatrialen Funktion im Management von PH Patienten mehr Aufmerksamkeit geschenkt werden.

6.3. Extrakardiale Nebenbefunde

6.3.1. Häufigkeit und Relevanz extrakardialer Nebenbefunde

6.3.1.1. Cardiac MRI: diagnostic gain of an additional axial SSFP chest sequence for the detection of potentially significant extracardiac findings in the cardiac MRI examination setting

Wie die vorherigen Studien zeigen werden zunehmend neue MRT-Techniken oder bereits bestehende MRT-Techniken bei neuen Fragestellungen wissenschaftlich untersucht, was wiederum die Basis für neue klinische Anwendungen legt. Dies führt dann zwangsläufig zu einer weiter zunehmenden Anzahl an kardialen MRT-Untersuchungen.

Durch ein das Herz teils deutlich übersteigendes „field-of-view“ (FOV, Sichtfeld) und durch die Durchführung von Planungssequenzen werden thorakale und abdominelle Organe partiell oder gar vollständig abgebildet, was mit einer zufälligen Detektion von Nebenbefunden einhergeht. Grundsätzlich kann man dabei signifikante von nicht-signifikanten, zufällig detektierten extrakardialen Nebenbefunden unterscheiden. Signifikante zufällig detektierte Nebenbefunde sind Befunde die eine weitere Abklärung oder eine weitere Therapie erfordern.

Da in einigen Studien schon die Prävalenz von extrakardialen und potentiell signifikanten extrakardialen Nebenbefunden untersucht wurde [29-31], war es das Ziel unserer Studie den Wert einer additiv durchgeführten axialen SSFP-Thorax-Sequenz, die den Thorax vom Apex bis zum Diaphragma erfasst, bei der Detektion von Nebenbefunden zu untersuchen.

Insgesamt wurden dafür 400 konsekutive kardiale MRT-Untersuchungen ausgewertet. Alle Sequenzen wurden separat hinsichtlich ihres Potentials bei der Detektion von Nebenbefunden und potentiell signifikanten extrakardialen Nebenbefunden untersucht.

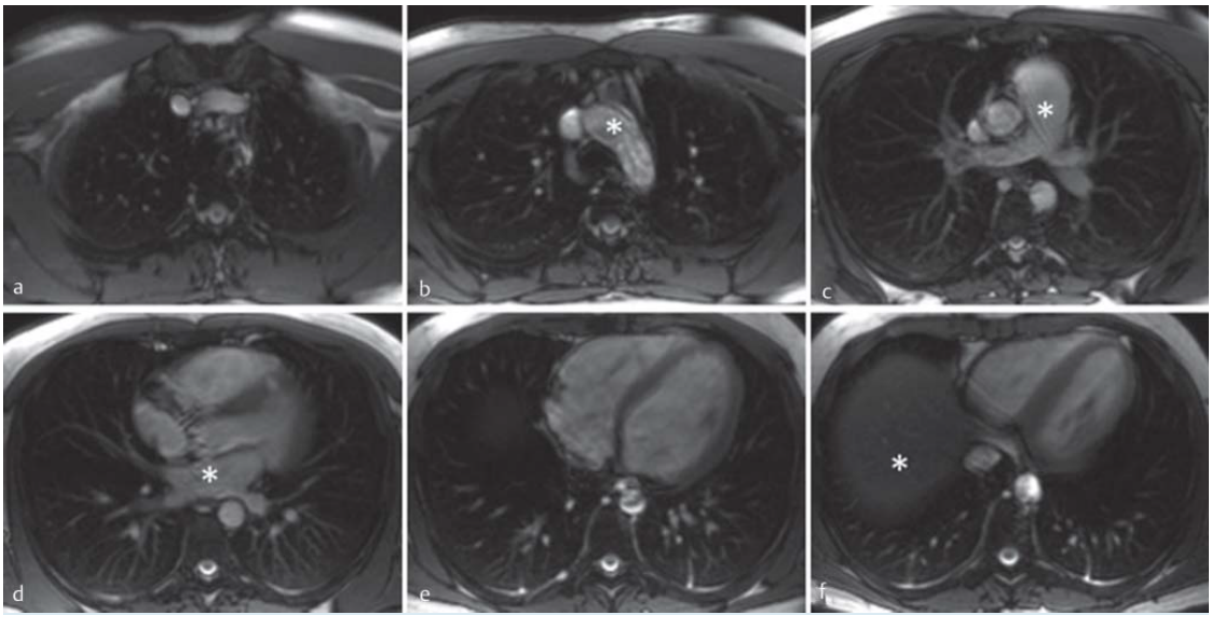

Abbildung 10: Die Abbildung zeigt Beispielbilder der additiven SSFP-Sequenz des Thorax: a.) in der Lungenspitze, b.) auf Höhe des Aortenbogens (weißer Stern), c.) auf Höhe des Truncus pulmonalis (weißer Stern), d.) auf Höhe des rechten Vorhofes (weißer Stern), e.) mit beiden Herzkammern, f.) mit partiell angeschnittenem Diaphragma rechts (weißer Stern).

Dabei wurden 25 potentiell signifikante extrakardiale Befunde detektiert, d.h. bei 6,25% der kardialen MRT-Untersuchungen wurde ein potentiell relevanter extrakardialer Befund erhoben. Neben großen Pleuraergüssen zeigten sich unter anderem eine neue Nebennierenmetastase, eine mediastinale Lymphadenopathie, eine amiodaroninduzierte Lungenfibrose oder ein Rezidiv eines Mammakarzinoms.

Während in den Planungssequenzen (engl. Survey) alle potentiell signifikanten extrakardialen Befunde abgrenzbar waren, waren in der additiven SSFP-Sequenz des Thorax nur 24 potentiell signifikante extrakardiale Befunde abgrenzbar.

Hieraus kann man schlussfolgern, dass eine additive SSFP-Thorax-Sequenz gegenüber den Planungssequenzen keinen Zusatznutzen bei der Detektion von potentiell signifikanten extrakardialen Nebenbefunden hat. Allerdings sollten die Planungssequenzen in kardialen MRT-Untersuchungen immer gründlich hinsichtlich extrakardialer Nebenbefunde „gescreent“ werden.

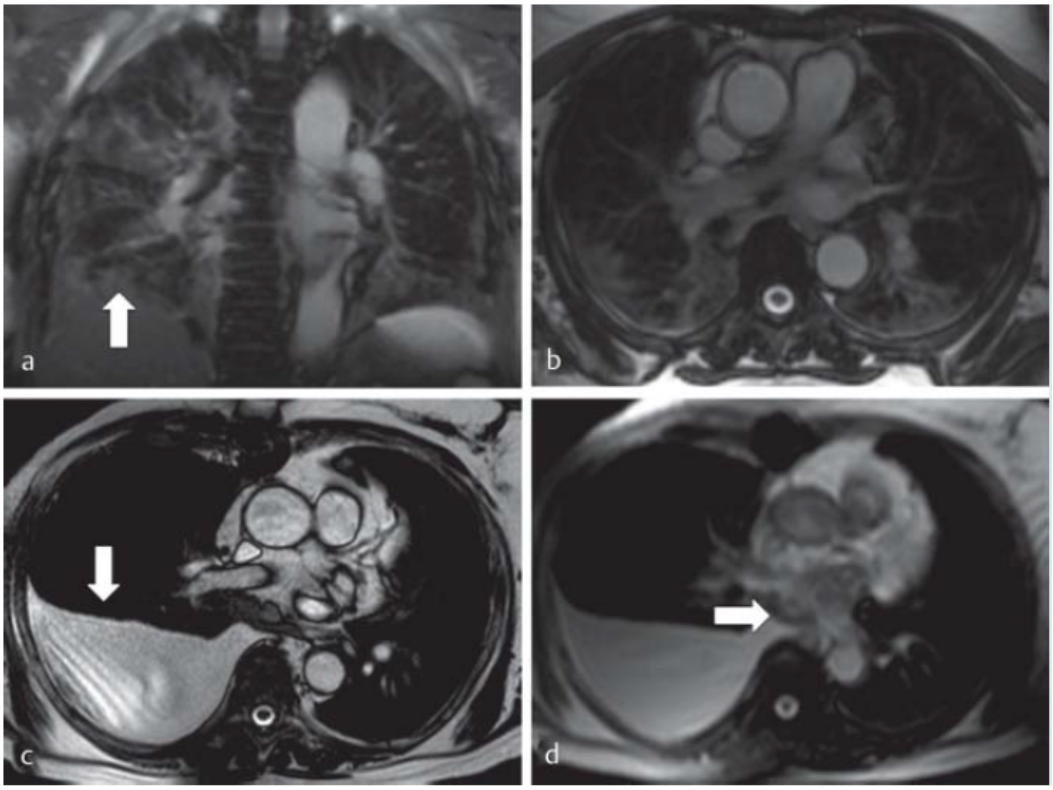

Abbildung 11: Die Abbildung zeigt eine amiodaroninduzierte Lungenfibrose in Bild (a) in der Planungssequenz sowie in Bild (b) in der additiven SSFP-Sequenz des Thorax. Bild (c) in der Planungssequenz und Bild (d) in der additiven SSFP-Sequenz zeigen einen großen Pleuraerguss und eine mediastinale Lymphadenopathie bei einem Mammakarzinomrezidiv.

7. Ergebnisse und Diskussion

7.1. Parametrische Bildgebung

Unsere Ergebnisse zum Nutzen des nativen T1-Mappings in der Diagnostik einer kardialen Beteiligung beim Morbus Fabry, mit deutlich reduzierten nativen T1-Zeiten verglichen zu einem Kontrollkollektiv, sind vergleichbar zu bisher veröffentlichten Ergebnissen anderer Autoren [51, 90]. Darüber hinaus konnten Thompson et al. sogar zeigen, dass die native T1-Zeit geeignet ist um zwischen einer kardialen Morbus Fabry Manifestation und anderen Kardiomyopathien mit LVH unabhängig von Funktion, Morphologie oder Geschlecht zu differenzieren [90]. Gegenüber den anderen Studienergebnissen ist der von uns nachgewiesene Zusammenhang mit einer guten Korrelation der nativen T1-Zeit zum fabryspezifischen Biomarker LysoGb3 als krankheitsspezifisches Äquivalent allerdings neu und äußerst vielversprechend. Hierdurch wird die diagnostische Eignung des nativen T1-Mappings zur Früherkennung einer kardialen Morbus Fabry Manifestation bestätigt und sogar weiter aufgewertet. Die gewonnenen Ergebnisse haben eine hohe therapeutische Relevanz, da Patienten mit einer kardialen Manifestation von einer Diagnosestellung in einem frühen Krankheitsstadium, d.h. ohne Nachweis von Narben oder einer LVH im konventionellen kardialen MRT, ausgesprochen gut von einer Enzymersatztherapie profitieren [86]. Auch besonders vor dem Hintergrund, da bei etwa der Hälfte aller Patienten mit einem Morbus Fabry ohne LVH schon native T1-Zeit Reduzierungen bestehen [142], während bei etwa 85% der Morbus Fabry Patienten mit LVH native T1-Zeit Reduzierungen [142] durch die Einlagerung von Glykosphingolipiden [51, 90] vorliegen.

Auch die von uns gewonnen Ergebnisse zur Visualisierung, Charakterisierung und Quantifizierung einer myokardialen Fibrose bei Patienten mit CTEPH sind vergleichbar zu den Ergebnissen anderer Autoren. Deren Studiengruppen konnten bereits native T1-

Zeit- und ECV-Erhöhungen bei unterschiedlichen Erkrankungen mit myokardialer Fibrose zeigen [143-146]. Darüber hinaus wurde in unserer Studie der Zusammenhang des nativen T1-Mappings zur rechtsventrikulären Funktion und zu Parametern der pulmonalen Hämodynamik (mPAP und PVR) untersucht, wobei sich vielversprechende und gute Korrelationen zeigten. Ähnliche Ergebnisse konnten schon im Tierexperiment bei chronischer PH gezeigt werden [111]. Zudem konnte bei Patienten mit präkapillärer pulmonaler Hypertonie [147] und bei Patienten mit „heart failure with preserved ejection fraction“ (HFpEF) mit begleitender postkapillärer pulmonaler Hypertonie [148] vergleichbare Ergebnisse gezeigt werden. Auch deswegen haben die von uns gewonnenen Ergebnisse eine hohe klinische Relevanz, da das native T1-Mapping unter Umständen sogar dafür geeignet sein könnte bzw. großes Potential besitzt die Krankheitsschwere bei Patienten mit PH über die native T1-Zeit als fibrosespezifisches Äquivalent zu beurteilen. Zudem könnte das native T1-Mapping als Prognostikator und für ein nicht-invasives Therapiemonitoring herangezogen werden.

Nicht zuletzt oder gerade deswegen wurde in unserer Anschlussstudie untersucht, ob das native T1-Mapping geeignet ist Therapieeffekte der Ballonangioplastie (BPA) bei Patienten mit inoperabler CTEPH abzubilden – Überprüfung der Eignung zur Beurteilung einer Therapie bzw. eines Therapieerfolges. Dafür wurden Veränderungen der nativen T1-Zeit, Rechtsherzfunktion und pulmonale Hämodynamik vor und 6 Monate nach erfolgter BPA-Therapie untersucht.

Verglichen zur diagnostischen Eignung des nativen T1-Mappings sind die Einflüsse von Therapieverfahren auf kardiale T1-Zeitveränderungen bislang erst sehr wenig untersucht. Erste Ergebnisse bei Patienten mit myokardialer Inflammation (Myokarditis) konnten im Follow-up eine Normalisierung bzw. ein Sinken der nativen T1-Zeit zeigen [149]. Bei Patienten mit systemischem Lupus erythematodes und begleitender Lupus

Myokarditis konnten zudem signifikante Verbesserungen der nativen T1-Zeit durch eine intensivierte antiinflammatorische Behandlung und somit ein Therapieansprechen gezeigt werden [150].

In unserem Patientenkollektiv legt die signifikante Verbesserung der septalen nativen T1-Zeit mit einer gleichzeitigen Normalisierung der rechtsventrikulären Funktion und der pulmonalen Hämodynamik nahe, dass die nativen T1-Zeiten zelluläre Gewebsveränderungen im Rahmen der PH, in diesem Fall der CTEPH, anzeigen. Zudem verbessert eine BPA-Therapie nicht nur die pulmonale Hämodynamik, sondern induziert offensichtlich auch einen Umbauprozess „reverse remodeling" des rechtsventrikulären, septalen Myokards, der wiederum mit einer Verbesserung der rechtsventrikulären Funktion einhergeht. Möglicherweise eignet sich das native T1-Mapping deswegen zukünftig sogar bei der Präselektion bzw. der Identifikation von Patienten, die besonders gut von einer BPA-Therapie profitieren könnten.

Zusammenfassend zeigen unsere Ergebnisse, dass die parametrische Bildgebung bzw. das native T1-Mapping eine verbesserte Gewebecharakterisierung erlaubt und eine Quantifizierung von Gewebsveränderungen ermöglicht, die mit krankheitsspezifischen Biomarkern sowie funktionellen und hämodynamischen Parametern korrelieren.

7.2. Myokardialer Strain

Unsere Ergebnisse zum Nutzen der linksventrikulären myokardialen Strainanalyse (FT Strainanalyse) zur Detektion einer kardialen Morbus Fabry Manifestation sind vergleichbar zu den Ergebnissen anderer Autoren, die ebenfalls Einschränkungen des GL Strains bei Morbus Fabry Patienten verglichen zu Kontrollkollektiven zeigen konnten [80, 151]. Darüber hinaus wurden in unserem Patientenkollektiv die Zusammenhänge des myokardialen Strains zur nativen T1-Zeit und zum fabryspezifischen Biomarker LysoGb3

untersucht. Ähnlich zu unseren Ergebnissen konnten auch Vijapurapu et al. [80] und Zhao et al. [151] Zusammenhänge zwischen dem GL Strain und der nativen T1-Zeit auch ohne Vorhandensein einer LVH [80] zeigen. Darüber hinaus konnten bei unseren Patienten moderate und gute, signifikante Korrelationen für alle erhobenen Strainparameter (GL Strain, GR Strain und GC Strain) zum fabryspezifischen Biomarker LysoGb3 gezeigt werden. Vielmehr noch konnte in einer Subgruppenanalyse gezeigt werden, dass der GL Strain von den LysoGb3 negativen Morbus Fabry Patienten, über die LysoGb3 positiven Patienten ohne LVH und LGE zu den LysoGb3 positiven Patienten mit LVH oder LGE kontinuierlich und begleitet von der nativen T1-Zeit abnimmt.

Aus unseren Ergebnissen kann somit abgeleitet werden, dass Zusammenhänge zwischen dem fabryspezifischen Biomarker LysoGb3, dem GL Strain und der nativen T1-Zeit vorliegen, die nahelegen, dass bei frühen kardialen Morbus Fabry Manifestationen bereits neben messbaren gewebsspezifischen Veränderungen auch Wandbewegungsstörungen vorhanden sind.

Der aus dem MRT über FT Strainanalysen abgeleitete rechtsventrikuläre myokardiale Strain bei Patienten mit PH wurde zuvor bereits in einigen Studien von unterschiedlichen Studiengruppen untersucht. Dabei wurden unter anderem Einschränkungen des rechtsventrikulären Strains beschrieben [152, 153]. Des Weiteren wurden auch Therapieeffekte der BPA bei Patienten mit CTEPH [154] oder die prognostische Wertigkeit [155] von FT-Strainanalysen untersucht. Darüber hinaus wurde in unserer Studie aber erstmalig die Assoziation von rechtsventrikulären FT-Strainanalysen zu „pressure volume loop“ abhängigen und aufwendig mittels Conductance-Katheter bestimmten Parametern wie der rechtsventrikulären Kontraktilität, der rechtsventrikuläre Steifheit und anderen Nachlastparametern bestimmt. Dabei konnten Zusammenhänge des FT Strains zur rechtsventrikulären enddiastolischen Steifheit (Eed),

zur pulmonalarteriellen Elastizität (Es) und zum rechtsventrikulären-pulmonalarteriellen Kopplung (Ees/Ea – „Coupling“) gezeigt werden. Insbesondere zeigt sich, dass der rechtsventrikuläre Strain ein vielversprechender Indikator für die rechtsventrikuläre enddiastolische Steifheit (Eed) und eine rechtsventrikuläre-pulmonalarterielle Entkopplung ist. Die Ergebnisse sind von großer Bedeutung, da das ohnehin schon breite Anwendungsspektrum der kardialen MRT im Follow-up bei Patienten mit PH um ein Anwendungsgebiet erweitert werden könnte und vielmehr noch zum weiteren Verständnis der Pathophysiologie bei chronischer Drucküberladung beiträgt.

Neben dem linksventrikulären und dem rechtsventrikulären myokardialen Strain kann auch der rechtsatriale Strain mittels FT-Strainanalysen bestimmt werden. Bisher gibt es allerdings nur sehr wenige Untersuchungen des rechtsatrialen Strains, insbesondere bei PH. Zuvor wurde nur in einigen echokardiographische Studien der Einfluss der PH auf die rechtsatriale Deformierung und Funktion untersucht [139-141]. Unsere Ergebnisse zeigen zunächst, dass eine Bestimmung des rechtsatrialen Strains via FT-Strainanalyse im MRT bei Patienten mit PH gut möglich ist. Zudem zeigen unsere Ergebnisse, dass eine Korrelation der rechtsventrikulären diastolischen Steifheit (Eed) und des Durchmessers der Vena cava inferior zur Phasenfunktion des rechten Vorhofes besteht. Hieraus lässt sich ableiten, dass sich die Phasenfunktion des rechten Vorhofes in Relation zur eingeschränkten diastolischen Funktion des chronisch überladenen rechten Ventrikels verändert und zum venösen Rückwärtsfluss und der venösen Kongestion beiträgt. Unsere Ergebnisse zum rechtsatrialen Strain bei PH Patienten sind somit von hoher klinischer und physiologischer Relevanz, da der rechtsatrialen-rechtsventrikulären Achse immer mehr Aufmerksamkeit gewidmet wird und unsere Ergebnisse erstmals das ihr

Zusammenspiel auf Basis aufwendiger invasiver Messungen und MRT-Analysen bei PH Patienten zeigen.

7.3. Extrakardiale Nebenbefunde

In unserer Studie zu den potentiell signifikanten extrakardialen Nebenbefunden wurde der zusätzliche Nutzen einer den kompletten Thorax umfassenden SSFP-Sequenz bei der Detektion von solchen Nebenbefunde untersucht. Der Anteil an potentiell signifikanten extrakardialen Nebenbefunden im kardialen MRT in unserer Studie vergleichbar zu den Ergebnissen anderer Autoren war, bei uns wurden 6.25% potentiell signifikante extrakardiale Nebenbefunde detektiert, in anderen Studien lag der Anteil zwischen 3.1% und 21.0% [29-31]. Eine große Metaanalyse aus 12 Studien und mit insgesamt 7062 eingeschlossenen Patienten, konnten bei 12% der Patienten signifikante, zufällig detektierte, extrakardiale Nebenbefunde zeigen, die bei 1% der Patienten sogar einen Wechsel des Patientenmanagements zur Folge hatten [32]. Für die additive SSFP-Thorax-Sequenz ergab sich in unserer Studie verglichen zu den standardisierten Planungssequenzen und Untersuchungssequenzen hingegen kein Zusatznutzen. Da relevante extrakardiale Nebenbefunde allerdings nicht selten sind und durchaus Einfluss auf das weitere Patientenmanagement haben, sollte immer auf allen vorhandenen Sequenzen auch eine erweiterte Bildanalyse abseits des Herzens erfolgen.

8. Zusammenfassung und Ausblick

Die kardiale Bildgebung ist schon lange ihren Kinderschuhen um die Jahrtausendwende entwachsen und hat sich über die letzten beiden Jahrzehnte zu einem absoluten „powerhouse“ in der nicht invasiven kardialen Bildgebung entwickelt. Während in ihren Anfängen noch die Abbildung von komplexen Herzfehlern und Herztumoren besonders

im Fokus standen, hat sie sich bei einer Vielzahl von Fragestellungen in der klinischen Routine, unter anderem in der Diagnostik der myokardialen Ischämie, den Kardiomyopathien und der Myokarditis, etabliert und durchgesetzt.

Im letzten Jahrzehnt wurde ausgehend von einer funktionellen und visuellen Analyse der kardialen Erkrankungen zunehmend eine Entwicklung zu einer semiquantitativen und nun auch quantitativen Diagnostik in der kardialen MRT vorangetrieben und vollzogen. Wie unsere Ergebnisse zeigen ermöglicht die Quantifizierung von myokardialen Gewebsveränderungen durch natives T1-Mapping und ECV und der Wandbewegung über myokardiale FT-Strainanalysen eine verbesserte Primärdiagnostik, ein Follow-up, ein Therapiemonitoring und auch zunehmend eine Prognoseabschätzung bei unterschiedlichen kardialen Erkrankungen.

Vielmehr noch bestehen gar vielversprechende Zusammenhänge mit kardialen und krankheitsspezifischen Biomarkern und Zusammenhänge zu nur sehr aufwendig und invasiv messbaren Parametern der Herzfunktion und der pulmonalen Hämodynamik. Zwar ist die kardiale MRT immer noch weit entfernt von einer One-Stop-Shop-Prozedur, da unter anderem die nicht-invasive Darstellung der Koronararterien auch weiterhin eine absolute Domäne der kardialen CT ist.

Allerdings haben neben den von uns analysierten Verfahren auch weitere Techniken wie das T2-Mapping [142], Weiterentwicklungen von Techniken wie z.B. die myokardiale Texturanalyse [156, 157] oder andere Techniken wie z.B. 4-D-Flussanalysen [158, 159] großes Potential die ohnehin schon so vielfältige und robuste Methode weiter aufzuwerten und den klinischen Stellenwert weiter auszubauen. Zusätzlich haben die kardiale Hybridbildgebung im PET/MRT [160] und die künstliche Intelligenz [161] mit bereits vorhandene Applikationen Potential die kardiale MRT aufzuwerten.

Nichtsdestotrotz liegt allerdings noch einiges an Arbeit vor den Akteuren der kardiovaskulären Radiologie, denn um die teils vielversprechenden Studienergebnisse für die klinische Routine auf ein höheres Evidenzniveau zu heben bedarf es dringend noch einiger multizentrischen Studien mit größeren Patientenkollektiven. In diesem Zuge müssen auch dringend weitere Anstrengungen unternommen werden Lösungen für die lokal teils sehr heterogenen Bedingungen mit unterschiedlichen Geräteherstellern, Feldstärken und Sequenztypen zu finden, damit definierte Normwerte für unterschiedliche Parameter auf eine breite Basis gestellt werden können.

9. Literaturverzeichnis

1. Bellenger NG, Davies LC, Francis JM, Coats AJ, Pennell DJ. Reduction in sample size for studies of remodeling in heart failure by the use of cardiovascular magnetic resonance. J Cardiovasc Magn Reson. 2000; 2(4): 271-278.
2. Nagel E, Lehmkuhl HB, Bocksch W, et al. Noninvasive diagnosis of ischemia-induced wall motion abnormalities with the use of high-dose dobutamine stress MRI: comparison with dobutamine stress echocardiography. Circulation. 1999; 99(6): 763-770.
3. Jahnke C, Nagel E, Gebker R, et al. Prognostic value of cardiac magnetic resonance stress tests: adenosine stress perfusion and dobutamine stress wall motion imaging. Circulation. 2007; 115(13): 1769-1776.
4. Sharma V, Binukrishnan S, Schoepf UJ, Ruzsics B. Myocardial tissue characterization with magnetic resonance imaging. J Thorac Imaging. 2014; 29(6): 318-330.
5. Achenbach S, Barkhausen J, Beer M, et al. Konsensusempfehlungen der DRG/DGK/DGPK zum Einsatz der Herzbildgebung mit Computertomografie und Magnetresonanztomografie [Consensus recommendations of the German Radiology Society (DRG), the German Cardiac Society (DGK) and the German Society for Pediatric Cardiology (DGPK) on the use of cardiac imaging with computed tomography and magnetic resonance imaging] [published correction appears in Rofo. 2012 Apr;184(4): E1. Marholdt, H [corrected to Mahrholdt, H]]. Rofo. 2012; 184(4): 345-368.
6. Moons P, Bovijn L, Budts W, Belmans A, Gewillig M. Temporal trends in survival to adulthood among patients born with congenital heart disease from 1970 to 1992 in Belgium. Circulation. 2010; 122(22): 2264-2272.
7. Fox CS, Evans JC, Larson MG, Kannel WB, Levy D. Temporal trends in coronary heart disease mortality and sudden cardiac death from 1950 to 1999: the Framingham Heart Study. Circulation. 2004; 110(5): 522-527.

8. Ferreira VM, Schulz-Menger J, Holmvang G, et al. Cardiovascular Magnetic Resonance in Nonischemic Myocardial Inflammation: Expert Recommendations. J Am Coll Cardiol. 2018; 72(24): 3158-3176.
9. Ferreira VM, Piechnik SK, Dall'Armellina E, et al. Native T1-mapping detects the location, extent and patterns of acute myocarditis without the need for gadolinium contrast agents. J Cardiovasc Magn Reson. 2014; 16(1): 36.
10. Roller FC, Fuest S, Meyer M, et al. Assessment of Cardiac Involvement in Fabry Disease (FD) with Native T1 Mapping. Natives T1-Mapping zur Beurteilung einer kardialen Beteiligung bei Morbus Fabry. Rofo. 2019; 191(10): 932-939.
11. Lurz P, Luecke C, Eitel I, et al. Comprehensive Cardiac Magnetic Resonance Imaging in Patients With Suspected Myocarditis: The MyoRacer-Trial. J Am Coll Cardiol. 2016; 67(15): 1800-1811.
12. Luetkens JA, Homsi R, Dabir D, et al. Comprehensive Cardiac Magnetic Resonance for Short-Term Follow-Up in Acute Myocarditis. J Am Heart Assoc. 2016; 5(7): e003603.
13. Roller FC, Kriechbaum S, Breithecker A, et al. Correlation of native T1 mapping with right ventricular function and pulmonary haemodynamics in patients with chronic thromboembolic pulmonary hypertension before and after balloon pulmonary angioplasty. Eur Radiol. 2019; 29(3): 1565-1573.
14. Hinojar R, Foote L, Sangle S, et al. Native T1 and T2 mapping by CMR in lupus myocarditis: Disease recognition and response to treatment. Int J Cardiol. 2016; 222: 717-726.
15. Puntmann VO, Carr-White G, Jabbour A, et al. T1-Mapping and Outcome in Nonischemic Cardiomyopathy: All-Cause Mortality and Heart Failure [published correction appears in JACC Cardiovasc Imaging. 2017 Mar;10(3): 384]. JACC Cardiovasc Imaging. 2016; 9(1): 40-50.
16. Lee H, Park JB, Yoon YE, et al. Noncontrast Myocardial T1 Mapping by Cardiac Magnetic Resonance Predicts Outcome in Patients With Aortic Stenosis. JACC Cardiovasc Imaging. 2018; 11(7): 974-983.

17. Luetkens JA, Petry P, Kuetting D, et al. Left and right ventricular strain in the course of acute myocarditis: a cardiovascular magnetic resonance study. Links- und rechtsventrikulärer Strain im Krankheitsverlauf der akuten Myokarditis: Eine kardiale MRT Studie. Rofo. 2018; 190(8): 722-732.
18. Luetkens JA, Schlesinger-Irsch U, Kuetting DL, et al. Feature-tracking myocardial strain analysis in acute myocarditis: diagnostic value and association with myocardial oedema. Eur Radiol. 2017; 27(11): 4661-4671.
19. Doerner J, Bunck AC, Michels G, Maintz D, Baeßler B. Incremental value of cardiovascular magnetic resonance feature tracking derived atrial and ventricular strain parameters in a comprehensive approach for the diagnosis of acute myocarditis. Eur J Radiol. 2018; 104: 120-128.
20. Dewey M, Schnapauff D, Teige F, et al. Non-cardiac findings on coronary computed tomography and magnetic resonance imaging. Eur Radiol 2007; 17: 2038–2043.
21. Haller S, Kaiser C, Buser P et al. Coronary artery imaging with contrastenhanced MDCT: extracardiac findings. Am J Roentgenol 2006; 187: 105–110.
22. Horton KM, Post WS, Blumenthal RS, et al. Prevalence of significant noncardiac findings on electron-beam computed tomography coronary artery calcium screening examinations. Circulation 2002; 106: 532–534.
23. Hunold P, Schmermund A, Seibel RM, et al. Prevalence and clinical significance of accidental findings in electron-beam tomographic scans for coronary artery calcification. Eur Heart J 2001; 22: 1748–1758.
24. Onuma Y, Tanabe K, Nakazawa G, et al. Noncardiac findings in cardiac imaging with multidetector computed tomography. J Am Coll Cardiol 2006; 48: 402–406.
25. Schragin JG,Weissfeld JL, Edmundowicz D, et al. Non-cardiac findings on coronary electron beam computed tomography scanning. J Thorac Imaging 2004; 19: 82–86.
26. Atalay MK, Prince EA, Pearson CA, et al. The prevalence and clinical significance of noncardiac findings on cardiac MRI. Am J Roentgenol 2011; 196: W387–W393.

27. MacMahon H, Naidich DP, Goo JM, et al. Guidelines for Management of Incidental Pulmonary Nodules Detected on CT Images: From the Fleischner Society 2017. Radiology. 2017; 284(1): 228-243.
28. Megibow AJ, Baker ME, Morgan DE, et al. Management of Incidental Pancreatic Cysts: A White Paper of the ACR Incidental Findings Committee. J Am Coll Radiol. 2017; 14(7): 911-923.
29. Chan PG, Smith MP, Hauser TH, et al. Noncardiac pathology on clinical cardiac magnetic resonance imaging. JACC Cardiovasc Imaging 2009; 980–986.
30. McKenna DA, Laxpati M, Colletti PM. The prevalence of incidental findings at cardiac MRI. Open Cardiovasc Med J 2008; 2: 20–25.
31. Wyttenbach R, Médioni N, Santini P, et al. Extracardiac findings detected by cardiac magnetic resonance imaging. Eur Radiol 2012; 22: 1295–1302.
32. Dunet V, Schwitter J, Meuli R, Beigelman-Aubry C. Incidental extracardiac findings on cardiac MR: Systematic review and meta-analysis. J Magn Reson Imaging. 2016; 43(4): 929-939.
33. Friedrich MG, Sechtem U, Schulz-Menger J, et al. Cardiovascular magnetic resonance in myocarditis: A JACC White Paper. J Am Coll Cardiol. 2009; 53(17): 1475-1487.
34. Abdel-Aty H, Boyé P, Zagrosek A, et al. Diagnostic performance of cardiovascular magnetic resonance in patients with suspected acute myocarditis: comparison of different approaches. J Am Coll Cardiol. 2005; 45(11): 1815-1822.
35. Gutberlet M, Spors B, Thoma T, et al. Suspected chronic myocarditis at cardiac MR: diagnostic accuracy and association with immunohistologically detected inflammation and viral persistence. Radiology. 2008; 246(2): 401-409.
36. Kellman, P., Aletras, A. H., Mancini, C, et al. T2-prepared SSFP improves diagnostic confidence in edema imaging in acute myocardial infarction compared to turbo spin echo. Magnetic Resonance in Medicine. 2007; 57(5): 891–7.

37. Adabag AS, Maron BJ, Appelbaum E, et al. Occurrence and frequency of arrhythmias in hypertrophic cardiomyopathy in relation to delayed enhancement on cardiovascular magnetic resonance. J Am Coll Cardiol. 2008; 51(14): 1369-1374.
38. O'Hanlon R, Grasso A, Roughton M, et al. Prognostic significance of myocardial fibrosis in hypertrophic cardiomyopathy. J Am Coll Cardiol. 2010; 56(11): 867-874.
39. Assomull RG, Prasad SK, Lyne J, et al. Cardiovascular magnetic resonance, fibrosis, and prognosis in dilated cardiomyopathy. J Am Coll Cardiol. 2006; 48(10): 1977-1985.
40. Greulich S, Deluigi CC, Gloekler S, et al. CMR imaging predicts death and other adverse events in suspected cardiac sarcoidosis. JACC Cardiovasc Imaging. 2013; 6(4): 501-511.
41. Kim RJ, Judd RM. Gadolinium-enhanced magnetic resonance imaging in hypertrophic cardiomyopathy: in vivo imaging of the pathologic substrate for premature cardiac death?. J Am Coll Cardiol. 2003; 41(9): 1568-1572.
42. Moon JC, Reed E, Sheppard MN, et al. The histologic basis of late gadolinium enhancement cardiovascular magnetic resonance in hypertrophic cardiomyopathy. J Am Coll Cardiol. 2004; 43(12): 2260-2264.
43. Yilmaz A, Kindermann I, Kindermann M, et al. Comparative evaluation of left and right ventricular endomyocardial biopsy: differences in complication rate and diagnostic performance. Circulation. 2010; 122(9): 900-909.
44. Mewton N, Liu CY, Croisille P, et al. Assessment of myocardial fibrosis with cardiovascular magnetic resonance. J Am Coll Cardiol. 2011; 57(8): 891-903.
45. Iles L, Pfluger H, Phrommintikul A, et al. Evaluation of diffuse myocardial fibrosis in heart failure with cardiac magnetic resonance contrast-enhanced T1 mapping. J Am Coll Cardiol. 2008; 52(19): 1574-1580.
46. Messroghli DR, Walters K, Plein S, et al. Myocardial T1 mapping: application to patients with acute and chronic myocardial infarction. Magn Reson Med. 2007; 58(1): 34-40.
47. Moon JC, Messroghli DR, Kellman P, et al. Myocardial T1 mapping and extracellular volume quantification: a Society for Cardiovascular Magnetic Resonance (SCMR) and CMR

Working Group of the European Society of Cardiology consensus statement. J Cardiovasc Magn Reson. 2013; 15(1): 92.

48. Dass S, Suttie JJ, Piechnik SK, et al. Myocardial tissue characterization using magnetic resonance noncontrast t1 mapping in hypertrophic and dilated cardiomyopathy. Circ Cardiovasc Imaging. 2012; 5(6): 726-733.
49. Ferreira VM, Piechnik SK, Dall'Armellina E, et al. Non-contrast T1-mapping detects acute myocardial edema with high diagnostic accuracy: a comparison to T2-weighted cardiovascular magnetic resonance. J Cardiovasc Magn Reson. 2012; 14(1): 42.
50. Karamitsos TD, Piechnik SK, Banypersad SM, et al. Noncontrast T1 mapping for the diagnosis of cardiac amyloidosis. JACC Cardiovasc Imaging. 2013; 6(4): 488-497.
51. Sado DM, White SK, Piechnik SK, et al. Identification and assessment of Anderson-Fabry disease by cardiovascular magnetic resonance noncontrast myocardial T1 mapping. Circ Cardiovasc Imaging. 2013; 6(3): 392-398.
52. Pedersen SF, Thrysøe SA, Robich MP, et al. Assessment of intramyocardial hemorrhage by T1-weighted cardiovascular magnetic resonance in reperfused acute myocardial infarction. J Cardiovasc Magn Reson. 2012; 14(1): 59.
53. Gai N, Turkbey EB, Nazarian S, et al. T1 mapping of the gadolinium-enhanced myocardium: adjustment for factors affecting interpatient comparison. Magn Reson Med. 2011; 65(5): 1407-1415.
54. Kellman P, Hansen MS. T1-mapping in the heart: accuracy and precision. J Cardiovasc Magn Reson. 2014; 16(1): 2. Published 2014 Jan 4.
55. Zou Z, Zhang HL, Roditi GH, Leiner T, Kucharczyk W, Prince MR. Nephrogenic systemic fibrosis: review of 370 biopsy-confirmed cases. JACC Cardiovasc Imaging. 2011; 4(11): 1206-1216.
56. White SK, Sado DM, Fontana M, et al. T1 mapping for myocardial extracellular volume measurement by CMR: bolus only versus primed infusion technique. JACC Cardiovasc Imaging. 2013; 6(9): 955-962.

57. Schelbert EB, Testa SM, Meier CG, et al. Myocardial extravascular extracellular volume fraction measurement by gadolinium cardiovascular magnetic resonance in humans: slow infusion versus bolus. J Cardiovasc Magn Reson. 2011; 13(1): 16.
58. Flett AS, Hayward MP, Ashworth MT, et al. Equilibrium contrast cardiovascular magnetic resonance for the measurement of diffuse myocardial fibrosis: preliminary validation in humans. Circulation. 2010; 122(2): 138-144.
59. Weber KT, Brilla CG. Pathological hypertrophy and cardiac interstitium. Fibrosis and renin-angiotensin-aldosterone system. Circulation. 1991; 83(6): 1849-1865.
60. Sibley CT, Noureldin RA, Gai N, et al. T1 Mapping in cardiomyopathy at cardiac MR: comparison with endomyocardial biopsy. Radiology. 2012; 265(3): 724-732.
61. Wong TC, Piehler K, Meier CG, et al. Association between extracellular matrix expansion quantified by cardiovascular magnetic resonance and short-term mortality. Circulation. 2012; 126(10): 1206-1216.
62. Kellman P, Wilson JR, Xue H, Ugander M, Arai AE. Extracellular volume fraction mapping in the myocardium, part 1: evaluation of an automated method. J Cardiovasc Magn Reson 2012; 14: 63.
63. Cerqueira MD, Weissman NJ, Dilsizian V, et al. Standardized myocardial segmentation and nomenclature for tomographic imaging of the heart: a statement for healthcare professionals from the Cardiac Imaging Committee of the Council on Clinical Cardiology of the American Heart Association. Circulation 2002; 105: 539–42.
64. Scatteia A, Baritussio A, Bucciarelli-Ducci C. Strain imaging using cardiac magnetic resonance. Heart Fail Rev 2017; 22: 465–476.
65. Swoboda PP, Erhayiem B, McDiarmid AK, et al. Relationship between cardiac deformation parameters measured by cardiovascular magnetic resonance and aerobic fitness in endurance athletes. J Cardiovasc Magn Reson 2016; 18: 48.
66. Rankin JS, McHale PA, Arentzen CE, et al. The three-dimensional dynamic geometry of the left ventricle in the conscious dog. Circ Res 1976; 39: 304–313.

67. Villarreal FJ, Waldman LK, Lew WY. Technique for measuring regional two-dimensional finite strains in canine left ventricle. Circ Res 1988; 62: 711–721.
68. Ingels NB, Daughters GT, Stinson EB, et al. Evaluation of methods for quantitating left ventricular segmental wall motion in man using myocardial markers as a standard. Circulation 1980; 61: 966–972.
69. Zerhouni EA, Parish DM, Rogers WJ, et al. Human heart. Tagging with MR imaging -- a method for noninvasive assessment of myocardial motion. Radiology 1988; 169: 59–63.
70. Pirat B, Khoury DS, Hartley CJ, et al. A novel feature-tracking echocardiographic method for the quantitation of regional myocardial function: validation in an animal model of ischemia-reperfusion. J. Am. Coll. Cardiol. 2008; 51:651–9.
71. Götte MJW, Germans T, Rüssel IK, et al. Myocardial strain and torsion quantified by cardiovascular magnetic resonance tissue tagging. Studies in normal and impaired left ventricular function. J Am Coll Cardiol 2006; 48: 2002–2011.
72. van Everdingen WM, Zweerink A, Nijveldt R, et al. Comparison of strain imaging techniques in CRT candidates. CMR tagging, CMR feature tracking and speckle tracking echocardiography. Int J Cardiovasc Imaging 2018; 34: 443–456.
73. Andre F, Steen H, Matheis P, et al. Age- and gender-related normal left ventricular deformation assessed by cardiovascular magnetic resonance feature tracking. J Cardiovasc Magn Reson 2015; 17:25.
74. Roy C, Slimani A, Meester C de, et al. Age and sex corrected normal reference values of T1, T2 T2* and ECV in healthy subjects at 3T CMR. J Cardiovasc Magn Reson 2017; 19: 72.
75. Truong VT, Safdar KS, Kalra DK, et al. Cardiac magnetic resonance tissue tracking in right ventricle: Feasibility and normal values. Magn Reson Imaging 2017; 38: 189–195.
76. Siqueira MEM de, Pozo E, Fernandes VR, et al. Characterization and clinical significance of right ventricular mechanics in pulmonary hypertension evaluated with cardiovascular magnetic resonance feature tracking. J Cardiovasc Magn Reson 2016; 18: 39.

77. Hinojar R, Zamorano JL, Fernández-Méndez M, et al. Prognostic value of left atrial function by cardiovascular magnetic resonance feature tracking in hypertrophic cardiomyopathy. Int J Cardiovasc Imaging. 2019; 35(6): 1055-1065.
78. Romano S, Judd RM, Kim RJ, et al. Feature-Tracking Global Longitudinal Strain Predicts Death in a Multicenter Population of Patients With Ischemic and Nonischemic Dilated Cardiomyopathy Incremental to Ejection Fraction and Late Gadolinium Enhancement. JACC Cardiovasc Imaging. 2018; 11(10): 1419-1429.
79. Williams LK, Forero JF, Popovic ZB, et al. Patterns of CMR measured longitudinal strain and its association with late gadolinium enhancement in patients with cardiac amyloidosis and its mimics. J Cardiovasc Magn Reson. 2017; 19(1): 61.
80. Vijapurapu R, Nordin S, Baig S, et al. Global longitudinal strain, myocardial storage and hypertrophy in Fabry disease. Heart. 2019; 105(6): 470-476.
81. MacDermot KD, Holmes A, Miners AH. Anderson-Fabry disease: clinical manifestations and impact of disease in a cohort of 98 hemizygous males. J Med Genet 2001; 38: 750e60.
82. Hoey ET, Neil-Gallagher E. Utility of gadolinium enhancedcardiovascular MRI to differentiate Fabry's disease from other causes of hypertrophic cardiomyopathy. Postgrad Med J 2012; 88: 731–732.
83. Eng CM, Guffon N, Wilcox WR, et al. Safety and efficacy of recombinant human alpha-galactosidase A-replacement therapy in Fabry's disease. N Engl J Med 2001; 345: 9–16.
84. Messalli G, Imbriaco M, Avitabile G, et al. Role of cardiac MRI in evaluating patients with Anderson-Fabry disease: assessing cardiac effects of longterm enzyme replacement therapy. Radiol Med 2012; 117: 19–28.
85. Moon JC, Sachdev B, Elkington AG et al. Gadolinium enhanced cardiovascularmagnetic resonance in Anderson-Fabry disease: evidence for a disease specific abnormality of the myocardial interstitium. Eur Heart J 2003; 24: 2151e5.
86. Arends M, Wijburg FA, Wanner C, et al. Favourable effect of early versus late start of enzyme replacement therapy on plasma globotriaosylsphingosine levels in men with classical Fabry disease. Mol Genet Metab 2017; 121: 157–161.

87. Reiter U, Reiter C, Kräuter C, Fuchsjäger M, Reiter G. Cardiac magnetic resonance T1 mapping. Part 2: Diagnostic potential and applications. Eur J Radiol. 2018; 109: 235-247.
88. Frustaci A, Morgante E, Russo MA, et al. Pathology and function of conduction tissue in Fabry disease cardiomyopathy. Circ Arrhythm Electrophysiol 2015; 8: 799–805.
89. Tanislav C, Gündüz D, Liebetrau C, et al. Cardiac Troponin I: A Valuable Biomarker Indicating the Cardiac Involvement in Fabry Disease. PLOS One 2016; 11: e0157640.
90. Thompson RB, Chow K, Khan A, et al. T1 mapping with cardiovascular MRI is highly sensitive for Fabry disease independent of hypertrophy and sex. Circ Cardiovasc Imaging 2013; 6: 637–645.
91. Pepke-Zaba J, Delcroix M, Lang I, et al. Chronic thromboembolic pulmonary hypertension (CTEPH). Results from an international prospective registry. Circulation 2011; 124: 1973–1981.
92. Becattini C, Agnelli G, Pesavento R, et al. Incidence of chronic thromboembolic pulmonary hypertension after a first episode of pulmonary embolism. Chest 2006; 130: 172–175.
93. Pengo V, Lensing AW, Prins MH, et al. Incidence of chronic thromboembolic pulmonary hypertension after pulmonary embolism. N Engl J Med 2004; 350: 2257–2264.
94. Klok FA, van Kralingen KW, van Dijk AP, et al. Prospective cardiopulmonary screening program to detect chronic thromboembolic pulmonary hypertension in patients after acute pulmonary embolism. Haematologica 2010; 95: 970–975.
95. Berghaus TM, Barac M, von Scheidt W, Schwaiblmair M. Echocardiographic evaluation for pulmonary hypertension after recurrent pulmonary embolism. Thromb Res2011; 128: e142–e147.
96. Lang I. Advances in understanding the pathogenesis of chronic thromboembolic pulmonary hypertension. Br J Haematol. 2010; 149:478–83.
97. Blauwet LA, Edwards WD, Tazelaar HD, McGregor CG. Surgical pathology of pulmonary thromboendarterectomy: a study of 54 cases from 1990 to 2001. Human Pathol. 2003; 34:1290–8.

98. Bradlow WM, Gibbs JS, Mohiaddin RH. Cardiovascular magnetic resonance in pulmonary hypertension. J Cardiovasc Magn Reson 2012; 14: 6.

99. D'Alonzo GE, Barst RJ, Ayres SM, et al. Survival in patients with primary pulmonary hypertension. Results from a national prospective registry. Ann Intern Med 1991; 115: 343–349.

100. Raymond RJ, Hinderliter AL, Willis PW, et al. Echocardiographic predictors of adverse outcomes in primary pulmonary hypertension. J Am Coll Cardiol 2002; 39: 1214–1219.

101. Walker CM, Chung JH, Reddy GP. Septal Bounce J Thorac Imaging 2012; 27: W1.

102. Sanz J, Dellegrottaglie S, Kariisa M, et al. Prevalence and correlates of septal delayed contrast enhancement in patients with pulmonary hypertension. Am J Cardiol 2007; 100: 731–735.

103. McCann GP, Beek AM, Vonk-Noordegraaf A, van Rossum AC. Delayed contrast-enhanced magnetic resonance imaging in pulmonary arterial hypertension. Circulation 2005; 112, e268.

104. Sato T, Tsujino I, Ohira H, et al. Paradoxial interventricular septal motion as a major determinat of late gadolinium enhancement in ventricular insertion points in pulmonary hypertension. PLoS One 2013; 8, e66724.

105. Swift AJ, Rajaram S, Capener D, et al. LGE patterns in pulmonary hypertension do not impact overall mortality. J Am Coll Cardiol Imaging 2014; 7: 1209–1217.

106. Bradlow WM, Assomull R, Kilner PJ, Gibbs JS, Sheppard MN, Mohiaddin RH. Understanding late gadolinium enhancement in pulmonary hypertension. Circ Cardiovasc Imaging 2010; 3: 501–503.

107. Kuribayashi T, RobertsWC. Myocardial disarray at junction of ventricular septum and left and right ventricular free walls in hypertrophic cardiomyopathy. Am J Cardiol 1992; 70: 1333–1340.

108. Bull S, White SK, Piechnik SK, et al. Human non-contrast T1 values and correlation with histology in diffuse fibrosis. Heart 2013; 99: 932–937.

109. Lee SP, Lee W, Lee JM, et al. Assessment of diffuse myocardial fibrosis by using mr imaging in asymptomatic patients with aortic stenosis. Radiology 2015; 274: 359–369.

110. Bandula S,White SK, Flett AS, et al. Measurement of myocardial extracellular volume fraction by using equilibrium contrast-enhanced CT: validation against histologic findings. Radiology 2013; 269: 396–403.

111. Garcia-Alvarez A, Garcia-Lunar I, Pereda D, et al. Association of myocardial T1-mapping CMR with hemodynamics and RV performance in pulmonary hypertension. J Am Coll Cardiol Imaging 2015; 8:76–82.

112. Simonneau G, Robbins IM, Beghetti M, et al. Updated clinical classification of pulmonary hypertension. J Am Coll Cardiol 2009; 54: 43–54.

113. Mayer E, Jenkins D, Lindner J, et al. Surgical management and outcome of patients with chronic thromboembolic pulmonary hypertension: results from an international prospective registry. J Thorac Cardiovasc Surg 2011; 141: 702–710.

114. Wirth G, Brüggemann K, Bostel T, Mayer E, Düber C, Kreitner KF. Chronic Thromboembolic Pulmonary Hypertension (CTEPH) – Potential Role of Multidetector-Row CT (MD-CT) and MR imaging in the diagnosis and differential diagnosis of the disease. Rofo 2014; 186(8): 751–761.

115. Galiè N, Humbert M, Vachiery JL, et al. 2015 ESC/ERS Guidelines for the diagnosis and treatment of pulmonary hypertension: The Joint Task Force for the Diagnosis and Treatment of Pulmonary Hypertension of the European Society of Cardiology (ESC) and the European Respiratory Society (ERS): Endorsed by: Association for European Paediatric and Congenital Cardiology (AEPC), International Society for Heart and Lung Transplantation (ISHLT). Eur Heart J 2016; 37: 67–119.

116. Ghofrani HA, D'Armini AM Grimminger F, et al. CHEST-1 Study Group. Riociguat for the treatment of chronic thromboembolic pulmonary hypertension. N Engl J Med 2013; 369: 319-329.

117. Olsson KM, Wiedenroth CB, Kamp JC, et al. Balloon pulmonary angioplasty for inoperable patients with chronic thromboembolic pulmonary hypertension: the initial German experience. Eur Resp J 2017; 49:6.

118. Muller DW, Liebetrau C. Percutaneous treatment of chronic thromboembolic pulmonary hypertension (CTEPH). EuroIntervention 2016; 12:X35–X43.

119. Wiedenroth C, Liebetrau C, Breithecher A, et al. Combined pulmonary endarterectomy and balloon pulmonary angioplasty in patients with chronic thromboembolic pulmonary hypertension. J Heart Lung Transplant. 2016 May; 35(5): 591-6.

120. Kreitner KF, Ley S, Kauczor HU, et al. Chronic thromboembolic pulmonary hypertension: Pre- and postoperative assessment with breath-hold MR imaging techniques. Radiology 2004; 232: 535–554.

121. Rolf A, Rixe J, KimWK, et al. Right ventricular adaptation to pulmonary pressure load in patients with chronic thromboembolic pulmonary hypertension before and after successful pulmonary endarterectomy–a cardiovascular magnetic resonance study. J Cardiovasc Magn Reson 2014; 16: 96.

122. van Wolferen SA, Marcus JT, Boonstra A, et al. Prognostic value of right ventricular mass, volume, and function in idiopathic pulmonary arterial hypertension. Eur Heart J 2007; 28: 1250–1257.

123. Sato H, Ota H, Sugimura K, et al. Balloon pulmonary angioplasty improves biventricular functions and pulmonary flow in chronic thromboembolic pulmonary hypertension. Circ J 2016; 80: 1470–1477.

124. Yamasaki Y, Nagao M, Abe K, et al. Balloon pulmonary angioplasty improves interventricular dyssynchrony in patients with inoperable chronic thromboembolic pulmonary hypertension: a cardiacMR imaging study. Int J Cardiovasc Imaging 2017; 33: 229–239.

125. Gruner C, Verocai F, Carasso S, et al. Systolic myocardial mechanics in patients with Anderson-Fabry disease with and without left ventricular hypertrophy and in comparison to nonobstructive hypertrophic cardiomyopathy. Echocardiography. 2012; 29:810–7.

126. Shanks M, Thompson RB, Paterson ID, et al. Systolic and diastolic function assessment in fabry disease patients using speckle-tracking imaging and comparison with conventional echocardiographic measurements. J Am Soc Echocardiogr. 2013; 26: 1407–14.

127. Labombarda F, Saloux E, Milesi G, Bienvenu B. Loss of base-to-apex circumferential strain gradient: a specific pattern of Fabry cardiomyopathy? Echocardiograph. 2017; 34: 504–10.

128. Krämer J, Niemann M, Liu D, et al. Two- dimensional speckle tracking as a non-invasive tool for identification of myocardial fibrosis in Fabry disease. Eur Heart J. 2013; 34: 1587–96.

129. Vonk Noordegraaf A, Westerhof BE, Westerhof N. The Relationship Between the Right Ventricle and its Load in Pulmonary Hypertension. J Am Coll Cardiol. 2017; 69(2): 236-243.

130. Lahm T, Douglas IS, Archer SL, et al. Assessment of Right Ventricular Function in the Research Setting: Knowledge Gaps and Pathways Forward. An Official American Thoracic Society Research Statement. Am J Respir Crit Care Med. 2018; 198(4): e15-e43.

131. van de Veerdonk MC, Kind T, Marcus JT, et al. Progressive right ventricular dysfunction in patients with pulmonary arterial hypertension responding to therapy. J Am Coll Cardiol. 2011; 58(24): 2511-2519.

132. Vanderpool RR, Pinsky MR, Naeije R, et al. RV-pulmonary arterial coupling predicts outcome in patients referred for pulmonary hypertension. Heart. 2015; 101(1): 37-43.

133. Vanderpool RR, Rischard F, Naeije R, Hunter K, Simon MA. Simple functional imaging of the right ventricle in pulmonary hypertension: Can right ventricular ejection fraction be improved?. Int J Cardiol. 2016; 223: 93-94.

134. Oyama-Manabe N, Sato T, Tsujino I, et al. The strain-encoded (SENC) MR imaging for detection of global right ventricular dysfunction in pulmonary hypertension. Int J Cardiovasc Imaging. 2013; 29(2): 371-378.

135. Trip P, Kind T, van de Veerdonk MC, et al. Accurate assessment of load-independent right ventricular systolic function in patients with pulmonary hypertension. J Heart Lung Transplant. 2013; 32(1): 50-55.

136. Jone PN, Schäfer M, Li L, Craft M, Ivy DD, Kutty S. Right Atrial Deformation in Predicting Outcomes in Pediatric Pulmonary Hypertension. Circ Cardiovasc Imaging. 2017; 10(12): e006250.

137. Querejeta Roca G, Campbell P, Claggett B, Solomon SD, Shah AM. Right Atrial Function in Pulmonary Arterial Hypertension. Circ Cardiovasc Imaging. 2015; 8(11): e003521.

138. Sato T, Tsujino I, Ohira H, et al. Right atrial volume and reservoir function are novel independent predictors of clinical worsening in patients with pulmonary hypertension. J Heart Lung Transplant. 2015; 34(3): 414-423.

139. Bhave NM, Visovatti SH, Kulick B, Kolias TJ, McLaughlin VV. Right atrial strain is predictive of clinical outcomes and invasive hemodynamic data in group 1 pulmonary arterial hypertension. Int J Cardiovasc Imaging. 2017; 33(6): 847-855.

140. Fukuda Y, Tanaka H, Ryo-Koriyama K, et al. Comprehensive Functional Assessment of Right-Sided Heart Using Speckle Tracking Strain for Patients with Pulmonary Hypertension. Echocardiography. 2016; 33(7): 1001-1008.

141. Sakata K, Uesugi Y, Isaka A, et al. Evaluation of right atrial function using right atrial speckle tracking analysis in patients with pulmonary artery hypertension. J Echocardiogr. 2016; 14(1): 30-38.

142. Messroghli DR, Moon JC, Ferreira VM, et al. Clinical recommendations for cardiovascular magnetic resonance mapping of T1, T2, T2* and extracellular volume: A consensus statement by the Society for Cardiovascular Magnetic Resonance (SCMR) endorsed by the European Association for Cardiovascular Imaging (EACVI) [published correction appears in J Cardiovasc Magn Reson. 2018 Feb 7;20(1):9]. J Cardiovasc Magn Reson. 2017; 19(1): 75.

143. Nakamori S, Dohi K, Ishida M, et al. Native T1 Mapping and Extracellular Volume Mapping for the Assessment of Diffuse Myocardial Fibrosis in Dilated Cardiomyopathy. JACC Cardiovasc Imaging. 2018 Jan;11(1): 48-59.

144. Ide S, Riesenkampff E, Chiasson DA, et al. Histological validation of cardiovascular magnetic resonance T1 mapping markers of myocardial fibrosis in paediatric heart transplant recipients. J Cardiovasc Magn Reson. 2017; Feb 1;19(1): 10.

145. Miller CA, Naish JH, Bishop P, et al. Comprehensive validation of cardiovascular magnetic resonance techniques for the assessment of myocardial extracellular volume. Circ Cardiovasc Imaging. 2013 May 1; 6(3): 373-83.

146. Flett AS, Sado DM, Quarta G, et al. Diffuse myocardial fibrosis in severe aortic stenosis: an equilibrium contrast cardiovascular magnetic resonance study. Eur Heart J Cardiovasc Imaging. 2012 Oct;13(10): 819-26.

147. Chen YY, Yun H, Jin H, et al. Association of native T1 times with biventricular function and hemodynamics in precapillary pulmonary hypertension. Int J Cardiovasc Imaging. 2017 Aug; 33(8): 1179-1189.

148. Nitsche C, Kammerlander AA, Binder C, et al. Native T1 time of right ventricular insertion points by cardiac magnetic resonance: relation with invasive haemodynamics and outcome in heart failure with preserved ejection fraction. Eur Heart J Cardiovasc Imaging. 2020 Jun 1;21(6): 683-691.

149. Bohnen S, Radunski UK, Lund GK, et al. Tissue characterization by T1 and T2 mapping cardiovascular magnetic resonance imaging to monitor myocardial inflammation in healing myocarditis. Eur Heart J Cardiovasc Imaging. 2017 Jul 1;18(7): 744-751.

150. Hinojar R, Foote L, Sangle S, et al. Native T1 and T2 mapping by CMR in lupus myocarditis: Disease recognition and response to treatment. Int J Cardiol. 2016 Nov 1;222: 717-726.

151. Zhao L, Zhang C, Tian J, et al. Quantification of myocardial deformation in patients with Fabry disease by cardiovascular magnetic resonance feature tracking imaging. Cardiovasc Diagn Ther. 2021 Feb;11(1): 91-101.

152. Bartels K, Brown RD, Fox DL, et al. Right Ventricular Longitudinal Strain Is Depressed in a Bovine Model of Pulmonary Hypertension. Anesth Analg. 2016 May;122(5): 1280-6.

153. Kamide H, Kato S, Hayakawa K, et al. Impairment of right ventricular strain evaluated by cardiovascular magnetic resonance feature tracking in patients with interstitial lung disease. Int J Cardiovasc Imaging. 2021 Mar; 37(3): 1073-1083.

154. Kawakubo M, Yamasaki Y, Kamitani T, et al. Clinical usefulness of right ventricular 3D area strain in the assessment of treatment effects of balloon pulmonary angioplasty in chronic thromboembolic pulmonary hypertension: comparison with 2D feature-tracking MRI. Eur Radiol. 2019 Sep;29(9): 4583-4592.

155. Kallifatidis A, Mouratoglou SA, Giannakoulas G, Finitsis S, Karvounis H, Sianos G. Myocardial deformation assessment in patients with precapillary pulmonary hypertension: A cardiac magnetic resonance study. Diagn Interv Imaging. 2021 Mar; 102(3): 153-161.

156. Baessler B, Luecke C, Lurz J, et al. Cardiac MRI Texture Analysis of T1 and T2 Maps in Patients with Infarctlike Acute Myocarditis. Radiology. 2018; 289(2): 357-365.

157. Baessler B, Luecke C, Lurz J, et al. Cardiac MRI and Texture Analysis of Myocardial T1 and T2 Maps in Myocarditis with Acute versus Chronic Symptoms of Heart Failure. Radiology. 2019; 292(3): 608-617.

158. Dyverfeldt P, Bissell M, Barker AJ, et al. 4D flow cardiovascular magnetic resonance consensus statement. J Cardiovasc Magn Reson. 2015; 17(1): 72.

159. Azarine A, Garçon P, Stansal A, et al. Four-dimensional Flow MRI: Principles and Cardiovascular Applications. Radiographics. 2019; 39(3): 632-648.

160. Nensa F, Bamberg F, Rischpler C, et al. Hybrid cardiac imaging using PET/MRI: a joint position statement by the European Society of Cardiovascular Radiology (ESCR) and the European Association of Nuclear Medicine (EANM). Eur Radiol. 2018; 28(10): 4086-4101.

161. Jiang B, Guo N, Ge Y, Zhang L, Oudkerk M, Xie X. Development and application of artificial intelligence in cardiac imaging [published online ahead of print, 2020 Feb 6]. Br J Radiol. 2020; 20190812.

10. Danksagung

Mein besonderer Dank gilt zu allererst Frau Prof. Gabriele Krombach für Ihre jahrelange und motivierende Unterstützung sowohl in der klinischen Routine als auch bei der wissenschaftlichen Arbeit und Ihr mir stets entgegengebrachtes Vertrauen.

Ebenfalls möchte ich mich bei Herrn Prof. Wigbert Rau bedanken, der in mir durch seine große Hartnäckigkeit das Interesse und die Liebe zur Radiologie gefördert hat.

Für meine klinische Ausbildung möchte ich mich besonders bei Dr. Christian Schneider, Dr. Andreas Breithecker, Dr. Detlef Litzlbauer, Prof. Alexander Langheinrich, PD Dr. Marian Kampschulte und Dr. Enrique Alejandre-Lafont bedanken.

Meinen Eltern Dr. Fritz Roller und Frau Christiane Roller (†) bin ich zutiefst für Ihre uneingeschränkte Unterstützung auf meinem bisherigen Lebensweg dankbar.

Mein ganz besonderer Dank gilt allerdings meiner Familie, meiner Frau Anna und unseren Kindern Fritz Hagen, Helene Sophia, Gregor Hubertus, Bendix Laurenz und Grete Maria, für Ihre liebevolle Unterstützung zu jeder Zeit und in allen Lebenslagen.

11. Erklärung

Eidesstattliche Erklärungen gem. § 4 Abs. 3, Nr. 8a und b und Nr. 9 HO

Hiermit erkläre ich, dass die vorliegende kumulative Habilitationsschrift „**Entwicklung und Stellenwert der kardialen Magnetresonanztomografie**“ eigenständig und ohne fremde Hilfe von mir verfasst wurde.

Ich erkläre hiermit, keine anderen als die angegebenen Quellen verwandt zu haben, wobei wörtlich oder annähernd wörtlich aus anderen Arbeiten entnommene Stellen als solche genau kenntlich gemacht worden sind.

Ich versichere zudem, dass ich mich bei keiner anderen Stelle zur Habilitation gemeldet habe, und dass ich mich vor Abschluss des Habilitationsverfahrens nicht an anderer Stelle zur Habilitation melden werde.

Dr. med. Fritz Christian Roller

12. Manuskripte

Published online: 2019-02-12

Assessment of Cardiac Involvement in Fabry Disease (FD) with Native T1 Mapping

Natives T1-Mapping zur Beurteilung einer kardialen Beteiligung bei Morbus Fabry

Authors

Fritz Christian Roller[1], Sven Fuest[2], Marco Meyer[2], Sebastian Harth[1], Dursun Gündüz[3], Pascal Bauer[3], Christian Schneider[1], Arndt Rolfs[4], Gabriele Anja Krombach[1], Christian Tanislav[2]

Affiliations

1 Diagnostic and Interventional Radiology, Justus-Liebig-University, Giessen, Germany
2 Neurology, Justus-Liebig-University, Giessen, Germany
3 Angiology, Justus-Liebig-University, Giessen, Germany
4 Neurology, University-Hospital Rostock, Germany

Key words

cardiac, technical aspects, MR imaging

received 28.10.2017
accepted 16.01.2019

Bibliography

DOI https://doi.org/10.1055/a-0836-2723
Published online: 12.2.2019
Fortschr Röntgenstr 2019; 191: 932–939

ISSN 1438-9029

Correspondence

Dr. Fritz Christian Roller
Radiologie, Universitätsklinikum Giessen, Klinikstraße 36, 35392 Giessen, Germany
Tel.: ++ 49/6 41/98 55 63 29
Fax: ++ 49/6 41/98 54 18 09
fritz.c.roller@radiol.med.uni-giessen.de

ZUSAMMENFASSUNG

Ziel Morbus Fabry (FD) ist eine X-chromosomale Multiorganerkrankung des lysosomalen Metabolismus, wobei die kardiale Beteiligung die Haupttodesursache der Erkrankung darstellt. Deswegen ist es wichtig, möglichst frühe Erkrankungsmanifestationen zu detektieren, um einen maximalen therapeutischen Nutzen zu erzielen. Das Ziel unserer Studie war es, die Wertigkeit des nativen T1-Mappings als krankheitsspezifisches Äquivalent zu untersuchen.

Material und Methoden 16 konsekutive FD-Patienten (9 weiblich, 7 männlich; Altersmedian 54 Jahre; IQR 17) und 16 Kontrollpatienten (9 weiblich, 7 männlich; Altersmedian 52 Jahre, IQR 20) wurden mit einem 1,5-Tesla MRT-System untersucht. Das native T1-Mapping wurde als modifizierte Look-Locker-Sequenz (MOLLI) durchgeführt, die Messungen erfolgten im septalen linksventrikulären Myokard auf mittventrikulären Kurzachsenschnitten. Zudem wurden die linksventrikuläre Funktion und Morphologie, das Vorhandensein einer Kontrastmittelspätanreicherung sowie cTnI- und Lyso-Gb3-Laborwerte ausgewertet.

Ergebnisse Die mediane native septale T1-Zeit bei FD-Patienten betrug 889,0 und 950,6 für die Kontrollgruppe ($p < 0{,}003$). 5 (31,25 %) Patienten hatten eine Kontrastmittelspätanreicherung und positive cTnI-Werte, 4 Patienten (25,0 %) eine linksventrikuläre Hypertrophie. Die 5 cTnI- und die 8 Lyso-Gb3-positiven Patienten hatten signifikant niedrigere native T1-Zeiten ($p < 0{,}05$, respektive $p < 0{,}01$). Unter der Annahme eines Grenzwertes von 900 ms für die Detektion eines erhöhten, zellulären Lipidgehalts zeigten 9 Patienten (56,25 %) pathologische Werte. Davon waren 8 Patienten Lyso-Gb3- und 4 Patienten cTnI-positiv. Zudem zeigte sich eine gute negative Korrelation der nativen T1-Zeit zu den Lyso-Gb3-Werten ($r = -0{,}582$; $p = 0{,}018$).

Schlussfolgerung Offensichtlich reflektiert eine pathologische native T1-Zeit eine kardiale Beteiligung bei FD-Patienten. Zukünftig könnte natives T1-Mapping als Biomarker in der Bildgebung behilflich sein, frühe kardiale Beteiligungen im Rahmen des FD zu detektieren, bevor andere morphologische Veränderungen zu erkennen sind.

Kernaussagen:

- Die native T1-Zeit ist bei Patienten mit Morbus Fabry signifikant niedriger.
- Die native T1-Zeit korreliert zu kardialen und erkrankungsspezifischen Biomarkern.
- Das native T1-Mapping könnte großes Potenzial in Diagnostik und Therapie-Monitoring haben.

ABSTRACT

Purpose Fabry disease (FD) is an X-linked multi-organ disorder of lysosomal metabolism with cardiac disease being the leading cause of death. Identifying early FD-specific pathologies is important in the context of maximum therapeutic benefit in these stages. Therefore, the aim of this study was to investigate the value of quantitative cardiac T1 mapping as a potential disease-specific surrogate.

Methods 16 consecutive FD patients (9 female, 7 male; median age: 54 years, IQR 17) and 16 control patients (9 female, 7 male; median age: 52 years, IQR 20) were investigated at 1.5 Tesla. Native T1 mapping was performed using a modified look locker inversion recovery sequence (MOLLI) and native T1 times were measured within the septal myocardium at the midventricular short-axis section. Also functional parameters, left ventricular morphology, presence of late-gadolinium enhancement, cTnI- and Lyso-Gb3-Levels were evaluated.

Results The median native septal T1 time for FD was 889.0 ms and 950.6 ms for controls ($p < 0.003$). LGE and positive cTnI values (0.26 ± 0.21) were present in 5 FD patients (31.25 %), and left ventricular hypertrophy (LVH) was present in 4 FD patients (25.00 %). The 4 cTnI and 8 Lyso-Gb3 positive FD patients had significantly lower native T1 values ($p < 0.05$, respectively $p < 0.01$). Assuming a T1 cut-off value of 900 ms for the identification of increased cardiac lipid deposit, 9 patients with FD (56.25 %) had pathologic values (4 patients cTnI and 8 patients Lyso-Gb3 positive). Moreover, native septal T1 showed a good negative correlation to Lyso-Gb3 ($r = -0.582$; $p = 0.018$).

Conclusion A pathologic cardiac native T1 time obviously reflects cardiac involvement in the scope of FD at tissue level. In the future native T1 mapping as an imaging biomarker might allow identification of early stages of cardiac involvement in FD before morphological changes are obvious.

Key Points:

- Native T1 values are significantly decreased in Fabry disease.
- Native T1 shows promising correlation to cardiac and Fabry-specific biomarkers.
- Native T1 mapping might have great potential for early disease detection and therapy monitoring.

Citation Format

- Roller FC, Fuest S, Meyer M et al. Assessment of Cardiac Involvement in Fabry Disease (FD) with Native T1 Mapping. Fortschr Röntgenstr 2019; 191: 932–939

Introduction

Fabry disease (FD) is an X-linked disorder of lysosomal metabolism with inability to catabolize glycosphingolipids due to a deficiency of the enzyme alpha-galactosidase [1]. It is a multisystem disorder and glycosphingolipids accumulate in many organs including the skin, myocardium and kidneys. Male homozygotes are more affected by the disease, which presents in adolescence with burning extremity pain (acroparesthesia) and progressive multi-organ failure [2].

FD can cause left ventricular hypertrophy (LVH) due to storage of glycosphingolipid in myocytes, valves and vascular endothelium [3]. Cardiac decompensation is triggered by myocardial fibrosis and is usually more extensive in men than in affected women [1, 4]. Proving heart involvement in FD cardiac magnetic resonance imaging (CMRI) is well established [5]. Beside nonspecific signs, like LVH and reduced left ventricular function, basal infero-lateral late gadolinium enhancement (LGE) without affecting the endocardium is a characteristic hallmark of cardiac FD manifestation [5]. The evidence of LGE also possesses a prognostic relevance. Once demonstrated, a lack of response to enzyme replacement therapy could be expected, which might be due to irreversible tissue damage with the development of fibrosis [5]. However, LGE as a surrogate is limited due to its dichotomous character. Its presence requires at least 15 % focal matrix expansion [6]. Stages prior to the development of fibrosis still remain hidden by investigating LGE. Identifying early cardiac changes at the tissue level requires other approaches. Assessment of myocardial lipid deposition by localized 1H magnetic resonance spectroscopy (1H-MRS) seems a suitable and time-efficient alternative [7] for the noninvasive assessment of myocardial lipid content [7 – 10] as several studies at 1.5 Tesla showed. A recent study by Petritsch et al. performed at 3.0 Tesla concluded that a comprehensive cardiac examination protocol in FD patients should include LGE imaging, 1H-MRS and native T1 mapping [11], which also seems to be a promising increment, as it allows the quantification of myocardial T1 times on a pixelwise basis (parametric imaging). Some previous case series indicated the potential benefit of native T1 mapping for identifying early stages of the disease [12, 13]. This is of great relevance as the early establishment of enzyme replacement therapy is associated with maximum benefit [14]. Therefore, we aimed to assess cardiac native T1 mapping in FD in the present case-control study and correlate the findings with the presence of LGE, LVH and biomarkers such as cardiac troponin I (cTnI) and lyso-globotriaosylceramide (Lyso-Gb3) [15 – 17].

Methods

Study design

In case-control design we included 16 patients with FD and 16 healthy volunteers in our study. Matching criteria were age and sex. In all patients the diagnosis of FD was proved by molecular genetic analysis verifying a heterozygous or homozygous mutation in the α-GAL-A-gene [15]. All patients and individuals in the control group underwent cardiac MRI. Contraindications for cardiac MRI and exclusion criteria were renal failure (glomerular filtration rate below 30 ml/min/1.73 m^2), incompatible cochlear or metallic implants, known gadolinium intolerance, claustrophobia, or the inability to lie supine for the duration of the protocol due to dyspnea. In controls cardiac disease was ruled out by follow-up and by validation and consultation of a cardiologist. The study protocol was reviewed and approved by the local ethical committee.

CMR imaging

Cardiac imaging was performed with a 1.5 Tesla MRI scanner (Somatom Avanto, Siemens Healthcare, Forchheim, Germany) using an eight-element phased array cardiac coil. An appropriate CMR protocol containing thoracic survey images (in axial, coronal, and sagittal orientation), steady-state-free precession (SSFP) CINE sequences aligned to 2-, 3- and 4-chamber view (CV), and short-axis (SA) obtained during breath-hold, black-blood imaging (T2 turbo spin echo), late gadolinium enhancement imaging (LGE; T1 gradient echo with inversion recovery) and native T1 mapping was used as previously described [18]. Gadobenate dimeglumine (Gd-BOPTA; Multihance, BRACCO Imaging) was injected at a dose of 0.1 mmol/kg and LGE imaging was performed 12 minutes after contrast agent injection. For the assessment of left ventricular (LV) function, the absolute LV volume was calculated on end-diastolic and end-systolic short-axis CINE images. The endocardial contours were drawn manually with exclusion of the papillary muscles and trabeculae from the LV cavity. Ventricular volume was estimated using the Simpson rule and EF was calculated as (end-diastolic volume (EDV) – end-systolic volume (ESV)/end-diastolic volume (EDV)). The end-systolic and end-diastolic diameter (ESD and EDD) were measured at the basal short-axis level. Argus software package (Siemens Syngo MMWP Version VE40A, Siemens Healthcare, Forchheim, Germany) was used for post-processing.

Native T1 maps were acquired at the basal, mid-ventricular, and apical short-axis sections with a modified Look-Locker inversion-recovery (MOLLI) sequence, with three images in the first two Look-Locker segments and five images for the third inversion (known as the "3-3-5" standard protocol; 11 images during 17 heartbeats) and maps were generated after in-line motion correction [19].

The imaging parameters were: slice thickness: 8 mm; spatial resolution: 2.2 mm × 1.8 mm × 8 mm; 6/8 partial Fourier acquisition; field of view: 240 × 340 mm; matrix: 192 × 124; flip angle 35°; TR 740 and TE 1.06; TI 100 ms and TI Increment 80 ms; trigger delay: 300 ms; inversions 3; acquisition heartbeats: 3-3-5; scan time: 17 heartbeats.

Qualitative and quantitative image assessment

The original generated images were assessed for artifacts caused by susceptibility, cardiac, diaphragmatic, or respiratory motion. Each motion-corrected series was evaluated for correct image alignment, and each T1 map was carefully checked for signal loss due to misalignment and motion [18].

Measurement of native T1

Native myocardial T1 measurements were performed in regions of interest (ROI) at the midventricular SA section (septum and the left ventricular free wall). Myocardial border areas – areas between the myocardium and blood pool – were excluded to avoid partial volume averaging artifacts and registration errors with gradual T1 value changes. To exclude size-dependent differences of native T1 values between the FD patients and the control group, the ROI sizes were also evaluated. All native T1 measurements were performed in agreement by two radiologists with experience in cardiac imaging (G.K./18 years of experience; F.R./7 years of experience). Both radiologists performed the measurements blinded to patient demographics. Moreover, assessment of LGE was performed blinded to native T1 maps and CINE images and vice versa. All T1 maps were of diagnostic quality and sufficient myocardial T1 measurements were reliably performed in all patients.

Laboratory assessment

Laboratory assessment was performed as previously described [20]. A sensitive immunoassay (ADVIA Centaur® TnI-Ultra™ immunoassay, Siemens Medical Solutions Diagnostics, Tarrytown, NY, USA), which fulfills the criteria mandated by the European Society of Cardiology and the American College of Cardiology, was used to measure cTnI values in plasma. As reported in the package leaflet, the imprecision of the immunoassay depends on the cTnI concentrations with a variation coefficient of 10 % at 0.03 ng/ml and a variation coefficient ≤ 10 % for cTnI concentrations ≥ 0.04 ng/ml. As recommended, a cTnI level of 0.04 ng/ml (99th percentile of healthy volunteers) was used as the clinical decision limit to rule out acute myocardial infarction. The test was calibrated to measure cTnI values ≥ 0.01 ng/ml (the lower detection limit of the immunoassay is 0.006 ng/ml) in our study. Therefore, we defined cTnI levels as follows: cTnI levels < 0.01 ng/ml were defined as subnormal, cTnI levels ≥ 0.01 ng/ml and < 0.04 ng/ml were defined as normal, and cTnI levels ≥ 0.04 ng/ml were defined as elevated. Lyso-Gb3 was measured in serum and values > 1.0 ng/ml were interpreted as elevated. All Lyso-Gb3 measurements were performed at the Centogene AG (Rostock; Germany).

Statistical analysis

SPSS statistical software version 20 (SPSS, Chicago, Ill) was used for statistical analysis. Patient characteristics were described by mean ± standard deviation (SD) and median with interquartile ratio (IQR). Data was tested for normal distribution using the Shapiro-Wilk test. The Student's t-test was used for data following normal distribution, and the Wilcoxon signed rank test (non-parametric test) was used for data not following normal distribution. Correlation strengths were tested using the Pearson correlation coefficient. Intra- and interobserver variability was tested with linear regression analysis and Bland-Altman plots. An alpha error of less than 0.05 was accepted as statistically significant.

Results

Cardiac function (▶ **Table 1**): Both the FD patients and the healthy controls showed normal left heart function. The median left ventricular ejection fraction (EF) was 64.5 % (IQR 9.8) for FD patients and 66.3 % (IQR 8.2) for healthy controls. Also the mean end-diastolic volume (EDV), end-systolic volume (ESV), stroke volume (SV), end-diastolic (EDD) and end-systolic diameters (ESD) revealed normal values for both groups. LVH, defined as a septal myocardial diameter ≥ 13 mm, was present in 4 FD patients

▶ **Table 1** Cardiac function and LGE.

▶ **Tab. 1** Kardiale Funktion und Kontrastmittelspätanreicherung.

	FD n = 16	Q25	Q75	controls n = 16	Q25	Q75	p
function:	**median (IQR)**			**median (IQR)**			
EF (%)	64.5 (9.8)	60.0	69.8	66.3 (8.20)	62.1	70.3	0.61
EDV (ml)	125.5 (25.8)	112.5	138.3	121.9 (24.4)	115.5	139.9	0.35
ESV (ml)	45 (22.8)	31.8	54.5	42.5 (23.1)	33.6	56.1	0.55
SV (ml)	80.5 (15.8)	73.8	89.5	83.5 (17.0)	76.0	93.0	0.59
diameters: (mm)							
Septum	9 (4.0)	7.8	11.8	8.5 (2.0)	7.7	9.7	0.19
Lateral wall	7 (3.3)	6.5	9.8	5.9 (0.9)	5.5	6.4	0.09
EDD	45.5 (7.5)	42.8	50.3	48.5 (6.0)	45.4	51.4	0.44
ESD	28.5 (8.3)	25.7	34.0	28.5 (4.1)	26.3	30.4	0.67
LGE	n (%)			n (%)			
	5 (31.25)			0			

FD – Fabry disease, EF – ejection fraction, EDV – enddiastolic volume, ESV – endsystolic volume, SV – stroke volume, EDD – enddiastolic diameter, ESD – endsystolic diameter, LGE – late gadolinium enhancement, IQR – interquartile ratio, Q25 – 25th quartile, Q75 – 75th quartile.

▶ **Table 2** Native T1 mapping: FD versus control subjects.

▶ **Tab. 2** Natives T1-Mapping: Morbus Fabry vs. Kontrollpatienten.

	FD			Controls			p
native T1: (ms)	**median (IQR)**	**Q25**	**Q75**	**median (IQR)**	**Q25**	**Q75**	
Septal	889.0 (76.8)	877.5	954.3	950.0 (34.3)	941.3	975.6	< 0.03
Lateral wall	925.0 (43.8)	910.0	953.8	960.0 (29.3)	949.6	978.9	0.09
Scar area	954.0 (33.8)	941.2	975.0	–			

FD – Fabry disease, IQR – interquartile ratio, Q25 – 25th quartile, Q75 – 75th quartile.

(25.0 %) and in none of the control group patients. The median septal myocardial diameter was 9.0 (IQR 4.0) mm for FD patients and 8.5 (IQR 2.0) for controls (p = 0.19).

Native T1 time: The median septal T1 time for FD patients was 889.0 ms (IQR 76.8) and was lower (p < 0.03) compared to the controls with a median septal T1 time of 950.0 ms (IQR 22.0). The median T1 time of the left ventricular free wall (lateral wall) was 925.0 ms (IQR 43.8) for FD patients and 960.0 ms (IQR 29.3) for the control subjects (p < 0.09). LGE at the infero-lateral wall was present in 5 FD patients (31.25 %) and in none of the control group subjects. The median native T1 time in the LGE affected areas was 954.0 ms (IQR 33.8) for the FD patients. The results are presented in ▶ **Table 2** and in ▶ **Fig. 1**. Moreover, the FD patients with LVH showed reduced septal T1 times with a median native T1 time of 884.0 ms (IQR 26.8) compared to the FD patients without LVH (▶ **Table 3**). ▶ **Fig. 2a, b** shows the native T1 map and LGE image of a 52-year-old male FD patient with LGE at the inferolateral wall, LVH and reduced septal native T1 times and ▶ **Fig. 3a, b** shows the native T1 map and LGE image of a 27-year-old male FD patient without LGE, or LVH but reduced septal native T1 times.

Correlation between native T1 time and cTni: 5 of 16 FD patients (31.25 %) were cTnI positive (median cTnI 0.01; IQR 0.01). cTnI positive FD patients had significantly reduced median septal native T1 times with 880.0 ms (IQR 68.0) compared to cTnI negative FD patients with 948.0 ms (IQR 84.0) (p < 0.05). Moreover, a moderate negative correlation between cTnI and native T1 was present for the cTnI positive FD patients (r = –0.442; p = 0.086) as presented in ▶ **Fig. 4**.

Correlation between native T1 time and Lyso-Gb3: The median Lyso-Gb3 level of the FD patients was 5.5 ng/ml (IQR 19.2). Lyso-Gb3 positive FD patients had significantly reduced median

▶ **Table 3** Native T1 mapping in FD.

▶ **Tab. 3** Natives T1-Mapping bei Patienten mit Morbus Fabry.

	LVH + n = 4			LVH – n = 12			p
	median (IQR)	Q25	Q75	median (IQR)	Q25	Q75	
native T1 (ms)	884.0 (26.8)	862.8	888.5	931.0 (85.5)	877.5	963.0	0.2214
	cTnI + n = 5			cTnI – n = 11			p
native T1 (ms)	880.0 (68.0)	820.0	888.0	948.0 (84.0)	881.0	965.0	0.048
	Lyso-Gb3 + n = 9			Lyso-Gb3 – n = 7			p
native T1 (ms)	880.0 (35.0)	853.0	888.0	961.0 (40.0)	933.0	973.0	0.0036

LVH – left ventricular hypertrophy, IQR – interquartile ratio, Q25 – 25th quartile, Q75 – 75th quartile.

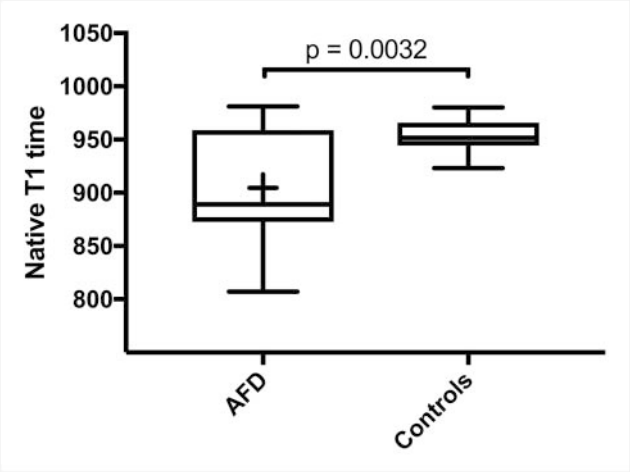

▶ **Fig. 1** The box plot presents the septal native T1 times for FD patient and controls.

▶ **Abb. 1** Der Boxplot zeigt die gemessenen septalen nativen T1-Zeiten für Morbus-Fabry-Patienten und das Kontrollkollektiv.

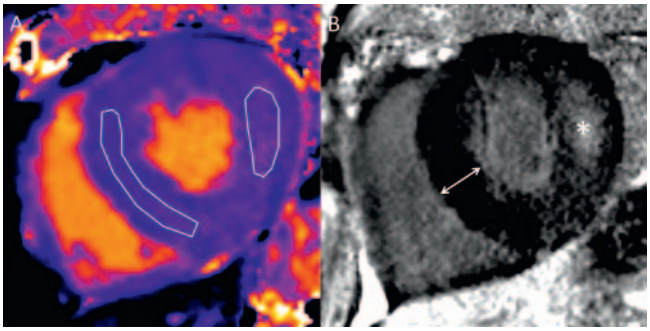

▶ **Fig. 2** Native T1 map **A** and LGE image **B** of a 52-year-old male FD patient. Typical LGE is at the inferolateral wall (white asterisk), and also a significant LVH with a septal diameter of 20 mm is present (white two-sided arrow). The measured septal native T1 time within in the region of interest is 888 ms, which is reduced, and the measured native T1 time within the scar area is 954 ms, which is normal.

▶ **Abb. 2** Die Abbildung zeigt die native T1-Map **A** und das Bild der Kontrastmittelspätanreicherung **B** auf mittventrikulären Kurzachsenschnitten bei einem 52 Jahre alten männlichen Patienten mit Morbus Fabry. An der Inferolateralwand zeigt sich eine typische Kontrastmittelspätanreicherung (weißer Stern), zudem besteht eine deutliche septale linksventrikuläre Hypertrophie mit 20 mm (weißer Pfeil). Die im septalen Myokard innerhalb der Region von Interesse gemessene native T1-Zeit beträgt 888 ms (reduziert) und die innerhalb der Lateralwand im Narbenareal gemessene native T1-Zeit beträgt 954 ms (normal).

septal native T1 times with 880.0 ms (IQR 35.0) compared to Lyso-Gb3 negative FD patients with 961.0 ms (IQR 40.0) ($p = 0.0036$). Compared to cTnI, a better moderate negative correlation between Lyso-Gb3 and native septal T1 was present ($r = -0.582$; $p < 0.02$) as shown in ▶ **Fig. 5**.

Cut-off-value: Assuming a cut-off value of 900 ms, which is more than 3 SD below the mean native septal T1 time of the healthy controls (952.6 ms ± 16.7 SD), for identification of cardiac FD involvement, 9 of 16 FD patients (56.25 %) revealed pathologic native septal T1 times. The cTnI level was increased in only 4 of these patients (44.44 %), while the Lyso-Gb3 level was increased in 8 (88.88 %). Interestingly, 3 FD patients (18.75 %) without the presence of LVH, LGE and cTnI increase showed a significant native septal T1 time decrease (values between 853 ms and 882 ms) but increased Lyso-Gb3 level (median: 24.1, IQR 44.15; range: 5.60 to 93.9).

Discussion

In patients with FD, we detected lower values for native T1 times as compared to controls, indicating potential lipid storage at the tissue level. Lower values for native T1 times were especially pronounced in the ventricular septum. This might represent a

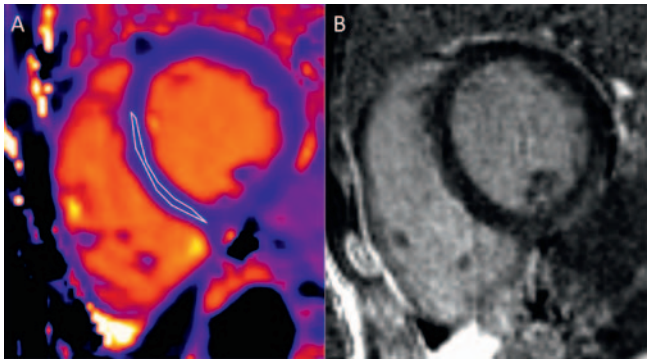

▶ **Fig. 3** Native T1 map **A** and LGE image **B** at midventricular short axis of a 27-year-old male FD patient without LGE, LVH but reduced septal native T1 times. The measured septal native T1 time within the region of interest is 872 ms.

▶ **Abb. 3** Die Abbildung zeigt die native T1-Map **A** und das Bild der Kontrastmittelspätanreicherung **B** auf mittventrikulären Kurzachsenschnitten bei einem 27 Jahre alten männlichen Patienten ohne Nachweis einer Kontrastmittelspätanreicherung und linksventrikulärer Hypertrophie, aber mit dem Nachweis einer reduzierten septalen nativen T1-Zeit. Innerhalb der Region von Interesse im septalen Myokard beträgt die native T1-Zeit 872 ms.

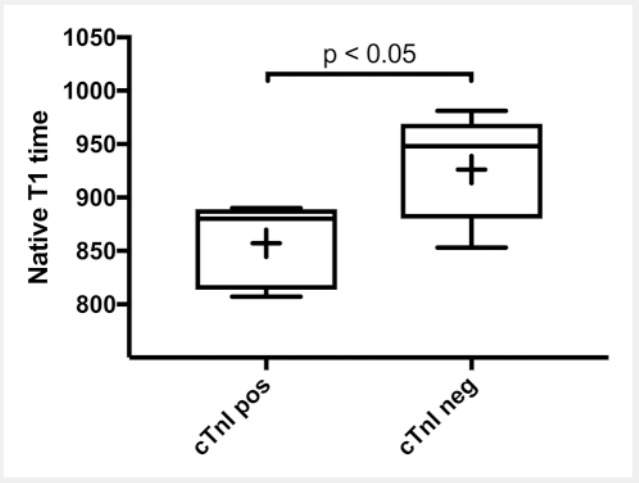

▶ **Fig. 4** The box plot presents the native septal T1 times measured in cTNI positive and cTNI negative FD subjects.

▶ **Abb. 4** Der Boxplot veranschaulicht die nativen septalen T1-Zeiten der cTnI-positiven und -negativen Morbus-Fabry-Patienten.

disease-specific finding, as far as the underlying pathological mechanism in FD is based on intracellular storage of sphingolipids [3]. Lower values for native T1 times in FD patients correlated with the presence of the cardiac biomarker cTnI as well as with elevated levels for Lyso-Gb3, the specific biomarker for FD, indicating the burden of disease [21]. In 4 FD patients with regular cardiac findings (no evidence of LVH, LGE or elevated cTnI), pathological native T1 values were detected, potentially indicating an early stage of the disease; this could also be supported by elevated Lyso-Gb3 values detected in these patients, which might rule out a silent stage of FD.

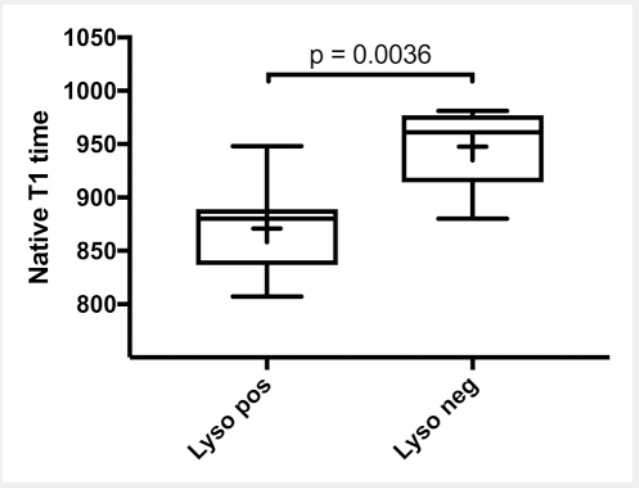

▶ **Fig. 5** The box plot presents the septal native T1 times measured in Lyso-Gb3 positive and Lyso-Gb3 negative FD subjects.

▶ **Abb. 5** Der Boxplot veranschaulicht die nativen septalen T1-Zeiten der Lyso-Gb3-positiven und -negativen Morbus-Fabry-Patienten.

In line with our findings, previous investigations also demonstrated lower values for native T1 times in patients with FD and cardiac involvement [12, 13]. Sato and coworkers showed that by applying cardiac MRI, native T1 times were even useful to discriminate between cardiac involvement in FD and other pathologies with cardiac LVH [13]. In a further study the investigators could emphasize pathologic native T1 values as one of the most important findings, indicating cardiac involvement in FD irrespective of sex and cardiac morphology und function [13].

In our investigations we added information on important biomarkers, specific to the disease such as Lyso-Gb3 and specific to cardiac damage such as cTnI. Dichotomizing FD patients according to cTnI elevation versus none showed that the patients with increased levels had lower native T1 time values. Even a moderate correlation between the degree of cTnI elevation and native T1 time was obvious. In the context of new evidence for the relevance of a cTnI elevation in FD as an early indicator of cardiac involvement [22], our findings support the hypothesis that lower native T1 times might also serve as an early surrogate indicating deposition of lipids, which is one of the first steps in the pathophysiology of FD. It might indicate directly the pathology of FD at the tissue level. In this context it needs to be taken into account that biomarkers might reliably indicate tissue damage. However, they are not measurable until a systematic release and furthermore other conditions with direct cardiac tissue damage could also induce their secretion. Especially the secretion of cTnI was demonstrated in several other disorders with no direct cardiac pathology for example in lung embolism [23]. In one of our FD patients we found no evidence of cardiac involvement regarding the morphology (echocardiography, standard MRI), electrophysiology (ECG, Holter-ECG) and also no elevation in serial cTnI measurements, but we did find pathologically reduced native T1 times as an indicator of tissue deposition of lipids as an indication of early cardiac pathol-

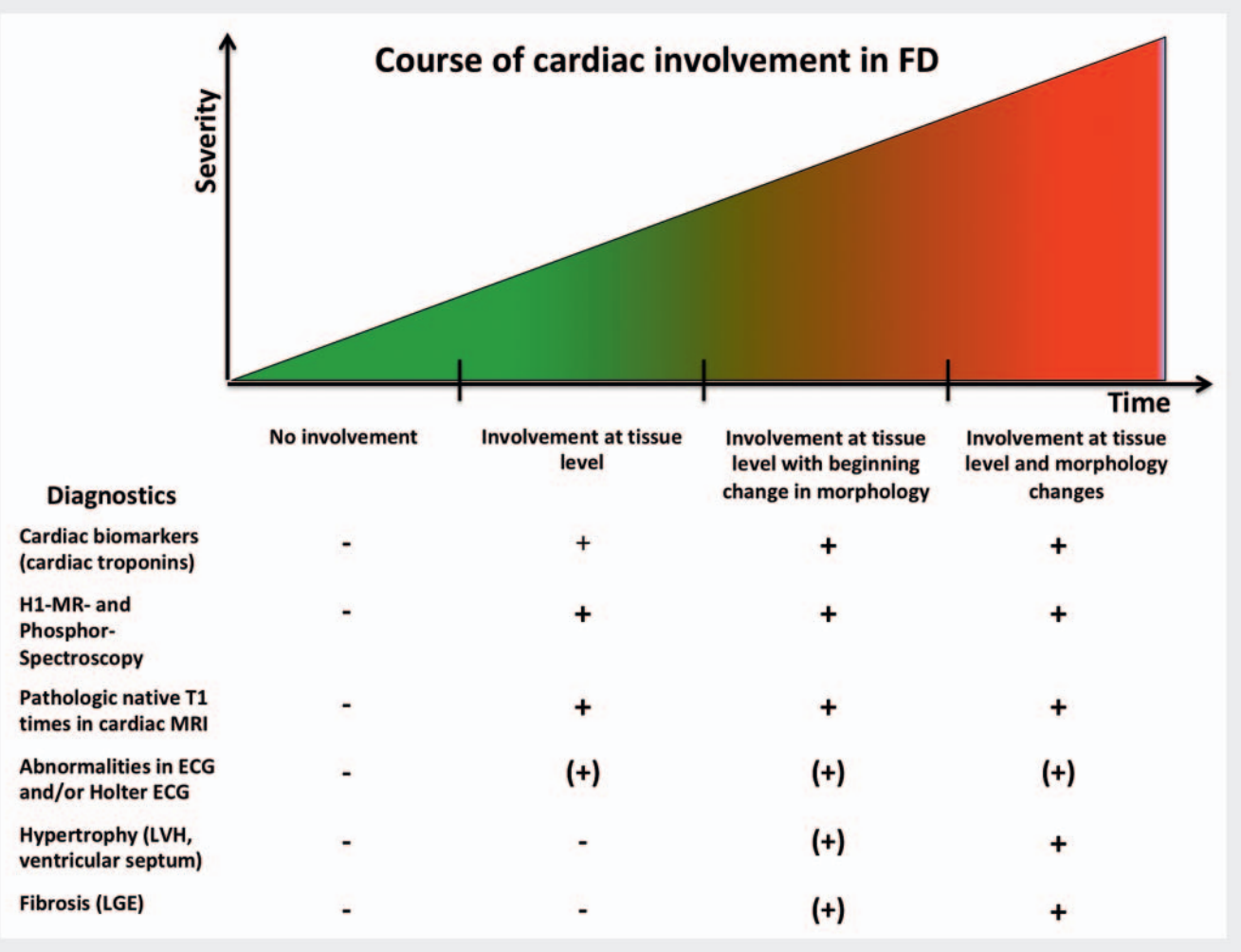

▶ **Fig. 6** The course of cardiac involvement in FD. In the stage without cardiac involvement, no pathological findings are evident. In the first stage with the beginning of sphingolipid accumulation especially pathological findings of native T1 times and pathologic measures in 1H-MRS and phosphor spectroscopy could be demonstrated. At this stage also specific cardiac biomarkers such as cardiac troponins could be measured. In the second stage beginning changes of heart morphology occur, such as hypertrophy (left ventricular hypertrophy (LVH) or increase in thickness of the ventricular septum) as well as evidence of fibrosis (in form of late gadolinium enhancement (LGE) are detectable. In the third stage morphological heart changes (LVH and/or LGE) and/or findings indicating involvement at the tissue level (pathological for native T1 times in the cardiac MRI and/or elevated cardiac biomarkers) are evident. At any stage ECG and/or Holter-ECG abnormalities could be detected.

▶ **Abb. 6** Die Abbildung zeigt den zeitlichen Verlauf einer kardialen Beteiligung bei Morbus Fabry. In der ersten Phase der Erkrankung lassen sich keine kardialen Pathologien nachweisen. In der zweiten Phase lassen sich, hervorgerufen durch eine Akkumulation von Sphingolipiden, reduzierte native T1-Zeiten im Myokard messen und Veränderungen mittels 1H-MR- und Phosphor-Spektroskopie feststellen. Zudem können in dieser Phase pathologische Werte spezifischer kardialer Biomarker (Troponine) vorliegen. In der dritten Phase lassen sich zudem nun morphologische kardiale Veränderungen, wie beginnende linksventrikuläre Hypertrophie oder auch Fibrose (im Rahmen der Kontrastmittelspätanreicherung), nachweisen. In der letzten Phase lassen sich sowohl sichere morphologische kardiale Veränderungen und auch kardiale Veränderungen auf zellulärer Ebene nachweisen (pathologische native T1-Zeiten und/oder kardiale Biomarker). Grundsätzlich können sich in jeder Phase der Erkrankung pathologische EKG- bzw. Langzeit-EKG-Veränderungen zeigen.

ogy in FD. In this patient a silent stage of the disease could be ruled out by proteinuria and a markedly elevated Lyso-Gb3 value of 93.90 ng/ml. This demonstrates that pathological native T1 times indicate cardiac involvement in FD at the tissue level, obviously prior to secretion of the biomarker cTnI. In a pathophysiological algorithm of a cardiac manifestation in FD, a pathologically reduced native T1 time is obviously the first pathological finding beside pathologic measures in 1H-MRS and phosphor spectroscopy indicating the disease, followed by the secretion of the cardiac biomarker cTnI. It is of particular relevance to consider these parameters in the diagnostic workup of FD, as greater benefit is expected when therapy is initiated at the stage in which these findings occurred, i. e., isolated without morphological changes. In the case of an ongoing process with the development of fibrosis and/or hypertrophy of the myocardium (LVH or LGE), limited therapeutic effects can be expected [24, 25]. As in the early stages of cardiac FD with only pathological native T1 times and/or biomarker elevations, structural damage at the tissue level of the heart is already obvious. This

finding should be considered and interpreted accordingly. In line with other investigations at this stage, irregular ECG and/or Holter-ECG findings could potentially be detected [26]. The course of cardiac involvement in FD and potential findings in the different diagnostic procedures are summarized in ▶ **Fig. 6**.

The main limitation of our investigation is the small number of patients. However, as a proof of principle, our findings might serve as a starting point for further investigations evaluating the value of native cardiac T1 mapping in the course of cardiac pathology in FD.

Conclusion

In our case-control study we could demonstrate lower native cardiac T1 times in patients with FD in comparison to healthy controls. In some of the cases pathological native T1 times were detected without any pathological findings regarding the heart morphology and even without elevation of the specific cardiac biomarker cTnI. Cardiac MRI including native T1 mapping might therefore be useful for the detection of cardiac involvement at the tissue level, which might be relevant in the early stage of the disease.

CLINICAL RELEVANCE OF THE STUDY

- Cardiac MRI is frequently used in the diagnostic cascade of Fabry disease.
- Native T1 mapping within cardiac MRI for the detection of Fabry disease involvement is superior to left ventricular hypertrophy and LGE imaging.
- Native T1 mapping might also enable therapy monitoring of cardiac involvement in Fabry disease in the future.

Conflict of Interest

The authors declare that they have no conflict of interest.

References

[1] MacDermot KD, Holmes A, Miners AH. Anderson-Fabry disease: clinical-manifestations and impact of disease in a cohort of 98 hemizygous males. J Med Genet 2001; 38: 750e60

[2] Hoey ET, Neil-Gallagher E. Utility of gadolinium enhancedcardiovascular MRI to differentiate Fabry's disease from other causes of hypertrophic cardiomyopathy. Postgrad Med J 2012; 88: 731 – 732

[3] Eng CM, Guffon N, Wilcox WR et al. Safety and efficacy of recombinant human alpha-galactosidase A-replacement therapy in Fabry's disease. N Engl J Med 2001; 345: 9 – 16

[4] Messalli G, Imbriaco M, Avitabile G et al. Role of cardiac MRI in evaluating patients with Anderson-Fabry disease: assessing cardiac effects of long-term enzyme replacement therapy. Radiol Med 2012; 117: 19 – 28

[5] Moon JC, Sachdev B, Elkington AG et al. Gadolinium enhanced cardiovascularmagnetic resonance in Anderson-Fabry disease: evidence for a disease specific abnormality of the myocardial interstitium. Eur Heart J 2003; 24: 2151e5

[6] Moon JC, Reed E, Sheppard MN et al. The histologic basis of late gadolinium enhancement cardiovascular magnetic resonance in hypertrophic cardiomyopathy. J Am Coll Cardiol 2004; 43: 2260 – 2264

[7] Reingold JS, McGavock JM, Kaka S et al. Determination of triglyceride in the human myocardium by magnetic resonance spectroscopy: reproducibility and sensitivity of the method. Am J Physiol Endocrinol Metab 2005; 289: E935 – E939

[8] O'Connor RD, Xu J, Ewald GA et al. Intramyocardial triglyceride quantification by magnetic resonance spectroscopy: In vivo and ex vivo correlation in human subjects. Magn Reson Med 2011; 65: 1234 – 1238

[9] den Hollander JA, Evanochko WT, Pohost GM. Observation of cardiac lipids in humans by localized 1H magnetic resonance spectroscopic imaging. Magn Reson Med 1994; 32: 175 – 180

[10] Petritsch B, Köstler H, Machann W et al. Non-invasive Determination of Myocardial Lipid Content in Fabry Disease by 1H-MR Spectroscopy. Fortschr Röntgenstr 2012; 184: 1020 – 1025

[11] Petritsch B, Köstler H, Weng AM et al. Myocardial lipid content in Fabry disease: a combined 1H-MR spectroscopy and MR imaging study at 3 Tesla. BMC Cardiovasc Disord 2016; 16: 205

[12] Sado DM, White SK, Piechnik SK et al. Identification and assessment of Anderson-Fabry Disease by Cardiovascular Magnetic Resonance Non-contrast myocardial T1 mapping clinical perspective. Circ Cardiovasc Imaging 2013; 6: 392 – 398

[13] Thompson RB, Chow K, Khan A et al. T1 mapping with cardiovascular MRI is highly sensitive for Fabry disease independent of hypertrophy and sex. Circ Cardiovasc Imaging 2013; 6: 637 – 645

[14] Arends M, Wijburg FA, Wanner C et al. Favourable effect of early versus late start of enzyme replacement therapy on plasma globotriaosylsphingosine levels in men with classical Fabry disease. Mol Genet Metab 2017; 121: 157 – 161

[15] Sueoka H, Ichihara J, Tsukimura T et al. Nano-LC-MS/MS for Quantification of Lyso-Gb3 and Its Analogues Reveals a Useful Biomarker for Fabry Disease. PLoS One 2015; 10: e0127048

[16] Lavoie P, Boutin M, Abaoui M et al. Fabry Disease Biomarkers: Analysis of Urinary Lyso-Gb3 and Seven Related Analogs Using Tandem Mass Spectrometry. Curr Protoc Hum Genet 2016; 90: 17.22.1 – 17.22.12

[17] Togawa T, Kodama T, Suzuki T et al. Plasma globotriaosylsphingosine as a biomarker of Fabry disease. Mol Genet Metab 2010; 100: 257 – 261

[18] Roller FC, Wiedenroth C, Breithecker A et al. Native T1 mapping and extracellular volume fraction measurement for assessment of right ventricular insertion point and septal fibrosis in chronic thromboembolic pulmonary hypertension. Eur Radiol 2017; 27: 1980 – 1991

[19] Messroghli DR, Radjenovic A, Kozerke S et al. Modified Look-Locker inversion recovery (MOLLI) for high resolution T1 mapping of the heart. Magn Reson Med 2004; 52: 141 – 146

[20] Tanislav C, Gündüz D, Liebetrau C et al. Cardiac Troponin I: A Valuable Biomarker Indicating the Cardiac Involvement in Fabry Disease. PLOS One 2016; 11: e0157640

[21] Rombach SM, Dekker N, Bouwman MG et al. Plasma globotriaosylsphingosine: diagnostic value and relation to clinical manifestations of Fabry disease. Biochim Biophys Acta 2010; 1802: 741 – 748

[22] Feustel A, Hahn A, Schneider C et al. Continuous cardiac troponin I release in Fabry disease. PLoS One 2014; 9: e91757

[23] Kilinc G, Dogan OT, Berk S et al. Significance of serum cardiac troponin I levels in pulmonary embolism. J Thorac Dis 2012; 4: 588 – 593

[24] Ries M, Clarke JT, Whybra C et al. Enzyme-replacement therapy with agalisade alfa in children with Fabry disease. Pediatrics 2006; 118: 924e32

[25] Germain DP, Waldek S, Banikazemi M et al. Sustained, long-term renal stabilization after 54 months of agalsidase beta therapy in patients with Fabry disease. J Am Soc Nephrol 2007; 18: 1547 – 1557

[26] Frustaci A, Morgante E, Russo MA et al. Pathology and function of conduction tissue in Fabry disease cardiomyopathy. Circ Arrhythm Electrophysiol 2015; 8: 799 – 805

Eur Radiol
DOI 10.1007/s00330-016-4585-y

CARDIAC

Native T1 mapping and extracellular volume fraction measurement for assessment of right ventricular insertion point and septal fibrosis in chronic thromboembolic pulmonary hypertension

Fritz C. Roller[1] · Christoph Wiedenroth[2] · Andreas Breithecker[1] · Christoph Liebetrau[3] · Eckhard Mayer[2] · Christian Schneider[1] · Andreas Rolf[3] · Christian Hamm[3,4] · Gabriele A. Krombach[1]

Received: 17 August 2015 / Revised: 25 July 2016 / Accepted: 29 August 2016

Abstract

Objectives The aim of this study was to assess septal and right ventricular insertion point (RVIP) fibrosis in patients with chronic thromboembolic pulmonary hypertension (CTEPH) via native T1 mapping and extracellular volume fraction (ECV) determination and to analyze correlations with functional parameters.

Methods Imaging was performed at 1.5 Tesla in 24 patients diagnosed with CTEPH and 24 controls. T1 values were measured within the septal myocardium, the upper and lower RVIP, and the lateral wall at basal short axis section.

Results The mean septal native T1 values were 1012.8 ms ± 50.5 in the CTEPH group and 956.9 ms ± 24.4 in controls ($p < 0.001$), upper RIVP 1050.8 ms ± 64.2 vs. 965.3 ms ± 37.1 ($p < 0.001$), and lower RVIP 1084.4 ms ± 93.1 vs. 959.8 ms ± 40.4 ($p < 0.001$). The corresponding mean ECV values were also significantly increased in the CTEPH group ($p < 0.001$). Native septal T1 showed a strong negative correlation with right ventricular ejection fraction (k = -0.92; $p = 0.01$).

Conclusions We conclude that native T1 mapping and ECV assessment enable visualization and quantification of septal fibrosis in CTEPH patients. The results also correlate well with right ventricular ejection fraction. Therefore, these parameters might be useful for prognosis and as therapy-monitoring tool in the future.

Key Points

- *Septal native T1 and ECV values are significantly higher in CTEPH patients.*
- *Native T1 and ECV values are elevated even in absence of LGE.*
- *These techniques therefore enable an improved quantification of septal fibrosis in CTEPH.*

✉ Fritz C. Roller
fritz.c.roller@radiol.med.uni-giessen.de

Christoph Wiedenroth
c.wiedenroth@kerckhoff-klinik.de

Andreas Breithecker
andreas.breithecker@radiol.med.uni-giessen.de

Christoph Liebetrau
c.liebetrau@kerckhoff-klinik.de

Eckhard Mayer
e.mayer@kerckhoff-klinik.de

Christian Schneider
christian.schneider@uniklinikum-giessen.de

Andreas Rolf
a.rolf@kerckhoff-klinik.de

Christian Hamm
christian.hamm@innere.med.uni-giessen.de

Gabriele A. Krombach
gabriele.krombach@uniklinikum-giessen.de

[1] Department of Diagnostic and Interventional Radiology, Justus-Liebig-University Giessen, Klinikstr. 33, 35392 Giessen, Germany

[2] Department of Thoracic Surgery, Kerckhoff Heart and Thorax Centre, Bad Nauheim, Germany

[3] Department of Cardiology, Kerckhoff Heart and Thorax Centre, Bad Nauheim, Germany

[4] Department of Cardiology, Justus-Liebig-University Giessen, Giessen, Germany

Published online: 20 September 2016

- *Native T1 values also correlate well with right ventricular EF and PA-pressure.*
- *Prognosis and therapy-monitoring might be assessable in the future with these parameters.*

Keywords MRI · PH · CTEPH · T1 Mapping · ECV

Abbreviations

BPA	balloon pulmonary angioplasty
CMR	cardiac magnetic resonance
CO	cardiac output
CTEPH	chronic thromboembolic pulmonary hypertension
ECV	extracellular volume fraction
EDD	end-diastolic diameter
EDV	end-diastolic volume
EF	ejection fraction
EMB	endomyocardial biopsy
ESD	end-systolic diameter
ESV	end-systolic volume
LGE	late gadolinium enhancement
LV	left ventricle
mPAP	mean pulmonary arterial pressure
PA	pulmonary artery
PAOP	pulmonary arterial occlusion pressure
PEA	pulmonary endarterectomy
PH	pulmonary hypertension
PVR	pulmonary vascular resistance
RAP	right atrial pressure
RVIP	right ventricular insertion point
PEA	pulmonary endarterectomy
ROI	region of interest
RV	right ventricle
SD	standard deviation
SV	stroke volume

Introduction

Pulmonary hypertension (PH) is defined as elevation of the mean pulmonary artery (PA) pressure to 25 mmHg or higher [1]. Different aetiologies of PH are known and have been categorized in the Updated Clinical Classification by Simonneau et al.: PA hypertension, PH due to left heart disease, PH due to lung disease and/or hypoxia (for example fibrosis or emphysema), chronic thromboembolic pulmonary hypertension (CTEPH), and unclear and/or multifactorial mechanisms [2]. In this setting CTEPH is defined as PH with persistent perfusion defects after single or recurrent pulmonary embolism [3]. It is a rare but under-diagnosed disease with an estimated incidence between 0.5 % and 3.8 % after acute pulmonary embolism and 10 % after repeated embolism [4–7]. In contrast to other aetiologies of PH, CTEPH is the only disease that is potentially curable by surgical pulmonary endarterectomy (PEA) [8, 9]. After surgery pulmonary vascular pressure and resistance are restored in most patients [10] and a high long-term survival rate of 84 % can be achieved [9].

In all types of PH elevated pulmonary pressure and resistance cause right ventricular remodelling. To compensate for emerging pressure overload and right ventricular wall stress, the right ventricular (RV) myocardium hypertrophies, which initially is an adaptive process. In later stages RV dysfunction and dilation ensue [11] and eventually RV function deteriorates and diastolic RV pressure increases [12, 13]. As a result the RV stroke volume (SV) decreases and abnormal interventricular septal motion (the so-called "septal bounce") in the early diastole can be detected [14]. Thus, left ventricular filling and hence diastolic function become impaired.

Because of enormous mechanical stress with compression, traction, and shear forces it appears likely that especially the septum and the interventricular insertion points (upper and lower RVIP) undergo myocardial remodelling. This hypothesis is supported by the fact that late gadolinium enhancement (LGE) limited to the RVIP, which is typically triangular in shape [11], has been encountered in 83.0 % to 91.3 % of patients with PH [15–18]. Findings in a case report, which showed post-mortem interventricular plexiform fibrosis in the RVIP in a CTEPH patient with typical LGE, strengthen this hypothesis [19]. A certain degree of fibre disarray and interstitial fibrosis, however, can also be found in healthy subjects [20], and the location may correspond to the tissue at which the highest amount of force is applied due to increased mechanical stress. Determining the precise histological basis of such findings is difficult because the insertion point areas are inaccessible for endomyocardial biopsy (EMB) [11].

In contrast to LGE imaging, mapping techniques allow pixel-wise parametric imaging based on curve fitting algorithms for varying inversion times displayed as colour maps. Native T1 mapping permits tissue characterization without the need for contrast agents, and in addition the measurement of myocardial T1 before and after contrast administration with hematocrit correction allows for quantification of the extracellular volume fraction (ECV) [21]. Both techniques show great potential for the quantification and visualization of myocardial fibrosis in different diseases, as previous studies have shown [22–25]. Moreover, the results of a very recent study by Garcia-Alvarez et al. in an experimental animal model suggest that T1 mapping and ECV quantification might be suitable non-invasive methods to assess fibrosis of the upper and lower RVIP in chronic PH [26].

In order to determine the potential of mapping as an imaging biomarker for patients with CTEPH, which might also have influence on therapy and monitoring in the future, the aim of our study was to assess septal and RVIP fibrosis via native T1 mapping and ECV in patients with CTEPH vs.

healthy subjects and to correlate the results with functional parameters (mPAP and PVR).

Methods

Patient population

A total of 24 consecutive CTEPH patients (17 female) with a mean age of 63.4 ± 10.6 years [± standard deviation (SD)] and a mean PA pressure (mPAP) of 39.1 ± 11.2 mmHg and 24 control subjects (12 female) with a mean age of 61.3 ± 12.0 years were enrolled in this prospective cohort study from January 2014 to February 2015. The 24 CTEPH patients were assessed by cardiac magnetic resonance (CMR) as part of their pre-interventional routine workup before PEA or balloon pulmonary angioplasty (BPA) with the need for further assessment of RV function and pulmonary arteries. In order to reduce magnetic field and contrast media risks for healthy subjects the control group consisted of patients who had all undergone CMR within the defined period for exclusion of myocardial ischemia and had inconspicuous results regarding heart size and motion, valvular defects and perfusion, ejection fraction, pericardial and pleural effusion or pulmonary oedema, and pulmonary trunk and aortic diameters. Clinical follow-up confirmed that the subjects did not suffer from any cardiac diseases. The first 24 patients who met the control group inclusion criteria within the study period were chosen for comparison with CTEPH patients.

Contraindications for CMR and exclusion criteria in all patients were renal failure (glomerular filtration rate below 30 mL/min/1.73 m^2), incompatible cochlear or metallic implants, known gadolinium intolerance, claustrophobia, or the inability to lie supine for the duration of the protocol due to dyspnoea.

The primary diagnosis of CTEPH was based on ventilation-perfusion scintigraphy, right heart catheter measurements (standard Swan-Ganz catheters were used in the pre-interventional evaluation), and pulmonary angiography findings. All patients gave written informed consent and the local ethics committee approved the study.

CMR Imaging

Imaging was performed with a 1.5 Tesla scanner system (Avanto, Siemens Healthcare, Forchheim, Germany) using a six-element phased array cardiac coil and a dedicated CMR protocol containing axial, coronal, and sagittal thoracic survey images, CINE sequences, steady-state-free precession sequences (SSFP) aligned to 2-chamber view (CV), 3 CV, 4 CV, and short-axis (SA), black-blood [T2 turbo spin echo (TSE)] and LGE [T1 gradient echo (GE) with inversion recovery] imaging. Native and post-contrast T1 mapping were also performed.

Gadobenate dimeglumine (Gd-BOPTA; Multihance, BRACCO Imaging) was injected at a dose of 0.15 mmol/kg. LGE imaging was performed 12 min after contrast media injection, and post-contrast T1 mapping was performed 15 min after contrast media injection. The SSFP and CINE images were obtained during breath hold and the LV and RV systolic and diastolic volumes (absolute values) were calculated from short-axis and axial CINE images. Measurements were performed on end-diastolic images (first cine after the R-wave trigger) and end-systolic images (cine with visually smallest cavity area). Endocardial contours of the LV and RV were obtained by manual tracing with exclusion of papillary muscles and trabeculae from the cavity. Ventricular volumes were estimated using the Simpson rule. The EF was calculated as (EDV - ESV)/EDV. ESD and EDD measurements were performed on basal short axis images. The post-processing was performed with the Argus software package (Siemens Syngo MMWP Version VE40A, Siemens Healthcare, Forchheim, Germany).

T1 mapping images were acquired at basal, mid-ventricular, and apical short-axis sections by using an optimized modified Look-Locker inversion-recovery (MOLLI) sequence, with three images in the first two Look-Locker segments and five images for the third inversion (known as the "3-3-5" standard protocol). Finally, 11 images were acquired during 17 heartbeats,

Table 1 Demographic data for CTEPH patients and control subjects

	CTEPH	Controls	*p* Value
Patients (n)	24	24	
Age ± SD* (years)	63.4 ± 10.6	61.3 ± 12.0	
Gender (male:female)	7:17	12:12	
Aortic diameter (mm)	32.4 ± 3.2	33.1 ± 3.5	0.97
PT diameter (mm)	34.5 ± 4.5	23.3 ± 2.2	0.001
Ratio aorta/PT	0.95 ± 0.13	1.42 ± 0.19	0.001
Heart rate (bpm)	77.2 ± 11.2	72.3 ± 10.4	0.26
mPAP (mmHg)	39.1 ± 11.2		
PVR (dyne × sec × cm^{-5})	498.6 ± 230.1		
RAP (mmHg)	6.2 ± 3.1		
PAOP (mmHg)	10.0 ± 3.5		
CO (l/min)	5.0 ± 1.1		

Values are mean ± SD or absolute values; *p* Value (Wilcoxson signed rank test)

SD standard deviation; *CTEPH* chronic thromboembolic pulmonary hypertension; *PT* pulmonary trunk; *mPAP* mean pulmonary arterial pressure; *PVR* pulmonary vascular resistance; *RAP* right atrial pressure; *PAOP* pulmonary arterial occlusion pressure; *CO* cardiac output

Table 2 Functional analysis and presence of LGE in CTEPH patients and control subjects*

		CTEPH (n = 24)	Controls (n = 24)	*p* Value
LV function	EF	67.0 ± 7.8 %	69.5 ± 6.7 %	0.43
	EDV	108.9 ± 27.1 ml	122.2 ± 25.1 ml	0.16
	ESV	36.5 ± 14.3 ml	42.6 ± 28.4 ml	0.65
	SV	72.5 ± 17.1 ml	84.0 ± 19.1 ml	0.06
	EDD	43.8 ± 7.1 mm	49.8 ± 4.0 mm	0.004
	ESD	25.1 + 6.5 mm	28.7 ± 3.9 mm	0.04
RV function	EF	40.1 ± 15.1 %	65.4 ± 7.0 %	<0.001
	EDV	197.7 ± 112.7 ml	127.5 ± 30.6 ml	<0.001
	ESV	127.1 ± 105.5 ml	47.9 ± 18.1 ml	<0.001
	SV	70.5 ± 24.2 ml	79.3 ± 15.3 ml	0.16
Wall thickness	Septal	6.9 ± 1.7 mm	8.9 ± 2.0 mm	0.001
	Lateral	6.3 ± 1.6 mm	6.6 ± 1.8 mm	0.44
LGE	Insertion points	15 (62.5 %)	0	

Values are mean ± SD or absolute values; *p* Value (Wilcoxson signed rank test)

CTEPH chronic thromboembolic pulmonary hypertension; *EF* ejection fraction; *EDV* end-diastolic volume; *ESV* end-systolic volume; *SV* stroke volume; *EDD* end-diastolic diameter; *ESD* end-systolic diameter; *LGE* late gadolinium enhancement

and in-line motion correction and map generation were performed [27].

Imaging parameters were: slice thickness: 8 mm; spatial resolution: 2.2 mm × 1.8 mm × 8 mm; 6/8 partial Fourier acquisition; field of view: 240 × 340 mm; matrix: 192 × 124; flip angle 35°; TR 740 and TE 1.06; TI 100 ms and TI increment 80 ms; trigger delay: 300 ms; inversions 3; acquisition heartbeats: 3,3,5; scan time: 17 heartbeats.

Qualitative and quantitative image assessment

All original images were assessed regarding artefacts due to susceptibility, cardiac, diaphragmatic, or respiratory motion. Each motion-corrected series was evaluated for correct image alignment and each map was evaluated whether the original images were transformed to an acceptably appearing map.

Image assessment and measurement of native T1 and ECV

After image acquisition T1 maps were generated after in-line motion correction from the MR workstation. Co-registration of pre- and postcontrast maps was performed by manually taking over the native T1 map slice positions for the planning of the postcontrast T1 maps. An experienced radiologist reviewed the matching of the postcontrast T1 maps afterwards (C.S., 9 years of experience). T1 times were measured for myocardium and blood pool in regions of interest (ROI) before and after contrast administration at basal SA section. Therefore, a total of four ROIs were manually drawn at the following locations: basal septum, upper and lower septal RVIP, and lateral wall as additional reference. It was emphasized that the ROIs were drawn only on the compact myocardium and did not include the myocardial borders because partial volume averaging artefacts and registration errors with gradual T1 value changes are present at the borders. In addition to the T1 values the size of the ROIs were also compared

Table 3 Functional analysis and wall thickness of CTEPH patients with and without LGE

		CTEPH LGE (n = 15)	CTEPH No LGE (n = 9)	*p* Value
LV function	EF	67.9 ± 8.0 %	65.7 ± 7.8 %	
	EDV	96.3 ± 22.6 ml	129.9 ± 20.6 ml	0.001
	ESV	31.3 ± 12.0 ml	45.1 ± 14.1 ml	0.02
	SV	65.1 ± 15.2 ml	84.8 ± 12.9 ml	0.004
	EDD	39.8 ± 5.2 mm	50.4 ± 4.1 mm	<0.001
	ESD	21.7 ± 4.6 mm	30.7 ± 5.4 mm	<0.001
RV function	EF	32.1 ± 12.2 %	53.3 ± 8.7 %	<0.001
	EDV	223.9 ± 134.7 ml	154.0 ± 35.8 ml	0.14
	ESV	160.3 ± 122.0 ml	71.9 ± 20.8 ml	0.04
	SV	63.6 ± 23.7 ml	82.0 ± 21.4 ml	0.07
Wall thickness	Septal	6.6 ± 1.7 mm	7.4 ± 1.6 mm	0.30
	Lateral	6.5 ± 1.8 mm	5.9 ± 1.2 mm	0.41

Values are mean ± SD; *p* Value (Wilcoxon signed rank test)

CTEPH chronic thromboembolic pulmonary hypertension; *EF* ejection fraction; *EDV* end-diastolic volume; *ESV* end-systolic volume; *SV* stroke volume; *EDD* end-diastolic diameter; *ESD* end-systolic diameter; *RV* right ventricular; *LV* left ventricular

Table 4 Native T1 Mapping in CTEPH patients and control subjects

	CTEPH (n = 24) ms	Mean ROI Size mm^2	Controls (n = 24) ms	Mean ROI Size mm^2	*p* Value
Upper RVIP	1050.8 ± 64.2	44.6	965.3 ± 37.1	37.4	<0.001
Lower RVIP	1084.4 ± 93.1	38.7	959.8 ± 40.4	32.0	<0.001
Septum	1012.8 ± 50.5	113.3	956.9 ± 24.4	106.8	<0.001
Lateral wall	957.5 ± 36.3	97.3	966.8 ± 35.1	109.4	0.38

Values are mean ± SD; *p* Value (Wilcoxon signed rank test)

CTEPH chronic thromboembolic pulmonary hypertension; *RVIP* right ventricular insertion point; *ROI* region of interest

and evaluated to exclude size-dependent differences between the two groups. For measurement of the post-contrast T1 values the pre-defined ROIs of the native T1 measurements were transferred to the post-contrast T1 maps in order to ensure a standardized measurement. The ECV calculations were performed according to the known standardized and previously published formula [20, 21]. Hematocrit levels for the calculation of ECV were determined within 1 day prior to the examinations. Two experienced radiologists performed all measurements in agreement (G.K./18 years of experience; F.R./4 years of experience). The measurements were performed blinded to patient demographics, and LGE assessment was performed blinded to T1 maps and CINE images and vice versa. Sufficient myocardial T1 measurements were performed reliably in all patients.

Statistical analysis

Statistical analysis was performed using SPSS statistical software version 20 (SPSS, Chicago, Il, USA). Patient characteristics were described by mean ± SD. All data were tested for normal distribution using the Shapiro-Wilk test. In cases of normal distribution Student's t-test was used, and if the data were not distributed normally the Wilcoxon signed rank test (non-parametric) was used. Strengths of correlations were tested using the Pearson correlation coefficient. Intra- and interobserver variability was tested with linear regression analysis and Bland-Altman plots. Linear regression analysis was also used for assessing the correlation of native T1 and functional parameters as presented in Fig. 6. The correlation coefficient k was interpreted according to Hinkle et al., where $k > 0.5$ would be considered a moderate correlation, $k > 0.7$ a strong correlation and $k > 0.9$ very strong correlation. An $k > 0.5$ would therefore considered to have clinical impact [28]. All results were tested at a 5 % level of significance and we accepted an alpha error of less than 0.05 as statistically significant.

Results

CTEPH patients and control subjects showed a similar age structure (Table 1). The mean pulmonary trunk diameter was clearly enlarged in the CTEPH group compared with the control group (34.5 mm vs. 23.3 mm; $p = 0.001$) and the

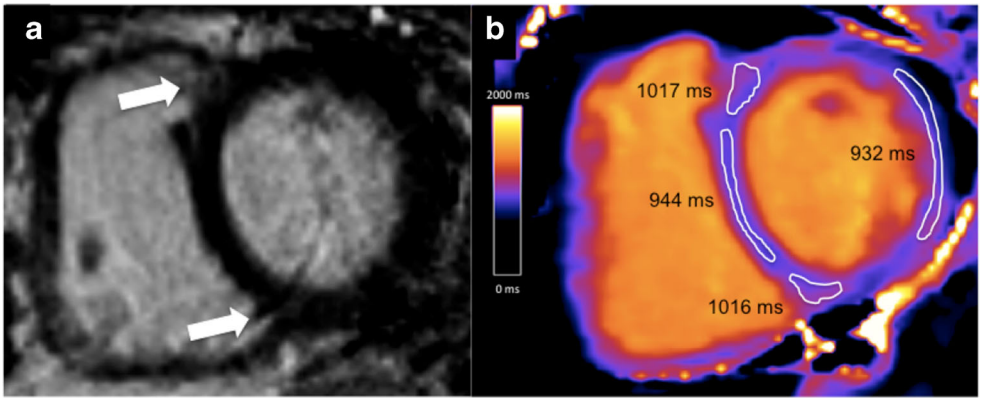

Fig. 1 Lack of LGE and corresponding native T1 map in a CTEPH patient. LGE image (**a**) and the corresponding native T1 map (**b**) in a 64-year-old female patient with CTEPH at the basal short-axis level (mPAP = 34 mmHg; RV EF = 54 %). Typical triangular LGE in the upper and in the lower RVIP is absent (*white arrows*). T1 measurements were performed within ROIs (*white borders*) in the native T1 map and revealed 1017 ms for the upper RVIP, 1016 ms for the lower RVIP, and 944 ms for the septal myocardium, with a value of 932 ms for the lateral wall

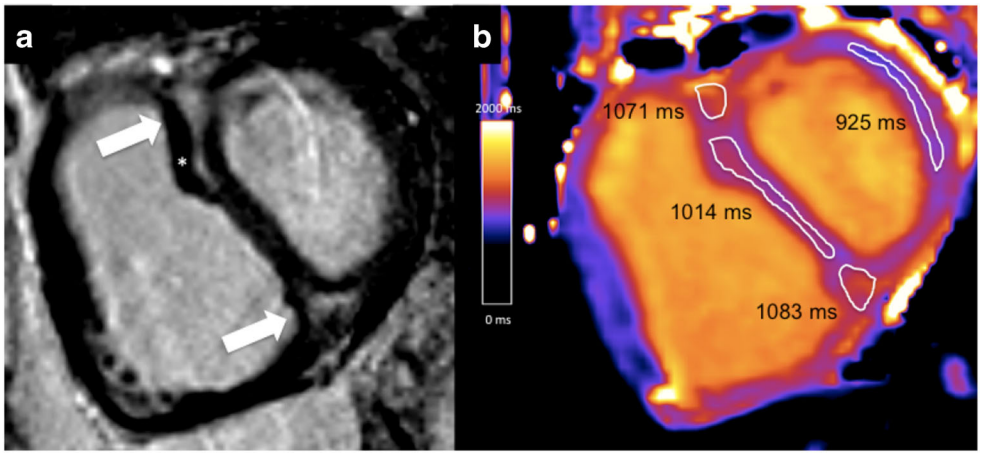

Fig. 2 Presence of LGE and corresponding native T1 map in a CETPH patient. LGE image (**a**) and the corresponding native T1 map (**b**) in a 58-year-old male patient with CTEPH at basal short-axis level (mPAP = 55 mmHg; RV EF = 23 %). The LGE image impressively demonstrates a triangular LGE in the upper and lower RVIPs (*white arrows*). An anteroseptal LGE is also visible that originates from the upper insertion point (*white star*). Compared with the images in Fig. 1, the presence of LGE is accompanied by greater T1 values. The T1 measurements within ROIs (*white borders*) revealed 1071 ms for the upper RVIP, 1083 ms for the lower RVIP, and 1014 ms for the septal myocardium, with a value of 925 ms for the lateral wall

difference in mean PT/aortic diameter ratio was also statistically significant ($p = 0.001$), as expected. CTEPH and control subjects had normal LV function regarding ejection fraction (EF), end-diastolic volume (EDV), and end-systolic volume (ESV), but statistically significant differences were observed for end-systolic (ESD) and end-diastolic diameters (EDD), with $p = 0.04$, and 0.004, respectively (Table 2). The RV EF of 40.1 % in the CTEPH group was significant reduced compared to the control group, whereas the RV ESV and EDV were significant increased. Furthermore, the septal diameter in the CTEPH group was significantly thinner than that of the control group ($p = 0.001$), whereas the diameter of the lateral wall was similar. Triangular septal LGE was present in 15 CTEPH patients (62.5 %), but in none of the controls.

CTEPH patients were further subdivided into those with and without the presence of RVIP LGE (Table 3). Both of these subgroups had normal LV EF, but the EDV, ESV, SV, EDD, and ESD were significantly reduced in CTEPH patients with LGE compared with CTEPH patients without LGE. Also, the RV EF, EDV, and ESV were significantly reduced in CTEPH patients with LGE. The septal wall diameter in the CTEPH patients with LGE compared with the CTEPH patients without LGE (6.6 mm vs. 7.4 mm) was reduced, but was not significant different ($p = 0.30$).

Significant differences in native T1 mapping values between CTEPH patients (elevated) and controls were present for the septum ($p < 0.001$) and the upper ($p < 0.001$) and lower RVIP ($p < 0.001$), whereas the mean T1 value of the lateral wall was not significantly different between the two groups (Table 4). In addition, the mean sizes of the ROIs in all areas measured were not significantly different, which means that comparable areas within the myocardium were measured for CTEPH patients and control subjects. Figure 1 shows the LGE image and corresponding native T1 map of a CTEPH patient without LGE, and Fig. 2 shows the comparable image and map from a CTEPH patient with LGE in the insertion point regions. As with native T1 mapping, the ECV for the septum ($p < 0.001$) and the upper and lower RVIP (both $p < 0.001$) was significantly different between the groups (Table 5). Figure 3 shows the LGE image and the native and post-contrast T1 maps with corresponding ECV values in a CTEPH patient.

Native T1 mapping and ECV values subdivided into CTEPH patients with and without LGE and for CTEPH patients without LGE compared with control subjects are shown in Tables 6 and 7, respectively. Here again, there were significant differences in T1 and ECV values for the septum and the RVIP (elevated). The inter- and intraobserver variability for native T1 and ECV was excellent in all areas, moreover Figs. 4 and 5 show the corresponding Bland-Altman plots

Table 5 ECV in CTEPH patients and control subjects

	CTEPH (n = 24)	Controls (n = 24)	*p* Value
ECV			
Upper RVIP	0.31 ± 0.05	0.25 ± 0.03	<0.001
Lower RVIP	0.33 ± 0.07	0.24 ± 0.03	<0.001
Septum	0.27 ± 0.04	0.23 ± 0.02	<0.001
Hematocrit	0.42 ± 0.06	0.42 ± 0.03	0.53

Values are mean ± SD; *p* Value (Wilcoxon signed rank test)

ECV extracellular volume fraction; *CTEPH* chronic thromboembolic pulmonary hypertension; *RVIP* right ventricular insertion point; *ROI* region of interest

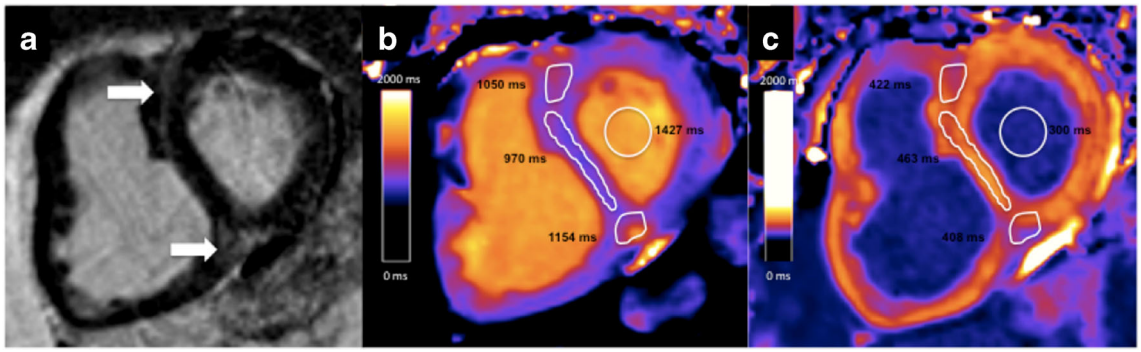

Fig. 3 LGE image and corresponding native and post-contrast T1 maps in a CTEPH patient. LGE image (**a**), corresponding native T1 map (**b**), and the post-contrast T1 map (**c**) in a 66-year-old male patient with CTEPH at the basal short-axis level (mPAP = 43 mmHg; RV EF = 51 %). As shown for Fig. 2 the LGE image demonstrates typical triangular LGE in the upper and lower RVIP (*white arrows*). As in Figs. 1 and 2, T1 measurements were made within ROIs (*white borders*) in the native and post-contrast T1 map and ECV was calculated (hematocrit 0.48). ECV was 0.28 for the upper RVIP, 0.31 for the lower RVIP, and 0.22 for the septal myocardium

for native T1 and ECV in different ROIs, which also demonstrate the low spreading width of the performed intra- and interobserver variability measurements.

Also, there was a moderate, but significant positive correlation between native T1 values and PA pressure (k = 0.60; $p = 0.002$), a moderate significant negative correlation between native T1 values and RV EF (k = -0.65; $p < 0.001$) and a moderate significant positive correlation between native T1 values and PVR (k = 0.67; $p < 0.001$) for the area adjusted septal T1 times (a total area-adjusted T1 value was calculated for septum and upper and lower RVIP and correlated with PA pressure, RV EF, and PVR). Figure 6 shows the scatter plots for the area adjusted T1 values correlated to PA pressure, RV EF and PVR. By analyzing the area adjusted native T1 thresholds as presented in Table 8 a significant negative correlation between native T1 value and RV EF (k = -0.92; $p = 0.01$) and a good positive correlation between native T1 value and PA pressure were present (k = 0.83; $p = 0.04$).

Discussion

CMR is a versatile diagnostic tool that enables reliable assessment of cardiac function, motion and perfusion. One of its key advantages is the possibility to characterize myocardial tissue: scar imaging, better known as LGE imaging, is carried out after intravenous administration of contrast medium. Myocardial fibrosis as measured by LGE imaging, for example, is known as a predictor of adverse outcome in dilated and hypertrophic cardiomyopathy, aortic stenosis, and coronary artery disease [29–32]. In advanced PH stages, typical triangular LGE in the RVIPs is a common disease feature [15, 16]. In addition, the presence of LGE in these areas correlates with altered interventricular septal motion, although it does not impact mortality or myocardial function in PH [17, 18], but was shown to be associated with increased estimated LV filling pressure and chronic diastolic burden in hypertrophic cardiomyopathy [33]. Nonetheless, LGE imaging is limited

Table 6 Native T1 and ECV in CTEPH patients with and without LGE

	CTEPH LGE (n = 15)	CTEPH No LGE (n = 9)	*p* Value
Native T1 upper RVIP (ms)	1073.1 ± 59.9	1013.6 ± 55.4	0.02
Native T1 lower RVIP (ms)	1135.7 ± 73.0	998.8 ± 49.3	<0.001
Native T1 septum (ms)	1032.9 ± 46.4	979.1 ± 39.1	0.008
ECV upper RVIP	0.33 ± 0.06	0.28 ± 0.03	0.02
ECV lower RVIP	0.35 ± 0.07	0.29 ± 0.04	<0.05
ECV septum	0.28 ± 0.04	0.27 ± 0.02	0.36

Values are mean ± SD; *p* Value (Wilcoxon signed rank test)

ECV extracellular volume fraction; *CTEPH* chronic thromboembolic pulmonary hypertension; *RVIP* right ventricular insertion point; *ROI* region of interest; *LGE* late gadolinium enhancement

Table 7 Native T1 mapping and ECV in LGE-negative CTEPH patients and control subjects

	CTEPH (n = 9)	Controls (n = 24)	*p* Value
Native T1 (ms)			
Upper RVIP	1013.6 ± 55.4	965.3 ± 37.1	0.006
Lower RVIP	998.8 ± 49.3	959.8 ± 40.4	0.02
Septum	979.1 ± 39.1	956.9 ± 24.4	0.07
ECV			
Upper RVIP	0.28 ± 0.03	0.25 ± 0.03	<0.001
Lower RVIP	0.29 ± 0.04	0.24 ± 0.03	<0.001
Septum	0.27 ± 0.02	0.23 ± 0.02	<0.001

Values are mean ± SD; *p* Value (Wilcoxon signed rank test)

ECV extracellular volume; *CTEPH* chronic thromboembolic pulmonary hypertension; *RVIP* right ventricular insertion point; *ROI* region of interest

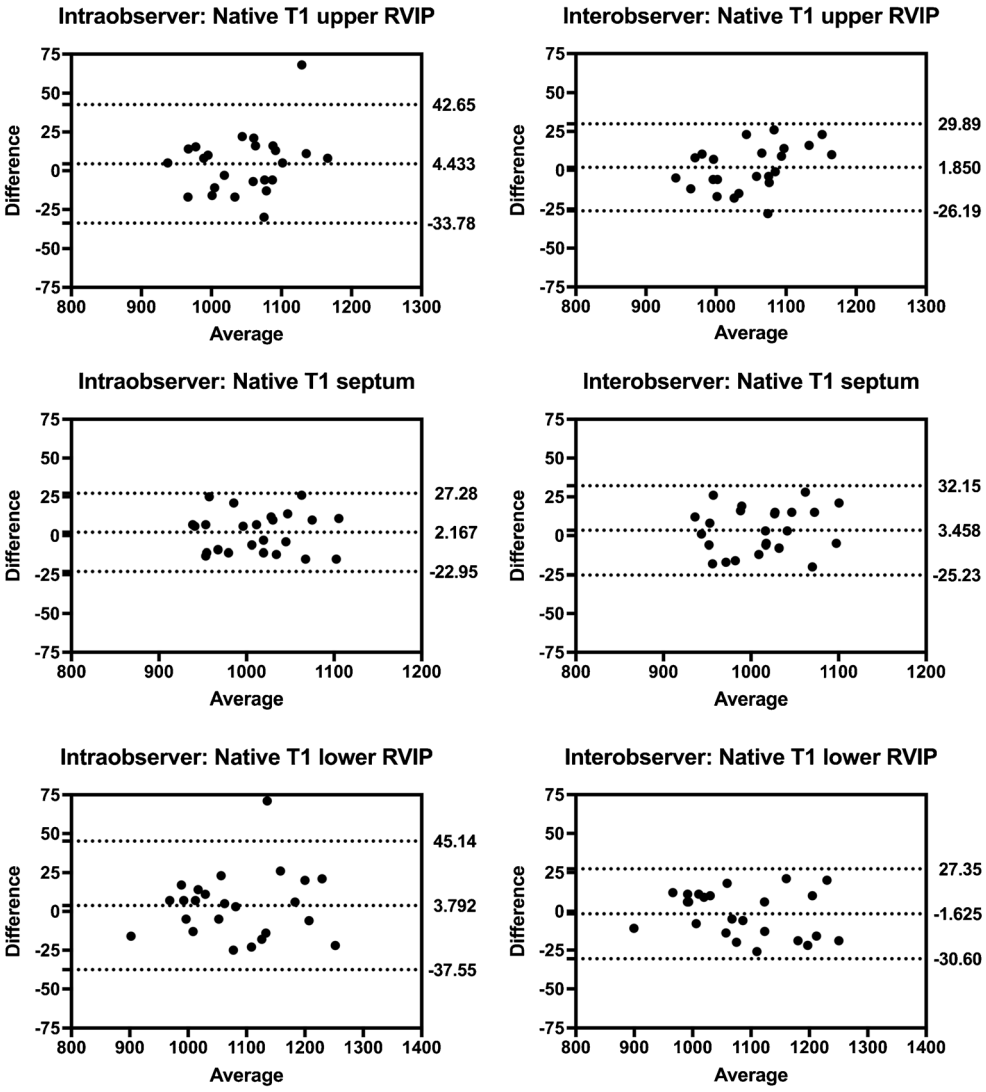

Fig. 4 Bland-Altman plots for native T1 measurements in different ROIs in CTEPH patients. All plots demonstrate the low spreading width within the performed intra- and interobserver variability measurements. The dotted lines show the upper and lower 95 % limit of agreement and the mean standard bias. The corresponding values are presented at the right Y-axis

regarding visualization and characterization of diffuse myocardial pathologies, as demonstrated by Moon et al. in patients with hypertrophic cardiomyopathy [34]. Thus, myocardial segments containing at least 15 % collagen fibre components were more likely to show LGE, whereas areas with less advanced fibrosis were not visualized by LGE imaging [35]. This clearly shows that detection of limited disease stages or early disease is not possible via LGE imaging.

As recently described for many different diseases, mapping shows great potential in overcoming these problems through parametric imaging of diffuse myocardial pathologies. For example, native T1 mapping and ECV determination showed promising results in assessment of myocardial fibrosis [22–25], and therefore, both techniques appear auspicious for non-invasive assessment of septal and RVIP fibrosis in patients with PH. Moreover, the results recently obtained from a PH porcine model also strengthen this thesis [26].

Biology underlying LGE, native T1 and ECV: LGE depends on spatial heterogeneity to display enhancement [36] and requires a certain degree of collage fibre components for visualization [35]. Myocardial fibrosis is characterized by a continuous spectrum between focal fibrotic changes and diffuse fibrotic conversion. In some patients, fibrosis might be limited truthfully to the displayed LGE area, but in others LGE might only show the most severe affected myocardial areas ("top of the iceberg") [36] and, therefore, underestimate myocardial fibrosis when non-enhanced myocardium is erroneously displayed as normal [37]. This means that LGE lacks in its ability to depict the continuous fibrotic spectrum and to quantify diffuse fibrosis, and we cannot be

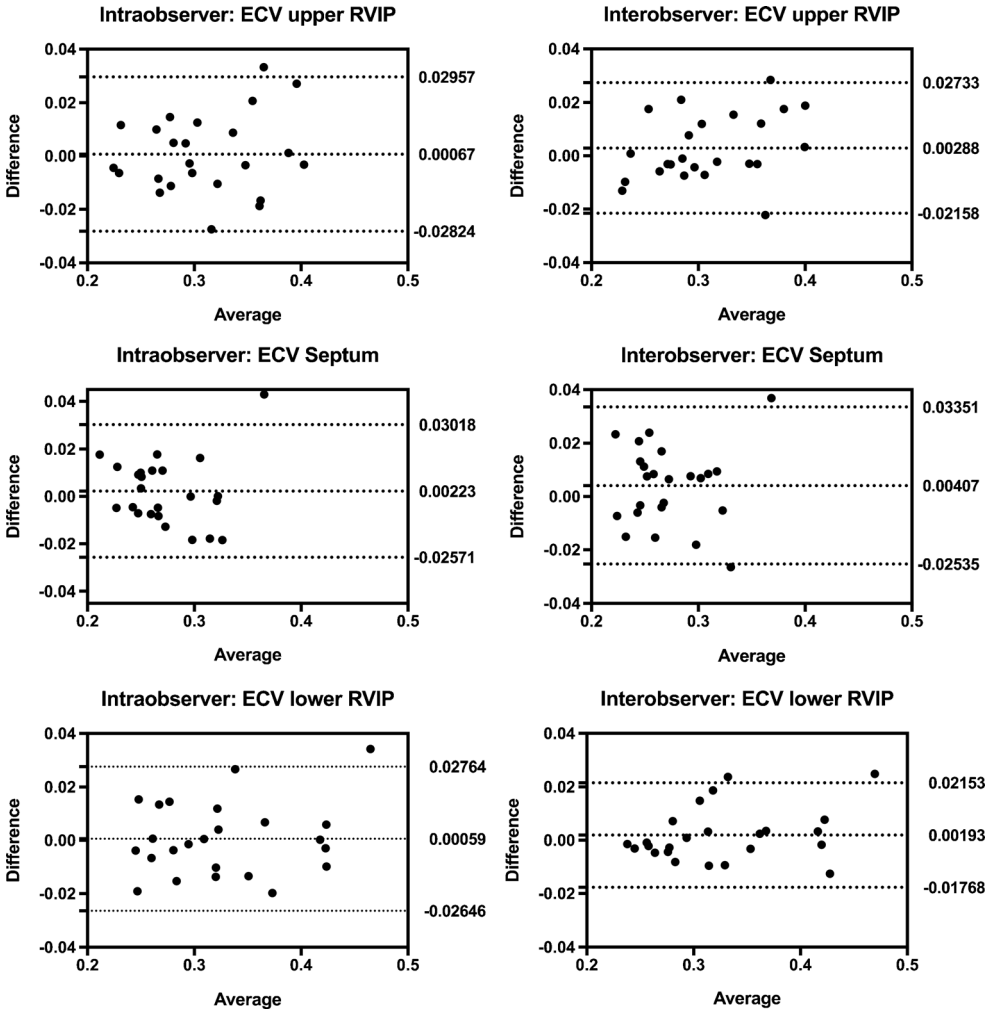

Fig. 5 Bland-Altman plots for ECV measurements in different ROIs in CTEPH patients. All plots demonstrate the low spreading width within the performed intra- and interobserver variability measurements. The dotted lines show the upper and lower 95 % limit of agreement and the mean standard bias. The corresponding values are presented at the right Y-axis

certain about visualized fibrosis extension and degree. Actually, no validated LGE thresholds for a recommended dichotomization of fibrotic and non-fibrotic myocardium exists, and also seem not success-promising in the view of the continuous character of fibrosis.

In contrast to LGE imaging parametric imaging methods, like native T1 and ECV, enable characterization and visualization of fundamental myocardial disease processes caused by alterations of tissue composition and structure on a pixelwise basis. Whereas native T1 measures characteristics relate to the whole myocardium, ECV exploits the extracellular nature of contrast material to measure the non-cellular space occupied mostly by extracellular matrix in the interstitium with inclusion of myocardial vasculature [36]. As previous studies showed native T1 times

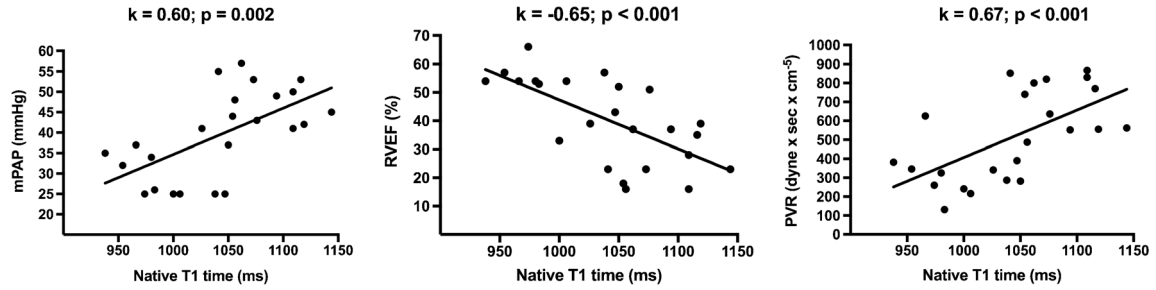

Fig. 6 Correlation between area-adjusted native T1 values and mPAP, RV EF, and PVR in CTEPH patients. The area-adjusted native T1 times were significantly related to mPAP, RVEF, and PVR

Table 8 Septal area-adjusted native T1 value thresholds in CTEPH patients and correlation with RV ejection fraction and PA pressure

T1 Values	RV EF %	PA Pressure mmHg
>975 ms	35.6	40.1
>1000 ms	34.7	42.1
>1025 ms	33.2	43.9
>1050 ms	29.4	47.5
>1075 ms	31.5	46.6
>1100 ms	28.2	45.3
Correlation		
k Pearson	-0.92	0.83
p Value	0.01	0.04

Values are mean and absolute values

CTEPH chronic thromboembolic pulmonary hypertension; *RV EF* right ventricular ejection fraction; *PA* pulmonary artery

and ECV measures are elevated in fibrosis [24], but also as a function of cellularity, myocardial disarray, oedema [38], and storage diseases such as amyloid [39], for example. Therefore, ECV expansion as measured in this paper does not necessarily reflect fibrosis. However, in the context of chronic pulmonary hypertension fibrosis is the most likely candidate for ECV expansion as extracellular oedema is rather linked to acute injury. There were no symptoms or signs in our patients indicating storage diseases. The same holds true for native T1 measures which are strongly influenced by cellular and extracellular water content. Again increased tissue water content is not a feature of chronic right heart disease. In light of these pathophysiological considerations it is plausible to assume that T1 and ECV results of our paper are indeed based on fibrosis.

To our knowledge, this is the first study on native T1 mapping and ECV in patients with CTEPH. An important finding is that the presence of LGE in the septum and RVIP in CTEPH patients was associated with a significant decrease in RV function, and there was also a significant limitation of LV functional parameters with the exception of LV EF. For both native T1 mapping and ECV, highly significant differences were found in the septal myocardium and the upper and lower RVIP in CTEPH patients compared with healthy subjects. Interestingly, even in the absence of LGE, T1 mapping and ECV determination revealed pathological, significantly elevated values in CTEPH patients. In contrast, the T1 measurements of the lateral wall, which were performed for comparison, showed similar results for the two groups. This suggests that the lateral wall is probably not affected by disease-related processes, emphasizing that increased septal T1 values are caused by RV load and not by LV alterations. Moreover, by adopting thresholds for area-adjusted septal native T1 values, a highly significant negative correlation between native T1 mapping values and RV EF and also a good positive correlation between native T1 values and PA pressure were observed.

As mentioned above LGE is only a dichotomous parameter that requires at least 15 % of focal matrix expansion. Conversely, parametric imaging allows the gradual detection of interstitial fibrosis even in the absence of LGE. This fact demonstrates the great potential of parametric imaging over LGE, a potential that might provide insight into fibrotic remodelling processes and yield prognostic information in the future. It would be interesting to see whether reverse remodelling processes with normalization of native T1 and ECV values are present after interventional or surgical therapies such as PEA or BPA, and if these changes are positively correlated with outcome parameters.

A main limitation of our study is that the results are based on a small group of patients. They are in good agreement, however, with the T1 values and ECV results of a recently published porcine model of PH [26]. Furthermore, an increase in native T1 and ECV values is not only and necessarily equivalent to fibrosis. Both values and LGE are also affected by cellularity, disarray, and oedema, for example.

Conclusion

Native septal and RVIP T1 mapping and ECV values in CTEPH patients are significantly increased compared with those in healthy subjects, even in the absence of LGE. Native T1 values correlate well with PA pressure and RV function. Thus, native T1 mapping and ECV assessment enable visualization, characterization, and quantification of septal fibrosis in patients with CTEPH; these parameters may become novel indices for disease severity and serve as a basis for prognosis or be useful as therapy-monitoring tools in the near future. Further assessment in large-scale trials is warranted.

Acknowledgments The scientific guarantor of this publication is Prof. Dr. Gabriele A. Krombach. The authors of this manuscript declare no relationships with any companies, whose products or services may be related to the subject matter of the article. The authors state that this work has not received any funding. One of the authors has significant statistical expertise. Institutional Review Board approval was obtained. Written informed consent was obtained from all subjects (patients) in this study. Methodology: prospective, diagnostic or prognostic study, performed at one institution.

References

1. Hoeper MM, Bogaard HJ, Condliffe R, Frantz R, Khanna D, Kurzyna M et al (2013) Definitions and diagnosis of pulmonary hypertension. J Am Coll Cardiol 62:42–50
2. Simonneau G, Gatzoulis MA, Adatia I, Celermajer D, Denton C, Ghofrani A et al (2013) Updated clinical classification of pulmonary hypertension. J Am Coll Cardiol 62:34–41
3. Pepke-Zaba J, Delcroix M, Lang I, Mayer E, Jansa P, Ambroz D et al (2011) Chronic thromboembolic pulmonary hypertension (CTEPH). Results from an international prospective registry. Circulation 124:1973–1981
4. Becattini C, Agnelli G, Pesavento R, Silingardi M, Poggio R, Taliani MR et al (2006) Incidence of chronic thromboembolic pulmonary hypertension after a first episode of pulmonary embolism. Chest 130:172–175
5. Pengo V, Lensing AW, Prins MH, Marchiori A, Davidson BL, Tiozzo F et al (2004) Incidence of chronic thromboembolic pulmonary hypertension after pulmonary embolism. N Engl J Med 350: 2257–2264
6. Klok FA, van Kralingen KW, van Dijk AP, Heyning FH, Vliegen HW, Huisman MV et al (2010) Prospective cardiopulmonary screening program to detect chronic thromboembolic pulmonary hypertension in patients after acute pulmonary embolism. Haematologica 95:970–975
7. Berghaus TM, Barac M, von Scheidt W, Schwaiblmair M (2011) Echocardiographic evaluation for pulmonary hypertension after recurrent pulmonary embolism. Thromb Res 128:e142–e147
8. Simonneau G, Robbins IM, Beghetti M, Channick RN, Delcroix M, Denton CP et al (2009) Updated clinical classification of pulmonary hypertension. J Am Coll Cardiol 54:43–54
9. Mayer E, Jenkins D, Lindner J, D'Armini A, Kloek J, Meyns B et al (2011) Surgical management and outcome of patients with chronic thromboembolic pulmonary hypertension: results from an international prospective registry. J Thorac Cardiovasc Surg 141:702–710
10. Wirth G, Brüggemann K, Bostel T, Mayer E, Düber C, Kreitner KF (2014) Chronic Thromboembolic Pulmonary Hypertension (CTEPH) – Potential Role of Multidetector-Row CT (MD-CT) and MR imaging in the diagnosis and differential diagnosis of the disease. Fortsch Röntgenstr 186:751–761
11. Bradlow WM, Gibbs JS, Mohiaddin RH (2012) Cardiovascular magnetic resonance in pulmonary hypertension. J Cardiovasc Magn Reson 14:6
12. D'Alonzo GE, Barst RJ, Ayres SM, Bergofsky EH, Brundage BH, Detre KM et al (1991) Survival in patients with primary pulmonary hypertension. Results from a national prospective registry. Ann Intern Med 115:343–349
13. Raymond RJ, Hinderliter AL, Willis PW, Ralph D, Caldwell EJ, Williams W et al (2002) Echocardiographic predictors of adverse outcomes in primary pulmonary hypertension. J Am Coll Cardiol 39:1214–1219
14. Walker CM, Chung JH, Reddy GP (2012) Septal Bounce J Thorac Imaging 27:W1
15. Sanz J, Dellegrottaglie S, Kariisa M, Sulica R, Poon M, O'Donnell TP et al (2007) Prevalence and correlates of septal delayed contrast enhancement in patients with pulmonary hypertension. Am J Cardiol 100:731–735
16. McCann GP, Beek AM, Vonk-Noordegraaf A, van Rossum AC (2005) Delayed contrast-enhanced magnetic resonance imaging in pulmonary arterial hypertension. Circulation 112, e268
17. Sato T, Tsujino I, Ohira H, Oyama-Manabe N, Ito YM, Noguchi T et al (2013) Paradoxial interventricular septal motion as a major determinat of late gadolinium enhancement in ventricular insertion points in pulmonary hypertension. PLoS One 8, e66724
18. Swift AJ, Rajaram S, Capener D, Elliot C, Condliffe R, Wild JM et al (2014) LGE patterns in pulmonary hypertension do not impact overall mortality. J Am Coll Cardiol Imaging 7:1209–1217
19. Bradlow WM, Assomull R, Kilner PJ, Gibbs JS, Sheppard MN, Mohiaddin RH (2010) Understanding late gadolinium enhancement in pulmonary hypertension. Circ Cardiovasc Imaging 3: 501–503
20. Kuribayashi T, Roberts WC (1992) Myocardial disarray at junction of ventricular septum and left and right ventricular free walls in hypertrophic cardiomyopathy. Am J Cardiol 70:1333–1340
21. Kellman P, Wilson JR, Xue H, Ugander M, Arai AE (2012) Extracellular volume fraction mapping in the myocardium, part 1: evaluation of an automated method. J Cardiovasc Magn Reson 14: 63
22. Bull S, White SK, Piechnik SK, Flett AS, Ferreira VM, Loudon M et al (2013) Human non-contrast T1 values and correlation with histology in diffuse fibrosis. Heart 99:932–937
23. Lee SP, Lee W, Lee JM, Park EA, Kim HK, Kim YJ et al (2015) Assessment of diffuse myocardial fibrosis by using mr imaging in asymptomatic patients with aortic stenosis. Radiology 274:359–369
24. Dass S, Suttie JJ, Piechnik SK, Ferreira VM, Holloway CJ, Banerjee R et al (2012) Myocardial tissue characterization using magnetic resonance non contrast T1 mapping in hypertrophic and dilated cardiomyopathy. Circ Cardiovasc Imaging 6:726–733
25. Bandula S, White SK, Flett AS, Lawrence D, Pugliese F, Ashworth MT et al (2013) Measurement of myocardial extracellular volume fraction by using equilibrium contrast-enhanced CT: validation against histologic findings. Radiology 269:396–403
26. Garcia-Alvarez A, Garcia-Lunar I, Pereda D, Fernandez-Jimenez R, Sanchez-Gonzalez J, Mirelis JG et al (2015) Association of myocardial T1-mapping CMR with hemodynamics and RV performance in pulmonary hypertension. J Am Coll Cardiol Imaging 8: 76–82
27. Messroghli DR, Radjenovic A, Kozerke S, Higgins DM, Sivananthan MU, Ridgway JP (2004) Modified look-locker inversion recovery (MOLLI) for high resolution T1 mapping of the heart. Magn Reson Med 52:141–146
28. Hinkle DE, Wiersma W, Jurs SG (2003) Applied statistics for the behavioral sciences, 5th edn. Houghton Mifflin, Boston
29. Assomull RG, Prasad SK, Lyne J, Smith G, Burman ED, Khan M et al (2006) Cardiovascular magnetic resonance, fibrosis, and prognosis in dilated cardiomyopathy. J Am Coll Cardiol 48: 1977–1985
30. O'Hanlon R, Grasso A, Roughton M, Moon JC, Clark S, Wage R et al (2010) Prognostic significance of myocardial fibrosis in hypertrophic cardiomyopathy. J Am Coll Cardiol 56:867–874
31. Barone-Rochette G, Pierard S, De Meester de Ravenstein C, Seldrum S, Melchior J, Maes F et al (2014) Prognostic significance of LGE by CMR in aortic stenosis patients undergoing valve replacement. J Am Coll Cardiol 64:144–154
32. Krittayaphong R, Saiviroonporn P, Boonyasirinant T, Udompunturak S (2011) Prevalence and prognosis of myocardial scar in patients with known or suspected coronary artery disease and normal wall motion. J Cardiovasc Magn Reson 13:2
33. Zhu Y, Park EA, Lee W, Kim HK, Chu A, Chung JW et al (2015) Extent of late gadolinium enhancement at right ventricular insertion points in patients with hypertrophic cardiomyopathy: relation with diastolic dysfunction. Eur Radiol 25:1190–1200
34. Moon JC, Reed E, Sheppard MN, Elkington AG, Ho SJ, Burke M et al (2004) The histologic basis of late gadolinium enhancement cardiovascular magnetic resonance in hypertrophic cardiomyopathy. J Am Coll Cardiol 43:2260–2264
35. Kim RJ, Judd RM (2003) Gadolinium-enhanced magnetic resonance imaging in hypertrophic cardiomyopathy: in vivo imaging

of the pathologic substrate for premature cardiac death? J Am Coll Cardiol 41:1568–1572
36. Schelbert EB, Messroghli DR (2016) State of the art: clinical applications of cardiac T1 mapping. Radiology 278:658–676
37. Kellman P, Wilson JR, Xue H, Bandettini WP, Shanbhag SM, Druey KM et al (2012) Extracellular volume fraction mapping in the myocardium, part 2: initial clinical experience. J Cardiovasc Magn Reson 14:64
38. Ferreira VM, Piechnik SK, Dall'Armellina E, Karamitsos TD, Francis JM, Choudhury RP et al (2012) Non contrast T1 mapping detects acute myocardial edema with high diagnostic accuracy: a comparison to T2-weighted cardiovascular magnetic resonance. J Cardiovasc Magn Reson 14:42
39. Karamitsos TD, Pichnik SK, Banypersad SM, Fontana M, Ntusi NB, Ferreira VM et al (2013) Non-contrast T1 mapping for the diagnosis of cardiac amyloidosis. J Am Coll Cardiol Img 6:488–497

European Radiology (2019) 29:1565–1573
https://doi.org/10.1007/s00330-018-5702-x

CARDIAC

Correlation of native T1 mapping with right ventricular function and pulmonary haemodynamics in patients with chronic thromboembolic pulmonary hypertension before and after balloon pulmonary angioplasty

F. C. Roller[1] · S. Kriechbaum[2,3] · A. Breithecker[1] · C. Liebetrau[2,3,5] · M. Haas[2,3] · C. Schneider[1] · A. Rolf[2,3,5] · S. Guth[4] · E. Mayer[4] · C. Hamm[2,3,5] · G. A. Krombach[1] · C. B. Wiedenroth[4]

Received: 13 March 2018 / Revised: 20 July 2018 / Accepted: 31 July 2018 / Published online: 29 August 2018

Abstract

Objectives The aim of this study was to assess native T1 mapping in patients with inoperable chronic thromboembolic pulmonary hypertension (CTEPH) before and 6 months after balloon pulmonary angioplasty (BPA) and compare the results with right heart function and pulmonary haemodynamics.

Methods Magnetic resonance imaging at 1.5 T and right heart catheterisation were performed in 21 consecutive inoperable CTEPH patients before and 6 months after BPA. T1 values were measured within the septal myocardium, the upper and lower right ventricular insertion points, and the lateral wall at the basal short-axis section. In addition, the area-adjusted septal native T1 time (AA-T1) was calculated and compared with right ventricular function (RVEF), mean pulmonary arterial pressure (mPAP) and pulmonary vascular resistance (PVR).

Results The mean AA-T1 value decreased significantly after BPA (1,045.8 ± 44.3 ms to 1,012.5 ± 50.4 ms; $p < 0.001$). Before BPA, native T1 values showed a moderate negative correlation with RVEF ($r = -0.61$; $p = 0.0036$) and moderate positive correlations with mPAP ($r = 0.59$; $p < 0.01$) and PVR ($r = 0.53$; $p < 0.05$); after BPA correlation trends were present ($r = -0.21$, $r = 0.30$ and $r = 0.35$, respectively).

Conclusions Native T1 values in patients with inoperable CTEPH were significantly lower after BPA and showed significant correlations with RVEF and pulmonary haemodynamics before BPA. Native T1 mapping seems to be indicative of reverse myocardial tissue remodelling after BPA and might therefore have good potential for pre-procedural patient selection, non-invasive therapy monitoring and establishing a prognosis.

Key Points

- *BPA is a promising treatment option for patients with inoperable CTEPH*
- *Native septal T1 values significantly decrease after BPA and show good correlations with right ventricular function and haemodynamics before BPA*
- *Prognosis and non-invasive therapy monitoring might be supported in the future by native T1 mapping*

Keywords Magnetic resonance imaging · Pulmonary hypertension · Pulmonary embolism · Angioplasty

✉ F. C. Roller
fritz.c.roller@radiol.med.uni-giessen.de

[1] Department of Diagnostic and Interventional Radiology, Justus-Liebig-University Giessen, Klinikstraße 33, 35392 Giessen, Germany

[2] Department of Cardiology, Kerckhoff Heart and Thorax Centre, Bad Nauheim, Germany

[3] DZHK (German Centre for Cardiovascular Research), Partner site Rhein-Main, Frankfurt am Main Germany

[4] Department of Thoracic Surgery Kerckhoff Heart and Thorax Centre, Bad Nauheim, Germany

[5] Department of Cardiology, Justus-Liebig-University Giessen, Klinikstraße 33, Giessen, Germany

Abbreviations

AA-T1	Area-adjusted native T1 time
BPA	Balloon pulmonary angioplasty
CMR	Cardiac magnetic resonance imaging
CTEPH	Chronic thromboembolic pulmonary hypertension
EDD	End-diastolic diameter
EDV	End-diastolic volume
EF	Ejection fraction
ESD	End-systolic diameter
ESV	End-systolic volume
LV	Left ventricle
mPAP	Mean pulmonary arterial pressure
PA	Pulmonary artery
PEA	Pulmonary endarterectomy
PH	Pulmonary hypertension
PVR	Pulmonary vascular resistance
RVEF	Right ventricular function
RVIP	Right ventricular insertion point
RV	Right ventricle
SV	Stroke volume

Introduction

Pulmonary hypertension (PH) is defined as elevation of the mean pulmonary artery (PA) pressure (mPAP) beyond 25 mmHg [1]. Different aetiologies of PH are known and have been categorised according to the Nice classification [2]. Thus, chronic thromboembolic pulmonary hypertension (CTEPH) is defined as PH with persistent perfusion defects after a single or recurrent pulmonary embolism [3]. It is a rare but underdiagnosed disease with an estimated incidence between 0.5% and 3.8% after acute pulmonary embolism and 10% after recurring embolism [4–7]. The persistence of thrombotic material leads to fibrotic obstruction of pulmonary arteries that is compounded by secondary inflammation, cell proliferation and vascular remodelling [8–10]. As a result, elevated mPAP and pulmonary vascular resistance (PVR) ensue, which lead to long-term impairment of right heart function accompanied by poor prognosis and high mortality [11, 12].

CTEPH is potentially curable by surgical pulmonary endarterectomy (PEA) [13–15]. PEA surgery leads to normalisation of pulmonary haemodynamics in most patients [16], and the long-term survival rate is excellent [14]. However, up to one-third of all CTEPH patients are not amenable to surgery, mostly due to the presence of peripherally located lesions [3]. For these patients, targeted medical treatment with riociguat, a stimulator of soluble guanylate cyclase which improves not only pulmonary haemodynamics but also physical capacity of CTEPH patients [17–19], is recommended [8], and balloon pulmonary angioplasty (BPA), an emerging interventional treatment option [8, 20, 21], should also be considered.

Non-invasive assessment with cardiac magnetic resonance imaging (CMR) is widely used to assess RV structure, function and morphology. For example, CMR was used by Kreitner et al [22] and Rolf et al [23] to investigate effects of PEA in CTEPH patients and Van Wolferen et al [24] likewise investigated effects of medical treatment on biventricular heart function in patients with idiopathic PH. Recently, Sato et al [25] and Yamasaki et al [26] investigated effects of BPA in patients with inoperable CTEPH via CMR and showed improvements in biventricular function, pulmonary flow and interventricular dys-synchrony.

Native cardiac T1 mapping provides useful diagnostic information in many cardiac diseases [27–30], permitting parametric tissue characterisation without the need for contrast agents. Initial results in patients with different causes of PH are promising and have shown good correlations with right ventricular function and pulmonary haemodynamics [31–33]. Furthermore, the results of a recent study by Garcia-Alvarez et al [34] in an experimental animal model suggest that native T1 mapping might be suitable as a non-invasive method to assess fibrosis of the upper and lower right ventricular insertion point (RVIP) in chronic PH, as T1 times increase with the degree of fibrosis (myocardial collagen content). In order to determine the potential of native T1 mapping as an imaging biomarker, the aims of our study were to assess native T1 values in patients with inoperable CTEPH before and 6 months after BPA and to examine how well they correlate with right heart function and pulmonary haemodynamics.

Methods

Patient population

A total of 21 consecutive CTEPH patients (12 women) with a mean age of 63.4 ± 10.6 years (± standard deviation [SD]) and a mPAP of 40.9 ± 12.6 mmHg were enrolled in this prospective cohort study from January 2014 to February 2015. The primary diagnosis of CTEPH was based on ventilation-perfusion scintigraphy, right heart catheterisation and biplanar pulmonary angiography. Pre- and post-procedural management of these patients has been recently published [17, 35, 36]. In brief, all patients were assessed by CMR and right heart catheterisation (RHC) as part of their pre-and post-interventional routine workup (assessment of RV function and pulmonary arteries).

Contraindications for CMR and exclusion criteria in all patients were renal failure (glomerular filtration rate below 30 ml/min/1.73 m^2), incompatible cochlear or metallic implants, known gadolinium intolerance, claustrophobia, or the inability to lie supine for the duration of the protocol due to dyspnoea.

All patients gave written informed consent, and the local ethics committee approved the study.

CMR imaging

Imaging was performed with a 1.5-T scanner system (Avanto; Siemens Healthineers, Erlangen, Germany; gradient strength and slew rate: SQ-Engine [45 mT/m at 200 T/m/s]) using a six-element phased array cardiac coil and a dedicated CMR protocol containing axial, coronal, and sagittal thoracic survey images, steady-state-free precession sequences (SSFP) CINE in two-chamber view (CV), three-CV, four-CV and stacked transaxial and short-axis (SA) from base to apex, black-blood (T2 turbo spin echo [TSE]), native T1 mapping and late gadolinium enhancement (LGE) (T1 gradient echo [GE] with inversion recovery) imaging. Gadobenate dimeglumine (Gd-BOPTA; Bracco Imaging, Milan, Italy) was injected at a dose of 0.15 mmol/kg. LGE imaging was performed 12 min after contrast media injection. SSFP imaging parameters were: slice thickness 8 mm; field of view: 300 × 400 mm; matrix 256 × 154; TR 59.62 and TE 1.15. LGE imaging parameters were: slice thickness 8 mm; field of view: 293 × 360 mm; matrix: 256 × 156; TR 843.2 and TE 3.19. Black-blood T2 images were not used for analysis.

The SSFP images were obtained during breath-hold, and the LV and RV systolic and diastolic volumes (absolute values) were calculated from short-axis and transaxial CINE images. Measurements were performed on end-diastolic images (first phase after the R-wave trigger) and end-systolic images (cine with the visually smallest cavity area). Endocardial contours of the LV and RV were obtained by manual tracing with exclusion of papillary muscles and trabeculae from the cavity. Ventricular volumes were estimated using the Simpson rule. The ejection fraction (EF) was calculated as [end-diastolic volume (EDV) – end-systolic volume (ESV)]/EDV**,** end-systolic diameter (ESD), and end-diastolic diameter (EDD) measurements were made using basal short-axis images. The post-processing was performed with the ARGUS software package (Siemens Syngo MMWP Version VE40A; Siemens Healthineers).

T1 mapping images were acquired at basal, mid-ventricular, and apical short-axis sections by using an optimised modified Look-Locker inversion-recovery (MOLLI) sequence, with three images in the first two Look-Locker segments and five images for the third inversion (known as the "3-3-5" standard protocol) [37]. Finally, 11 images were acquired during 17 heartbeats, and in-line motion correction and map generation were performed. Imaging parameters were [32]: slice thickness, 8 mm; spatial resolution, 2.2 mm × 1.8 mm × 8 mm; 6/8 partial Fourier acquisition; field of view, 240 × 340 mm; matrix, 192 × 124; flip angle, 35°; TR, 740; TE, 1.06; TI, 100 ms; TI increment, 80 ms; trigger delay, 300 ms; inversions, 3; acquisition heartbeats, 3, 3, 5; scan time, 17 heartbeats.

Qualitative and quantitative image assessment

All original images were assessed for artefacts due to susceptibility, cardiac, diaphragmatic or respiratory motion. Each motion-corrected series was evaluated for correct image alignment, and each map was carefully checked for signal loss due to misalignment and motion [32].

Image assessment and measurement of native T1

After image acquisition T1 maps were generated after in-line motion correction from the MR workstation [38]. T1 times were measured for myocardium at the basal short-axis section before and after BPA. Basal short-axis slices were chosen to facilitate proper T1 measurements caused by a greater septal myocardial diameter compared to midventricular and apical slices. Thus, a total of four regions of interest (ROIs) were drawn manually at the following locations: septum, upper and lower RVIP, and the lateral wall. ROIs were drawn carefully to exclude the myocardial borders, avoiding partial volume-averaging artefacts and registration errors with gradual T1 value changes that are present at the borders. In addition to the T1 values, the size of the ROIs was also compared and evaluated before and after BPA for each patient to exclude size-dependent differences. Moreover, a total area-adjusted septal native T1 value (AA-T1) was calculated that consisted of the mean T1 values and areas measured for the septum and the RVIPs [32]. The measured T1 values of the septum, the upper and lower RVIP were therefore added up to a sum and divided by the sum of the corresponding ROI areas. All measurements were performed by two experienced radiologists independently (G.K., 20 years of experience, and F.R., 7 years of experience), who were blinded to patient demographics, and LGE assessment was performed blinded to T1 maps and CINE images and vice versa. All studies were used for assessment of inter- and intra-rater variability.

Right heart catheterisation

RHC was performed as a part of the diagnostic workup [8]. RHC was repeated 6 months after the final BPA procedure in all patients. RHC was performed routinely via the right internal jugular vein using a 6-F sheath and a standard Swan-Ganz catheter. The medication of the patients was not modified prior to or during RHC.

Balloon pulmonary angioplasty

As described before [20], BPA was performed as staged procedure under smooth sedation using femoral or jugular access.

Table 1 Demographic data for CTEPH patients before and after BPA

	Pre-BPA	Post-BPA	*p* value
Patients (*n*)	21	21	
Age (years)	58.8 ± 12.2		
Sex (male:female)	9:12		
BSA (m^2)	1.8 ± 0.2		
mPAP (mmHg)	40.9 ± 12.6	34.4 ± 15.4	0.0016
PVR (dyn × s/cm^5)	538.2 ± 246.3	402.6 ± 190.5	0.0001
PCWP (mmHg)	10.3 ± 3.5	9.2 ± 2.6	
CO (l/m)	4.6 ± 1.3	5.0 ± 1.1	0.1649
Treated pulmonary segments (*n*)		10.0 ± 3.2	

Values are mean ± SD or absolute values

BPA balloon pulmonary angioplasty, *BSA* body surface area, *CO* cardiac output, *CTEPH* chronic thromboembolic pulmonary hypertension, *mPAP* mean pulmonary artery pressure, *PCWP* pulmonary capillary wedge pressure, *PVR* pulmonary vascular resistance, *SD* standard deviation

A 6-F sheath (Vista britetip; Cordis, Johnson & Johnson, New Brunswick, NJ, USA) was placed in the pulmonary artery, and a 6-F guiding catheter (in most cases multi-purpose; Medtronic, Minneapolis, MN, USA) was inserted into the pulmonary artery to intubate the target segmental arteries. During the procedure, patients received heparin intravenously to maintain an activated clotting time >250 s. The guide wire (Runthrough NS-PTCA Guide Wire; Terumo, Tokyo, Japan) was placed into the subsegmental arterial branches, passing the obstructing endoluminal material. Subsequently, the subsegmental branches were dilated by multiple inflations of semi-compliant balloons (Emerge™ 2.0/20 mm and 4.0/20 mm; Boston Scientific, Voisins-le-Bretonneux, France). Final fluoroscopy imaging documented the post-procedural morphological results. Expected results were improvement of parenchymal perfusion as well as a quick venous return, which were used to indicate successful intervention. Signs of successful interventions were seen in most patients.

Statistical analysis

Statistical analysis was performed using SPSS statistical software version 20 (SPSS, IBM, Armonk, New York, USA). Patient characteristics were described by mean ± standard deviation (SD). All data were tested for normal distribution using the Shapiro-Wilk test. In cases of normal distribution Student's *t*-test was used, and if the data were not distributed normally the Wilcoxon signed rank test (non-parametric) was used. Intra- and inter-observer variability was tested with simple linear regression analysis. Linear regression analysis was also used for assessing the correlation of native T1 and functional parameters. The correlation coefficient k was interpreted according to Hinkle et al [39], where $r > 0.5$ would be considered a moderate correlation, $r > 0.7$ a strong correlation, and $r > 0.9$ very strong correlation. An $r > 0.5$ would therefore be considered to have clinical impact. Strengths of correlations were tested using the Pearson correlation coefficient. All results were tested at a 5% level of significance and we accepted an alpha error of less than 0.05 as statistically significant.

Results

Table 1 presents patient demographics, RHC measurements and the mean number of treated pulmonary segments. A total of 10.0 ± 3.2 pulmonary segments were treated by BPA per

Table 2 Functional analysis before and after BPA (CMR)

n = 21		Pre-BPA	Post-BPA	*p* value
LV function				
	EF (%)	65.4 ± 10.3	66.5 ± 6.2	0.5603
	EDV (ml)	100.4 ± 24.9	115.4 ± 23.1	0.0187
	ESV (ml)	35.0 ± 13.5	39.3 ± 12.7	0.05
	SV (ml)	65.5 ± 18.4	76.1 ± 13.6	0.0295
	EDD (mm)	42.5 ± 5.8	46.6 ± 4.5	0.0002
	ESD (mm)	24.7 + 6.5	27.5 ± 4.3	0.01
RV function				
	EF (%)	38.2 ± 11.7	47.9 ± 7.6	0.001
	EDV (ml)	191.1 ± 66.3	161.6 ± 52.5	0.0093
	ESV (ml)	124.8 ± 50.2	85.5 ± 38.7	0.0003
	SV (ml)	71.0 ± 17.7	75.9 ± 19.4	0.4168
Wall thickness				
	Septal (mm)	7.3 ± 1.0 mm	7.5 ± 0.9 mm	0.548

Values are mean ± SD or absolute values

BPA balloon pulmonary angioplasty, *CMR* cardiac magnetic resonance imaging, *CTEPH* chronic thromboembolic pulmonary hypertension, *EF* ejection fraction, *EDV* end-diastolic volume, *ESV* end-systolic volume, *SV* stroke volume, *EDD* end-diastolic diameter, *ESD* end-systolic diameter, *LV* left ventricular, *RV* right ventricular

Table 3 Native T1 mapping in CTEPH patients before and after BPA

	Pre-BPA (n = 21) ms	Mean ROI size mm^2	Post-BPA (n = 21) ms	Mean ROI size mm^2	p value
Upper RVIP	1,059.0 ± 49.4	44.6	1,012.1 ± 67.4	37.4	0.0004
Lower RVIP	1,087.9 ± 78.2	38.7	1,062.5 ± 78.9	32.0	0.0637
Septum	1,008.3 ± 41.8	113.3	987.9 ± 40.1	106.8	0.0215
AA-T1	1,045.8 ± 44.3	97.3	1,012.5 ± 50.4	109.4	0.0009
Lateral wall	965 ± 44.3	116.5	972 ± 41.7	114.6	0.43

Values are mean ± SD

BPA balloon pulmonary angioplasty, *CTEPH* chronic thromboembolic pulmonary hypertension, *RVIP* right ventricular insertion point, *AA-T1* area-adjusted T1 time, *ROI* region of interest

patient. The mPAP decreased from 40.9 ± 12.6 mmHg before BPA to 34.4 ± 15.4 mmHg after BPA ($p < 0.01$), and PVR decreased from 538.2 ± 246.3 (dyn × s/cm^5) to 402.6 ± 190.5 (dyn × s/cm^5) ($p < 0.001$). Pulmonary capillary wedge pressure and cardiac output were not significantly affected by BPA.

Pre- and post-procedural LV and RV function as determined by CMR are displayed in Table 2. Before and after BPA all patients had normal LV function regarding EF but stroke volume (SV), EDV and ESV were significantly higher after BPA ($p = 0.0187$, $p = 0.05$ and $p = 0.0295$, respectively). Moreover, BPA resulted in significantly higher RV EF ($p = 0.001$) and significantly lower RV EDV and RV ESV ($p = 0.0093$ and 0.0003, respectively). The RV SV was not significantly different. The end-diastolic and end-systolic LV diameters were significantly higher after BPA ($p = 0.0002$ and 0.01, respectively). Seventeen of the 21 patients (81.0%) displayed typical LGE in the RVIPs pre- and post-procedurally with partially triangular extension to the septum.

The pre- and post-procedural T1 mapping values are presented in Table 3. Significant differences were observed for the septum ($p < 0.05$), the upper RVIP ($p < 0.001$) and for the AA-T1 values ($p < 0.001$), whereas the mean T1 values of the lower RVIP ($p > 0.06$) and the lateral wall ($p = 0.43$) were not significantly different. In addition, the ROIs in all areas measured were not significantly different in size, which means that comparable areas within the myocardium were measured before and after BPA. The inter-observer (upper RVIP, $r = 0.919$; lower RVIP, $r = 0.934$; septum, $r = 0.963$; lateral wall, $r = 0.947$; AA-T, $r = 1$ 0.935; all $p < 0.001$) and intra-observer ($r = 0.937$; $r = 0.939$; $r = 0.976$; $r = 0.939$; $r = 0.956$; all $p < 0.001$) variability for native T1 was very low in all areas.

Figure 1 shows the pre- and post-procedural native T1 maps and corresponding LGE images in a patient who was successfully treated by BPA and demonstrated improved right ventricular function and pulmonary haemodynamics. The T1 measurements were performed within ROIs (white borders) in the native T1 maps pre- and post-BPA and revealed significant decreases for the upper RVIP (1,090 ms to 1,043 ms), for the lower RVIP (1,063 ms to 1,023 ms), for the septum (1,022 ms to 1,005 ms), and for the lateral wall (997 ms to 982 ms). Correlations of native T1 mapping with RV function (RVEF) and pulmonary haemodynamics (mPAP and PVR) are given in Table 4 and corresponding scatter plots are presented in Fig. 2. Before BPA there were moderate significant positive correlations between native T1 values and mPAP ($r = 0.59$; $p < 0.01$) or PVR ($r = 0.53$; $p < 0.05$) and a moderate negative correlation between native T1 values and RVEF ($r =$

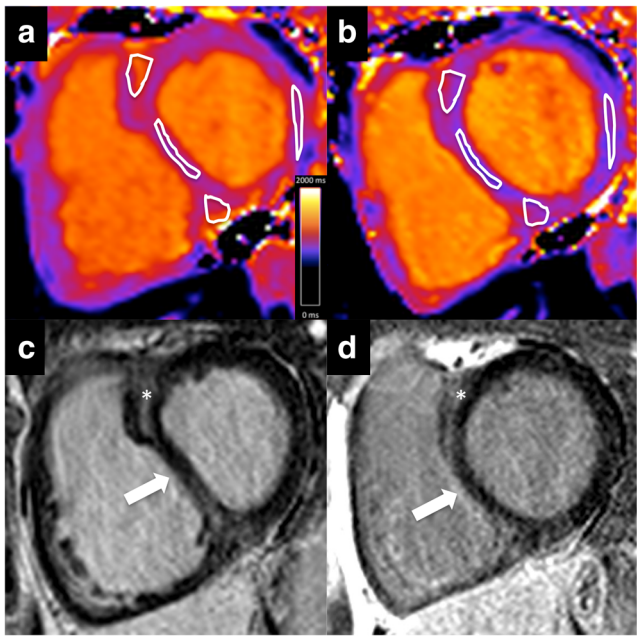

Fig. 1 Native T1 maps and LGE images at basal short axis section in a CTEPH patient pre-and post-BPA. Native T1 maps pre-BPA (**a**) and post-BPA (**b**) and corresponding LGE images pre-BPA (**c**) and post-BPA (**d**) in a 55-year-old man with CTEPH at the basal short-axis level. Pre-procedurally the patient had a mPAP of 51 mmHg at rest and an RVEF of 23.3%. Post-procedurally, mPAP decreased to 35 mmHg and RVEF increased to 45.4%. The patient had a PH-typical LGE pattern in the upper and lower RVIP (*white asterisk*), but the inversed septum receded after BPA (*white arrow*). Consequently, the left and right heart chamber sizes normalised

Table 4 Parameter correlations

	r	CI 95%	*p* value
RVEF to AA-T1			
Pre-BPA	-0.6064	-0.8227 to -0.2367	0.0036
Post-BPA	-0.2105	-0.5887 to 0.2433	0.3596
AA-T1 to mPAP			
Pre-BPA	0.5854	0.2057 to 0.8119	0.0053
Post-BPA	0.3013	-0.1499 to 0.6486	0.1844
AA-T1 to PVR			
Pre-BPA	0.5327	0.1311 to 0.7841	0.0129
Post-BPA	0.3545	-0.0911 to 0.6818	0.1149

Values are mean ± SD or absolute values

BPA balloon pulmonary angioplasty, *mPAP* mean pulmonary artery pressure, *PVR* pulmonary vascular resistance, *RVEF* right ventricular ejection fraction, *SD* standard deviation, *AA-T1* area-adjusted T1 time

-0.61; $r < 0.01$). Six months after BPA these correlations were no longer significant, but a trend towards positive and negative correlation levels still existing ($r = -0.21$, $r = 0.30$ and $r = 0.35$, respectively).

Discussion

To the best of our knowledge, this is the first study to determine the effects of BPA in inoperable CTEPH patients on native T1 time and to correlate the results with RV function and pulmonary haemodynamics. The changes in native T1 times and the moderate correlations with RV function (RVEF) and haemodynamics (mPAP and PVR) in our study are in line with results of previous investigations [31–33]. The increase in RVEF and the decrease in mPAP and PVR were accompanied by significantly decreased T1 times of

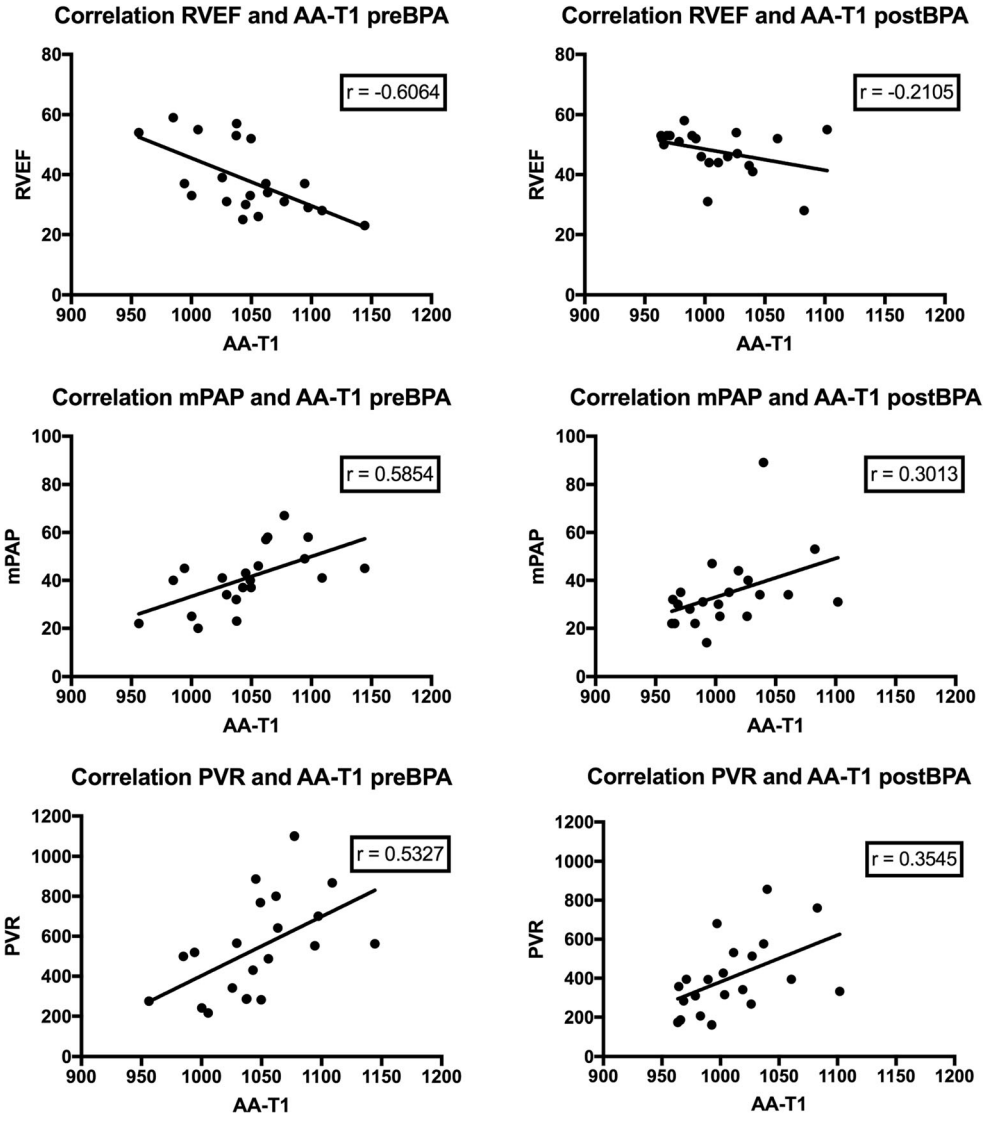

Fig. 2 Scatter plots showing the correlations of AA-T1 to RVEF, mPAP and PVR before and after BPA

the septum, suggesting reverse remodelling of the RV. Septal myocardial remodelling might be explained or rather triggered by possible mechanisms including traction, compression and shear forces due to the RV overload, deterioration and dyskinesia. Normal T1 values could be observed for the RV lateral wall, which therefore might not to be affected [32]. Interestingly, the post-procedural native septal T1 times still correlated weakly with RV function and haemodynamics.

Up to one-third of all CTEPH patients are not eligible for PEA due to the presence of peripherally located lesions [3]. BPA is considered an emerging interventional treatment option for these patients [20, 21, 40]. Non-invasive CMR is useful in PH to assess RV structure, function and morphology. In MRI follow-up studies with CTEPH patients undergoing PEA and BPA, promising results showing enhanced biventricular function and pulmonary flow [25] and improved interventricular dys-synchrony [26] have been reported.

Although improvements in right ventricular function and haemodynamics are well documented for PEA and BPA, little is known about therapy-related cardiac tissue remodelling. LGE in the RVIPs and the septum, which is frequently present in patients with PH [41, 42], is associated with worse outcome in several cardiac diseases [43–46]. However, LGE is only a dichotomous parameter that requires at least 15% of focal matrix expansion to display a myocardial scar [47]; therefore, LGE is limited for characterisation of diffuse tissue alterations, which makes it unsuitable for assessment of treatment effects in diffusely diseased right ventricles. In contrast, mapping techniques (parametric imaging) are increasingly being used within CMR protocols with promising results due to their ability to characterise and to quantify myocardial tissue on a pixel-by-pixel basis.

Native T1 mapping enables characterisation (with characteristics related to the whole myocardium) and visualisation of fundamental myocardial disease processes caused by alterations of tissue composition and structure without the need for contrast agent. Initial results in patients with pre-capillary PH or CTEPH showed good correlations between native T1 mapping and RV function and haemodynamics [31–33]. Since follow-up studies are still lacking, we asked whether the effects of treatment might be assessable via native T1 mapping at the tissue level.

The main limitation of the study is the relatively small number of patients. However, our pre-procedural native T1 mapping results and pre- and post-procedural functional and haemodynamic results are in good agreement with previously published studies [31–33], and experienced cardiac radiologists performed all measurements. Measurement and analysis of post-contrast T1 times and extracellular volume calculation might have provided additional information on the underlying nature of tissue alterations.

Conclusions

Our results suggest two primary conclusions: (1) native T1 measurements of the septal wall reflect tissue alterations that are associated with PH, especially against the background that native T1 values significantly decrease and haemodynamics return to almost normal after successful BPA; (2) BPA not only improves pulmonary arterial haemodynamics but also causes reverse remodelling of the right ventricular myocardium, which is paralleled by improved RV function. These assumptions are based on previous findings that T1 times reflect the myocardial collagen content and hence the degree of fibrosis [34]. Therefore, native T1 mapping holds promise to distinguish patients who will develop reverse remodelling after BPA and those who will not. Further research employing large-scale trials is needed to corroborate these findings.

Acknowledgements We are grateful to Elizabeth Martinson, PhD, from the KHFI Editorial Office for her editorial assistance.

Funding The authors state that this work has not received any funding.

Compliance with ethical standards

Guarantor The scientific guarantor of this publication is Prof. Dr. Gabriele A. Krombach.

Conflict of interest The authors of this manuscript declare no relationships with any companies, whose products or services may be related to the subject matter of the article.

Statistics and biometry One of the authors has significant statistical expertise.

Informed consent Written informed consent was obtained from all subjects (patients) in this study.

Ethical approval Institutional review board approval was obtained.

Methodology
- prospective
- prognostic study/observational/experimental
- performed at one institution

References

1. Hoeper MM, Bogaard HJ, Condliffe R et al (2013) Definitions and diagnosis of pulmonary hypertension. J Am Coll Cardiol 62:42–50
2. Simonneau G, Gatzoulis MA, Adatia I et al (2013) Updated Clinical Classification of Pulmonary Hypertension. J Am Coll Cardiol 62:34–41
3. Pepke-Zaba J, Delcroix M, Lang I et al (2011) Chronic thromboembolic pulmonary hypertension (CTEPH). Results from an international prospective registry. Circulation 124:1973–1981
4. Becattini C, Agnelli G, Pesavento R et al (2006) Incidence of chronic thromboembolic pulmonary hypertension after a first episode of pulmonary embolism. Chest 130:172–175

5. Pengo V, Lensing AW, Prins MH et al (2004) Incidence of chronic thromboembolic pulmonary hypertension after pulmonary embolism. N Engl J Med 350:2257–2264
6. Klok FA, van Kralingen KW, van Dijk AP, Heyning FH, Vliegen HW, Huisman MV (2010) Prospective cardiopulmonary screening program to detect chronic thromboembolic pulmonary hypertension in patients after acute pulmonary embolism. Haematologica 95:970–975
7. Berghaus TM, Barac M, von Scheidt W, Schwaiblmair M (2011) Echocardiographic evaluation for pulmonary hypertension after recurrent pulmonary embolism. Thromb Res 128:e142–e147
8. Galiè N, Humbert M, Vachiery JL et al (2016) 2015 ESC/ERS Guidelines for the diagnosis and treatment of pulmonary hypertension: The Joint Task Force for the Diagnosis and Treatment of Pulmonary Hypertension of the European Society of Cardiology (ESC) and the European Respiratory Society (ERS): Endorsed by: Association for European Paediatric and Congenital Cardiology (AEPC), International Society for Heart and Lung Transplantation (ISHLT). Eur Heart J 37:67–119
9. Lang IM, Pesavento R, Bonderman D, Yuan JX (2013) Risk factors and basic mechanisms of chronic thromboembolic pulmonary hypertension: a current understanding. Eur Respir J 41:462–468
10. Matthews DT, Hemnes AR (2016) Current concepts in the pathogenesis of chronic thromboembolic pulmonary hypertension. Pulm Circ 6:145–154
11. Riedel M, Stanek V, Widimsky J, Prerovsky I (1982) Longterm follow-up of patients with pulmonary thromboembolism: late prognosis and evolution of hemodynamic and respiratory data. Chest 81:151–158
12. Lewczuk J, Piszko P, Jagas J et al (2001) Prognostic factors in medically treated patients with chronic pulmonary embolism. Chest 119:818–823
13. Simonneau G, Robbins IM, Beghetti M et al (2009) Updated clinical classification of pulmonary hypertension. J Am Coll Cardiol 54:43–54
14. Mayer E, Jenkins D, Lindner J et al (2011) Surgical management and outcome of patients with chronic thromboembolic pulmonary hypertension: results from an international prospective registry. J Thorac Cardiovasc Surg 141:702–710
15. Lankeit M, Krieg V, Hobohm L et al (2017) Pulmonary endarterectomy in chronic thromboembolic pulmonary hypertension. J Heart Lung Transplant. https://doi.org/10.1016/j.healun.2017.06.011
16. Wirth G, Brüggemann K, Bostel T, Mayer E, Düber C, Kreitner KF (2014) Chronic thromboembolic pulmonary hypertension (CTEPH)—potential role of multidetector-row CT (MD-CT) and MR imaging in the diagnosis and differential diagnosis of the disease. Rofo 186:751–761
17. Ghofrani HA, D'Armini AM, Grimminger F et al (2013) CHEST-1 Study Group. Riociguat for the treatment of chronic thromboembolic pulmonary hypertension. N Engl J Med 369:319–329
18. Simonneau G, D'Armini AM, Ghofrani HA et al (2015) Riociguat for the treatment of chronic thromboembolic pulmonary hypertension: a long-term extension study (CHEST-2). Eur Respir J 45:1293–1302
19. Simonneau G, D'Armini AM, Ghofrani HA et al (2016) Predictors of long-term outcomes in patients treated with riociguat for chronic thromboembolic pulmonary hypertension: data from the CHEST-2 open-label, randomised, long-term extension trial. Lancet Respir Med 4:372–380
20. Olsson KM, Wiedenroth CB, Kamp JC et al (2017) Balloon pulmonary angioplasty for inoperable patients with chronic thromboembolic pulmonary hypertension: the initial German experience. Eur Resp J 49:6
21. Muller DW, Liebetrau C (2016) Percutaneous treatment of chronic thromboembolic pulmonary hypertension (CTEPH). EuroIntervention 12:X35–X43
22. Kreitner KF, Ley S, Kauczor HU et al (2004) Chronic thromboembolic pulmonary hypertension: Pre- and postoperative assessment with breath-hold MR imaging techniques. Radiology 232:535–554
23. Rolf A, Rixe J, Kim WK et al (2014) Right ventricular adaptation to pulmonary pressure load in patients with chronic thromboembolic pulmonary hypertension before and after successful pulmonary endarterectomy–a cardiovascular magnetic resonance study. J Cardiovasc Magn Reson 16:96
24. van Wolferen SA, Marcus JT, Boonstra A et al (2007) Prognostic value of right ventricular mass, volume, and function in idiopathic pulmonary arterial hypertension. Eur Heart J 28:1250–1257
25. Sato H, Ota H, Sugimura K et al (2016) Balloon pulmonary angioplasty improves biventricular functions and pulmonary flow in chronic thromboembolic pulmonary hypertension. Circ J 80:1470–1477
26. Yamasaki Y, Nagao M, Abe K et al (2017) Balloon pulmonary angioplasty improves interventricular dyssynchrony in patients with inoperable chronic thromboembolic pulmonary hypertension: a cardiac MR imaging study. Int J Cardiovasc Imaging 33:229–239
27. Bull S, White SK, Piechnik SK et al (2013) Human non-contrast T1 values and correlation with histology in diffuse fibrosis. Heart 99:932–937
28. Lee SP, Lee W, Lee JM et al (2015) Assessment of diffuse myocardial fibrosis by using MR imaging in asymptomatic patients with aortic stenosis. Radiology 274:359–369
29. Dass S, Suttie JJ, Piechnik SK et al (2012) Myocardial tissue characterization using magnetic resonance non contrast T1 mapping in hypertrophic and dilated cardiomyopathy. Circ Cardiovasc Imaging 6:726–733
30. Bandula S, White SK, Flett AS et al (2013) Measurement of myocardial extracellular volume fraction by using equilibrium contrast-enhanced CT: validation against histologic findings. Radiology 269:396–403
31. Reiter U, Reiter G, Kovacs G et al (2017) Native myocardial T1 mapping in pulmonary hypertension: correlations with cardiac function and hemodynamics. Eur Radiol 27:157–166
32. Roller FC, Wiedenroth C, Breithecker A et al (2017) Native T1 mapping and extracellular volume fraction measurement for assessment of right ventricular insertion point and septal fibrosis in chronic thromboembolic pulmonary hypertension. Eur Radiol 27:1980–1991
33. Spruijt OA, Vissers L, Boogard HJ, Hofmann MB, Vonk-Noordegraaf A, Marcus JT (2016) Increased native T1-values at the interventricular insertion regions in precapillary pulmonary hypertension. Int J Cardiovasc Imaging 32:451–459
34. García-Álvarez A, García-Lunar I, Pereda D et al (2015) Association of myocardial T1-mapping CMR with hemodynamics and RV performance in pulmonary hypertension. JACC Cardiovasc Imaging 8:76–82
35. Kriechbaum SD, Wiedenroth CB, Wolter JS et al (2017) N-terminal pro-B-type natriuretic peptide for monitoring after balloon pulmonary angioplasty for chronic thromboembolic pulmonary hypertension. J Heart Lung Transplant. https://doi.org/10.1016/j.healun.2017.12.006
36. Wiedenroth CB, Olsson KM, Guth S et al (2017) Balloon pulmonary angioplasty for inoperable patients with chronic thromboembolic disease. Pulm Circ. https://doi.org/10.1177/2045893217753122
37. Roller FC, Harth S, Schneider C, Krombach GA (2015) T1, T2 mapping and extracellular volume fraction (ECV): application, value and further perspectives in myocardial inflammation and cardiomyopathies. Rofo 187:760–770
38. Kellman P, Wilson JR, Xue H, Ugander M, Arai AE (2012) Extracellular volume fraction mapping inthe myocardium, part 1: evaluation of an automated method. J Cardiovasc Magn Reson 14:63

39. Hinkle DE, Wiersma W, Jurs SG (2003) Applied statistics for the behavioral sciences, 5th edn. Houghton Mifflin, Boston
40. Aoki T, Sugimura K, Tatebe S et al (2017) Comprehensive evaluation of the effectiveness and safety of balloon pulmonary angioplasty for inoperable chronic thrombo-embolic pulmonary hypertension: long-term effects and procedure-related complications. Eur Heart J 38:3152-3159
41. Sanz J, Dellegrottaglie S, Kariisa M et al (2007) Prevalence and correlates of septal delayed contrast enhancement in patients with pulmonary hypertension. Am J Cardiol 100:731–735
42. McCann GP, Beek AM, Vonk-Noordegraaf A, van Rossum AC (2005) Delayed contrast-enhanced magnetic resonance imaging in pulmonary arterial hypertension. Circulation 112:e268
43. Assomull RG, Prasad SK, Lyne J et al (2006) Cardiovascular magnetic resonance, fibrosis, and prognosis in dilated cardiomyopathy. J Am Coll Cardiol 48:1977–1985
44. O'Hanlon R, Grasso A, Roughton M et al (2010) Prognostic significance of myocardial fibrosis in hypertrophic cardiomyopathy. J Am Coll Cardiol 56:867–874
45. Barone-Rochette G, Piérard S, De Meester de Ravenstein C et al (2014) Prognostic significance of LGE by CMR in aortic stenosis patients undergoing valve replacement. J Am Coll Cardiol 64:144–154
46. Krittayaphong R, Saiviroonporn P, Boonyasirinant T, Udompunturak S (2011) Prevalence and prognosis of myocardial scar in patients with known or suspected coronary artery disease and normal wall motion. J Cardiovasc Magn Reson 13:2
47. Moon JC, Reed E, Sheppard MN et al (2004) The histologic basis of late gadolinium enhancement cardiovascular magnetic resonance in hypertrophic cardiomyopathy. J Am Coll Cardiol 43:2260–2264

Journal of
Clinical Medicine

MDPI

Article

Value of Left Ventricular Feature Tracking Strain Analysis for Detection of Early Cardiac Involvement in Fabry Disease (FD)

Fritz Christian Roller [1,*], Alexander Brose [1], Martin Richter [1], Armin Schüssler [1], Sebastian Harth [1], Christian Tanislav [2] and Gabriele Anja Krombach [1]

[1] Department of Diagnostic and Interventional Radiology, University Hospital Giessen, Justus-Liebig-University Giessen, Klinikstraße 33, 35392 Giessen, Germany; alexander.brose@radiol.med.uni-giessen.de (A.B.); martin.richter@radiol.med.uni-giessen.de (M.R.); armin.schuessler@radiol.med.uni-giessen.de (A.S.); sebastian.harth@radiol.med.uni-giessen.de (S.H.); gabriele.krombach@uniklinikum-giessen.de (G.A.K.)
[2] Department of Neurology, University Hospital Giessen, Justus-Liebig-University Giessen, Klinikstraße 33, 35392 Giessen, Germany; christian.tanislav@diakonie-sw.de
* Correspondence: fritz.c.roller@radiol.med.uni-giessen.de

Abstract: Purpose: Detection of cardiac involvement in Fabry disease (FD) is of high importance for treatment management. Native T1 mapping especially showed great potential for detection of early cardiac manifestations. Echocardiographic studies showed strain abnormalities in FD patients, but data on MRI feature tracking strain analysis (FT-SA) is limited. Therefore, the aim of our study was to evaluate the potential of FT-SA compared to native T1 and the FD specific biomarker Globotriaosylsphingosine (LysoGb3). Methods: 28 consecutive FD patients (18 female; 47.8 years ± 17.4 standard deviation (SD)) and 28 control subjects (18 female; 46.6 years ± 18.2 SD) underwent cardiac MRI at 1.5 Tesla. Global native T1 times and left ventricular FT-SA were evaluated. Results were correlated to serum Lyso-Gb3-levels. Results: Native T1 times, global longitudinal (GLS) and global radial strain (GRS) were significantly reduced in FD patients ($p < 0.0064$, $p = 0.0009$ and $p = 0.0184$, respectively). Moreover, native T1 times and GLS were significantly lower in Lyso-Gb3 positive FD patients ($p < 0.005$ and $p = 0.03$). GLS, native T1 times showed significant moderate correlations to LysoGb3 ($p = 0.002$ and $p < 0.001$). Furthermore, GLS and native T1 times reduce when LysoGb3 was elevated and increasingly with presence of left ventricular hypertrophy (LVH) or late gadolinium enhancement (LGE). Conclusions: Native T1 times and strain values differ significantly between FD patients and control subjects and showed promising correlations to the FD specific biomarker LysoGb3. We therefore conclude that strain abnormalities occur early beside native T1 reductions in cardiac FD involvement. Large scale trials are needed to verify our findings.

Keywords: Cardiac MRI; Fabry disease; Native T1 mapping; Feature tracking strain

Citation: Roller, F.C.; Brose, A.; Richter, M.; Schüssler, A.; Harth, S.; Tanislav, C.; Krombach, G.A. Value of Left Ventricular Feature Tracking Strain Analysis for Detection of Early Cardiac Involvement in Fabry Disease (FD). *J. Clin. Med.* **2021**, *10*, 3734. https://doi.org/10.3390/jcm10163734

Academic Editor: Maciej Banach

Received: 26 July 2021
Accepted: 19 August 2021
Published: 22 August 2021

1. Introduction

Fabry disease (FD) is an X-linked disorder of lysosomal metabolism. It is characterized by accumulation of glycosphingolipids (more precisely globotriaosylceramide) in many organs (inter alia skin, myocardium and kidneys) due to a deficiency of the enzyme alpha-galactosidase [1]. Classically, male homozygotes are affected and present with burning extremity pain (acroparaesthesia) and progressive multi-organ failure in adolescence [2]. Heterozygous female carriers may present with milder disease forms compared to men [3].

Due to the storage of glycosphingolipids in cardiomyocytes, left ventricular hypertrophy (LVH) is induced, moreover, valves and vascular endothelium are also affected [4]. Later on, cardiac decompensation is triggered by myocardial fibrosis, which is usually more extensive in men than in affected women [1]. Cardiac involvement is a major factor for morbidity and mortality in FD [5].

Cardiac magnetic resonance imaging (CMRI) is well established to verify cardiac involvement. Midmyocardial inferolateral late gadolinium enhancement (LGE) without endocardial affection is a characteristic hallmark beside unspecific cardiac findings such as reduced left ventricular (LV) function and LVH [6]. In genetically confirmed FD, LGE is present in up to 50% of the patients [6]. The presence of LGE is associated with a lack in response to enzyme-replacement therapy (ERT) [7], although ERT offers good potential in reduction of LVH in patients without LGE [8] and best outcomes in early treated patients [9]. This equally underscores the diagnostic and prognostic importance of LGE in the course of FD. Conversely, LGE imaging is limited due to its dichotomous character because 15% of focal matrix expansion are required to prove LGE [10]. Hence, the benefit of LGE in FD is restricted because early cardiac involvement remains hidden and most suitable patients for ERT may not be detected by CMRI.

Native cardiac T1 mapping may solve the diagnostic dilemma. Low native T1 values are postulated to indicate accumulation of glycosphingolipids in FD and can be demonstrated in up to 59% of LVH-negative FD patients [11].

Moreover, different studies showed significant reductions of native T1 times in patients with FD [12–14] compared to healthy volunteers and to other cardiac diseases with LVH without any overlap [12]. A recent study showed promising correlations for native T1 times to Lyso-Gb3 [14], which is an FD specific biomarker suitable for diagnostic and monitoring [15]. In addition to native T1 times, myocardial strain analysis may serve as a further diagnostic increment because myocardial strain abnormalities in FD patients haven been shown in echocardiography studies [16–19]. However, data on CMRI-derived feature tracking strain analyses (FT-SA) in FD is limited.

FT-SA allows quantification of myocardial deformation on the basis of standardized acquired cine images without the need for additional dedicated sequences. Post myocardial infarction and in hypertrophic cardiomyopathy prediction of adverse clinical outcomes can be shown via FT-SA [20,21]. Therefore, the aim of our study is to assess the relations of FT-SA with native T1 values and the FD specific biomarker LysoGb3 in order to evaluate its diagnostic potential.

2. Methods

Study population: 28 consecutive and genetically confirmed enzyme replacement therapy naive FD patients (18 female) and 28 control subjects (18 female) were enrolled in this prospective cohort study from January 2014 to June 2020.

FD diagnosis was based on a molecular genetic analysis demonstrating a heterozygous or homozygous mutation in the α-GAL-A-gene [22]. All FD patients underwent CMRI for assessment of cardiac involvement as part of their routine workup prior to therapy. To reduce magnetic field and contrast media risks for healthy volunteers, the first 28 age- and sex-matched patients, who had undergone CMRI for other reasons (myocardial ischemia or myocardial inflammation) within the predefined period, were selected as control subjects instead of healthy volunteers. It was absolutely mandatory that patients as control subjects were only included when CMRI was unremarkable concerning heart size and function, wall motion, valve disease, perfusion, signs of myo- or pericardial inflammation, pericardial and pleural effusion or pulmonary edema, and pulmonary trunk and aortic diameter. Further clinical patient observation confirmed control subject suitability. Contraindications for CMRI and exclusion criteria were: renal failure with a glomerular filtration rate below 30 mL/min/1.73 m^2, incompatible implants (cochlear or metallic), gadolinium intolerance, claustrophobia, or patient inability.

CMR technique: Standardized imaging was performed at a 1.5 Tesla MRI system (Somatom Avanto, Siemens Healthineers, Forchheim, Germany) using a six-element phased array cardiac coil. The CMRI protocol contained thoracic survey images, CINE sequences, steady-state-free precession sequences (SSFP) aligned to short-axis, 2-, 3- and 4-chamber view (SA, 2-CV, 3-CV and 4-CV), T2-wighted imaging ("black-blood" T2 turbo spin echo), LGE imaging (T1 gradient echo with inversion recovery) and native T1-mapping. Gado-

teridol (Gd-HP-DO3A; ProHance, BRACCO Imaging, Milan, Italy) was injected at a dose of 0.15 mmol/kg. LGE imaging was performed 12 min after contrast media injection. SSFP and CINE images were obtained during breath hold. The LV volume (absolute values) was calculated from short-axis CINE images. Measurements were performed on end-diastolic images and end-systolic images. Endocardial contours of the LV were obtained by manual tracing with exclusion of papillary muscles and trabeculae from the cavity. Ventricular volumes were estimated using the Simpson rule. T1 mapping images were acquired at basal, mid-ventricular, and apical short-axis section by using a modified Look-Locker inversion-recovery (MOLLI "3-3-5") sequence—11 images were acquired during 17 heartbeats, and after in-line motion, correction maps were generated [23]. Imaging parameters for native T1 mapping were: slice thickness: 8 mm; spatial resolution: 2.2 mm × 1.8 mm × 8 mm; 6/8 partial Fourier acquisition; field of view: 240 × 340 mm; matrix: 192 × 124; flip angle 35°; TR 740 and TE 1.06; TI 100 ms and TI Increment 80 ms; trigger delay: 300 ms; inversions 3; acquisition heartbeats: 3-3-5; and scan time: 17 heartbeats.

CMR analysis: Postprocessing was performed by using the cardiovascular imaging version 42 (cvi42) software including feature and tissue tracking (Circle Cardiovasculare Imaging, Calgary, Alberta, Canada). LV strain was quantified on contiguous SA CINE images (8 to 10 slices on average, depending on patient and cardiac size) and log-axis CINE images aligned to 2-, 3- and 4-CV using the feature and tissue tracking software tool. Global longitudinal (GLS), radial (GRS) and circumferential (GCS) strains were analyzed for the left ventricle and were defined as the peak value of each strain. GLS analysis was performed via 4-CH CINE imaging and GRS or GCS was based on SA CINE imaging at midventricular level.

Septal native T1 times were measured in region of interest (ROI) at basal short-axis section to guarantee proper T1 measurements caused by greater septal myocardial diameters compared to midventricular and apical sections. To avoid measuring of partial volume-averaging artefacts and registration errors with gradual T1 changes at myocardial borders, the ROI were drawn carefully, and software assisted by predefining an epicardial and endocardial offset of 10 percent. All measurements were performed by two experienced radiologists with 10 and 25 years of experience in cardiovascular imaging. LGE assessment was performed blinded to native T1 maps and CINE images. All T1 maps and LGE images were of diagnostic quality and could sufficient be evaluated.

Intraobserver and interobserver variability were analyzed for septal native T1 mapping and feature tracking strain analysis including GLS, GRS and GCS. Initially, the first investigator (10 years of experience in cardiovascular imaging) performed septal native T1 measurements and feature tracking strain analysis blinded to patient demographics. To assess intraobserver variability, measurements were repeated after a period of 14 days. Moreover, a second experienced investigator (25 years of experience in cardiovascular imaging), who was also blinded to patient demographics, performed septal native T1 measurements and feature tracking strain analysis to determine interobserver variabilities.

Laboratory assessment: Lyso-globotriaosylceramide (LysoGb3) was measured in serum at the (blinded for review). LysoGb3 values > 1.0 ng/mL were interpreted as elevated.

3. Statistical Analysis

Statistical analysis was performed using PRISM statistical software version 9 (Graphpad Software, San Diego, CA, USA). Patient characteristics were described by mean ± SD. All data were tested for normal distribution using the Shapiro–Wilk test. In cases of normal distribution, Student's *t*-test was used, and if the data were not distributed normally, the Mann–Whitney test (non-parametric) was used. Strengths of correlations were tested using the Spearman correlation coefficient. The correlation coefficient r was interpreted according to Hinkle et al. [24] where r > 0.3 would be considered a weak correlation, r > 0.5 would a moderate correlation, r > 0.7 a strong correlation, and r > 0.9 very strong correlation. An r > 0.5 would therefore be considered to have clinical impact. To assess intraobserver and interobserver agreement intra-class concordance correlation coefficient (ICC) was used.

An excellent agreement was defined as ICC > 0.8. All results were tested at a 5% level of significance and alpha error of less than 0.05 was accepted as statistically significant.

4. Results

Table 1 presents patient and control subject demographics. The mean age of the FD patients was 49.9 years ± 16.8 standard deviation (± SD) and the mean age of the control subjects was 47.5 years ± 13.2 SD. Both, FD patients and control subjects showed normal left heart function with normal left ventricular ejection fraction (LVEF). LVEF was 65.9% ± 8.1 SD (range, 44 to 79%) for FD patients and 67.7% ± 7.9 SD (range, 58 to 78%) for control subjects. End diastolic volume (EDV) and stroke volume (SV) revealed normal values for FD patients and control subjects but EDV and SV were significantly higher for the control subjects ($p = 0.025$ and $p = 0.026$), whereas end systolic volume (ESV) differed not significantly. Intra- and interobserver variability were excellent for LVEF and for all measured cardiac volumes (EDV, ESV and SV) in FD patients and control subjects (r between 0.9488 and 0.9823).

Table 1. Baseline characteristics.

	FD	Control Group
Patients (*n*)	28	28
Sex (male:female)	10:18	10:18
Age ± SD (years)	49.9 ± 16.8	47.5 ± 13.2
Lyso-Gb3 (ng/mL)	17.8 ± 38.1	

Values are mean ± SD or absolute values.

LVH, defined as a septal myocardial diameter equally or greater than 13 mm in diastole, was present in six FD patients (21.4%) and in none of the control subjects. Septal diameter and myocardial mass did not differ significantly between FD patients and control subjects. The mean septal myocardial diameter was 9.8 mm ± 3.6 SD for FD patients and 8.4 m ± 1.6 SD for control subjects and the mean LV myocardial mass was 123.1 g ± 55.5 SD for FD patients and 103.6 g ± 30.0 SD for control subjects.

The mean septal native T1 time for the FD patients was 921.1 ms ± 49.4 SD (range, 820 to 989 ms) and was statistically significant lower ($p = 0.0064$) compared to the control subjects, who had a mean native septal T1 time of 951.0 ms ± 47.3 SD (range, 917 to 985 ms). LGE at the inferolateral wall was present in seven of the FD patients (25%) and in none of the control subjects.

With exception of GCS (−19.9% ± 3.2 versus −21.6% ± 2.7 SD; $p = 0.1218$), FD patients had significant GLS and GRS reductions compared to the control subjects: GLS −18.0% ± 3.3 versus −20.5% ± 1.7 SD ($p = 0.0009$), GRS 33.6% ± 8.7 versus 41.4% ± 11.0 SD ($p = 0.0184$). Intra- and interobserver variability were excellent for septal native T1 time in FD patients (r = 0.9836, 95% CI 0.9723–0.9898; r = 0.9788, 95% CI 0.9684–0.9865) and for control subjects (r = 0.9812, 95% CI 0.9722–0.9912; r = 0.9815, 95% CI 0.9675–0.9888), for GLS (r = 0.8774, 95% CI 0.8627–0.8956; r = 0.8698, 95% CI 0.8488–0.8967) and (r = 0.8856, 95% CI 0.8698–0.9012; r = 0.8731, 95% CI 0.8643–0.8866), GRS (r = 0.8626, 95% CI 0.8456–0.8844; r = 0.8598, 95% CI 0.8412–0.8729) and (r = 0.8688, 95% CI 0.8522–0.8810; r = 0.8602, 95% CI 0.8468–0.8798), GCS (r = 0.8512, 95% CI 0.8366–0.8788; r = 0.8688, 95% CI 0.8422–0.8866) and (r = 0.8498, 95% CI 0.8343–0.8688; r = 0.8523, 95% CI 0.8388–0.8652).

Figure 1 shows native T1 and strain measurements in an FD patient and Figure 2 shows the boxplots for septal native T1 times and GLS in FD patients and control subjects. Cardiac function, cardiac morphology and strain values for FD patients and control subjects are presented in Table 2.

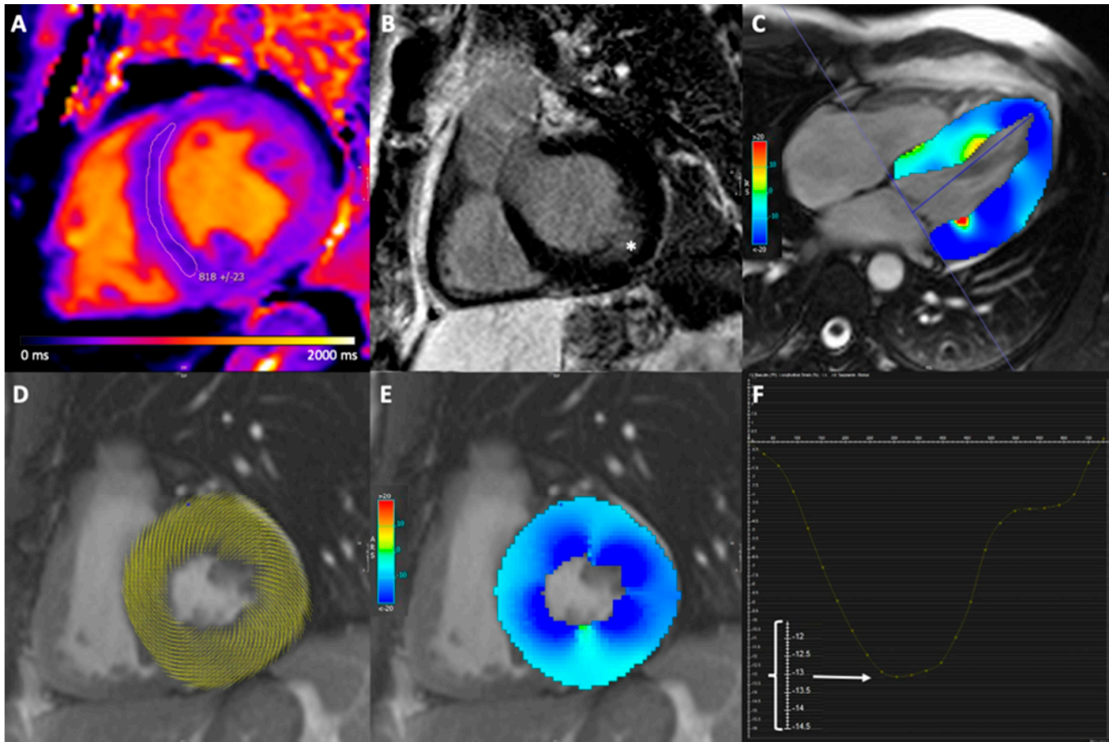

Figure 1. Imaging example including native T1 map, LGE image and strain images. Cardiovascular magnetic resonance images of a 38-year-old male with Fabry disease. Midventricular short-axis native T1 map (**A**) demonstrates reduced septal native T1 time, and basal short-axis late gadolinium enhanced (LGE) image (**B**) demonstrates intramural LGE at the inferior lateral wall (white asterisk). Short-axis CINE steady state free precession (SSFP) image with circumferential myocardial strain analysis points (**D**) and color-coded myocardial circumferential strain map (**E**). Long-axis CINE SSFP image with color-coded myocardial longitudinal strain map (**C**). Global longitudinal strain was −13.2%, as the enlarged scale on the Y-axis showed (**F**).

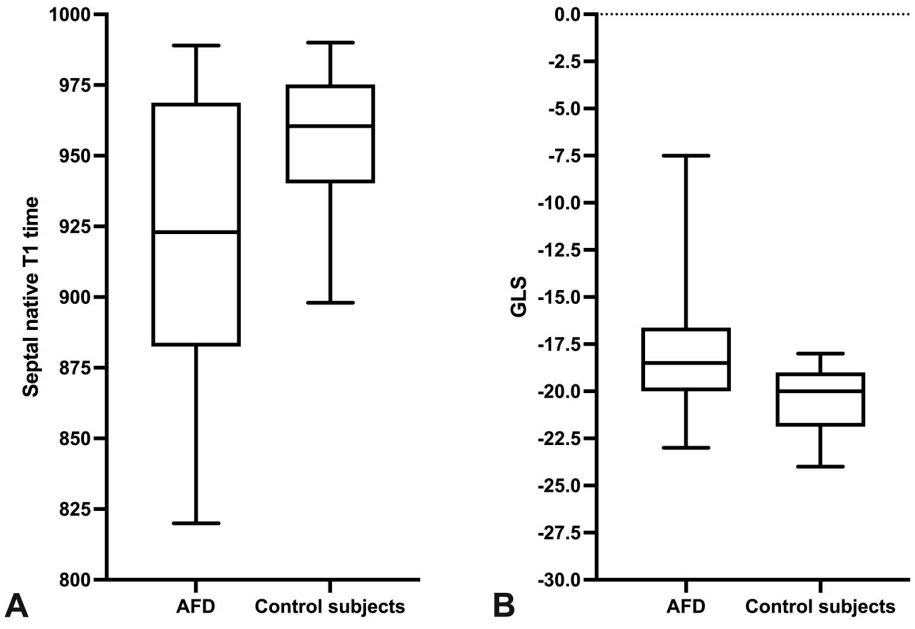

Figure 2. Septal native T1 times and GLS in FD patients and control subjects. The boxplots present the septal native T1 times (**A**) and the global longitudinal strain (GLS) (**B**) in FD patients and in control subjects.

Table 2. Cardiac function and morphology: FD versus control group.

	FD $n = 28$	Control Group $n = 28$	p
LVEF (%)	65.9 ± 8.1	67.7 ± 7.9	0.68
EDV (mL)	108.5 ± 32.4	125.9 ± 30.1	0.025
ESV (mL)	37.5 ± 14.0	41.8 ± 16.5	0.32
SV (mL)	72.1 ± 21.3	84.1 ± 17.4	0.026
Septal diameter (mm)	9.8 ± 3.6	8.4 ± 1.6	0.266
Myocardial mass (g)	123.1 ± 55.5	103.6 ± 30.0	0.189
Septal native T1 time (ms)	921.1 ± 49.4	951.0 ± 47.3	0.006
GRS (%)	33.6 ± 8.7	41.4 ± 11.0	0.018
GCS (%)	−19.9 ± 3.2	−21.6 ± 2.7	0.122
GLS (%)	−18.0 ± 3.3	−20.5 ± 1.7	<0.001
LGE (*n*; %)	7 (25%)	-	

Values are mean ± SD, LVEF—left ventricular ejection fraction, EDV—end diastolic volume, ESV—end systolic volume, SV—stroke volume, GRS—global radial strain, GCS—global circumferential strain, GLS—global longitudinal strain, LGE—late gadolinium enhancement, *p*—significance value.

Correlation of septal native T1 times, strain values and LysoGb3: The mean LysoGb3 level of the FD patients was 17.8 ng/mL ± 38.1 SD (range, 0.3 to 169). Septal native T1 time and GLS revealed the best correlations to LysoGb3 with a significant moderate positive correlation for GLS and LysoGb3 (r = 0.5498; $p = 0.0024$) and a significant negative moderate correlation for septal native T1 times and LysoGb3 (r = −0.6519; $p = 0.0002$). All correlations are presented in Table 3.

Table 3. Correlations of strain values, LysoGb3, myocardial mass and native T1.

	r	95% CI	p
Septal native T1 to GRS	0.3272	−0.06385 to 0.6311	0.089
Septal native T1 to GCS	−0.4687	−0.7221 to −0.1044	0.012
Septal native T1 to GLS	−0.3251	−0.6297 to −0.06620	0.092
LysoGb3 to GRS	−0.288	−0.6028 to 0.1091	0.14
LysoGb3 to GCS	0.384	0.00114 to 0.6687	0.044
LysoGb3 to GLS	0.5498	0.2114 to 0.7706	0.002
Septal native T1 to LysoGb3	−0.6519	−0.8281 to −0.3584	<0.001

GRS—global radial strain, GCS—global circumferential strain, GLS—global longitudinal strain, r—correlation coefficient, CI—confidence interval, *p*—significance value.

LysoGb3 positive and LysoGb3 negative FD patients: LGE was only present in LysoGb3 positive FD patients. Cardiac function, septal diameter and myocardial mass differed not significantly between LysoGb3 positive and LysoGb3 negative FD patients, whereas septal native T1 times and GLS were significantly reduced in LysoGb3 positive FD compared to LysoGb3 negative patients ($p = 0.005$ and $p = 0.03$). Cardiac function, cardiac morphology and strain values for LysoGb3 positive and negative FD patients are presented in Table 4. Continuously, a moderate negative correlation for septal native T1 times and LysoGb3 in the LysoGb3 positive patients was present (r = −0.6279; $p = 0.0053$). Apart from the correlation of septal native T1 times to GLS all other correlations of septal native T1 times, strain values (GCS, GRS) were increased in LysoGb3 positive patients compared to all FD patients. Correlations are presented in Table 5 and Figure 3. Thereby, GCS showed the best correlations to septal native T1 times and LysoGb3 with a significant negative moderate correlation for GCS and septal native T1 times (r = −0.612; $p = 0.0069$) and a significant moderate correlation for GCS and LysoGb3 (r = 0.6522; $p = 0.034$).

Table 4. Cardiac function and morphology: FD Lyso-Gb3+ versus Lyso-Gb3-.

	LysoGb3+ $n = 18$	LysoGb3− $n = 10$	p
LVEF (%)	65.9 ± 8.8	66.1 ± 6.9	0.98
EDV (mL)	111.5 ± 34.1	103.0 ± 30.0	0.86
ESV (mL)	38.4 ± 16.3	35.8 ± 9.1	0.98
SV (mL)	73.1 ± 22.5	70.3 ± 20.0	0.76
Septal diameter (mm)	10.7 ± 4.1	8.0 ± 1.3	0.059
Myocardial mass (g)	135.4 ± 64.1	96.8 ± 25.5	0.10
Septal native T1 time (ms)	902.0 ± 49.4	955.5 ± 25.8	0.005
GRS (%)	32.2 ± 10.0	36.3 ± 5.1	0.41
GCS (%)	−19.6 ± 3.7	−20.5 ± 2.3	0.58
GLS (%)	−17.0 ± 3.7	−19.7 ± 1.4	0.03
LGE (n; %)	7 (70%)	0	

Values are mean ± SD, LVEF—left ventricular ejection fraction, EDV—end diastolic volume, ESV—end systolic volume, SV—stroke volume, GRS—global radial strain, GCS—global circumferential strain, GLS—global longitudinal strain, late gadolinium enhancement, p—significance value.

Table 5. Correlations of strain values, LysoGb3 and native T1 in LysoGb3+ patients.

	r	95% CI	p
Septal native T1 to GRS	0.4410	−0.04752 to 0.7593	0.067
Septal native T1 to GCS	−0.612	−0.8435 to −0.1889	0.007
Septal native T1 to GLS	−0.394	−0.7370 to 0.09780	0.101
LysoGb3 to GRS	−0.4708	−0.7747 to 0.009960	0.049
LysoGb3 to GCS	0.6522	0.2524 to 0.8617	0.034
LysoGb3 to GLS	0.4602	−0.02347 to 0.7693	0.043
Septal native T1 to LysoGb3	−0.6279	−0.8508 to −0.2136	0.005

GRS—global radial strain, GCS—global circumferential strain, GLS—global longitudinal strain, r—correlation coefficient, CI—confidence interval, p—significance value.

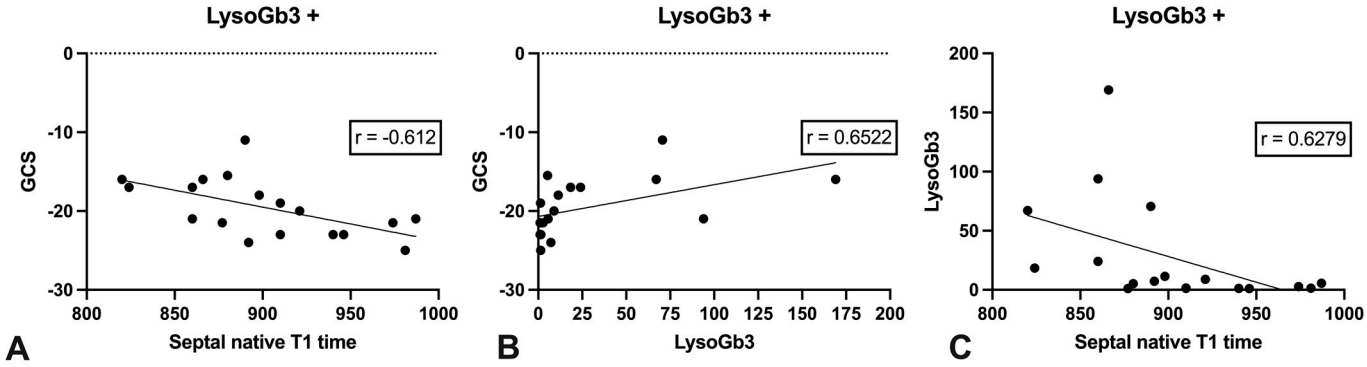

Figure 3. Correlations of LysoGb3 positive FD patients to GCS and septal native T1 time. Scatter plots showing the correlations of GCS and septal native T1 time (**A**), GCS and LysoGb3 (**B**), and septal native T1 time and LysoGb3 (**C**) in LysoGb3 positive (+) FD patients.

Moreover, FD subgroup analysis between LysoGb3 negative FD patients without LGE and LVH, LysoGb3 positive FD patients without LGE or LVH and LysoGb3 positive patients with either LGE or LVH showed increasing and significantly different LysoGb3 levels between all groups and significant reductions of septal native T1 times between LysoGb3 negative, and both LysoGb3 positive patient groups and a significant reduction in GLS between LysoGb3 negative FD patients and LysoGb3 positive patients with either LGE or LVH. Subgroup FD analysis is presented in Figure 4 via boxplots and in Figure 5.

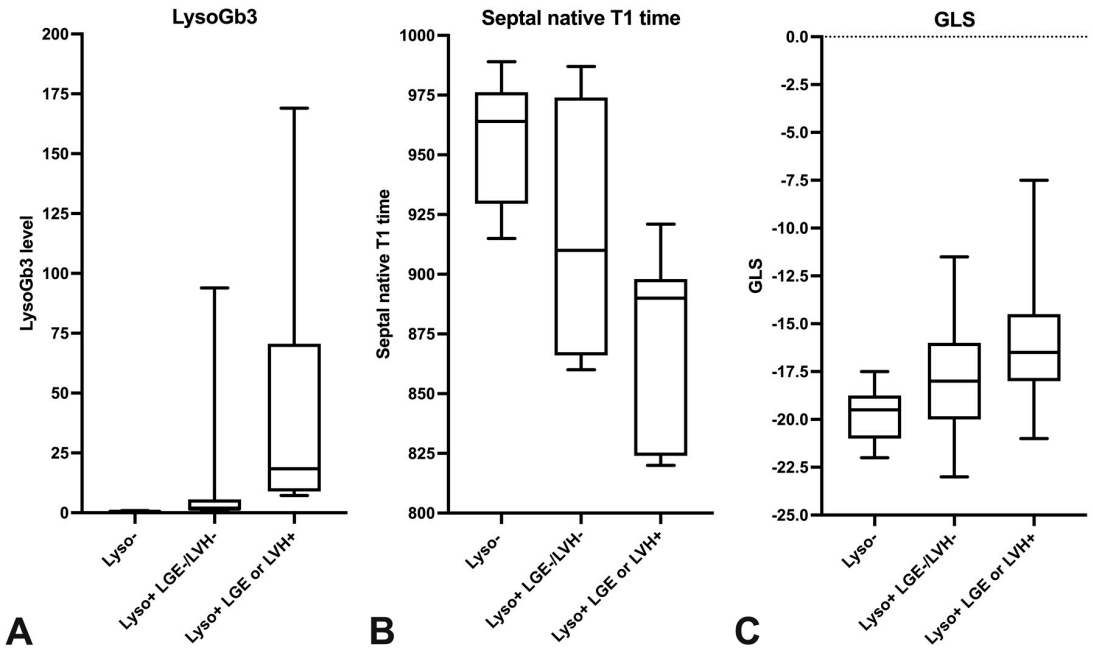

Figure 4. FD patient subgroup analysis. The boxplots present the LysoGb3 level (**A**), the septal native T1 times (**B**) and the global longitudinal strain (GLS) (**C**) of FD patients depending on LysoGb3 positivity and presence of late gadolinium enhancement (LGE) or left ventricular hypertrophy (LVH).

	LysoGb3-	LysoGb3+ LVH and LGE-	LysoGb3+ LVH or LGE+
	n = 10	*n* = 11	*n* = 7
LysoGb3 (ng/ml)	0.64 ± 0.20	12.65 ± 27.77	50.40 ± 59.00
p		**< 0.001**	**< 0.001**
p		**0.008**	
Native T1 time (ms)	955.5 ± 25.8	913.7 ± 50.1	873.0 ± 38.4
p		**0.06**	0.22
p		**0.002**	
GLS (%)	19.7 ± 1.4	17.9 ± 3.2	15.7 ± 4.2
p		0.17	0.28
p		**0.01**	

Figure 5. LysoGb3, septal native T1 and GLS in FD subgroups. GLS—global longitudinal strain, *p*—significance value.

Key points:

Native T1 times are significantly decreased in FD.
Feature tracking strain values are also decreased in FD.
Native T1 times and strain values showed promising correlations to biomarker LysoGb3.
Moreover, GLS and native T1 times reduce with LysoGb3 increase.
Mechanical dysfunction may occur early in FD.

5. Discussion

In the last decade, CMRI has been changed from semiquantitative assessment to quantitative phenotyping. The mainly descriptive imaging with visual assessment of edema, hyperemia, LGE and wall motion abnormalities has changed to quantitative functional and morphologic imaging due to rapid technical development.

Hereby, improved disease burden quantification, therapy monitoring, follow-up and prognosis estimation is enabled in many cardiac diseases. In the course of FD, especially native T1 mapping showed great potential for detection of early cardiac involvement [12–14] as myocardial storage and accumulation of glycosphingolipids shorten the native T1 time.

In contrast to FD, other cardiomyopathies show native T1 time elevations and cardiac FD involvement can therefore be proven well independently of LVH [12]. Reductions of native T1 times in FD are present in absence of LVH, and diagnosis of early cardiac manifestation is possible prior to development of typical ("hallmark") LGE at the inferolateral wall. Hence, the most appropriate patients for ERT may be detectable via native T1 mapping.

FT-SA showed promising results in different cardiac diseases [20,21], but data on CMR derived FT-SA in FD is still limited. Besides previous performed echocardiographic studies, which showed strain abnormalities in FD patients [16–19], first CMRI studies dealing with FT-SA in FD patients showed promising results. Based on their results with association of impairment in GLS and reduction of native T1 times without presence of LVH, the authors of a recent study suggested that mechanical dysfunction in the course of FD occurs before evidence of glycosphingolipid deposition [25]. Another study concluded that base to apex circumferential strain may be an early marker of cardiac FD involvement with independent and incremental value beyond native T1 [26].

The goal of our study was to investigate the relations of FT-SA to native T1 times and to the FD specific biomarker LysoGb3.

The main findings of our study are:

1. Septal native T1 times, GLS and GRS are significantly reduced in FD patients compared to control subjects, whereas cardiac function (LVEF), septal diameter and myocardial mass differed not significantly. Moreover, septal native T1 times and GLS showed moderate correlations to LysoGb3 (FD specific biomarker);
2. Compared to LysoGb3 negative FD patients, LysoGb3 positive FD patients had significantly reduced septal T1 times. Furthermore, correlations of strain values with LysoGb3 and septal native T1 times increased in LysoGb3 positive FD patients.
3. Finally, subgroup analysis between 1. LysoGb3 negative FD patients, 2. LysoGb3 positive FD patients without LVH or LGE and 3. LysoGb3 positive FD patients with either LVH or LGE showed a steady decrease of septal native T1 time and GLS accompanied by a steady increase of LysoGb3. Hence, GLS initially reduces with storage (low native T1 times and elevated LysoGb3 level) and later with increasing LysoGb3 level and hypertrophy or scar (LGE).

Consistent with the results of previously published studies [12–14], the native T1 times were significantly reduced in our FD patients. Moreover, the significantly reduced strain values in our FD patients also support the findings of the previous published studies [25,26]. To the best of our knowledge, this is the first study in the field that investigated the relations of FT-SA values with native T1 times and the FD specific biomarker LysoGb3. LysoGb3 plasma levels are higher in all subgroups of FD than in healthy subjects and tend to be high in FD patients with proceeded disease stages inter alia in patients with developed heart disease [15].

The main limitation of our study is the small number of patients. Otherwise, it is a prospective cohort analysis in a rare disease with untreated patients, and the results of the FD subgroup analysis revealed significant differences regarding native T1 times and FT-SA values. Our results may therefore serve as a starting point for further investigations assessing biomarkers, native T1 times and strain values in the course of FD.

6. Conclusions

The steady GLS and native T1 decrease from LysoGb3 negative FD patients over LysoGb3 positive FD patients to LysoGb3 positive FD patients with presence of LVH or LGE and the promising correlations of strain values, native T1 times and LysoGb3 suggests that wall motion abnormalities occur early in cardiac FD involvement. We therefore suggest a diagnostic cardiac MRI algorithm in FD containing FT-SA beside native T1 measurements and LysoGb3 analysis to enable best possible early cardiac disease manifestation detection with the goal to avoid unfavorable disease progression due to early initiation of ERT. 1. LysoGb3 elevation and native T1 or FT-SA decrease—cardiac FD manifestation seems to be likely, 2. LysoGb3 elevation with both, native T1 and FT-SA decrease—cardiac FD manifestation seems likely, 3. LysoGb3 elevation with normal native T1 and FT-SA values—cardiac FD manifestation remains unclear and close controls should be performed.

Author Contributions: F.C.R., M.R., C.T. and G.A.K. were involved in study conception and design. F.C.R., A.S., A.B., S.H., M.R., C.T. and G.A.K. contributed to acquisition of data. F.C.R., A.S., A.B., S.H., M.R., C.T. and G.A.K. helped in analysis and interpretation of data. F.C.R., A.S., A.B., S.H., M.R., C.T. and G.A.K. helped in drafting of manuscript. F.C.R., A.S., A.B., S.H., M.R., C.T. and G.A.K. were involved in critical revision. All authors have read and agreed to the published version of the manuscript.

Funding: This research received no external funding.

Institutional Review Board Statement: The study was conducted according to the guidelines of the Declaration of Helsinki and approved by the Institutional Review Board (or Ethics Committee) of Justus-Liebig-University Giessen, Faculty of Medicine (protocol code XXX and date of approval).

Informed Consent Statement: Informed consent was obtained from all subjects involved in the study.

Data Availability Statement: The datasets used or analyzed during the current study are available from the corresponding author on reasonable request.

Conflicts of Interest: The authors declare no conflict of interest.

Abbreviations

FD	Fabry Disease
CMRI	cardiac magnetic resonance imaging
CV	chamber view
FT-SA	feature tracking strain analysis
EDV	end diastolic volume
ESV	end systolic volume
ERT	enzyme replacement therapy
GCS	global circumferential strain
GLS	global longitudinal strain
GRS	global radial strain
LGE	late gadolinium enhancement
LV	left ventricular
LVEF	left ventricular ejection fraction
LVH	left ventricular hypertrophy
ROI	region of interest
SA	short axis
SD	standard deviation
SSFP	steady-state-free precession
SV	stroke volume

References

1. MacDermot, K.D.; Holmes, A.; Miners, A.H. Anderson-Fabry disease: Clinicalmanifestations and impact of disease in a cohort of 98 hemizygous males. *J. Med. Genet.* **2001**, *38*, 750–760. [CrossRef]
2. Hoey, E.T.; Neil-Gallagher, E. Utility of gadolinium enhanced cardiovascular MRI to differentiate Fabry's disease from other causes of hypertrophic cardiomyopathy. *Postgrad. Med. J.* **2012**, *88*, 731–732. [CrossRef]
3. Messalli, G.; Imbriaco, M.; Avitabile, G.; Russo, R.; Iodice, D.; Spinelli, L.; Dellegrottaglie, S.; Cademartiri, F.; Salvatore, M.; Pisani, A. Role of cardiac MRI in evaluating patients with Anderson-Fabry disease: Assessing cardiac effects of long-term enzyme replacement therapy. *Radiol. Med.* **2012**, *117*, 19–28. [CrossRef]
4. Eng, C.M.; Guffon, N.; Wilcox, W.R.; Germain, D.P.; Lee, P.; Waldek, S.; Caplan, L.; Linthorst, G.E.; Desnick, R.J. Safety and efficacy of recombinant human alpha-galactosidase A-replacement therapy in Fabry's disease. *N. Engl. J. Med.* **2001**, *345*, 9–16. [CrossRef] [PubMed]
5. Patel, M.R.; Cecchi, F.; Cizmarik, M.; Kantola, I.; Linhart, A.; Nicholls, K.; Strotmann, J.; Tallaj, J.; Tran, T.C.; West, M.L.; et al. Cardiovascular events in patients with fabry disease natural history data from the fabry registry. *J. Am. Coll. Cardiol.* **2011**, *57*, 1093–1099. [CrossRef]
6. Moon, J.C.; Sachdev, B.; Elkington, A.G.; McKenna, W.J.; Mehta, A.; Pennell, D.J.; Leed, P.J.; Elliott, P.M. Gadolinium enhanced cardiovascularmagnetic resonance in Anderson-Fabry disease: Evidence for a disease specific abnormality of the myocardial interstitium. *Eur. Heart J.* **2003**, *24*, 2151.e5. [CrossRef] [PubMed]
7. Ries, M.; Clarke, J.T.; Whybra, C.; Timmons, M.; Robinson, C.; Schlaggar, B.L.; Pastores, G.; Lien, Y.H.; Kampmann, C.; Brady, R.O.; et al. Enzyme-replacement therapy with agalisade alfa in children with Fabry disease. *Pediatrics* **2006**, *118*, 924–932. [CrossRef] [PubMed]
8. Collin, C.; Briet, M.; Tran, T.C.; Beaussier, H.; Benistan, K.; Bensalah, M.; Mousseaux, E.; Froissart, M.; Bozec, E.; Laurent, S. Long-term changes in arterial structure and function and left ventricular geometry after enzyme replacement therapy in patients affected with Fabry disease. *Eur. J. Prev. Cardiol.* **2012**, *19*, 43–54. [CrossRef] [PubMed]
9. Weidemann, F.; Niemann, M.; Breunig, F.; Herrmann, S.; Beer, M.; Störk, S.; Voelker, W.; Ertl, G.; Wanner, C.; Strotmann, J. Long-term effects of enzyme replacement therapy on fabry cardiomyopathy: Evidence for a better outcome with early treatment. *Circulation* **2009**, *119*, 524–529. [CrossRef] [PubMed]
10. Moon, J.C.; Reed, E.; Sheppard, M.N.; Elkington, A.G.; Ho, S.; Burke, M.; Petrou, M.; Pennell, D.J. The histologic basis of late gadolinium enhancement cardiovascular magnetic resonance in hypertrophic cardiomyopathy. *J. Am. Coll. Cardiol.* **2004**, *43*, 2260–2264. [CrossRef] [PubMed]
11. Nordin, S.; Kozor, R.; Baig, S.; Abdel-Gadir, A.; Medina-Menacho, K.; Rosmini, S.; Captur, G.; Tchan, M.; Geberhiwot, T.; Murphy, E. Cardiac phenotype of prehypertrophic fabry disease. *Circ. Cardiovasc. Imaging* **2018**, *11*, e007168. [CrossRef] [PubMed]
12. Sado, D.M.; White, S.K.; Piechnik, S.K.; Banypersad, S.M.; Treibel, T.; Captur, G.; Fontana, M.; Maestrini, V.; Flett, A.S.; Robson, M.D. Identification and assessment of Anderson-Fabry Disease by Cardiovascular Magnetic Resonance Non-contrast myocardial T1 mapping clinical perspective. *Circ. Cardiovasc. Imaging* **2013**, *6*, 392–398. [CrossRef] [PubMed]
13. Thompson, R.B.; Chow, K.; Khan, A.; Chan, A.; Shanks, M.; Paterson, I.; Oudit, G.Y. T extsubscript1 mapping with cardiovascular MRI is highly sensitive for Fabry disease independent of hypertrophy and sex. *Circ. Cardiovasc. Imaging* **2013**, *6*, 637–645. [CrossRef]
14. Roller, F.C.; Fuest, S.; Meyer, M.; Harth, S.; Gündüz, D.; Bauer, P.; Schneider, C.; Rolfs, A.; Krombach, G.A.; Tanislav, C. Assessment of Cardiac Involvement in Fabry Disease (FD) with Native T_1 Mapping. *Rofo* **2019**, *191*, 932–939. [CrossRef]
15. Sueoka, H.; Ichihara, J.; Tsukimura, T.; Togawa, T.; Sakuraba, H. Nano-LC-MS/MS for Quantification of Lyso-Gb3 and Its Analogues Reveals a Useful Biomarker for Fabry Disease. *PLoS ONE* **2015**, *10*, e0127048. [CrossRef]
16. Gruner, C.; Verocai, F.; Carasso, S.; Vannan, M.A.; Jamorski, M.; Clarke, J.T.; Care, M.; Iwanochko, R.M.; Rakowski, H. Systolic myocardial mechanics in patients with Anderson-Fabry disease with and without left ventricular hypertrophy and in comparison to nonobstructive hypertrophic cardiomyopathy. *Echocardiography* **2012**, *29*, 810–817. [CrossRef]
17. Shanks, M.; Thompson, R.B.; Paterson, I.D.; Putko, B.; Khan, A.; Chan, A.; Becher, H.; Oudit, G.Y. Systolic and diastolic function assessment in fabry disease patients using speckle-tracking imaging and comparison with conventional echocardiographic measurements. *J. Am. Soc. Echocardiogr.* **2013**, *26*, 1407–1414. [CrossRef]
18. Labombarda, F.; Saloux, E.; Milesi, G.; Bienvenu, B. Loss of base-to-apex circumferential strain gradient: A specific pattern of Fabry cardiomyopathy? *Echocardiograph* **2017**, *34*, 504–510. [CrossRef] [PubMed]
19. Krämer, J.; Niemann, M.; Liu, D.; Hu, K.; Machann, W.; Beer, M.; Wanner, C.; Ertl, G.; Weidemann, F. Two-dimensional speckle tracking as a non-invasive tool for identification of myocardial fibrosis in Fabry disease. *Eur. Heart J.* **2013**, *34*, 1587–1596. [CrossRef]
20. Eitel, I.; Stiermaier, T.; Lange, T.; Rommel, K.P.; Koschalka, A.; Kowallick, J.T.; Lotz, J.; Kutty, S.; Gutberlet, M.; Hasenfuß, G. Cardiac magnetic resonance myocardial feature tracking for optimized prediction of cardiovascular events following myocardial infarction. *JACC Cardiovasc. Imaging* **2018**, *11*, 1433–1444. [CrossRef] [PubMed]
21. Smith, B.M.; Dorfman, A.L.; Yu, S.; Russell, M.W.; Agarwal, P.P.; Mahani, M.G.; Lu, J.C. Relation of strain by feature tracking and clinical outcome in children, adolescents, and young adults with hypertrophic cardiomyopathy. *Am. J. Cardiol.* **2014**, *114*, 1275–1280. [CrossRef] [PubMed]

22. Rolfs, A.; Fazekas, F.; Grittner, U.; Dichgans, M.; Martus, P.; Holzhausen, M.; Böttcher, T.; Heuschmann, P.U.; Tatlisumak, T.; Tanislav, C. Acute cerebrovascular disease in the young: The Stroke in Young Fabry Patients study. *Stroke* **2013**, *44*, 340–349. [CrossRef] [PubMed]
23. Roller, F.C.; Harth, S.; Schneider, C.; Krombach, G.A. T1, T2 mapping and extracellular volume fraction (ECV): Application, value and further perspectives in myocardial inflammation and cardiomyopathies. *Rofo* **2015**, *187*, 760–770. [CrossRef] [PubMed]
24. Hinkle, D.E.; Wiersma, W.; Jurs, S.G. *Applied Statistics for the Behavioral Sciences*, 5th ed.; Houghton Mifflin: Boston, MA, USA, 2003.
25. Vijapurapu, R.; Nordin, S.; Baig, S.; Liu, B.; Rosmini, S.; Augusto, J.; Tchan, M.; Hughes, D.A.; Geberhiwot, T.; Moon, J.C. Global longitudinal strain, myocardial storage and hypertrophy in Fabry disease. *Heart* **2019**, *105*, 470–476. [CrossRef] [PubMed]
26. Mathur, S.; Dreisbach, J.G.; Karur, G.R.; Iwanochko, R.M.; Morel, C.F.; Wasim, S.; Nguyen, E.T.; Wintersperger, B.J.; Hanneman, K. Loss of base-to-apex circumferential strain gradient assessed by cardiovascular magnetic resonance in Fabry disease: Relationship to T_1 mapping, late gadolinium enhancement and hypertrophy. *J. Cardiovasc. Magn. Reson.* **2019**, *21*, 45. [CrossRef] [PubMed]

JACC: CARDIOVASCULAR IMAGING VOL. 12, NO. 11, 2019

PUBLISHED BY ELSEVIER

ORIGINAL RESEARCH

Cardiac Magnetic Resonance Imaging-Based Right Ventricular Strain Analysis for Assessment of Coupling and Diastolic Function in Pulmonary Hypertension

Khodr Tello, MD,[a] Antonia Dalmer,[a] Rebecca Vanderpool, PhD,[b] Hossein A. Ghofrani, MD,[a,c,d] Robert Naeije, MD, PhD,[e] Fritz Roller, MD,[f] Werner Seeger, MD,[a] Jochen Wilhelm, PhD,[a] Henning Gall, MD, PhD,[a] Manuel J. Richter, MD[a]

ABSTRACT

OBJECTIVES This study sought to compare cardiac magnetic resonance (CMR) imaging-derived right ventricular (RV) strain and invasively measured pressure-volume loop-derived RV contractility, stiffness, and afterload and RV-arterial coupling in pulmonary hypertension (PH).

BACKGROUND In chronic RV pressure overload, RV-arterial uncoupling is considered the driving cause of RV maladaptation and eventual RV failure. The pathophysiological and clinical value of CMR-derived RV strain relative to that of invasive pressure-volume loop-derived measurements in PH remains incompletely understood.

METHODS In 38 patients with PH, global RV CMR strain was measured within 24 h of diagnostic right heart catheterization and conductance (pressure-volume) catheterization. Associations were evaluated by correlation, multivariate logistic binary regression, and receiver operating characteristic analyses.

RESULTS Long-axis RV longitudinal and radial strain and short-axis RV radial and circumferential strain were −18.0 ± 7.0%, 28.9% [interquartile range (IQR): 17.4% to 46.6%]; 15.6 ± 6.2%; and −9.8 ± 3.5%, respectively. RV-arterial coupling (end-systolic [Eds]/arterial elastance [Ea]) was 0.76 (IQR: 0.47 to 1.07). Peak RV strain correlated with Ees/Ea, afterload (Ea), RV diastolic dysfunction (Tau), and stiffness (end-diastolic elastance [Eed]) but not with contractility (Ees). In multivariate analysis, long-axis RV radial strain was associated with RV-arterial uncoupling (Ees/Ea: <0.805; odds ratio [OR]: 5.50; 95% confidence interval [CI]: 1.50 to 20.18), whereas long-axis RV longitudinal strain was associated with increased RV diastolic stiffness (Eed: ≥0.124 mm Hg/ml; OR: 1.23; 95% CI: 1.10 to 1.51). The long-axis RV longitudinal strain-to-RV end-diastolic volume/body surface area ratio strongly predicted RV diastolic stiffness (area under receiver operating characteristic curve: 0.908).

CONCLUSIONS In chronic RV overload, CMR-determined RV strain is associated with RV-arterial uncoupling and RV end-diastolic stiffness and represents a promising noninvasive alternative to current invasive methods for assessment of RV-arterial coupling and end-diastolic stiffness in patients with PH. (Right Ventricular Haemodynamic Evaluation and Response to Treatment [Rightheart I]; NCT03403868) (J Am Coll Cardiol Img 2019;12:2155–64)

From the [a]Department of Internal Medicine, Justus-Liebig-University Giessen, Universities of Giessen and Marburg Lung Center, Giessen, Germany; [b]Division of Translational and Regenerative Medicine, University of Arizona, Tucson, Arizona; [c]Department of Pneumology, Kerckhoff Heart, Rheuma, and Thoracic Center, Bad Nauheim, Germany; [d]Department of Medicine, Imperial College London, London, United Kingdom; [e]Department of Cardiology, Erasme University Hospital, Brussels, Belgium; and the [f]Department of Radiology, Justus-Liebig-University Giessen, Universities of Giessen and Marburg Lung Center, Giessen, Germany. Supported by the Excellence Cluster Cardio-Pulmonary System and Collaborative Research Center 1213 Pulmonary Hypertension and Cor Pulmonale grant SFB1213/1, and German Research Foundation project B08. Dr. Tello has received speaker

ISSN 1936-878X/$36.00 https://doi.org/10.1016/j.jcmg.2018.12.032

ABBREVIATIONS AND ACRONYMS

AUC = area under the curve

BSA = body surface area

CMR = cardiac magnetic resonance

Ea = arterial elastance

EDV = end-diastolic volume

Eed = end-diastolic elastance

Ees = end-systolic elastance

GCS = global circumferential strain

GLS = global longitudinal strain

GRS = global radial strain

PH = pulmonary hypertension

RV = right ventricular

Pulmonary hypertension (PH) is associated with progressive afterload-induced right ventricular (RV) remodeling with an increase in contractility (to preserve RV-pulmonary arterial coupling), diastolic stiffening, and eventual evolution to RV dilation and clinical right heart failure (1). In this regard, evaluation of RV function plays an essential role in managing patients with PH. Cardiac magnetic resonance (CMR) imaging was recently described by the American Thoracic Society as the standard imaging technique for measurement of RV function (2). Surrogates of RV contractility derived from CMR imaging, such as RV ejection fraction and stroke volume divided by end-systolic volume, help to predict the onset of RV dilation and have shown prognostic relevance (3–5). In addition, CMR feature tracking is a novel method for quantification of myocardial strain that has been associated with RV ejection fraction in PH (6) and has shown a stronger association with mortality than left ventricular ejection fraction in dilated cardiomyopathy (7). Nevertheless, the physiological correlate of RV strain remains to be defined, as it is still unclear whether

SEE PAGE 2165

RV strain in the setting of chronic overload is associated with direct measurements of RV diastolic stiffness (Eed), end-systolic elastance (Ees), arterial elastance (Ea), and the Ees/Ea ratio, which represents RV-arterial coupling. Assessing Eed and Ees/Ea requires the generation of pressure-volume loops measured with high-fidelity catheters, which is invasive, technically demanding, and expensive (8). CMR imaging-based surrogates of these variables would thus be of major clinical benefit.

Therefore, this study sought to assess the association between CMR-derived RV strain and that of invasively measured pressure-volume loop-derived RV contractility, stiffness, and afterload parameters and to define the pathophysiological and clinical value of CMR strain analysis in PH.

METHODS

STUDY DESIGN AND PATIENTS. This study examined consecutive patients with pulmonary arterial hypertension and chronic thromboembolic PH (diagnosed according to current guidelines [9]) who were prospectively enrolled in the Rightheart I (Right Ventricular Haemodynamic Evaluation and Response to Treatment study; NCT03403868) study and the Giessen PH Registry (10) between January 2016 and April 2018. A multidisciplinary board including pulmonary physicians and radiologists assessed each diagnosis before the patient was enrolled. All patients underwent CMR imaging on day 1 and pressure-volume/Swan-Ganz catheterization on day 2. All patients received targeted pulmonary arterial hypertension therapies based on clinical grounds and best standard of care. All participating patients gave written informed consent. The investigation conforms to Declaration of Helsinki tenets and was approved by the ethics committee of the Faculty of Medicine at the University of Giessen (approval 108/15).

CMR IMAGING. Imaging was performed using a 1.5-T scanner (Avanto, Siemens Healthineers, Erlangen, Germany) with a gradient strength and slew rate (SQ-engine, 45 mT/m at 200 T/m per s) using a 6-element phased array cardiac coil and a dedicated CMR protocol including axial, coronal, and sagittal thoracic survey images, steady-state free precession cine sequences in 2-, 3-, and 4-chamber views, and transaxial and short-axis stacks from base to apex (black-blood T2 turbo spin echo). Gadoteridol (Bracco Imaging, Milan, Italy) was injected at a dose of 0.15 mmol/kg. Late gadolinium enhancement imaging was performed 12 min after contrast medium was injected. Steady-state free precession imaging

fees from Actelion and Bayer. Dr. Ghofrani is a consultant for Bayer, Actelion, Pfizer, Merck, GlaxoSmithKline, and Novartis; is a compensated advisory board member for Bayer, Pfizer, GlaxoSmithKline, Actelion, and Takeda; has received lecture fees from Bayer HealthCare, GlaxoSmithKline, Actelion, and Encysive/Pfizer; and has received grants from Bayer HealthCare, Aires, Encysive/Pfizer, Novartis, the German Research Foundation, Excellence Cluster Cardiopulmonary Research, and the German Ministry for Education and Research. Dr. Naeije has received research support from, is a consultant for, and sits on scientific advisory boards of AOPOrphan Pharmaceuticals, Actelion, Bayer, Reata, Lung Biotechnology Corporation, and United Therapeutics. Dr. Seeger is a compensated speaker and consultant for Pfizer, Bayer Pharma AG, United Therapeutics, and Liquidia. Dr. Gall has received fees from Actelion, AstraZeneca, Bayer, Bristol-Myers Squibb, GlaxoSmithKline, Janssen-Cilag, Lilly, Merck Sharpe & Dohme, Novartis, Optimal Medical Therapies, Pfizer, and United Therapeutics. Dr. Richter has received support from United Therapeutics and Bayer; has received speaker fees from Actelion, Mundipharma, Roche, and Optimal Medical Therapies; and has received consultant fees from Bayer. All other authors have reported that they have no relationships relevant to the contents of this paper to disclose.

Manuscript received July 31, 2018; revised manuscript received November 16, 2018, accepted December 20, 2018.

parameters were: 8-mm slice thickness; 300 × 400-mm field of view; 256 × 154 matrix; 59.62-ms temporal resolution; and 1.15-ms echo time. Late gadolinium enhancement imaging parameters were: 8-mm slice thickness; 293 × 360-mm field of view; 256 × 156 matrix; 843.2-ms temporal resolution; and 3.19-ms echo time. The steady-state free precession images were obtained during breath holds, and RV systolic and diastolic volumes (absolute values) were calculated from short-axis and transaxial cine images. Measurements were taken on end-diastolic images (first phase after the R-wave trigger) and end-systolic images (based on cine images with the visually smallest cavity area). RV endocardial contours were obtained semi-automatically with exclusion of papillary muscles and trabeculae from the cavity and with subsequent manual correction by the agreement of 2 investigators. Ventricular volumes were estimated using the Simpson rule. Ejection fraction was calculated as: [(end-diastolic volume [EDV] – end-systolic volume)/EDV]. End-systolic and end-diastolic diameters were measured using basal short-axis images. Post-processing was performed by using the cardiovascular imaging version 42 (cvi[42]) software including feature/tissue tracking (Circle Cardiovascular Imaging, Calgary, Alberta, Canada). RV strain was quantified on contiguous short-axis cine images (8 to 10 slices on average, depending on patient and cardiac size) and long-axis cine images (2-, 3-, and 4-chamber views), using the feature/tissue tracking software tool. Global RV longitudinal, radial, and circumferential peak strains were analyzed (**Figure 1A**) (for further details see the Supplemental Appendix).

Pulmonary arterial stiffness, capacitance, and distensibility were measured using CMR data as described previously (11) (Supplemental Appendix).

RIGHT HEART CATHETERIZATION. An 8-F introducer sheath was used to insert a Swan-Ganz catheter through the internal jugular vein. Pressures were assessed continuously. Cardiac index was recorded as the average of 3 to 5 measurements, using the direct or indirect Fick method as available. Pulmonary vascular resistance was calculated as: [(mean pulmonary arterial pressure – pulmonary arterial wedge pressure)/cardiac output] (9).

PRESSURE-VOLUME CATHETERIZATION. A 4-F pressure-volume catheter (model CA-Nr 41063, CD Leycom, Zoetermeer, the Netherlands) was inserted through the same 8-F introducer sheath as indicated above and positioned in the RV apex, guided by transthoracic echocardiography and analysis of online pressure-volume loops (12). Pressure-volume loops were displayed beat-to-beat in real time by connection to an intracardiac analyzer (Inca, CD Leycom). Ees was calculated using the RV single-beat method (13), and Ea was calculated as end-systolic pressure/stroke volume (13). RV-arterial coupling was defined as the Ees/Ea ratio (Supplemental Methods, Supplemental Figure 1).

Diastolic stiffness β was calculated by fitting a nonlinear exponential curve $P = \alpha(e\beta V - 1)$ through the diastolic portion of the pressure-volume loops, using a customized MATLAB (MathWorks, Natick, Massachusetts) program (4). Three points were used for the exponential fit: origin (0,0), beginning diastolic point, and end-diastolic point. Eed was obtained from the relationship [$dP/dV = \alpha\beta \times e\beta \times EDV$] at calculated end-diastolic volumes (EDV) (14,15). When the pressure-volume loops showed a clear overlap, a single beat was chosen for extrapolation to a sinusoidal curve and for analysis of Eed. Volume measurements were calibrated with CMR imaging data.

STATISTICAL ANALYSES. Adherence to a Gaussian distribution was determined using the Kolmogorov-Smirnov test and visual assessment of histograms. Associations between variables were measured with Spearman's rank correlation, and trend lines were least square fittings of straight-line models and second-order polynomial models.

To determine which strain parameters were most strongly related to Ees/Ea, Ea, and Eed, all RV strain parameters were included in a multivariate logistic binary regression analysis. Receiver operating characteristic curve analysis was used to identify the RV strain parameter with the highest sensitivity and specificity for discriminating RV uncoupling (based on the Ees/Ea ratio), increased afterload (based on Ea), and diastolic stiffness (based on Eed). Reference values for Ees/Ea, Ea, and Eed that would indicate RV uncoupling, increased afterload, and diastolic stiffness are not yet available; therefore, receiver operating characteristic curve analysis and the Youden index to identify cutoff values that would discriminate RV maladaptation (defined as RV ejection fraction <35% [3,5]) and stroke volume/end-systolic volume of <0.534) were used (16,17). The cutoff values identified were 0.805 for Ees/Ea, 0.66 for Ea, and 0.124 for Eed (Supplemental Figure 2); these cutoff values were used to indicate RV uncoupling, increased afterload, and diastolic stiffness, respectively.

To determine which RV strain parameter was most impaired during RV dilation, RV EDV normalized to body surface area (BSA) was split into tertiles, classifying patients in the lowest tertile as the reference

FIGURE 1 Associations Among RV Global Strain and CMR RV Maladaptation, Invasive Pulmonary Hemodynamics, and Pressure-Volume Loop Measurements

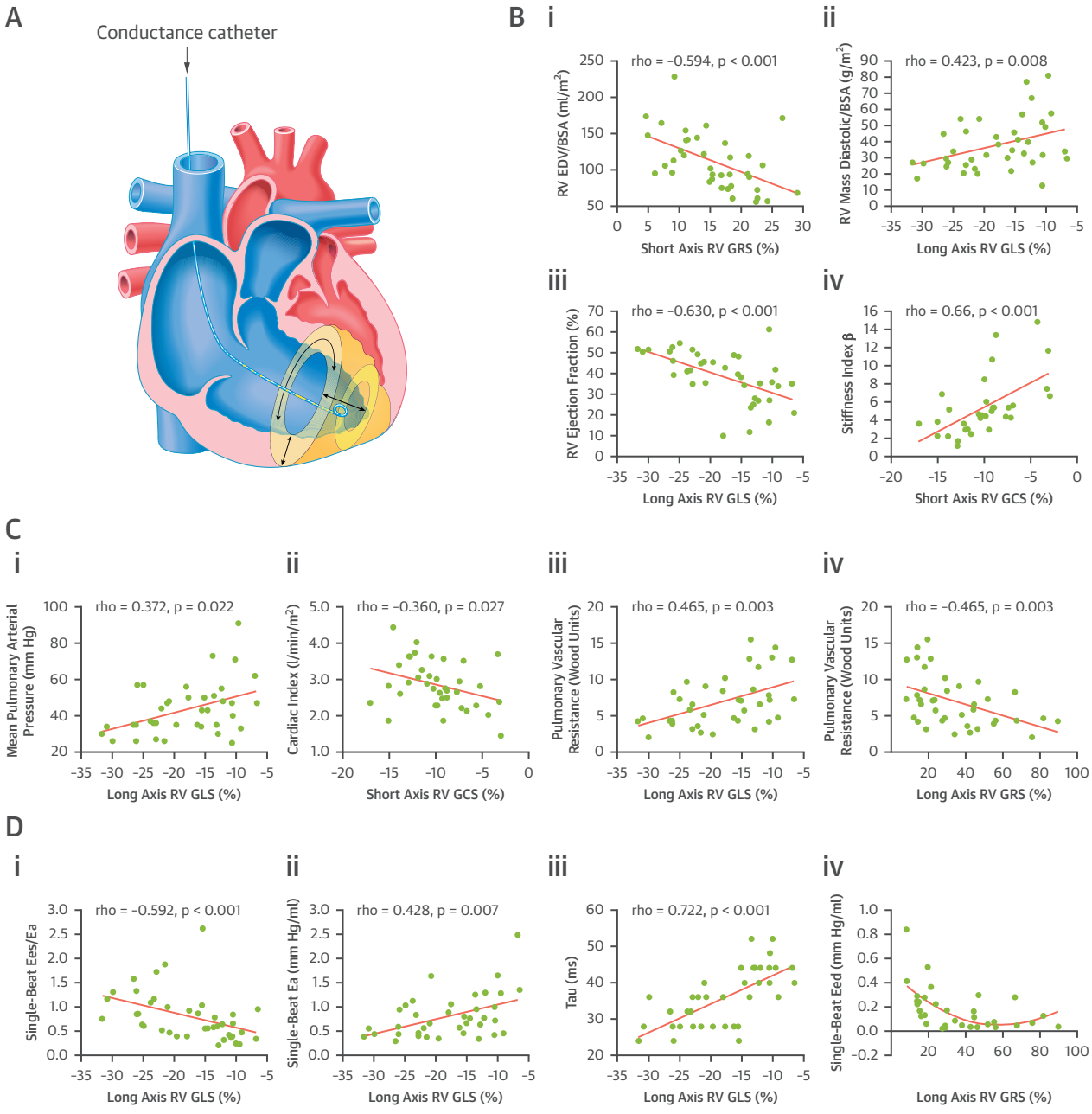

(A) RV longitudinal, radial, and circumferential peak strains were measured as shown. **(Bi, Bii, Biii)** RV maladaptation and **(Biv)** pulmonary arterial stiffness were related to RV strain. **(C)** Key invasive pulmonary hemodynamic parameters and **(D)** pressure-volume loop parameters were associated with RV strain. BSA = body surface area; Ea = arterial elastance; EDV = end-diastolic volume; Eed = end-diastolic elastance; GCS = global circumferential strain; GLS = global longitudinal strain; GRS = global radial strain; RV = right ventricular.

(nondilated) group. RV strain in patients with dilation (RV EDV/BSA tertiles 2 and 3) was expressed as a percentage of the median strain in the reference group. Differences between multiple groups were analyzed with the independent samples Kruskal-Wallis test or 1-way analysis of variance as appropriate.

For all analyses, a p value of <0.05 was considered statistically significant. SPSS version 23.0 software

(IBM, Armonk, New York) was used for statistical analyses.

RESULTS

PATIENTS. Characteristics of the 38 patients with PH, which included CMR and pressure-volume loop measurements, are presented in **Table 1**. Exemplary CMR images, strain curves, and pressure-volume loops are shown in Supplemental Figure 3. Idiopathic pulmonary arterial hypertension was diagnosed in most patients. The patients presented with severe PH and had high EDV (indicating RV dilation) and decreased RV ejection fraction and stroke volume/end-systolic volume ratio compared with values reported in healthy individuals (18).

ASSOCIATION BETWEEN CMR RV STRAIN AND RV MALADAPTATION. RV short-axis radial strain was correlated with RV dilation (RV EDV/BSA) (**Figure 1B**), and RV longitudinal, radial, and circumferential strain showed significant decreases in patients with severely dilated versus nondilated right ventricles (stratified by tertiles of RV EDV/BSA). Short-axis radial strain showed the most pronounced decrease, whereas only a trend was observed for long-axis radial strain (Supplemental Figure 4). Long-axis longitudinal strain was also correlated with hypertrophy (RV mass diastolic/BSA) and RV ejection fraction (**Figure 1B**). Short-axis circumferential strain (**Figure 1B**) and long-axis longitudinal strain (rho: 0.398; $p = 0.024$ [figure not shown]) were associated with pulmonary arterial stiffness. Moreover, long-axis longitudinal strain showed a significant correlation with distensibility (rho: −0.406; $p = 0.019$ [figure not shown]).

ASSOCIATION BETWEEN CMR RV STRAIN AND PULMONARY HEMODYNAMICS. Long-axis RV longitudinal strain was correlated with mean pulmonary arterial pressure and pulmonary vascular resistance (**Figure 1C**). Short-axis RV circumferential strain and long-axis RV radial strain were correlated with cardiac index and pulmonary vascular resistance, respectively (**Figure 1C**).

ASSOCIATION BETWEEN CMR RV STRAIN AND PRESSURE-VOLUME LOOP PARAMETERS. Ees/Ea (which showed a nonlinear relationship with RV ejection fraction) (Supplemental Figure 5) was related to long-axis RV radial strain (rho: 0.579; $p < 0.001$ [figure not shown]) and longitudinal strain (**Figure 1D**). Ea and Tau showed correlations with long-axis RV

TABLE 1 Patient Characteristics, Pulmonary Hemodynamics, and Pressure-Volume Loop and CMR Measurements (N = 38)

Males/females	17/21
Age, yrs	55.5 (44.8-65.3)
PH subtype	
Idiopathic pulmonary arterial hypertension	25 (66)
Pulmonary arterial hypertension associated with	7 (18)
Human immunodeficiency virus infection	1
Portal hypertension	2
Connective tissue disease	3
Congenital heart disease	1
Chronic thromboembolic PH	6 (16)
Right heart catheterization	
Mean pulmonary arterial pressure, mm Hg	41.5 (34.0-50.3)
Right atrial pressure, mm Hg	7.0 (5.0-9.0)
Pulmonary vascular resistance, Wood units	6.6 (4.3-8.8)
Mean cardiac index, l/min per m^2	2.8 ± 0.7
Pulmonary arterial wedge pressure, mm Hg	8.5 ± 3.3
Treatment	
Phosphodiesterase type 5 inhibitor	17 (45)
Endothelin receptor antagonist	22 (58)
Soluble guanylate cyclase stimulator	16 (42)
Prostanoid	6 (16)
Combination therapy	
Dual therapy	12 (32)
Triple therapy	9 (24)
Pressure-volume loop measurements	
Ea, mm Hg/ml	0.70 (0.45-1.04)
Ees, mm Hg/ml	0.49 (0.35-0.74)
Ees/Ea ratio	0.76 (0.47-1.07)
End-systolic pressure, mm Hg	58.0 (42.8-78.3)
End-diastolic pressure, mm Hg	6.5 (3.0-11.0)
Tau, ms	36.0 (28.0-44.0)
Eed, mm Hg/ml*	0.124 (0.047-0.262)
CMR measurements	
RV EDV/BSA, ml/m^2	104.3 (83.1-140.9)
RV end-systolic volume/BSA, ml/m^2	61.4 (44.7-94.8)
RV mass diastolic/BSA, g/m^2	33.8 (27.1-47.5)
RV mass systolic/BSA, g/m^2	35.2 ± 13.3
RV mass/volume ratio, g/ml	0.33 (0.25-0.44)
RV ejection fraction, %	38.7 ± 12.3
RV stroke volume/end-systolic volume	0.69 (0.40-1.01)
Stiffness index β†	4.6 (3.1-6.5)
Capacitance, mm^3/mm Hg*	1.8 (1.4-2.7)
Distensibility, %/mm Hg*	0.44 (0.25-0.73)
Short-axis	
RV global radial strain, %	15.6 ± 6.2
RV global circumferential strain, %	−9.8 ± 3.5
Long-axis	
RV global radial strain, %	28.9 (17.4-46.6)
RV global longitudinal strain, %	−18.0 ± 7.0

Values are median (interquartile range), n (%), or mean ± SD, unless otherwise specified. *n = 33. †n = 32.

BSA = body surface area; CMR = cardiac magnetic resonance; Ea = arterial elastance; EDV = end-diastolic volume; Eed = end-diastolic elastance; Ees = end-systolic elastance; IQR = interquartile range; PH = pulmonary hypertension; RV = right ventricular.

FIGURE 2 Receiver Operating Characteristic Curve Analysis and Corresponding Cutoff Values

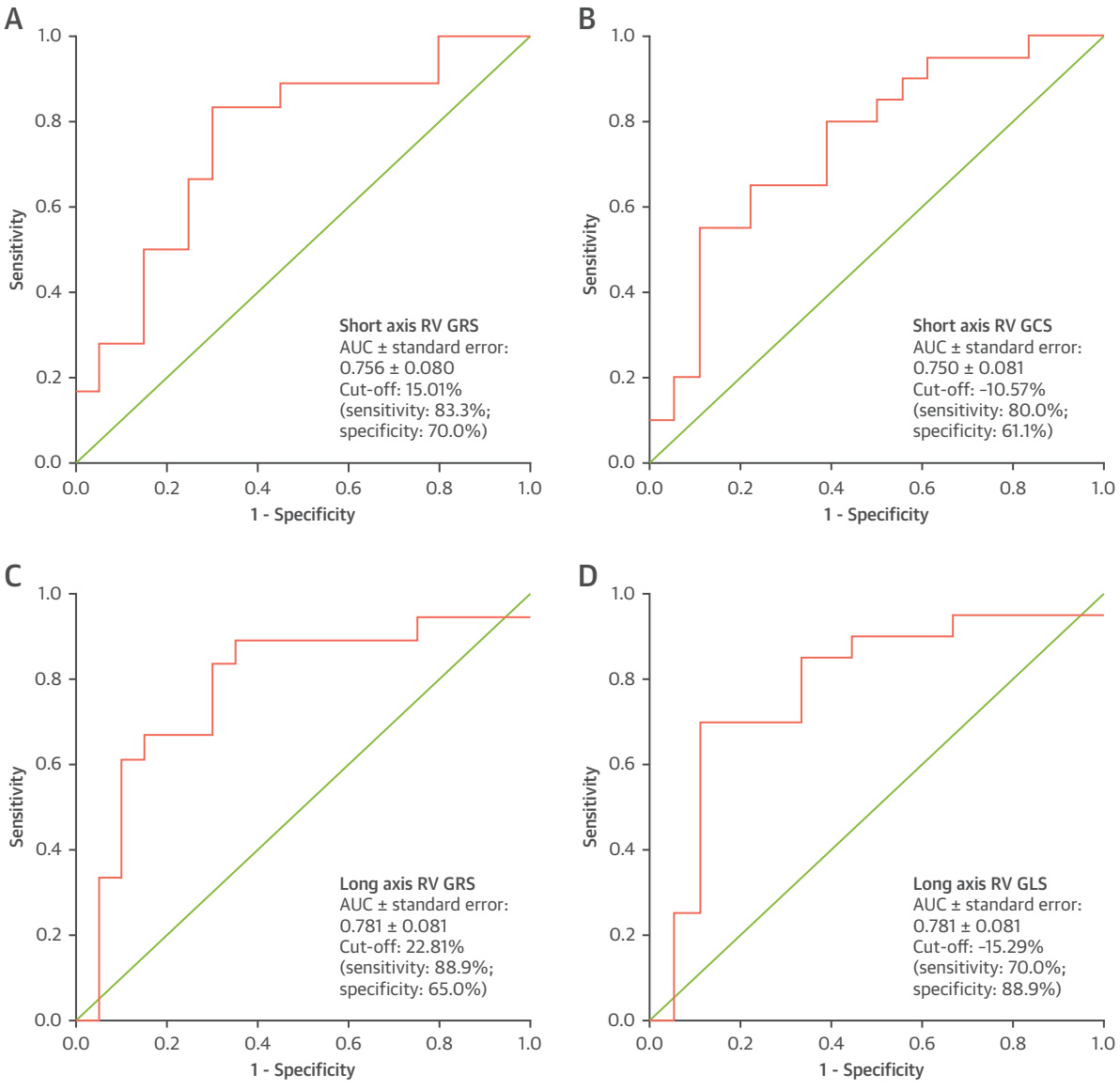

(A) Short-axis RV GRS; **(B)** Short-axis RV GCS; **(C)** Long-axis RV GRS, and **(D)** Long-axis RV GLS for discriminating RV-pulmonary arterial coupling. RV-pulmonary arterial coupling was defined as a single-beat Ees/Ea value ≥0.805 mm Hg/ml. AUC = area under the curve; Ees = end-systolic elastance; other abbreviations as in Figure 1.

longitudinal strain (Figure 1D) and radial strain (Ea: rho: −0.426; p = 0.008; Tau rho: −0.721; p < 0.001 [figures not shown]). Eed showed a nonlinear association with long-axis RV radial strain (Figure 1D). No correlation between Ees and RV strain was observed (Supplemental Figure 6).

PREDICTIVE RELEVANCE OF RV STRAIN FOR RV-ARTERIAL COUPLING. In multivariate logistic regression analysis, long-axis RV radial strain remained independently associated with Ees/Ea dichotomized at 0.805 mm Hg/ml (multivariate odds ratio [OR]: 5.50; 95% confidence interval [CI]: 1.50 to 20.18; p = 0.010) and Ea dichotomized at 0.66 mm Hg/ml (multivariate OR: 0.96; 95% CI: 0.92 to 0.995; p = 0.026). Long-axis RV longitudinal strain remained independently associated with Eed dichotomized at 0.124 mm Hg/ml (multivariate OR: 1.23; 95% CI: 1.10 to 1.51; p = 0.002). Using receiver operating characteristic curve analyses and the Youden index,

cutoff values of 22.81% for long-axis RV radial strain and −15.29% for long-axis RV longitudinal strain for discriminating RV-arterial coupling (area under the curve [AUC]) were identified in each case (AUC: 0.781; p = 0.003) (Figure 2). Compared with the long-axis RV strain parameters, short-axis RV radial and circumferential strain showed somewhat lower AUC values (0.756 and 0.750, respectively) (Figure 2).

ASSOCIATIONS AMONG CMR RV VOLUME AND STRAIN/VOLUME RATIO AND DIASTOLIC RV DYSFUNCTION. RV EDV/BSA (dilation) showed linear correlations with Tau (diastolic dysfunction) and Eed (diastolic stiffness) in chronic pressure overload (Supplemental Figures 7A and 7B). RV EDV/BSA stratified by Eed (dichotomized at 0.124 mm Hg/ml) was also a strong discriminator of preserved or reduced long-axis RV longitudinal strain (Supplemental Figure 7C). The Eed/RV EDV/BSA ratio showed a nonlinear association with long-axis RV longitudinal strain (Supplemental Figure 7D). Moreover, the long-axis RV longitudinal strain-to-RV EDV/BSA ratio was related to Eed (Figure 3A), Tau, Ea, and pulmonary arterial stiffness (Supplemental Figure 8) and strongly predicted RV diastolic stiffness in receiver operating characteristic analysis (AUC = 0.908; p < 0.001) (Figure 3B).

FIGURE 3 Associations Between Cardiac Magnetic Resonance RV Strain/Volume Ratio and RV Diastolic Stiffness

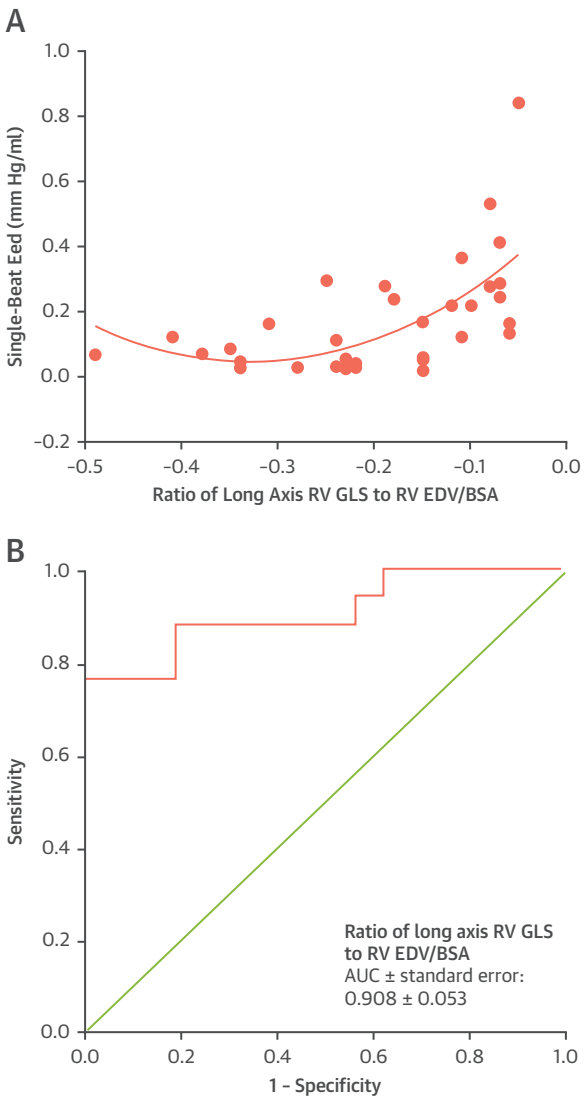

(A) The long-axis RV GLS-to-RV EDV/BSA ratio was associated with Eed, and **(B)** discriminated RV diastolic stiffness (Eed dichotomized at 0.124 mm Hg/ml) in receiver operating characteristic analysis. Abbreviations as in Figure 1.

DISCUSSION

The present data show for the first time a significant association between CMR imaging-derived RV strain parameters and the pressure-volume loop-derived parameters Ees/Ea, Ea, and Eed. RV strain assessed by CMR feature tracking was significantly associated with RV diastolic function (Tau), diastolic stiffness (Eed), and afterload (pulmonary arterial stiffness and Ea). Moreover, CMR RV strain mirrored RV-arterial coupling and was associated with RV dilation and hypertrophy as well as with conventional invasive hemodynamic parameters. Data show that CMR RV strain is a promising indicator of RV-arterial uncoupling and diastolic RV stiffness, broadening the already substantial range of potential applications for CMR in the assessment of RV function during follow-up of patients with PH. Furthermore, the present findings help to close the knowledge gap regarding the physiology of RV strain in chronic pressure overload, which was recently set as a research target by the American Thoracic Society (2).

The ability of the right ventricle to adapt to an increase in afterload (Ea) is related to its potential to increase contractility (Ees) (19). The optimal ratio between Ees and Ea ranges between 1.5 and 2.0, based on research of the left ventricle (20). However, several studies have shown that, as PH progresses, the increase in ventricular contractility becomes insufficient to compensate for the increase in afterload, leading to altered RV-arterial coupling (16,21–23). When the Ees/Ea ratio falls below a certain threshold (not yet precisely defined for the right ventricle but estimated to be 0.805 in the current study), RV dysfunction and failure may occur. Present

data demonstrate a nonlinear association between RV-arterial coupling and RV ejection fraction (Supplemental Figure 5), confirming this assumption.

Our findings may therefore have two pathophysiological explanations. First, in the present cohort with chronic pressure overload, the maximum increase in Ees may already have been reached. This possibility is supported by previous studies of Ees in settings of chronic pressure overload (24,25). Second, the present patients may have been in a state of relative RV-arterial uncoupling, in which Eed and Ea continue to increase without any further increase in Ees (1). Increased afterload has been reported to lead to elevated RV stiffness and fibrosis (26). Notably, our pressure-volume curve analysis shows not only that RV maladaptation is linked with RV dilation and thus "overexpansion" of the RV scaffold but also that the Eed/EDV ratio increases in the maladapted right ventricle and that this loss in lusitropic function is reflected by a decrease in CMR strain variables. Increases in Ea and Eed combined with an unchanging Ees explain why strain correlates with the Ees/Ea ratio but not with Ees. These findings are supported by results obtained previously by Guihaire et al. (27) in a porcine model of chronic pressure overload in which the usual indices of RV function were associated with RV-arterial coupling rather than with ventricular contractility. In addition, Vanderpool et al. (28) demonstrated that, because of the curvilinearity of both Ees and Eed curves, V0 increases with increasing Ea and that increased Ees and Eed are then mechanically associated, along with eventual increases in end-systolic volume and EDV.

This could lead to the conclusion, as shown in the present study, that Eed and Tau of the right ventricle play a crucial role in the setting of chronic pressure overload in PH. The present data are consistent with those from the study by Okumura et al. (29), who showed a significant correlation between RV diastolic function and strain assessed by echocardiography. Single beat-derived Eed has been shown to be increased in patients with pulmonary arterial hypertension and closely associated with markers of disease severity (15). In addition, the long-axis RV longitudinal strain-to-RV EDV/BSA ratio was identified as a novel parameter mirroring afterload (Ea) and RV diastolic dysfunction (Tau) and stiffness (Eed). Reduced RV longitudinal strain was in itself associated with elevated Eed and RV dilation, and the longitudinal strain-to-RV EDV/BSA ratio emerged as a robust noninvasive parameter for the prediction of RV diastolic stiffness. The association between strain and the load-independent measurement of Eed in the present study indicates that CMR strain analysis is a promising tool for the follow-up examination of patients with PH and has the potential to make invasive measurements of Eed and RV-arterial coupling superfluous.

Additionally, with increasing RV EDV/BSA, a significant reduction in each plane of strain is seen, indicating a change of the shape of the right ventricle leading to a reduction in its ability to deform during the cardiac cycle. This reduction is strongest for radial strain, with >50% loss of radial deformation in RV EDV/BSA tertile 3 compared with that in tertile 1. This finding is of interest because it was proposed previously that RV contractility occurs predominantly in the longitudinal plane due to the principal orientation of myocardial fibers (30,31). Previous studies have predominantly focused on RV longitudinal strain and have demonstrated impaired RV longitudinal strain in patients with PH, with subsequent associations between disease severity and mortality (32–34). However, the present data suggest a stronger decrease in radial strain than longitudinal strain in the maladaptive right ventricle. Nevertheless, the degree of longitudinal strain in this cohort of patients with PH ($-18.0 \pm 7.0\%$) was consistent with the impaired longitudinal strain reported previously by Puwanant et al. (32) ($-15.9 \pm 7.6\%$ in patients with PH compared with $-25.5 \pm 6.1\%$ in control subjects) (32). However, the present data lead to the conclusion that the predominant loss of RV radial strain in the setting of chronic pressure overload may mirror maladaptive processes in RV failure.

STUDY LIMITATIONS. The single-beat method was used to estimate Eed, Ees, and Ea parameters. It is not yet known if the multiple-beat approach would generate the same results. However, Inuzuka et al. (35) recently showed a good correlation between single-beat and multi-beat approaches. Reference values for Ees, Ea, and Eed and the Ees/Ea cutoff value at which RV maladaptation begins have not yet been precisely determined and were estimated for the current study. The temporal resolution of nearly 60 ms combined with the smoothing out of minor beat-to-beat differences across several beats may lead to underestimation of strain. The receiver operating characteristic curve and logistic regression analyses are biased by the moderate sample size. The sample size also prevents meaningful analysis of the effects of race and sex on the results but is reasonable given the comprehensive and demanding approach.

CONCLUSIONS

Our study reveals that diastolic stiffness significantly correlates with strain in the chronic pressure-overloaded right ventricle in PH. RV strain mirrors RV-arterial uncoupling, and its assessment also provides information on the adaptation of RV inotropic function to afterload, the associated alteration in lusitropic function, and adaptive versus maladaptive remodeling.

ACKNOWLEDGMENT The authors thank Claire Mulligan, PhD (Beacon Medical Communications Ltd., Brighton, United Kingdom), for manuscript and editorial assistance.

ADDRESS FOR CORRESPONDENCE: Dr. Khodr Tello, Department of Internal Medicine, Justus-Liebig-University Giessen, Klinikstrasse 32, 35392 Giessen, Germany. E-mail: Khodr.Tello@innere.med.uni-giessen.de.

PERSPECTIVES

COMPETENCY IN MEDICAL KNOWLEDGE: In the setting of chronic pressure overload in PH, RV strain parameters indicate that RV diastolic stiffness and RV-arterial uncoupling expand the scope of CMR in the follow-up examination of patients with PH. Furthermore, the present data provide new insights into RV maladaptation, suggesting that radial strain may decrease to a greater extent than longitudinal strain in the maladaptive right ventricle in PH.

TRANSLATIONAL OUTLOOK: Additional catheterization studies of conductance (using multiple-beat as well as single-beat approaches) will be needed to confirm the relationship between RV strain and RV maladaptation in larger populations of patients with PH and to further evaluate the effect of RV maladaptation on radial versus longitudinal strain.

REFERENCES

1. Vonk Noordegraaf A, Westerhof BE, Westerhof N. The relationship between the right ventricle and its load in pulmonary hypertension. J Am Coll Cardiol 2017;69:236–43.

2. Lahm T, Douglas IS, Archer SL, et al. Assessment of right ventricular function in the research setting: knowledge gaps and pathways forward. an Official American Thoracic Society research statement. Am J Respir Crit Care Med 2018;198:e15–43.

3. van de Veerdonk MC, Kind T, Marcus JT, et al. Progressive right ventricular dysfunction in patients with pulmonary arterial hypertension responding to therapy. J Am Coll Cardiol 2011;58:2511–9.

4. Vanderpool RR, Pinsky MR, Naeije R, et al. RV-pulmonary arterial coupling predicts outcome in patients referred for pulmonary hypertension. Heart 2015;101:37–43.

5. Vanderpool RR, Rischard F, Naeije R, Hunter K, Simon MA. Simple functional imaging of the right ventricle in pulmonary hypertension: can right ventricular ejection fraction be improved? Int J Cardiol 2016;223:93–4.

6. Oyama-Manabe N, Sato T, Tsujino I, et al. The strain-encoded (SENC) MR imaging for detection of global right ventricular dysfunction in pulmonary hypertension. Int J Cardiovasc Imaging 2013;29:371–8.

7. Romano S, Judd RM, Kim RJ, et al. Feature-tracking global longitudinal strain predicts death in a multicenter population of patients with ischemic and nonischemic dilated cardiomyopathy incremental to ejection fraction and late gadolinium enhancement. J Am Coll Cardiol Img 2018;11:1419–29.

8. Trip P, Kind T, van de Veerdonk MC, et al. Accurate assessment of load-independent right ventricular systolic function in patients with pulmonary hypertension. J Heart Lung Transplant 2013;32:50–5.

9. Galie N, Humbert M, Vachiery JL, et al. 2015 ESC/ERS Guidelines for the diagnosis and treatment of pulmonary hypertension: the Joint Task Force for the Diagnosis and Treatment of Pulmonary Hypertension of the European Society of Cardiology (ESC) and the European Respiratory Society (ERS): endorsed by: Association for European Paediatric and Congenital Cardiology (AEPC), International Society for Heart and Lung Transplantation (ISHLT). Eur Heart J 2016;37:67–119.

10. Gall H, Felix JF, Schneck FK, et al. The Giessen Pulmonary Hypertension Registry: survival in pulmonary hypertension subgroups. J Heart Lung Transplant 2017;36:957–67.

11. Sanz J, Kariisa M, Dellegrottaglie S, et al. Evaluation of pulmonary artery stiffness in pulmonary hypertension with cardiac magnetic resonance. J Am Coll Cardiol Img 2009;2:286–95.

12. Tello K, Richter MJ, Axmann J, et al. More on single-beat estimation of right ventriculoarterial coupling in pulmonary arterial hypertension. Am J Respir Crit Care Med 2018;198:816–8.

13. Brimioulle S, Wauthy P, Ewalenko P, et al. Single-beat estimation of right ventricular end-systolic pressure-volume relationship. Am J Physiol Heart Circ Physiol 2003;284:H1625–30.

14. Trip P, Rain S, Handoko ML, et al. Clinical relevance of right ventricular diastolic stiffness in pulmonary hypertension. Eur Respir J 2015;45:1603–12.

15. Rain S, Handoko ML, Trip P, et al. Right ventricular diastolic impairment in patients with pulmonary arterial hypertension. Circulation 2013;128:2016–25.

16. Sanz J, Garcia-Alvarez A, Fernandez-Friera L, et al. Right ventriculo-arterial coupling in pulmonary hypertension: a magnetic resonance study. Heart 2012;98:238–43.

17. Brewis MJ, Bellofiore A, Vanderpool RR, et al. Imaging right ventricular function to predict outcome in pulmonary arterial hypertension. Int J Cardiol 2016;218:206–11.

18. Petersen SE, Aung N, Sanghvi MM, et al. Reference ranges for cardiac structure and function using cardiovascular magnetic resonance (CMR) in Caucasians from the UK Biobank population cohort. J Cardiovasc Magn Reson 2017;19:18.

19. Naeije R, Brimioulle S, Dewachter L. Biomechanics of the right ventricle in health and disease (2013 Grover Conference series). Pulm Circ 2014;4:395–406.

20. Suga H, Sagawa K, Shoukas AA. Load independence of the instantaneous pressure-volume ratio of the canine left ventricle and effects of epinephrine and heart rate on the ratio. Circ Res 1973;32:314–22.

21. Sagawa K. The end-systolic pressure-volume relation of the ventricle: definition, modifications and clinical use. Circulation 1981;63:1223–7.

22. Maughan WL, Shoukas AA, Sagawa K, Weisfeldt ML. Instantaneous pressure–volume relationship of the canine right ventricle. Circ Res 1979;44:309–15.

23. Chantler PD, Lakatta EG, Najjar SS. Arterial-ventricular coupling: mechanistic insights into cardiovascular performance at rest and during exercise. J Appl Physiol (1985) 2008;105:1342–51.

24. Guihaire J, Haddad F, Noly PE, et al. Right ventricular reserve in a piglet model of chronic pulmonary hypertension. Eur Respir J 2015;45:709–17.

25. Spruijt OA, de Man FS, Groepenhoff H, et al. The effects of exercise on right ventricular

contractility and right ventricular-arterial coupling in pulmonary hypertension. Am J Respir Crit Care Med 2015;191:1050–7.

26. Cheng TC, Philip JL, Tabima DM, Hacker TA, Chesler NC. Multiscale structure-function relationships in right ventricular failure due to pressure overload. Am J Physiol Heart Circ Physiol 2018;315:H699–708.

27. Guihaire J, Haddad F, Boulate D, et al. Non-invasive indices of right ventricular function are markers of ventricular-arterial coupling rather than ventricular contractility: insights from a porcine model of chronic pressure overload. Eur Heart J Cardiovasc Imaging 2013;14:1140–9.

28. Vanderpool RR, Desai AA, Knapp SM, et al. How prostacyclin therapy improves right ventricular function in pulmonary arterial hypertension. Eur Respir J 2017;50:1700764.

29. Okumura K, Slorach C, Mroczek D, et al. Right ventricular diastolic performance in children with pulmonary arterial hypertension associated with congenital heart disease: correlation of echocardiographic parameters with invasive reference standards by high-fidelity micromanometer catheter. Circ Cardiovasc Imaging 2014;7:491–501.

30. Rushmer RF, Crystal DK, Wagner C. The functional anatomy of ventricular contraction. Circ Res 1953;1:162–70.

31. Leather HA, Ama R, Missant C, Rex S, Rademakers FE, Wouters PF. Longitudinal but not circumferential deformation reflects global contractile function in the right ventricle with open pericardium. Am J Physiol Heart Circ Physiol 2006;290:H2369–75.

32. Puwanant S, Park M, Popovic ZB, et al. Ventricular geometry, strain, and rotational mechanics in pulmonary hypertension. Circulation 2010;121:259–66.

33. Marwick TH. Measurement of strain and strain rate by echocardiography: ready for prime time? J Am Coll Cardiol 2006;47:1313–27.

34. Sachdev A, Villarraga HR, Frantz RP, et al. Right ventricular strain for prediction of survival in patients with pulmonary arterial hypertension. Chest 2011;139:1299–309.

35. Inuzuka R, Hsu S, Tedford RJ, Senzaki H. Single-beat estimation of right ventricular contractility and its coupling to pulmonary arterial load in patients with pulmonary hypertension. J Am Heart Assoc 2018;7:e007929.

KEY WORDS contractility, coupling, lusitropic function, morphology, pulmonary hypertension, right ventricular contractile function, speckle tracking, strain

APPENDIX For an expanded Methods section and supplemental figures, please see the online version of this paper.

Am J Physiol Heart Circ Physiol 318: H156–H164, 2020.
First published November 22, 2019; doi:10.1152/ajpheart.00485.2019.

RESEARCH ARTICLE | *Integrative Cardiovascular Physiology and Pathophysiology*

Right ventricular function correlates of right atrial strain in pulmonary hypertension: a combined cardiac magnetic resonance and conductance catheter study

Khodr Tello,[1] Antonia Dalmer,[1] Rebecca Vanderpool,[2] Hossein A. Ghofrani,[1,3,4] Robert Naeije,[5] Fritz Roller,[6] Werner Seeger,[1] Merle Wiegand,[1] Henning Gall,[1] and Manuel J. Richter[1]

[1]*Department of Internal Medicine, Justus Liebig University Giessen, Universities of Giessen and Marburg Lung Center, German Center for Lung Research, Giessen, Germany;* [2]*Division of Translational and Regenerative Medicine, University of Arizona, Tucson, Arizona;* [3]*Department of Pneumology, Kerckhoff Heart, Rheuma and Thoracic Center, Bad Nauheim, Germany;* [4]*Department of Medicine, Imperial College London, London, United Kingdom;* [5]*Erasme University Hospital, Brussels, Belgium; and* [6]*Department of Radiology, Justus Liebig University Giessen, Universities of Giessen and Marburg Lung Center, German Center for Lung Research, Giessen, Germany*

Submitted 27 August 2019; accepted in final form 15 November 2019

Tello K, Dalmer A, Vanderpool R, Ghofrani HA, Naeije R, Roller F, Seeger W, Wiegand M, Gall H, Richter MJ. Right ventricular function correlates of right atrial strain in pulmonary hypertension: a combined cardiac magnetic resonance and conductance catheter study. *Am J Physiol Heart Circ Physiol* 318: H156–H164, 2020. First published November 22, 2019; doi:10.1152/ajpheart.00485.2019.— The functional relevance of right atrial (RA) function in pulmonary hypertension (PH) remains incompletely understood. The purpose of this study was to explore the correlation of cardiac magnetic resonance (CMR) feature tracking-derived RA phasic function with invasively measured pressure-volume (P-V) loop-derived right ventricular (RV) end-diastolic elastance (E_{ed}) and RV-arterial coupling [ratio of end-systolic elastance to arterial elastance (E_{es}/E_a)]. In 54 patients with severe PH, CMR was performed within 24 h of diagnostic right heart catheterization and P-V measurements. RA phasic function was assessed by CMR imaging of RA reservoir, passive, and active strain. The association of RA phasic function with indexes of RV function was evaluated by Spearman's rank correlation and linear regression analyses. Median [interquartile range] RA reservoir strain, passive strain, and active strain were 19.5% [11.0–24.5], 7.0% [4.0–12.0], and 13.0% [7.0–18.5], respectively. E_{es}/E_a was 0.73 [0.48–1.08], and E_{ed} was 0.14 mmHg/mL [0.05–0.22]. RV diastolic impairment [RV end-diastolic pressure (EDP) and E_{ed}] was correlated with RA phasic function, but E_a and E_{es} were not. In addition, RA phasic function was correlated with inferior vena cava diameter. In multivariate linear regression analysis, adjusting for key P-V loop indexes, E_{ed} and EDP remained significantly associated with RA phasic function. We conclude that RA phasic function is altered in relation to impaired diastolic function of the chronically overloaded right ventricle and contributes to backward venous flow and systemic congestion. These results call for more attention to RA function in the management of patients with PH.

NEW & NOTEWORTHY There is growing awareness of the importance of the right atrial (RA)-right ventricular (RV) axis in pulmonary hypertension (PH). Our results uncover alterations in RA phasic function that are related to depressed RV lusitropic function and contribute to backward venous return and systemic congestion in chronic RV overload. Assessment of RA function should be part of the management and follow-up of patients with PH.

coupling; feature tracking; pulmonary hypertension; right atrial strain; right ventricular diastolic function

INTRODUCTION

Pulmonary hypertension (PH) is characterized by an increase in afterload, which induces progressive right ventricular (RV) remodeling with increased contractility (to maintain RV-arterial coupling) and diastolic stiffening, eventually leading to RV dilatation and clinical right heart failure (28, 34). RV failure is the leading cause of mortality in PH (18). PH and RV failure also lead to changes in right atrial (RA) size, function, and pressure, which are associated with a poor prognosis (15, 26, 27, 35). A recent two-dimensional echocardiographic speckle-tracking study suggested that RA reservoir and passive conduit functions are impaired in severe PH independently of RA size and pressure, likely reflecting RV failure and overload (26). Thus, the impact of RV failure on the right atrium is an essential part of the pathophysiology of PH, and the assessment of RA function appears essential to a better understanding of RV function in PH.

Awareness of the importance of the RA-RV axis in PH is growing. Several echocardiographic speckle tracking studies have reported on RA deformation and function in patients with PH (3, 7, 32), and RA reservoir function has been suggested to play a key role in the progression of PH (3, 7, 32). Cardiac magnetic resonance (CMR) imaging remains the reference imaging modality in patients with PH (6, 13, 37). Accordingly, it has also been recently applied to feature-tracking assessment of RA phasic function (19). However, the functional relevance of imaging studies of RA function remains incompletely understood.

Therefore, the purpose of the present study was to relate CMR imaging of RA function to invasively measured pressure-volume (P-V) relationships of the right ventricle including gold-standard determinations of contractility [measured as end-systolic elastance (E_{es})], afterload [measured as arterial elas-

Address for reprint requests and other correspondence: K. Tello, Dept. of Internal Medicine, Justus-Liebig-Univ. Giessen, Klinikstrasse 32, 35392 Giessen, Germany (e-mail: khodr.tello@innere.med.uni-giessen.de).

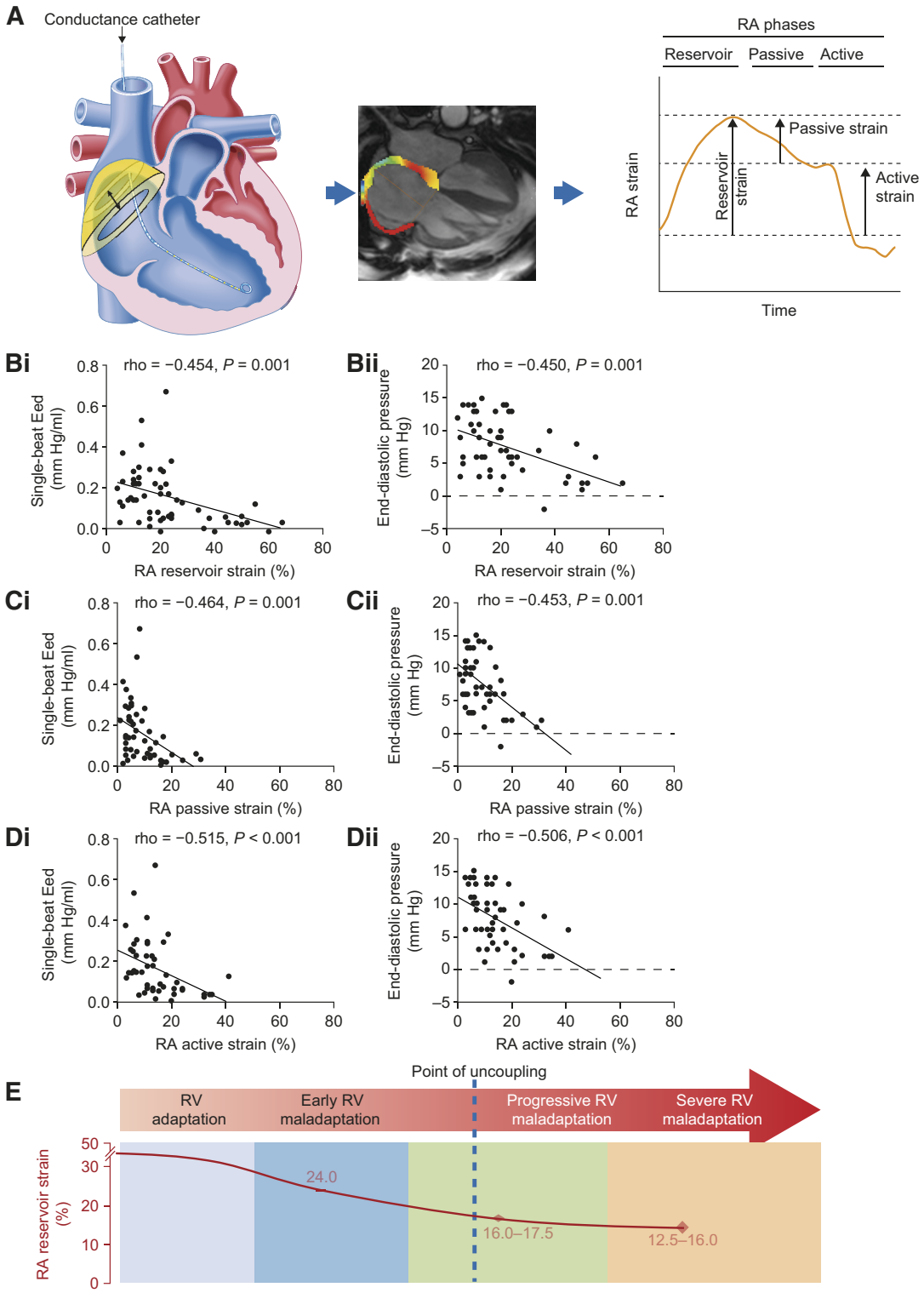

Fig. 1. Association of cardiac magnetic resonance (CMR) right atrial (RA) phasic function with right ventricular (RV) diastolic function derived from pressure-volume loop measurements. Schematic illustration of CMR-derived RA strain assessment in combination with pressure-volume catheterization, and an example of CMR feature tracking of RA reservoir, passive, and active strain (*A*). Correlation of CMR RA reservoir strain (*B*), passive strain (*C*), and active strain (*D*) with end-diastolic elastance (E_{ed}; *Bi*, *Ci*, and *Di*) and end-diastolic pressure (*Bii*, *Cii*, and *Dii*; in each panel, $n = 49–54$ patients). Spearman's rank was used to measure associations between variables (trend lines were least-squares fits of straight-line models). Progressive RV maladaptation is accompanied by decreasing RA reservoir strain [*E*; concept adapted from Vonk Noordegraaf et al. (45)]. The initial level of RA reservoir strain (before RV adaptation and maladaptation) was estimated on the basis of previous publications (14, 24). Values for RA reservoir strain during RV adaptation and maladaptation were based on median values obtained after stratification by E_{ed} and the end-systolic elastance-to-arterial elastance ratio (E_{es}/E_a) tertiles (Supplemental Fig. S1 and Supplemental Tables S1 and S2; all Supplemental Material is available at https://dx.doi.org/10.17504/protocols.io.8wjhxcn).

Table 1. *Patient characteristics and pulmonary hemodynamics*

	Value
Patients, *n*	54
Male/female, *n*/*n*	27/27
Age, yr	55 ± 14
PH subtype, *n* (%)	
Idiopathic pulmonary arterial hypertension	37 (68.5)
Heritable pulmonary arterial hypertension	1 (1.9)
Pulmonary arterial hypertension associated with	
Human immunodeficiency virus infection	2 (3.7)
Portal hypertension	3 (5.6)
Connective tissue disease	3 (5.6)
Congenital heart disease	1 (1.9)
Pulmonary arterial hypertension with overt features of venous/capillary involvement	2 (3.7)
Chronic thromboembolic PH	5 (9.3)
WHO functional class, *n* (%)	
I	3 (5.6)
II	19 (35.2)
III	29 (53.7)
IV	3 (5.6)
Right heart catheterization	
Mean pulmonary arterial pressure, mmHg	45 ± 14
Right atrial pressure, mmHg	7 ± 3
Pulmonary vascular resistance, Wood units	6.8 [4.4–10.1]
Cardiac index, $L \cdot min^{-1} \cdot m^{-2}$	2.8 ± 0.7
Pulmonary arterial wedge pressure, mmHg	9 ± 3
Treatment, *n* (%)	
Phosphodiesterase type 5 inhibitor	27 (50)
Endothelin receptor antagonist	32 (59.3)
Soluble guanylate cyclase stimulator	19 (35.2)
Selexipag	4 (7.4)
Prostanoid	13 (24.1)
Combination therapy, *n* (%)	
Therapy naïve	5 (9.3)
Monotherapy	17 (31.5)
Dual therapy	16 (29.6)
Triple therapy	15 (27.8)
Laboratory	
BNP, pg/mL	102 [38–333]
Echocardiography	
Inferior vena cava diameter,* cm	1.9 ± 0.5

Values are means ± SD or medians [interquartile range], unless otherwise specified; *n* = no. of patients. BNP, B-type natriuretic peptide; PH, pulmonary hypertension; WHO, World Health Organization. *Here, *n* = 46 patients.

tance (E_a)], and diastolic stiffness [measured as end-diastolic elastance (E_{ed})] as previously described by our group (38, 43).

METHODS

Study design and patients. The analysis included consecutive patients with pulmonary arterial hypertension (PAH) and chronic thromboembolic PH who were prospectively enrolled into the Right Heart I study (ClinicalTrials.gov identifier: NCT03403868) and the Giessen PH Registry (9) between January 2016 and December 2018. Patients with atrial flutter or fibrillation were excluded. Diagnoses were made according to current guidelines (8) and updated recommendations (36), and each diagnosis was assessed by a multidisciplinary board including pulmonologists and radiologists before enrollment. The study population included a proportion of previously published patients (29, 38–42). P-V/Swan-Ganz catheterization was performed 1 day after CMR imaging. B-type natriuretic peptide (BNP) was measured in all patients with a commercially available, fully automated, two-site sandwich immunoassay (ADVIA Centaur BNP Test; Siemens Healthineers, Erlangen, Germany). Diameter of the inferior vena cava was measured as recommended (16). All patients were treated with targeted PH medications on the basis of clinical grounds and best standard of care. The investigation conforms with the principles of the Declaration of Helsinki and was approved by the ethics committee of the Faculty of Medicine at the University of Giessen (approval no. 108/15). Written informed consent was provided by all participating patients.

CMR imaging. CMR imaging of RV and left ventricular volumes was performed with the Avanto 1.5-T scanner system [gradient strength and slew rate: SQ-Engine (45 mT/m at 200 $T \cdot m^{-1} \cdot s^{-1}$); Siemens Healthineers, Erlangen, Germany].

RA myocardial feature tracking was performed off-line on the basis of balanced steady-state free precession cine images using dedicated software (cvi[42]; Circle Cardiovascular Imaging, Calgary, AB, Canada).

RA strain analysis was based on the four-chamber view only. Endocardial contours were drawn manually in end-systolic images with subsequent automatic tracking of the endocardial contour throughout the cardiac cycle. The quality of automatic tracking was checked. In case of insufficient automated border tracking, manual adjustments were made to the initial contour, and the algorithm was repeated. Segments were not excluded from the analysis, since contour drawing and tracking were not hindered by the right atrial appendage or the presence of a Eustachian valve in our cohort. Tracking was repeated three times, and averages were used for analysis as described in a comparable study (47). To test intraobserver and interobserver reproducibility of RA reservoir strain, 10 randomly sampled analyses were repeated twice by the same observer and by a second observer, respectively. As previously described (19), RA total reservoir strain and RA active strain were assessed by measuring the corresponding peak strains (Fig. 1*A*). RA passive strain was calculated as the difference between RA total reservoir strain and RA active strain.

RA maximum and minimum volumes were assessed at ventricular systole and diastole, respectively, using cvi[42] software. From these measurements, RA total emptying fraction was calculated as (RA maximum volume − RA minimum volume)/RA maximum volume.

Right heart catheterization. We inserted a Swan-Ganz catheter via the internal jugular vein using an 8-F introducer sheath. We assessed pressures continuously and recorded cardiac index as the average of

Table 2. *Pressure-volume loop and CMR measurements*

	Value
Pressure-volume loop measurements	
E_a, mmHg/mL	0.75 [0.46–1.01]
E_{es}, mmHg/mL	0.55 [0.33–0.76]
E_{es}-to-E_a ratio	0.73 [0.48–1.08]
E_{ed}, mmHg/mL	0.14 [0.05–0.22]
End-systolic pressure, mmHg	66 ± 23
End-diastolic pressure, mmHg	8 ± 4
CMR measurements of right atrium	
RA reservoir strain, %	19.5 [11.0–24.5]
RA passive strain,* %	7.0 [4.0–12.0]
RA active strain,* %	13.0 [7.0–18.5]
RA total emptying fraction,† %	35 ± 14
RA maximum volume indexed to BSA,† mL/m^2	58.9 [46.6–90.0]
RA minimum volume indexed to BSA,† mL/m^2	36.2 [27.5–60.2]
CMR measurements of right ventricle	
RV EDV indexed to BSA, mL/m^2	116.9 ± 40.0
RV end-diastolic mass indexed to BSA, g/m^2	41.1 ± 18.0
RV mass-to-volume ratio, g/mL	0.4 ± 0.1
RV ejection fraction, %	39.3 [27.2–48.2]
Left ventricle	
LV ejection fraction,‡ %	62.8 [56.3–68.1]

Values are means ± SD or medians [interquartile range]. BSA, body surface area; CMR, cardiac magnetic resonance; E_a, arterial elastance; EDV, end-diastolic volume; E_{ed}, end-diastolic elastance; E_{es}, end-systolic elastance; LV, left ventricular; RA, right atrial; RV, right ventricular. *Here, *n* = 49 patients; †*n* = 53 patients; ‡*n* = 48 patients.

three to five measurements (taken using the direct or indirect Fick method as available). We calculated pulmonary vascular resistance (PVR) as [mean pulmonary arterial pressure (mPAP) − pulmonary arterial wedge pressure]/cardiac output (8).

P-V catheterization. We obtained and analyzed P-V loops as described previously (38). Briefly, we positioned a 4-Fr P-V catheter (CA-41063; CD Leycom, Zoetermeer, The Netherlands) in the RV apex and used an intracardiac analyzer (Inca; CD Leycom) to display P-V loops in real time. We calculated E_a as the ratio of end-systolic pressure (ESP) to stroke volume and used the RV single-beat method to calculate E_{es} (4). RV-arterial coupling was defined as the ratio of E_{es} to E_a (E_{es}/E_a). We calculated diastolic stiffness β by fitting a nonlinear exponential curve $P = \alpha(e^{\beta V} - 1)$ through three points on the diastolic portion of the P-V loops using a custom MATLAB program, and we obtained E_{ed} from the relationship $dP/dV = \alpha\beta \times e^{\beta \times EDV}$ at calculated end-diastolic volumes (EDV; α is a curve-fit parameter; 44). When the P-V loops showed a clear overlap, we chose a single beat for extrapolation to a sinusoidal curve and for analysis of E_{ed}. Volume measurements were calibrated with CMR imaging data.

Statistical analyses. Statistical analysis and presentation followed the Guidelines in Cardiovascular Research article by Lindsey et al.

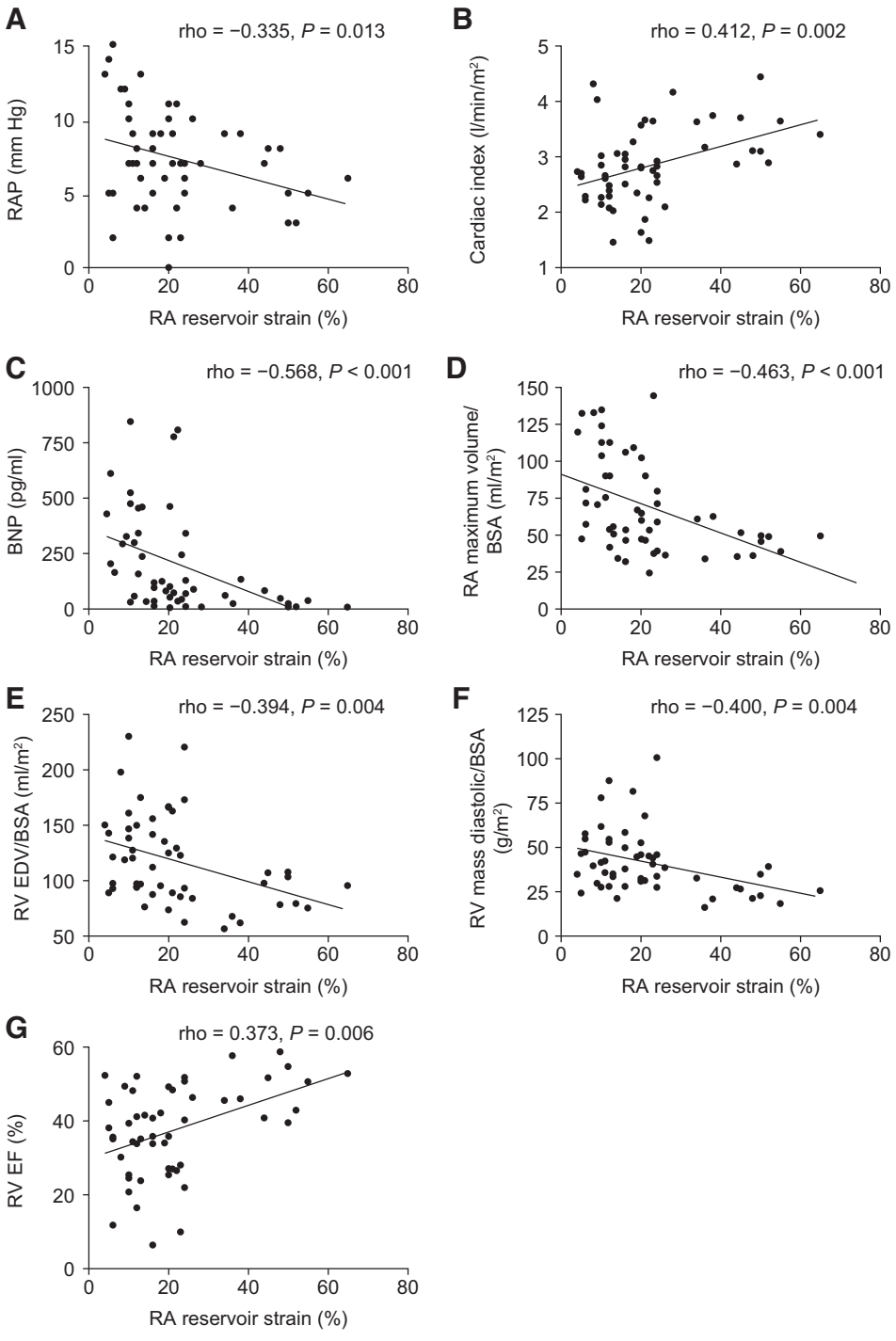

Fig. 2. Correlation of cardiac magnetic resonance imaging-derived right atrial (RA) reservoir function with pulmonary hemodynamics, B-type natriuretic peptide (BNP) levels, RA volume, and right ventricular (RV) function, dilatation, and hypertrophy. RA reservoir strain was correlated with right atrial pressure (RAP; *A*), cardiac index (*B*), BNP levels (*C*), RA maximum volume indexed to body surface area (BSA; *D*), RV end-diastolic volume (EDV) indexed to BSA (*E*), RV end-diastolic mass indexed to BSA (*F*), and RV ejection fraction (EF; *G*). In each panel, $n = 53$ to 54 patients. Spearman's rank was used to measure associations between variables (trend lines were least-squares fits of straight-line models).

(20). We determined adherence to a Gaussian distribution using the Kolmogorov-Smirnov test and visual assessment of histograms. Spearman's rank was used to measure associations between variables (trend lines were least-squares fits of straight-line models). We used univariate and multivariate linear regression analysis with RA phasic function as the dependent variable to determine the association with P-V loop parameters. Multivariable analyses were adjusted to all P-V loop parameters with $P < 0.05$ in univariate analysis (31). Multicollinearity was assessed using the variance inflation factor. Nonnormally distributed parameters were natural log transformed for linear regression analysis and rechecked by visual assessment of histograms. For all analyses, $P < 0.05$ was considered statistically significant. SPSS version 23.0 (IBM, Armonk, NY) was used for statistical analyses.

RESULTS

Patients. In total, 54 patients with PH were included; most of the patients had idiopathic PAH, and the majority presented in World Health Organization (WHO) functional class III (Table 1). Pulmonary hemodynamics showed precapillary PH. A substantial proportion of the patients were receiving dual or triple combination targeted PH therapy. Five patients with incident PH without specific pulmonary vascular therapy were included, one of whom had chronic thromboembolic PH (CTEPH) that was judged operable; this patient was referred for pulmonary endarterectomy surgery. The remaining four patients with CTEPH were previously judged inoperable by the local CTEPH board, had already received soluble guanylate cyclase stimulators, and were reevaluated for balloon pulmonary angioplasty.

P-V loop measurements (Table 2) showed impaired RV-arterial coupling [E_{es}/E_a was substantially lower than the optimal ratio, which is considered to be 1.5–2.0 (12)]. CMR imaging-derived RA and RV measurements (Table 2) showed RA enlargement and a high RV EDV (indicating RV dilatation) and decreased RV ejection fraction (EF) compared with values reported in healthy individuals (25). The intraclass correlation coefficient for agreement between the different observers was 0.86 (95% confidence interval: 0.417–0.970; $P = 0.05$) with a coefficient of variation of 11% regarding the RA reservoir strain measurement.

Association of CMR RA phasic function with RV function and biomarkers. RA reservoir strain, passive strain, and active strain were significantly correlated with P-V loop-derived measurements of RV diastolic function [E_{ed} and end-diastolic pressure (EDP); Fig. 1, *B–D*], but no association with RV contractility (E_{es}) or afterload (E_a) or mPAP was observed (data not shown). Figure 1*E* presents our findings regarding worsening RA reservoir function in the context of the current pathophysiological concept of progressive RV maladaptation leading to RV failure [adapted from previous work by Vonk Noordegraaf and colleagues (45, 46)].

In addition, RA reservoir strain showed significant correlations with RA pressure (RAP), cardiac index, BNP, and RA maximum volume (Fig. 2, *A–D*). Moreover, significant correlations with RV dilatation (RV EDV), RV hypertrophy (RV end-diastolic mass), and RV EF were observed (Fig. 2, *E–G*). We observed significant correlations of RA passive strain with RAP (rho = −0.368; $P = 0.009$), cardiac index (rho = 0.389; $P = 0.006$), BNP (rho = −0.455; $P = 0.002$), RA maximum volume (rho = −0.405; $P = 0.004$), RV EDV (rho = −0.337; $P = 0.020$), RV end-diastolic mass (rho = −0.463; $P = 0.001$), and RV EF (rho = 0.482; $P = 0.001$). Of note, we also observed significant correlations of RA active strain with RAP (rho = −0.307; $P = 0.032$), cardiac index (rho = 0.426; $P = 0.002$), BNP (rho = −0.512; $P < 0.001$), RA maximum volume (rho = −0.556; $P < 0.001$), RV EDV (rho = −0.454; $P = 0.001$), RV end-diastolic mass (rho = −0.477; $P = 0.001$), and RV EF (rho = 0.455; $P = 0.001$). In addition, significant associations of RA reservoir strain (rho = 0.317; $P = 0.032$) and RA active strain (rho = 0.404; $P = 0.008$) with left ventricular EF were observed. RA reservoir strain, passive strain, and active strain were all significantly associated with the diameter of the inferior vena cava (Fig. 3).

Determinants of RA phasic function. In univariate linear regression analysis, the B-coefficient indicated that an increase in E_{ed} and EDP was significantly associated with a reduction of RA reservoir strain. In the corresponding multivariate model, we found that increased EDP was independently associated with reduced RA reservoir strain (Table 3). In addition, an increase in E_{ed}, EDP, and ESP and a decrease in E_{es}/E_a were

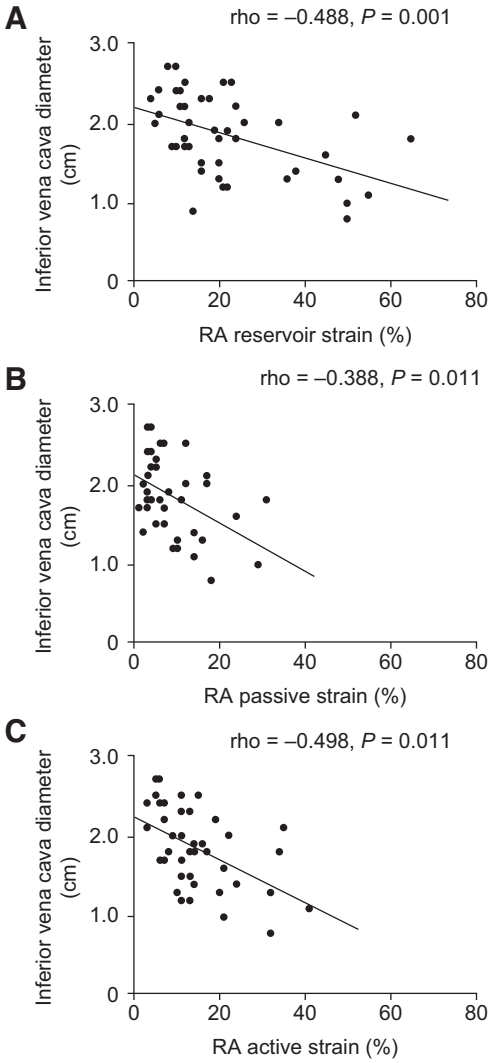

Fig. 3. Correlation of right atrial (RA) reservoir strain (*A*), RA passive strain (*B*), and RA active strain (*C*) with inferior vena cava diameter (in each panel, $n = 46$ patients). Spearman's rank was used to measure associations between variables (trend lines were least-squares fits of straight-line models).

Table 3. *Pressure-volume loop determinants of RA phasic function in univariate and multivariable linear regression analysis*

	RA Reservoir Strain		RA Passive Strain		RA Active Strain	
	B-coefficient (95% CI)*	*P*	B-coefficient (95% CI)*	*P*	B-coefficient (95% CI)*	*P*
Univariate						
E_a, mmHg/mL	−4.80 (−12.39 to 2.79)	0.210	−3.39 (−7.11 to 0.34)	0.074	−2.57 (−7.43 to 2.29)	0.292
E_{es}, mmHg/mL	3.06 (−3.50 to 9.61)	0.353	2.27 (−0.93 to 5.47)	0.160	2.48 (−1.62 to 6.58)	0.229
E_{es}-to-E_a ratio	5.42 (−0.38 to 11.21)	0.066	4.13 (1.32 to 6.95)	0.005	3.81 (0.07 to 7.55)	0.046
E_{ed}, mmHg/mL	−7.84 (−11.68 to −4.00)	<0.001	−3.49 (−5.40 to −1.58)	0.001	−4.76 (−7.16 to −2.36)	<0.001
ESP, mmHg	−9.34 (−19.80 to 1.12)	0.079	−5.60 (−10.84 to −0.37)	0.037	−5.77 (−12.56 to 1.01)	0.094
EDP, mmHg	−11.21 (−16.30 to −6.12)	<0.001	−5.93 (−8.26 to −3.61)	<0.001	−5.87 (−9.18 to −2.56)	<0.001
Multivariate†						
E_{ed}, mmHg					−3.25 (−6.50 to −0.001)	0.050
EDP, mmHg	−7.46 (−14.21 to −0.70)	0.031	−4.67 (−7.96 to −1.37)	0.007		

CI, confidence interval; E_a, arterial elastance; EDP, end-diastolic pressure; E_{ed}, end-diastolic elastance; E_{es}, end-systolic elastance; ESP, end-systolic pressure; RA, right atrial. *Unstandardized coefficients. †Adjusted with backward stepwise selection for pressure-volume loop parameters with $P < 0.05$ in univariate analysis.

significantly associated with a reduction of RA passive strain in univariate analysis. In a multivariate model with RA passive strain as the dependent variable, we found that an increase in EDP was independently associated with a reduction of RA passive strain (Table 3). Moreover, an increase in E_{ed} and EDP and a decrease in E_{es}/E_a were also significantly associated with a reduction of RA active strain in univariate analysis. In multivariate analysis, we found that increased E_{ed} was independently associated with reduced RA active strain (Table 3).

DISCUSSION

The present results show that in the setting of chronic pressure overload, RA phasic performance assessed with CMR feature tracking is predominantly altered in relation to RV diastolic function. Our data suggest that impairment of RV lusitropic function directly influences RA deformation, which in turn may be a cause of increased backward venous flow.

Untreated PH is a progressive disease, with the chronic pressure overload resulting in RV failure and maladaptation characterized by inappropriate RV hypertrophy, dilatation, fibrosis, remodeling, and impairment of both systolic and diastolic function (28, 45). The effect of progressive RV dysfunction on RA phasic performance remains incompletely understood and is therefore among the research areas open for exploration by advanced imaging of the right heart combined with state-of-the-art invasive functional assessment, as recently mentioned by an American Thoracic Society Research Statement (18). Our study provides further insights into this topic as we directly measured load-independent RV function via the acquisition of RV P-V loops with the assessment of E_{ed} as a measure of RV diastolic stiffness (33, 44), E_a as a lumped parameter of afterload (43), E_{es} as a marker of load-independent contractility (43), and E_{es}/E_a to describe RV-arterial coupling (43).

Impairment of RA phasic function was predominantly related to alterations of RV lusitropy rather than RV contractility or coupling as assessed by invasive measurements of P-V relationships. In the course of pulmonary hypertension, the right ventricle adapts either through homeometric adaptation (increased contractility) or through heterometric adaptation (increased volumes) to maintain stroke volume. At a certain threshold of E_{es}/E_a (recently shown to be 0.805), E_{es} decreases (with no further possibility to increase) and E_{ed} increases (38). Median [interquartile range] E_{es}/E_a in our present study was 0.73 [0.48–1.08]. Therefore, one of the possible explanations for the lack of association of E_{es}/E_a with RA strain parameters is that most of the patients had surpassed the "point of uncoupling" of 0.805.

Altered RA phasic function may be a cause and consequence of RV stiffness and increased EDP; the direction of causality is not clear. Similar to the right ventricle, the right atrium appears to respond to increased loading by both increased dimension and increased contractility to boost RV filling (10, 11) until excessive RA dilation and stiffness occurs, with subsequent RA-RV "uncoupling." Therefore, the observed association between RV diastolic stiffness and RA phasic function is consistent with the fact that RV myocardial stiffening leads to reduced passive inflow and a backward diastolic flow, impairing early diastolic filling and causing a large proportion of RV filling to be dependent on the final atrial contraction (2, 5). When atrial function is impaired, there is increased backward venous flow and subsequent deterioration of clinical signs of RV failure. Our data show significant correlations of RA phasic strain with RA size and inferior vena cava diameter, indicating that loss of reservoir function leads to backward venous flow. This is supported by recent data from Marcus et al., who measured load-independent RV parameters using a modified method without P-V loops and showed an association of backward venous flow during atrial contraction with RV diastolic stiffness (21). Although the main cause for venous backflow seems to be RV diastolic stiffness rather than RV-arterial uncoupling, the latter might contribute indirectly by first leading to elevation of RV volumes, with significant elevation of diastolic stiffness occurring as a second step.

Our findings are consistent with previous studies of RA strain demonstrating the prognostic relevance of RA reservoir function (14) and showing significant associations of RA

phasic function with RAP (assessed via echocardiography; 48), disease severity (WHO functional class; 22), and outcome (1, 3). Of note, we also observed a significant association with left ventricular EF. However, the extent to which alterations in RA phasic function might contribute to ventricular interdependency (23) deserves further investigation.

The present results are also consistent with a previous demonstration of impaired echocardiography-derived RA reservoir function (longitudinal strain) that was not correlated with mPAP or PVR in patients with PAH (26). However, a study in pediatric patients with PAH reported significant associations of echocardiography-derived RA reservoir function with PVR and mPAP as well as echocardiography-derived systolic parameters (tricuspid annular plane systolic excursion, fractional area change, and RV reservoir strain; 15). The reasons for these discrepancies are difficult to assess but may be further elucidated by more robust CMR imaging studies.

Limitations. We used a single-beat method rather than a multibeat method to estimate E_{ed}, E_{es}, and E_a. It is unclear whether this would affect the results, as the single-beat method was recently validated against the multibeat method (30). The sample size precluded meaningful race- and sex-specific analysis but was reasonable given the demanding methodology. The study population showed a near-equal distribution between women and men. Interestingly, our cohort is quite comparable to that of the Swedish Pulmonary Arterial Hypertension Registry, which has been published recently (17). Absence of female predominance in the present study may be related to sample size and yet-unclear evolution of referral biases (17). Diastolic echocardiographic indexes of ventricular function were not assessed and need further evaluation since echocardiography is more accessible than CMR in most PH centers. Also, information of RV function is provided by longitudinal RV shortening; the association of RA and RV feature tracking deserves further investigation in dedicated studies. Our limited sample size affected the regression analysis. The lack of a control group is another limitation to our study.

Of note, our analyses were performed with CMR feature tracking of the RA in the four-chamber view as previously published by other groups (19, 47). However, higher reliability and validity may have been achieved with a second plane in analyzing RA strain. Furthermore, there is a lack of standardization of the terms used to describe RA function. We used the terms "active," "passive," and "reservoir" strain, whereas some groups use "booster," "conduit," and/or "total" strain as corresponding terms (14, 19). Standardization of the methods and nomenclature would contribute to a better understanding of RA strain.

Conclusion. In the setting of chronic pressure overload, impaired RV diastolic function appears to be the dominant determinant of altered RA phasic performance, which in turn contributes to backward venous flow and systemic congestion. These observations call for improved therapeutic strategies targeting the RA-RV axis.

ACKNOWLEDGMENTS

For the manuscript, editorial assistance was provided by Claire Mulligan (Beacon Medical Communications Ltd., Brighton, UK).

GRANTS

This work was funded by the Excellence Cluster Cardio-Pulmonary System and by Deutsche Forschungsgemeinschaft (German Research Foundation) Projektnummer 268555672, Sonderforschungsbereich 1213, Project B08. Editorial assistance was funded by the University of Giessen.

DISCLOSURES

K. Tello has received speaking fees from Actelion and Bayer. H. A. Ghofrani has received consultancy fees from Bayer, Actelion, Pfizer, Merck, GSK, and Novartis; fees for participation in advisory boards from Bayer, Pfizer, GSK, Actelion, and Takeda; lecture fees from Bayer HealthCare, GSK, Actelion, and Encysive/Pfizer; industry-sponsored grants from Bayer HealthCare, Aires, Encysive/Pfizer, and Novartis; and sponsored grants from the German Research Foundation, Excellence Cluster Cardiopulmonary Research, and the German Ministry for Education and Research. R. Naeije has relationships with drug companies including AOPOrphan Pharmaceuticals, Actelion, Bayer, Reata, Lung Biotechnology Corporation, and United Therapeutics. In addition to being an investigator in trials involving these companies, relationships include consultancy service, research grants, and membership of scientific advisory boards. W. Seeger has received speaker/consultancy fees from Pfizer, Bayer Pharma AG, United Therapeutics, and Liquidia. H. Gall has received fees from Actelion, AstraZeneca, Bayer, BMS, GSK, Janssen-Cilag, Lilly, MSD, Novartis, OMT, Pfizer, and United Therapeutics. M. J. Richter has received support from United Therapeutics and Bayer; speaker fees from Actelion, Mundipharma, Roche, and OMT; and consultancy fees from Bayer. None of the other authors has any conflicts of interest, financial or otherwise, to disclose.

AUTHOR CONTRIBUTIONS

K.T., H.A.G., W.S., H.G., and M.J.R. conceived and designed research; K.T., A.D., F.R., W.S., M.W., H.G., and M.J.R. performed experiments; K.T., A.D., R.V., H.A.G., R.N., F.R., W.S., H.G., and M.J.R. analyzed data; K.T., A.D., R.V., H.A.G., R.N., F.R., W.S., M.W., H.G., and M.J.R. interpreted results of experiments; K.T. and M.J.R. prepared figures; K.T., A.D., R.V., H.A.G., R.N., F.R., W.S., M.W., H.G., and M.J.R. drafted manuscript; K.T., A.D., R.V., H.A.G., R.N., F.R., W.S., M.W., H.G., and M.J.R. edited and revised manuscript; K.T., A.D., R.V., H.A.G., R.N., F.R., W.S., M.W., H.G., and M.J.R. approved final version of manuscript.

REFERENCES

1. **Alenezi F, Mandawat A, Il'Giovine ZJ, Shaw LK, Siddiqui I, Tapson VF, Arges K, Rivera D, Romano MM, Velazquez EJ, Douglas PS, Samad Z, Rajagopal S.** Clinical utility and prognostic value of right atrial function in pulmonary hypertension. *Circ Cardiovasc Imaging* 11: e006984, 2018. doi:10.1161/CIRCIMAGING.117.006984.
2. **Andersen S, Nielsen-Kudsk JE, Vonk Noordegraaf A, de Man FS.** Right ventricular fibrosis. *Circulation* 139: 269–285, 2019. doi:10.1161/CIRCULATIONAHA.118.035326.
3. **Bhave NM, Visovatti SH, Kulick B, Kolias TJ, McLaughlin VV.** Right atrial strain is predictive of clinical outcomes and invasive hemodynamic data in group 1 pulmonary arterial hypertension. *Int J Cardiovasc Imaging* 33: 847–855, 2017. doi:10.1007/s10554-017-1081-7.
4. **Brimioulle S, Wauthy P, Ewalenko P, Rondelet B, Vermeulen F, Kerbaul F, Naeije R.** Single-beat estimation of right ventricular end-systolic pressure-volume relationship. *Am J Physiol Heart Circ Physiol* 284: H1625–H1630, 2003. doi:10.1152/ajpheart.01023.2002.
5. **Burlew BS, Weber KT.** Cardiac fibrosis as a cause of diastolic dysfunction. *Herz* 27: 92–98, 2002. doi:10.1007/s00059-002-2354-y.
6. **Crowe T, Jayasekera G, Peacock AJ.** Non-invasive imaging of global and regional cardiac function in pulmonary hypertension. *Pulm Circ* 8: 2045893217742000, 2018. doi:10.1177/2045893217742000.
7. **Fukuda Y, Tanaka H, Ryo-Koriyama K, Motoji Y, Sano H, Shimoura H, Ooka J, Toki H, Sawa T, Mochizuki Y, Matsumoto K, Emoto N, Hirata K.** Comprehensive functional assessment of right-sided heart using speckle tracking strain for patients with pulmonary hypertension. *Echocardiography* 33: 1001–1008, 2016. doi:10.1111/echo.13205.
8. **Galiè N, Humbert M, Vachiery JL, Gibbs S, Lang I, Torbicki A, Simonneau G, Peacock A, Vonk Noordegraaf A, Beghetti M, Ghofrani A, Gomez Sanchez MA, Hansmann G, Klepetko W, Lancellotti P, Matucci M, McDonagh T, Pierard LA, Trindade PT, Zompatori M, Hoeper M.** 2015 ESC/ERS Guidelines for the diagnosis and treatment of pulmonary hypertension: The Joint Task Force for the Diagnosis and Treatment of Pulmonary Hypertension of the European Society of Cardiology (ESC) and the European Respiratory Society (ERS): Endorsed by: Association for European Paediatric and Congenital Cardiology (AEPC),

International Society for Heart and Lung Transplantation (ISHLT). *Eur Respir J* 46: 903–975, 2015. [Erratum in *Eur J Respir* 46: 1855–1856, 2015.] doi:10.1183/13993003.01032-2015.

9. **Gall H, Felix JF, Schneck FK, Milger K, Sommer N, Voswinckel R, Franco OH, Hofman A, Schermuly RT, Weissmann N, Grimminger F, Seeger W, Ghofrani HA.** The Giessen Pulmonary Hypertension Registry: survival in pulmonary hypertension subgroups. *J Heart Lung Transplant* 36: 957–967, 2017. doi:10.1016/j.healun.2017.02.016.
10. **Gaynor SL, Maniar HS, Bloch JB, Steendijk P, Moon MR.** Right atrial and ventricular adaptation to chronic right ventricular pressure overload. *Circulation* 112, *Suppl*: I212–I218, 2005. doi:10.1161/CIRCULATIONAHA.104.517789.
11. **Gaynor SL, Maniar HS, Prasad SM, Steendijk P, Moon MR.** Reservoir and conduit function of right atrium: impact on right ventricular filling and cardiac output. *Am J Physiol Heart Circ Physiol* 288: H2140–H2145, 2005. doi:10.1152/ajpheart.00566.2004.
12. **Hsu S.** Coupling right ventricular-pulmonary arterial research to the pulmonary hypertension patient bedside. *Circ Heart Fail* 12: e005715, 2019. doi:10.1161/CIRCHEARTFAILURE.118.005715.
13. **Jaijee S, Quinlan M, Tokarczuk P, Clemence M, Howard LS, Gibbs JS, O'Regan DP.** Exercise cardiac MRI unmasks right ventricular dysfunction in acute hypoxia and chronic pulmonary arterial hypertension. *Am J Physiol Heart Circ Physiol* 315: H950–H957, 2018. doi:10.1152/ajpheart.00146.2018.
14. **Jain S, Kuriakose D, Edelstein I, Ansari B, Oldland G, Gaddam S, Javaid K, Manaktala P, Lee J, Miller R, Akers SR, Chirinos JA.** Right atrial phasic function in heart failure with preserved and reduced ejection fraction. *JACC Cardiovasc Imaging* 12: 1460–1470, 2019. doi:10.1016/j.jcmg.2018.08.020.
15. **Jone PN, Schäfer M, Li L, Craft M, Ivy DD, Kutty S.** Right atrial deformation in predicting outcomes in pediatric pulmonary hypertension. *Circ Cardiovasc Imaging* 10: e006250, 2017. doi:10.1161/CIRCIMAGING.117.006250.
16. **Kiely DG, Levin D, Hassoun P, Ivy DD, Jone PN, Bwika J, Kawut SM, Lordan J, Lungu A, Mazurek J, Moledina S, Olschewski H, Peacock A, Puri GD, Rahaghi F, Schafer M, Schiebler M, Screaton N, Tawhai M, Van Beek EJ, Vonk-Noordegraaf A, Vanderpool RR, Wort J, Zhao L, Wild J, Vogel-Claussen J, Swift AJ.** Statement on imaging and pulmonary hypertension from the Pulmonary Vascular Research Institute (PVRI). *Pulm Circ* 9: 2045894019841990, 2019. doi:10.1177/2045894019841990.
17. **Kjellström B, Nisell M, Kylhammar D, Bartfay SE, Ivarsson B, Rådegran G, Hjalmarsson C.** Sex-specific differences and survival in patients with idiopathic pulmonary arterial hypertension 2008–2016. *ERJ Open Res* 5: 00075-2019, 2019. [Erratum in *ERJ Open Res* 5: 00075-2019-ERR, 2019]. doi:10.1183/23120541.00075-2019.
18. **Lahm T, Douglas IS, Archer SL, Bogaard HJ, Chesler NC, Haddad F, Hemnes AR, Kawut SM, Kline JA, Kolb TM, Mathai SC, Mercier O, Michelakis ED, Naeije R, Tuder RM, Ventetuolo CE, Vieillard-Baron A, Voelkel NF, Vonk-Noordegraaf A, Hassoun PM; American Thoracic Society Assembly on Pulmonary Circulation.** Assessment of right ventricular function in the research setting: knowledge gaps and pathways forward. an official American Thoracic Society Research Statement. *Am J Respir Crit Care Med* 198: e15–e43, 2018. doi:10.1164/rccm.201806-1160ST.
19. **Leng S, Dong Y, Wu Y, Zhao X, Ruan W, Zhang G, Allen JC, Koh AS, Tan RS, Yip JW, Tan JL, Chen Y, Zhong L.** Impaired cardiovascular magnetic resonance-derived rapid semiautomated right atrial longitudinal strain is associated with decompensated hemodynamics in pulmonary arterial hypertension. *Circ Cardiovasc Imaging* 12: e008582, 2019. doi:10.1161/CIRCIMAGING.118.008582.
20. **Lindsey ML, Gray GA, Wood SK, Curran-Everett D.** Statistical considerations in reporting cardiovascular research. *Am J Physiol Heart Circ Physiol* 315: H303–H313, 2018. doi:10.1152/ajpheart.00309.2018.
21. **Marcus JT, Westerhof BE, Groeneveldt JA, Bogaard HJ, de Man FS, Vonk Noordegraaf A.** Vena cava backflow and right ventricular stiffness in pulmonary arterial hypertension. *Eur Respir J* 54: 1900625, 2019. doi:10.1183/13993003.00625-2019.
22. **Meng X, Li Y, Li H, Wang Y, Zhu W, Lu X.** Right atrial function in patients with pulmonary hypertension: a study with two-dimensional speckle-tracking echocardiography. *Int J Cardiol* 255: 200–205, 2018. doi:10.1016/j.ijcard.2017.11.093.
23. **Naeije R, Badagliacca R.** The overloaded right heart and ventricular interdependence. *Cardiovasc Res* 113: 1474–1485, 2017. doi:10.1093/cvr/cvx160.
24. **Padeletti M, Cameli M, Lisi M, Malandrino A, Zacà V, Mondillo S.** Reference values of right atrial longitudinal strain imaging by two-dimensional speckle tracking. *Echocardiography* 29: 147–152, 2012. doi:10.1111/j.1540-8175.2011.01564.x.
25. **Petersen SE, Aung N, Sanghvi MM, Zemrak F, Fung K, Paiva JM, Francis JM, Khanji MY, Lukaschuk E, Lee AM, Carapella V, Kim YJ, Leeson P, Piechnik SK, Neubauer S.** Reference ranges for cardiac structure and function using cardiovascular magnetic resonance (CMR) in Caucasians from the UK Biobank population cohort. *J Cardiovasc Magn Reson* 19: 18, 2017. doi:10.1186/s12968-017-0327-9.
26. **Querejeta Roca G, Campbell P, Claggett B, Solomon SD, Shah AM.** Right atrial function in pulmonary arterial hypertension. *Circ Cardiovasc Imaging* 8: e003521, 2015. doi:10.1161/CIRCIMAGING.115.003521.
27. **Raymond RJ, Hinderliter AL, Willis PW IV, Ralph D, Caldwell EJ, Williams W, Ettinger NA, Hill NS, Summer WR, de Boisblanc B, Schwartz T, Koch G, Clayton LM, Jöbsis MM, Crow JW, Long W.** Echocardiographic predictors of adverse outcomes in primary pulmonary hypertension. *J Am Coll Cardiol* 39: 1214–1219, 2002. doi:10.1016/S0735-1097(02)01744-8.
28. **Ren X, Johns RA, Gao WD.** Right heart in pulmonary hypertension: from adaptation to failure. *Pulm Circ* 9: 2045894019845611, 2019. doi:10.1177/2045894019845611.
29. **Richter MJ, Grimminger J, Krüger B, Ghofrani HA, Mooren FC, Gall H, Pilat C, Krüger K.** Effects of exercise training on pulmonary hemodynamics, functional capacity and inflammation in pulmonary hypertension. *Pulm Circ* 7: 20–37, 2017. doi:10.1086/690553.
30. **Richter MJ, Peters D, Ghofrani HA, Naeije R, Roller F, Sommer N, Gall H, Grimminger F, Seeger W, Tello K.** Evaluation and prognostic relevance of right ventricular-arterial coupling in pulmonary hypertension. *Am J Respir Crit Care Med*. 2019 Sep 20. doi:10.1164/rccm.201906-1195LE.
31. **Rose L, Prins KW, Archer SL, Pritzker M, Weir EK, Misialek JR, Thenappan T.** Survival in pulmonary hypertension due to chronic lung disease: Influence of low diffusion capacity of the lungs for carbon monoxide. *J Heart Lung Transplant* 38: 145–155, 2019. doi:10.1016/j.healun.2018.09.011.
32. **Sakata K, Uesugi Y, Isaka A, Minamishima T, Matsushita K, Satoh T, Yoshino H.** Evaluation of right atrial function using right atrial speckle tracking analysis in patients with pulmonary artery hypertension. *J Echocardiogr* 14: 30–38, 2016. doi:10.1007/s12574-015-0270-4.
33. **Sanz J, Kariisa M, Dellegrottaglie S, Prat-González S, Garcia MJ, Fuster V, Rajagopalan S.** Evaluation of pulmonary artery stiffness in pulmonary hypertension with cardiac magnetic resonance. *JACC Cardiovasc Imaging* 2: 286–295, 2009. doi:10.1016/j.jcmg.2008.08.007.
34. **Sanz J, Sánchez-Quintana D, Bossone E, Bogaard HJ, Naeije R.** Anatomy, function, and dysfunction of the right ventricle: JACC state-of-the-art review. *J Am Coll Cardiol* 73: 1463–1482, 2019. doi:10.1016/j.jacc.2018.12.076.
35. **Sato T, Tsujino I, Ohira H, Oyama-Manabe N, Ito YM, Yamada A, Ikeda D, Watanabe T, Nishimura M.** Right atrial volume and reservoir function are novel independent predictors of clinical worsening in patients with pulmonary hypertension. *J Heart Lung Transplant* 34: 414–423, 2015. doi:10.1016/j.healun.2015.01.984.
36. **Simonneau G, Montani D, Celermajer DS, Denton CP, Gatzoulis MA, Krowka M, Williams PG, Souza R.** Haemodynamic definitions and updated clinical classification of pulmonary hypertension. *Eur Respir J* 53: 1801913, 2019. doi:10.1183/13993003.01913-2018.
37. **Stam K, van Duin RW, Uitterdijk A, Cai Z, Duncker DJ, Merkus D.** Exercise facilitates early recognition of cardiac and vascular remodeling in chronic thromboembolic pulmonary hypertension in swine. *Am J Physiol Heart Circ Physiol* 314: H627–H642, 2018. doi:10.1152/ajpheart.00380.2017.
38. **Tello K, Dalmer A, Axmann J, Vanderpool R, Ghofrani HA, Naeije R, Roller F, Seeger W, Sommer N, Wilhelm J, Gall H, Richter MJ.** Reserve of right ventricular-arterial coupling in the setting of chronic overload. *Circ Heart Fail* 12: e005512, 2019. doi:10.1161/CIRCHEARTFAILURE.118.005512.
39. **Tello K, Dalmer A, Husain-Syed F, Seeger W, Naeije R, Ghofrani HA, Gall H, Richter MJ.** Multibeat right ventricular-arterial coupling during a positive acute vasoreactivity test. *Am J Respir Crit Care Med* 199: e41–e42, 2019. doi:10.1164/rccm.201809-1787IM.
40. **Tello K, Dalmer A, Vanderpool R, Ghofrani HA, Naeije R, Roller F, Seeger W, Dumitrescu D, Sommer N, Brunst A, Gall H, Richter MJ.** Impaired right ventricular lusitropy is associated with ventilatory ineffi-

ciency in PAH. *Eur Respir J* 54: 1900342, 2019. doi:10.1183/13993003.00342-2019.

41. **Tello K, Dalmer A, Vanderpool R, Ghofrani HA, Naeije R, Roller F, Seeger W, Wilhelm J, Gall H, Richter MJ.** Cardiac magnetic resonance imaging-based right ventricular strain analysis for assessment of coupling and diastolic function in pulmonary hypertension. *JACC Cardiovasc Imaging* 12: 2155–2164, 2019. doi:10.1016/j.jcmg.2018.12.032.
42. **Tello K, Richter MJ, Axmann J, Buhmann M, Seeger W, Naeije R, Ghofrani HA, Gall H.** More on single-beat estimation of right ventriculoarterial coupling in pulmonary arterial hypertension. *Am J Respir Crit Care Med* 198: 816–818, 2018. doi:10.1164/rccm.201802-0283LE.
43. **Tello K, Seeger W, Naeije R, Vanderpool R, Ghofrani HA, Richter M, Tedford RJ, Bogaard HJ.** Right heart failure in pulmonary hypertension: diagnosis and new perspectives on vascular and direct right ventricular treatment. *Br J Pharmacol*. 2019 Sep 13. doi:10.1111/bph.14866.
44. **Vanderpool RR, Puri R, Osorio A, Wickstrom K, Desai A, Black S, Garcia JG, Yuan J, Rischard F.** Surfing the right ventricular pressure waveform: methods to assess global, systolic and diastolic RV function from a clinical right heart catheterization. *Pulm Circ*. 2019 Apr 29. doi:10.1177/2045894019850993.
45. **Vonk Noordegraaf A, Chin KM, Haddad F, Hassoun PM, Hemnes AR, Hopkins SR, Kawut SM, Langleben D, Lumens J, Naeije R.** Pathophysiology of the right ventricle and of the pulmonary circulation in pulmonary hypertension: an update. *Eur Respir J* 53: 1801900, 2019. doi:10.1183/13993003.01900-2018.
46. **Vonk Noordegraaf A, Westerhof BE, Westerhof N.** The relationship between the right ventricle and its load in pulmonary hypertension. *J Am Coll Cardiol* 69: 236–243, 2017. doi:10.1016/j.jacc.2016.10.047.
47. **von Roeder M, Kowallick JT, Rommel KP, Blazek S, Besler C, Fengler K, Lotz J, Hasenfuß G, Lücke C, Gutberlet M, Thiele H, Schuster A, Lurz P.** Right atrial-right ventricular coupling in heart failure with preserved ejection fraction. *Clin Res Cardiol*. 2019 May 3. doi:10.1007/s00392-019-01484-0.
48. **Wright LM, Dwyer N, Wahi S, Marwick TH.** Association with right atrial strain with right atrial pressure: an invasive validation study. *Int J Cardiovasc Imaging* 34: 1541–1548, 2018. doi:10.1007/s10554-018-1368-3.

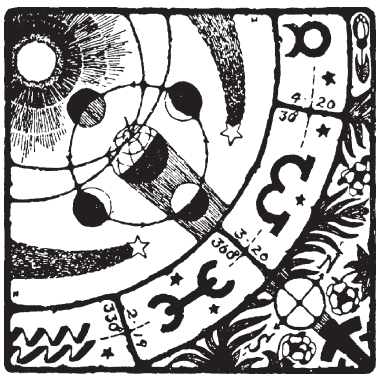

Cardiac MRI: Diagnostic Gain of an Additional Axial SSFP Chest Sequence for the Detection of Potentially Significant Extracardiac Findings in the Cardiac MRI Examination Setting

Diagnostischer Nutzen einer zusätzlichen axialen true-FISP Sequenz in der kardialen MRT-Untersuchung für die Detektion potentiell signifikanter extrakardialer Befunde?

Authors F. C. Roller[1], C. Schneider[1], A. Schuhbäck[2], A. Rolf[3], G. A. Krombach[1]

Affiliations
[1] University Hospital Giessen, Department Radiology
[2] University Hospital Giessen, Department Cardiology
[3] Kerckhoff Hospital Bad Nauheim, Department Cardiology

Key words
- cardiac
- MR imaging
- MR angiography

Zusammenfassung

Ziel: Die kardiale Magnetresonanztomografie (MRT) stellt eine sehr effektive Untersuchungsmethode des Herzens dar. Ziel unserer Studie war es zu untersuchen, ob sich die Integration einer zusätzlichen axialen Thoraxsequenz in der MRT-Untersuchung des Herzens vorteilhaft in Bezug auf die Detektion potentiell signifikanter extrakardialer Befunde auswirkt.

Material und Methoden: Insgesamt wurden 400 aufeinanderfolgende MRT-Untersuchungen des Herzens ausgewertet. Bei diesen Untersuchungen wurde zusätzlich zu den standardisierten kurzachsen und langachsen Sequenzen eine axiale SSFP Sequenz hinzugefügt, die den Thorax von der Lungenspitze bis zum Diaphragma abbildet. Es erfolgte eine separate Auswertung der Sequenzen hinsichtlich potentiell signifikanter extrakardialer Befunde.

Ergebnisse: Insgesamt wurden 25 potentiell signifikante extrakardiale Befunde in den 400 Patienten diagnostiziert. Hierunter waren 16 Pleuraergüsse mit unterschiedlichen Ausmaßen, eine Lungenfibrose, eine Spondylodiszitis, Aszites, mediastinale Lymphadenopathie, ein Mammakarzinomrezidiv mit Metastasen im Mediastinum, das Wachstum von Nebennierenmetastasen und unklarer Zwerchfellhochstand. Alle 25 potentiell signifikanten Nebenbefunde konnten in den Survey-Sequenzen detektiert werden. 24 der 25 potentiell signifikanten Nebenbefunde konnten in der zusätzlichen axialen Thoraxsequenz (SSFP) detektiert werden.

Schlussfolgerung: Unsere Studie zeigt, dass die Einführung einer axialen SSFP Sequenz zusätzlich zu den kardialen Standardsequenzen keine Mehrnutzen bei der Detektion potentiell signifikanter extrakardialer Befunde hat. Mit Hilfe der Survey-Sequenzen war es möglich alle potentiell signifikanten extrakardialen Nebenbefunde zu detektieren. Somit kommen wir zu dem Schluss, dass die

Abstract

Purpose: Cardiac MRI (CMRI) is an effective method for imaging of the heart. The aim of our study was to assess whether an axial chest sequence in addition to the standard CMR examination setting has advantages in the detection of potentially significant extracardiac findings (PSEF).

Materials and Methods: 400 consecutive patients were imaged at 1.5 T for clinical reasons. In addition to the standard long and short-axis views, an axial SSFP sequence was obtained covering the thorax from the lung apex to the diaphragm. All sequences were separately evaluated for PSEF.

Results: A total of 25 PSEF were diagnosed in 400 patients, including 16 pleural effusions, a pulmonary fibrosis, a spondylodiscitis, ascites, lymphadenopathies, relapse of a mamma carcinoma, growth of adrenal glands metastases and diaphragmatic elevation. All 25 PSEF were detected by reading survey sequences. 24 of the 25 PSEF were detected by the additional SSFP chest sequence as well as the CINE sequences.

Conclusion: In our study the additional axial SSFP chest sequence didn't show a benefit in the detection of PSEF. With the survey sequences we were able to detect all PSEF. We conclude that survey images should be assessed for additional findings.

Citation Format:
- Roller FC, Schneider C, Schuhbäck A et al. Cardiac MRI: Diagnostic Gain of an Additional Axial SSFP Chest Sequence for the Detection of Potentially Significant Extracardiac Findings in the Cardiac MRI Examination Setting. Fortschr Röntgenstr 2014; 186: 42–46

received 9.9.2012
accepted 25.6.2013

Bibliography
DOI http://dx.doi.org/10.1055/s-0033-1350193
Published online: 24.7.2013
Fortschr Röntgenstr 2014; 186: 42–46 © Georg Thieme Verlag KG Stuttgart · New York · ISSN 1438-9029

Correspondence
Herr Dr. Fritz Christian Roller
Radiologie, Universitätsklinikum Giessen
Klinikstraße 36
35392 Giessen
Germany
Tel.: ++ 49/06 41/98 55 63 29
Fax: ++ 49/06 41/98 54 18 09
fritz.c.roller@radiol.med.uni-giessen.de

Survey-Sequenzen in der kardialen MRT-Untersuchung gründlich hinsichtlich extrakardialer Nebenbefunde betrachtet werden sollten.

Introduction

Cardiac MRI (CMRI) is a noninvasive and effective method for imaging the heart and provides excellent visualization of cardiac structure and quantification of heart function. The imaging problems of the past due to cardiac motion were widely resolved by designing new sequences and increasing the imaging speeds at the beginning of this century. In the last decade CMRI has become a powerful diagnostic tool and now plays a significant role in the diagnosis of myocardial infarction, coronary artery diseases, congenital heart disease, non-ischemic cardiomyopathies, heart insufficiency, inflammation of the heart, infiltrative disorders, valvular diseases and heart tumors. To predict the suitability of CMRI and cardiac computed tomography (CT) for different issues and clinical scenarios, a German consensus document was developed in collaboration by the German Cardiac Society, the German Radiology Society and the German Society of Pediatric Cardiology [1]. For this purpose a 5-point scale was designed to rate the indication level for the use of CMRI and cardiac CT.

Beside the evaluation of the heart, additional imaging information is generated in the CMRI examination setting. Delineation of partly and totally included thoracic and abdominal structures with incidental detection of non-cardiac pathology is obtained. Potentially significant extracardiac findings (PSEF) and non-significant extracardiac findings can be distinguished. PSEF are defined as potentially important additional findings which perhaps require further evaluation with additional imaging or laboratory tests, tissue sampling, further clinical assessment or possibly therapeutic intervention in the patient management [2]. The prevalence of incidental findings in other cross-sectional imaging methods, for example CT-colonography [3 – 5] and cardiac CT, is already well described [6 – 12]. A newer study also assessed the prevalence of incidental findings in CT of the lumbar spine [13]. CMRI studies are less thoroughly investigated and only a few studies deal with the prevalence of potentially significant and non-significant extracardiac findings. In these studies extracardiac findings are reported with a wide range between 7.6 % and 81 % with a prevalence of potentially significant extracardiac findings between 3.1 % and 21 % [14 – 16]. In addition to these prevalence rates, the study of Wyttenbach et al. compared the intraobserver variability between the original clinical reading and the second dedicated reading of the CMR study. Wyttenbach et al. showed a significantly higher detection rate of secondary findings in the secondary image reading [16].

At our institution an additional axial SSFP (steady state free precession) chest sequence is implemented in the CMRI setting. This SSFP chest sequence covers the thorax from the lung apex to the diaphragm and requires an acquisition time of 20 to 30 seconds (**Fig. 1**). The reason for obtaining this sequence is to generate an overview of cardiac anatomy and to evaluate the thorax for additional findings.

The aim of our study was to systematically analyze the diagnostic gain of the additional axial SSFP sequence for the detection of PSEF.

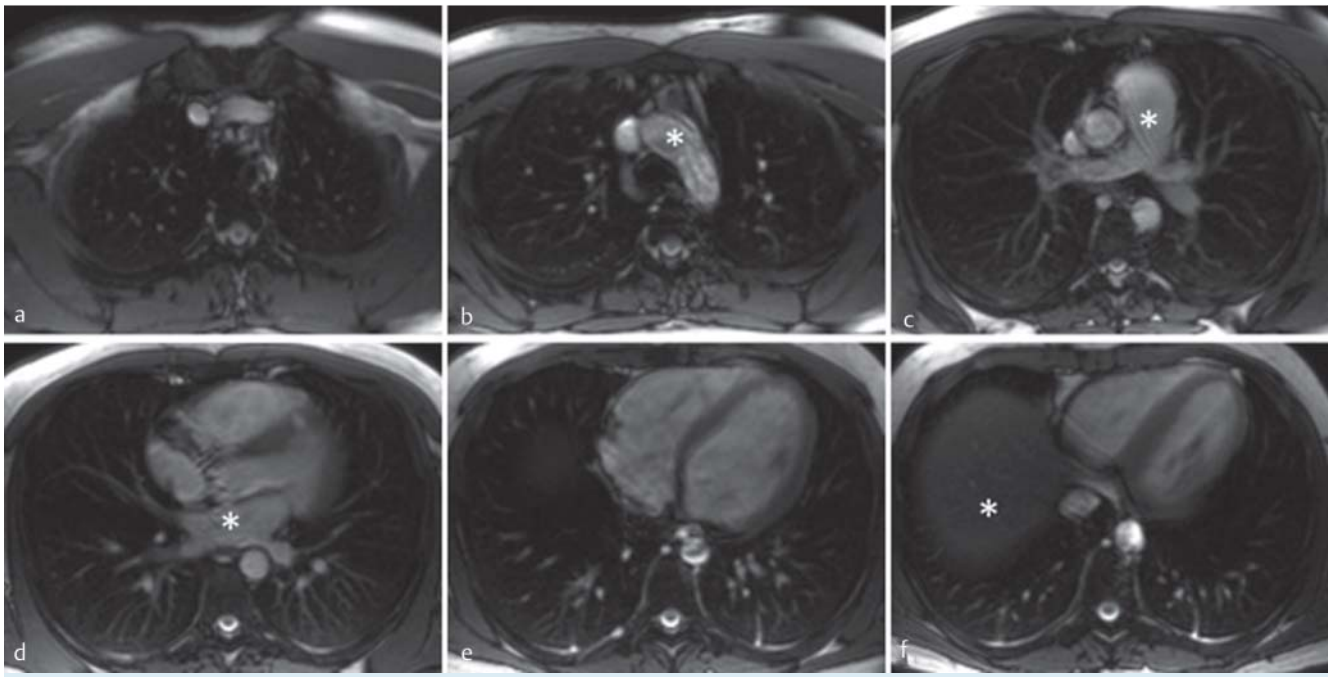

Fig. 1 The figure shows examples of the additional axial SSFP chest sequence at different heights in a healthy patient. **a** Apex of the lung **b** Aortic arch (white star) **c** Pulmonary trunk (white star) **d** Central lung veins (white star) **e** Two-chamber view of the heart **f** Including the diaphragm of the right side (white star)

Abb. 1 Die Abbildung zeigt Beispielbilder der axialen thorakalen SSFP Sequenz auf unterschiedlichen Höhen des Thorax in einem Normalbefund. **a** Lungenspitzenfeld **b** Aortenbogen (weißer Stern) **c** Truncus pulmonalis (weißer Stern) **d** Zentrale Lungenvenen (weißer Stern) **e** Zwei Kammer Blick des Herzens **f** Auf Höhe des rechten Zwerchfellschenkels (weißer Stern)

Materials and Methods

Imaging was performed with a Siemens Avanto 1.5 Tesla scanner and a Philips Intera 1.5 Tesla scanner using a dedicated cardiac coil. Standardized CMR examination protocols based on the clinical indications containing axial, coronal and sagittal thoracic survey images, balanced fast field echo sequences, SSFP sequences, black-blood sequences, late gadolinium enhancement sequences (LGE) and, when indicated clinically, myocardial perfusion sequences with intravenous adenosine infusion were used. In addition to the standard sequences, an axial SSFP sequence covering the thorax from the lung apex to the diaphragm with a slice thickness of 6 mm or 8 mm depending on the MRI scanner being used was obtained. The imaging parameters were: TR 285.16 ms, TE 1.14 ms, FoV 400x400, matrix 256x168 and 7.2 mm gap.

400 consecutive investigations were analyzed. All patients were imaged between April 2010 and September 2011. 223 males and 177 females were included in the current study. The mean age was 52 years (+/- 18 years standard deviation) with a range between 17 and 88 years. The most common indications for CMRI were ischemic heart diseases in 149 patients (37.25 %) and an aggregation of indications including cardiomyopathy, myocarditis and evaluation prior to implantation of implantable cardiac defibrillator (ICD) in 162 patients (40.5 %). The indications for the CMR studies are summarized in **Table 1**.

The axial SSFP images, the survey images covering the thorax from the lung apex to the upper abdomen (SSFP, TR 323.84 ms, TE 1.14 ms, FoV 352x356, matrix 272x170, slice thickness 8 mm and 32 mm gap) and the sequences tailored to imaging of the heart were evaluated in consensus for the presence of PSEF by two experienced readers. In addition, the age of all patients with PSEF was evaluated and the patients were summarized in age groups.

Results

A total of 25 PSEF were diagnosed including 16 pleural effusions with greater or lesser degrees of dystelectasis, an amiodarone-induced pulmonary fibrosis (**Fig. 2a, b**), a relapse of a mamma carcinoma with a mass in the upper mediastinum (**Fig. 2c, d**), a spondylodiscitis (**Fig. 3**), a lymphadenopathy at the hilum, a lymphadenopathy of the mediastinum, growth of adrenal gland

Table 1 CMRI indications.

Tab. 1 Indikationen für die Kardio-MRT Untersuchungen.

	total (n)	percent (%)
ischemic heart disease	149	37.25
cardiomyopathy, myocarditis and arrhythmia	162	40.5
congenital heart disease	18	4.5
Sarcoidosis	11	2.75
transposition of pulmonary veins	9	2.25
fabry disease	7	1.75
aortic aneurysm	7	1.75
thrombus	5	1.25
others (tumors)	22	5.5

Table 2 Summary of potentially significant extracardiac findings (PSEF).

Tab. 2 Zusammenfassung der potentiell signifikanten extrakardialen Befunde.

	total (n)
pleural effusion with dystelectasis	16
pulmonary fibrosis	1
spondylodiscitis	1
adrenal glands metastases	1
relapse of mamma carcinoma	1
hilary lymphadenopathy	1
mediastinal lymphadenopathy	1
liver cirrhosis with ascites	1
diaphragmatic elevation	2

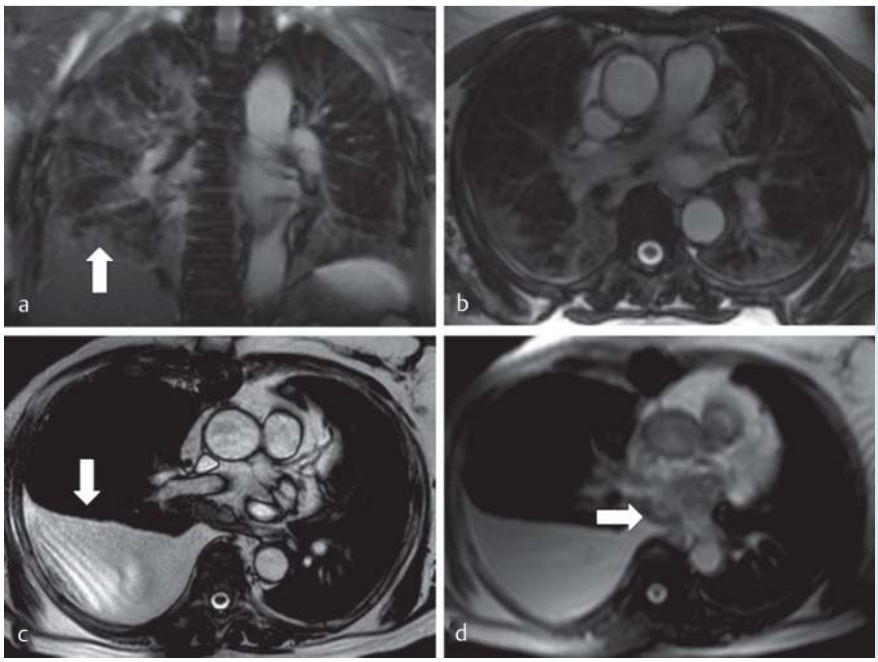

Fig. 2 Amiodarone-induced pulmonary fibrosis with thickening of the interlobular septa (white arrow) and indicated honeycombing are shown in a coronary survey sequence **a** and in the axial SSFP chest sequence **b**. Pleural effusion (white arrow) on the right side and a mediastinal mass (white star) in the case of a mamma carcinoma relapse are shown in an axial survey sequence **c** and in the axial SSFP chest sequence **d**.

Abb. 2 Die Abbildungen **a, b** zeigen die Amiodaron induzierte Lungenfibrose mit Verdickung des interlobulären Bindegewebes (weißer Pfeil) und angedeutete Wabenbildungen im Survey **a** und in der axialen SSFP Sequenz **b**. Die Abbildungen **c, d** zeigen eine Pleuraerguss (weißer Pfeil) und mediastinale Metastasen (weißer Stern) in einem Fall eines Mammakarzinom Rezidives im Survey **c** und in der axialen SSFP Sequenz **d**.

metastasis in a case of renal cancer (**Fig. 4a, b**), ascites in a patient with liver cirrhosis (**Fig. 4c, d**) and two cases of diaphragmatic elevation. The PSEF are summarized in **Table 2**.
A total of 16 PSEF (61.5 %) including the relapse of the mamma carcinoma, the growth of the adrenal gland metastasis, the spondylodiscitis and the amiodarone-induced pulmonary fibrosis were not known previously. In these 4 cases further additional imaging was required. In the case of the mamma carcinoma relapse, CT and PET (positron emission tomography)-CT were required, in the case of the adrenal gland metastases, CT was also required for further diagnostic measures, the spondylodiscitis required MRI, and the pulmonary fibrosis required HRCT (high-resolution computed tomography). 24 of the 25 PSEF were visible on the additional axial SSFP chest sequence and all PSEF were visible in the survey sequences. The adrenal gland metastases were not visualized in the cardiac examination sequences and in the additional SSFP chest sequence. This pathology was only delineated in the survey sequences. **Table 3** shows the PSEF in relation to the cardiac MRI sequences in which they were visible. 64 % of the PSEF were detected in the patient group older than 50 years and 78 % were detected in the patient group older than 40 years. **Table 4** shows the relationship between PSEF and patient age.

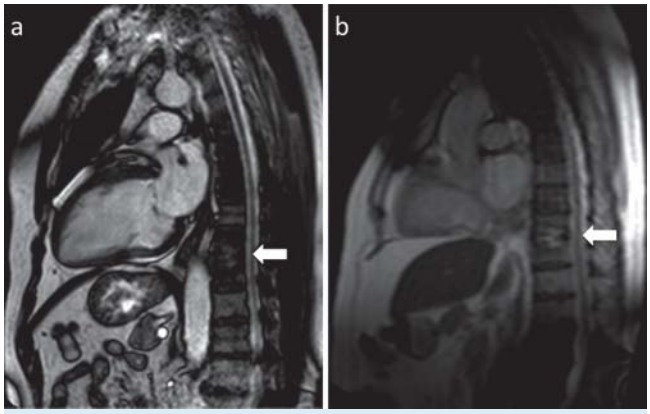

Fig. 3 The images show the spondylodiscitis (white arrows) with irregular signal intensity in the lesser thoracic spine – hypointense in the sagittal survey sequence **a** and hyperintense in the cardiac examination sequence **b**.

Abb. 3 Die Abbildung zeigt eine Spondylodiszitis (weiße Pfeile) in der unteren Brustwirbelsäule mit einem irregulären Signalmuster in der sagittalen Survey Sequenz mit hypointensem Signal **a** und in einer kardialen Untersuchungssequenz mit hyperintensem Signal **b**.

Discussion

With 6.25 % PSEF our study showed a comparable prevalence to previously published results [14 – 16]. A total of 16 PSEF (61.5 %) were not known previously. In 4 cases further imaging including HRCT, PET-CT, MRI and CT was required.
The implemented additional axial SSFP chest sequence in the CMRI setting poses an additional time loss of 20 – 30 seconds

Table 3 PSEF according to detecting sequences.

Tab. 3 Visualisierbarkeit potentiell signifikanter extrakardialer Befunde aufgegliedert nach kardialen MRT Sequenzen.

	total (n)	percent (%)
survey sequence	25	100
functional heart sequences	24	96
true-FISP sequence	24	96

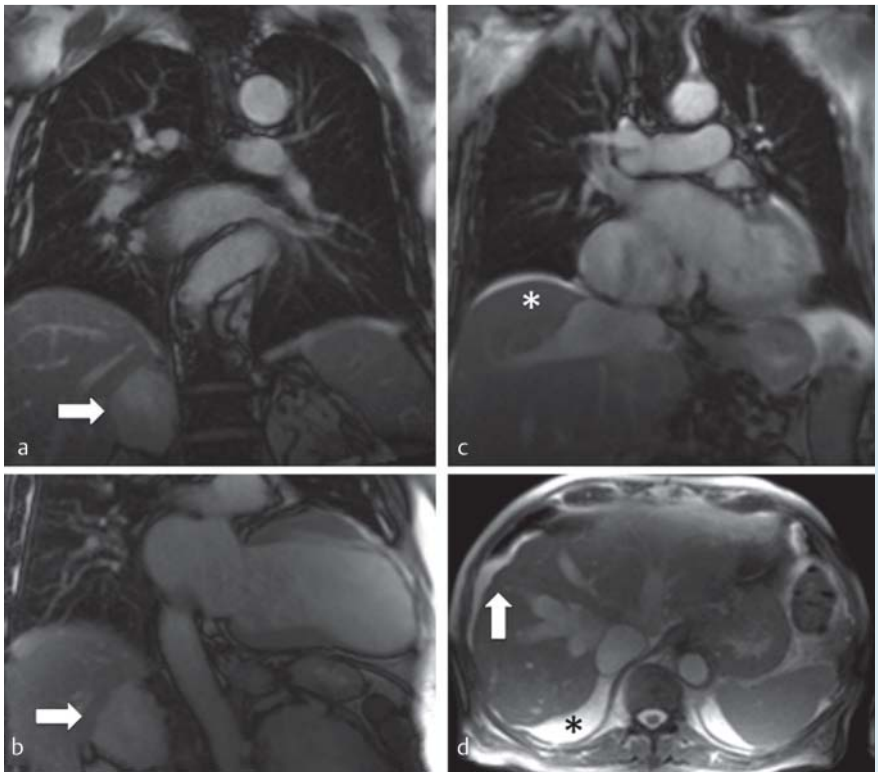

Fig. 4 The figure **a** shows huge adrenal gland metastases (white arrows) on the right side in the coronary survey sequence with a hyperintese signal and in a cardiac examination sequence **b** also with hyperintense signal (white arrows). Figure **c** shows hyperintense perihepatic fluid (ascites) in a case of liver cirrhosis in a coronary survey sequence and figure **d** shows the liver cirrhosis with perihepatic and perisplenic hyperintense fluid (ascites) (white and black star) and an inhomogeneous wavy liver contour (white arrow) in the axial SSFP sequence. The liver veins are also enlarged.

Abb. 4 Die Abbildung **a** zeigt eine große Nebennierenmetastase (weiße Pfeile) rechts in der koronaren Survey Sequenz mit hyperintensem Signalmuster und in einer koronaren kardialen Untersuchungssequenz ebenfalls mit hyperintensem Signalmuster **b**. Die Abbildung **c** zeigt in der koronaren Survey Sequenz einen hyperintensens perihepatischen Flüssigkeitssaum (Aszites) (weißer Stern) bei einer Leberzirrhose. Die Lebervenen sind aufgeweitet. Die Abbildung **d** zeigt eine inhomogene wellige Leberoberfläche (weißer Pfeil) bei aufgeweiteten Lebervenen sowie perihepatischer und perilienaler Flüssigkeit (hyperintenser Flüssigkeitssaum) (weißer und schwarzer Stern) in einem Fall von Leberzirrhose in der axialen SSFP Sequenz.

Table 4 PSEF according to summarized age groups.

Tab. 4 Zusammenfassung potentiell signifikanter extrakardialer Befunde in unterschiedliche Altersgruppen.

	total (n)	percent (%)
20 – 29	3	13
30 – 39	2	8.7
40 – 49	3	13
50 – 59	5	21.74
60 – 69	3	13
70 – 79	3	13
patients over 80 years	4	17.4
patients under 40 years	5	21.74
patients over 40 years	18	78.26
patients over 50 years	15	65.21

and didn't show a benefit in the detection of PSEF. Actually with the sequences tailored to imaging of the heart and with the survey sequences, we were able to detect all of the 25 PSEF.

One pathologic finding was not visible in the additional SSFP chest sequence. The adrenal gland metastases were only delineated by the survey sequences and were not known previously. Therefore, all pathologic findings were detectable by reading the survey images.

PSEF were preferentially detected among older age groups with 65 % of the PSEF detected in the age group older than 50 years. In a further study by Atalay et al., the most PSEF were detected in the patient group older than 60 years (85.6 %) [2].

In general, radiologists usually don't like reading survey images since these sequences with a large field of view are less appealing due to lower resolution and optimization for the delineation of prominent anatomical landmarks. Survey sequences only contain several slices in all three dimensions and do not cover the imaged region without a gap. In this context the larger field of view of the survey sequences compared to the additional axial SSFP chest sequence surely contributed to our result with better detection of additional findings. Otherwise, in our group of patients for example no smaller lung lesions or masses were detected and it remains unanswered if an additional axial SSFP chest sequence might be preferential in the detection of such lesions due to the smaller gap.

In the survey sequences as well as in the additional SSFP chest sequence, the diagnosis of PSEF is based on MRI morphologic characteristics without contrast agent injection. In this setting tailored imaging protocols, which contain multiple sequences with different weighting, are not available. Consequently, in some cases further and adequate characterization of the detected lesions upon CMRI is not possible. Scheduling further imaging sessions for patients or triaging them to different imaging modalities such as CT or PET-CT (positron emission tomography CT) might be necessary or required. For example, when uncertain liver lesions are detected, dynamic T1 sequences are needed to exclude hyper-vascularization in the case of questions regarding hepatocellular carcinomas.

Furthermore, when additional findings in cross-sectional imaging methods are described and additional and optimized imaging sessions in accordance with the respective research question are required, additional personnel costs and equipment costs are generated by the diagnosis of uncertain lesions. If the result is the detection of a previously unknown PSEF, early treatment might increase the success of the therapy and also effectively save costs. However, if the second examination reveals an insignificant finding or is still inconclusive, the follow-up costs might be increased without any benefit.

Conclusion

The results of the current study demonstrate that an axial SSFP chest sequence in the CMRI setting covering the chest from the lung apex to the diaphragm without a gap, optimized for the visualization of the heart and the mediastinum, did not show a benefit in detecting additional findings. In our group of patients all PSEF were visible on the survey images. In times of cost-effectiveness and time pressure, an additional axial SSFP chest sequence might not be necessary especially when high quality survey sequences are generated.

We conclude that the survey images in CMRI patients should be assessed for additional findings.

References

1 *Achenbach S, Barkhausen J, Beer M et al.* Konsensusempfehlung der DRG, DGK, DGPK zum Einsatz der Herzbildgebung mit Computertomografie und Magnetresonanztomografie. Fortsch Röntgenstr 2012; 184: 345 – 368

2 *Atalay MK, Prince EA, Pearson CA et al.* The prevalence and clinical significance of noncardiac findings on cardiac MRI. Am J Roentgenol Am J Roentgenol 2011; 196: W387 – W393

3 *Ginnerup Pedersen B, Rosenkilde M, Christiansen TE et al.* Extracolonic findings at computed tomography colonography are a challenge. Gut 2003; 52: 1744 – 1747

4 *Hara AK, Johnson CD, MacCarty RL et al.* Incidental extracolonic findings at CT colonography. Radiology 2000; 215: 353 – 357

5 *Hellstrom M, Svensson MH, Lasson A.* Extracolonic and incidental findings on CT colonography (virtual colonoscopy). Am J Roentgenol Am J Roentgenol 2004; 182: 631 – 638

6 *Dewey M, Schnapauff D, Teige F et al.* Non-cardiac findings on coronary computed tomography and magnetic resonance imaging. Eur Radiol 2007; 17: 2038 – 2043

7 *Haller S, Kaiser C, Buser P et al.* Coronary artery imaging with contrast-enhanced MDCT: extracardiac findings. Am J Roentgenol Am J Roentgenol 2006; 187: 105 – 110

8 *Horton KM, Post WS, Blumenthal RS et al.* Prevalence of significant noncardiac findings on electron-beam computed tomography coronary artery calcium screening examinations. Circulation 2002; 106: 532 – 534

9 *Hunold P, Schmermund A, Seibel RM et al.* Prevalence and clinical significance of accidental findings in electron-beam tomographic scans for coronary artery calcification. Eur Heart J 2001; 22: 1748 – 1758

10 *Mueller J, Jeudy J, Poston R et al.* Cardiac CT angiography after coronary bypass surgery: prevalence of incidental findings. Am J Roentgenol Am J Roentgenol 2007; 189: 414 – 419

11 *Onuma Y, Tanabe K, Nakazawa G et al.* Noncardiac findings in cardiac imaging with multidetector computed tomography. J Am Coll Cardiol 2006; 48: 402 – 406

12 *Schragin JG, Weissfeld JL, Edmundowicz D et al.* Non-cardiac findings on coronary electron beam computed tomography scanning. J Thorac Imaging 2004; 19: 82 – 86

13 *Lee SY, Landis MS, Ross IG et al.* Extraspinal findings at lumbar spine CT examination: Prevalence and clinical importance. Radiology 2012; 263: 502 – 509

14 *Chan PG, Smith MP, Hauser TH et al.* Noncardiac pathology on clinical cardiac magnetic resonance imaging. JACC Cardiovasc Imaging 2009; 2: 980 – 986

15 *McKenna DA, Laxpati M, Colletti PM.* The prevalence of incidental findings at cardiac MRI. Open Cardiovasc Med J 2008; 2: 20 – 25

16 *Wyttenbach R, Médioni N, Santini P et al.* Extracardiac findings detected by cardiac magnetic resonance imaging. Eur Radiol 2012; 22: 1295 – 1302